Analysis and Simulation of the Deformation Behaviour at Quasi-Static Compressive Stressing of Bonded Model Pellets

Dissertation

zur Erlangung des akademischen Grades

Doktoringenieurin / Doktoringenieur

(Dr.-Ing.)

von M.Sc. Zheni Radeva

geb. am 11.09.1987 in Dobrich, Bulgarien

genehmigt durch die Fakultät für Verfahrens-und Systemtechnikder Otto-von-Guericke-Universität Magdeburg

Promotionskommission: Prof. Berend van Wachem (Vorsitz)

Prof. Dr.-Ing. habil. Evangelos Tsotsas (Gutachter)

Prof. Dr.-Ing. Dr. h. c Sergiy Antonyuk (Gutachter)

Prof. Dr.-Ing. habil. Dr. h. c. Lothar Mörl (Gutachter)

eingereicht am: 24.01.2019

Promotionskolloquium am: 11.07.2019

Abstract

The main objective of this thesis is to experimentally investigate and simulate the influence of pelletising process parameters on the compression behaviour of model-pellets with different structures, sizes and shapes. Pelletising is applied in many industry branches for improving the flow and dosage behaviour and for regulating the bulk density of various materials. Its wide use creates the need to investigate the pellets and their properties in depth.

In order to gain better understanding about pellet properties and the behaviour of pellets under loading, model pellets were produced in a laboratory pelletizing plate. The primary particles used were aluminium oxide (γ-Al_2O_3) and zeolite 4A granules of various sizes. Their properties are well known and can be taken as a reference. Water solution of hydroxypropylmethyl cellulose (HPMC) having various concentrations was used as a binder. During production, the process parameters of rotation speed, process duration and binder content were varied in order to analyze their influence on the properties of the pellets produced.

Upon completing the manufacturing process, the model pellets were allowed to dry in atmospheric conditions. The pellets were divided into two fractions - tetrahedra (regular) and blackberry aggregates (irregular). The two fractions were studied separately to investigate the influence of the structure. Properties such as particle size distribution, density and porosity, internal spatial structure and behaviour of the pellets under load were examined in detail.

The results obtained were further used for carrying out DEM simulations of the fracturing process during loading of the pellets. Tomographic data for primary particle number and spatial coordinates allow for a very accurate replication of the pellets in the simulation software. Virtual compression tests were performed on the simulated pellets and the results were compared with the experimental data.

Pellet characterization has shown that the process parameters are of decisive importance for the formation and shape of the pellets. The detailed tomographic analysis has though proven that the process parameters influence only the binder distribution, not the arrangement and structure of the pellets. The experimental compression tests could be simulated using DEM and the results have been compared. For some of the simulations there is no possibility to realistically represent the solid bridges with their defects and micro-porosity in the DEM tool, so that the results deviate. The replication of experiments by means of DEM simulations is not possible in these cases.

Kurzzusammenfassung

Das Hauptziel dieser wissenschaftlichen Arbeit ist die experimentelle Untersuchung und nummerische Simulation des Einflusses von Prozessparametern beim Pelletieren auf das Bruchverhalten von Modellpellets unterschiedlicher Strukturen, Größen und Formen. Pelletieren wird in vielen Industrien zur Verbesserung des Fließ- und Dosierverhaltens und zur Regulierung der Schüttdichte verschiedener Materialien eingesetzt. Seine breite Verwendung macht es nötig, die Pellets und ihre Eigenschaften im Detail zu untersuchen.

Um bessere Kenntnisse über die Eigenschaften und das Verhalten von Pellets beim Belasten zu gewinnen, wurden Modellpellets in einem Labor-Pelletierteller hergestellt. Die Primärpartikel waren Granulate verschiedener Größe aus Aluminiumoxid (γ-Al_2O_3) und Zeolith 4A. Ihre Eigenschaften sind bekannt und können als Referenz genommen werden. Als Bindemittel wurden wassrige Lösungen von Hydroxypropyl-methylcellulose (HPMC) mit verschiedenen Konzentrationen verwendet. Bei der Herstellung wurden die Prozessparameter Rotationsgeschwindigkeit, Prozesszeit und Bindemittelanteil variiert, um ihren Einfluss auf die Eigenschaften der erzeugten Pellets zu analysieren.

Nach der Herstellung wurden die Modellpellets bei atmosphärischen Bedingungen getrocknet. Die Pellets wurden in zwei Fraktionen geteilt – Tetraeder (regulärförmig) und brombeerförmig (irregulär). Die beiden Fraktionen wurden separat untersucht, um den Einfluss der Pelletform zu erschließen. Eigenschaften wie Partikelgrößenverteilung, Dichte und Porosität, innere räumliche Struktur und das Verhalten unter Belastung wurden eingehend untersucht.

Charakterisierungsergebnisse wurden für die Durchführung von DEM Simulationen des Bruchprozesses der Pellets verwendet. Tomographische Daten zur Anzahl und zu den räumlichen Koordinaten der Primärpartikel, ermöglichen eine sehr genaue Nachbildung der Pellets in der Simulationssoftware. Mit den simulierten Pellets wurden Kompressionstests durchgeführt, und die Ergebnisse wurden mit den experimentellen Daten verglichen.

Die Charakterisierung hat gezeigt, dass die Prozessparameter bei Herstellung von entscheidender Bedeutung für die Formgebung und die Eigenschaften der Pellets sind. Die detaillierte tomographische Analyse hat aber deutlich gemacht, dass der Prozessparametereinfluß sich nur auf die Bindemittelverteilung bezieht, nicht jedoch auf Anordnugung und Aufbau eines Pellets. Die experimentellen Kompressionstests konnten mittels DEM nachgebildet und die Ergebnisse verglichen werden. Allerdings führt die fehlende

Möglichkeit, die Feststoffbrücken mit ihren Defekten und Mikro-Porosität in der DEM realisitsch darzustellen, mitunter zu Abweichungnen vom Experiment. Die Nachstellung der Druckversuche mittels DEM ist in solchen Fällen nicht möglich.

Content

Symbols

A_b	Bond cross-cut surface area	m^2
A_i	Projected area of a pellet	m^2
A_k	Contact surface area	m^2
A_{el}	Contact surface area during elastic deformation	m^2
A_{pl}	Contact surface area during are plastic deformation	m^2
A_s	Surface area	m^2
A_v	Function of Poisson's ratio	-
a	Scale parameter	$(kg/J)^z\ m^{-2}$
b	Shape parameter	-
D	Deformation	m
D_b	Diameter of bond	m
D_d	Disc diameter	m
D_f	Fractal dimension	-
$d_{50,3}$	Average diameter	m
d	Diameter of primary particle	m
$d_{c,max}$	Shortest maximal chord of particle projection	m
d_{eq}	Equivalent diameter	m
$d_{eq,Pa}$	Projected area equivalent diameter	m
$d_{eq,Stokes}$	Stokes diameter	m
$d_{eq,Surface}$	Equivalent surface diameter	m
$d_{eq,Volume}$	Volume equivalent diameter	m
d_f	Heuristically determined factor	-
d_i	Diameter of the particle i	m
E^*	Average modulus of elasticity for the contact partners	Pa
E_B	Breakage energy	J

E_b	Young's modulus of elasticity of the solid bonds	Pa
E_m	Specific breakage energy	J/kg
E_f	Young's modulus of elasticity measured in flexion	Pa
E_i	Modulus of elasticity / Young's modulus	Pa
F	Contact force	N
$\bar{F}$	Mean breakage force	N
$F_{A/O}$	Centrifugal force	N
$F_{b,n}$	Force in normal direction	N
$F_{b,t}$	Force in tangential direction	N
F_c	Centripetal force	N
F_{el}	Elastic contact force	N
$F_{el,1}$	Continius acting contac force	N
F_{el-pl}	Elastic-plastic contact force	N
$F_{el,w-p-w}$	Elastic contact force for wall-particle-wall contact	N
F_F	Yield force	N
F_G	Gravitational force	N
F_{pl}	Plastic contact force	N
F_R	Friction force	N
g	Gravitational acceleration	m/s^2
I	Mass moment of inertia	$kg{\cdot}m^2$
J	Polar moment of inertia	m^4
k	Coordination number	-
k_{el*}	Elastic contact stiffness in normal direction	N/m
k_{el}	Elastic stiffness	N/m
$k_{el,w-p-w}$	Overall elastic stiffness during wall-particle-wall contact	N/m
k_{el-pl}	Elastic-plastic stiffness	N/m
K_g	Frtactal pre-factor	-

k_n	Normal inter-particle contact stiffness	N/m
k_p, k_{pi}	Stiffness of the particle	N/m
k_{pl}	Plastic stiffness	N/m
$k_{p\text{-}w}$	Overall contact stiffness during wall-particle contact	N/m
k_{rot}	Stiffness of rotation	N/m
k_t	Tangential inter-particle contact stiffness	N/m
k_{tran}	Stiffness of translation	N/m
k_w, k_{wi}	Stiffness of the wall	N/m
$k_{w\text{-}p\text{-}w}$	Overall contact stiffness during wall-particle-wall contact	N/m
L	Length	m
L_b	Bond length	m
$L_{b,cur}$	Current length of the bond	m
$L_{b,in}$	Initial length of bond	m
$L_{b,rec}$	Recovery length	m
L_{pp}	Distance between two particles	m
$M_{b,n}$	Normal moment	kg
$M_{b,t}$	Tangential moment	kg
m_i	Mass	kg
m_g	Mass of granule	kg
m_s	Mass of the solid phase	kg
m_p	Mass of primary particle	kg
m_{mp}	Model pellet mass	kg
N_c	Number of inter-particle contacts	-
N_P	Number of particles	-
n_i	Single value	-
$\overrightarrow{n_{(ij)}}$	Normal vector	-
n_{cr}	Critical number of revolutions per minute	rpm

x

Symbol	Description	Unit
P	Probability function	-
P_{el}	Elastic pressure	Pa
P_F	Applied load at fracture	Pa
P_{max}	Maximal stress	Pa
P_p	Perimeter/circumference of a particle projection	m
p	Pressure	Pa
p_{max}	Maximal stress	Pa
$\dot{Q}$	Enthalpy	J
$Q_{0(x)}$	Cumulative number distribution	%
$Q_{1(x)}$	Cumulative length distribution	%
$Q_{2(x)}$	Cumulative area distribution	%
$Q_{3(x)}$	Cumulative mass distribution	%
R	Radius of circular contact area between two particle	m
R^{*}	Average radius of the contact partners	m
R^2	Regression coefficient	
R_b	Bond radius	m
R_e	Equivalent radius	m
R_g	Radius of gyration	m
R_i	Radius of contact partner	m
R_{ij}	Interval	m
r_d	Disc radius	m
r_k	Contact radius	m
$r_{k,el}$	Elastic contact radius	m
$r_{k,F}$	Contact radius at yield point	m
$r_{k,max}$	Maximum contact radius	m
$r_{k,pl}$	Plastic contact radius	m
$\overline{r}_n$	Unit vector between particles	m

r_p	Primary particle radius	m
$\vec{r_{(i)}}$	Particle centre vector coordinates	m
$\vec{r_{(w)}}$	Wall vector coordinates	m
$\vec{r_k^{(xw)}}$	Coordinates of the particle centres for a particle-wall contact	m
$\vec{r_k^{(xy)}}$	Coordinates of the particle centres for a particle-particle contact	m
S_m	Specific surface	m^2
s	Contact deformation	m
s_0	Starting position of the piston	m
s_B	Deformation of the bond	m
s_b	Displacement at breakage	m
s_F	Contact flattening	m
s_{ki}	Contact deformation of contact partner i	m
$s_n^{(xz)}$	Overlap at the contact point in normal direction	m
$s_t^{(xy)}$	Overlap at the contact point in tangential direction	m
T	Transformation matrix	-
$\overline{T}$	Density function	-
$T_{Rayleigh}$	Reyleigh time	s
t	Time	s
t_0	Total contact time	s
t_1	Time required to reach the peak contact force	s
$t_{cr,i}$	Critical time step	s
$t_{sim,recom}$	Recommended time step in the numerical simulation	s
V_e	Volume of empty cell	m^3
V_{exp}	Volume of reference cell	m^3
V_f	Volume of cell with sample	m^3

V_g	Granule volume	m^3
$V_{i,j}$	Space vector	m
V_P	Particle volume	m^3
$V_{rel,t}$	Tangential component of relative velocity vector	-
V_s	Solid phase volume	m^3
v_c	Critical velocity	m/s
v_p	Volume of pores	m^3
$v_t^{(xy)}$	Tangential component of the relative velocity	-
$x_{c,\,max}$	Shortest chord of the measured set of maximum chords	m
x_i, y_i, z_i	Centre Cartesian coordinates	m
$\dot{x}_i, \dot{y}_i, \dot{z}_i$	Velocity vectors	m

Greek Symbols

Γ	factorial function (gamma function)	-
γ	Tensile strength	Pa
δ	Angle of pelletiser bottom disc	°
ε	Porosity	-
ε_p	Porosity of primary particles	-
η	Fluid viscosity	Pa.s
κ_A	Elastic-plastic contact surface ratio	-
μ_R	Frictional coefficient	-
μ_V	Mean value	-
ν, ν_i	Poisson's ratio	-
ν_b	Poisson's ratio of a bond	-
ν_l	Loading velocity	m/s
ν_S	Sedimentation velocity	m/s
$\overrightarrow{v_{(ij)}}$	Contact velocity	m/s

ξ_B	Deformation of the bond	m
ρ	Specific density	kg/m³
ρ_b	Binder density	kg/m³
ρ_L	Density of the fluid	kg/m³
ρ_p	Apparent density	kg/m³
ρ_{pp}	Apparent density of primary particles	kg/m³
ρ_s	Skeletal (true) density	kg/m³
ρ_{sp}	Skeletal density of primary particles	kg/m³
ρ_t	Tap (bulk) denisity	kg/m³
σ	Strain	Pa
σ_B	Fracture strength	Pa
σ_F	Yield strain	Pa
σ_{st}	Standard deviation	-
σ_V	Variance	-
τ	Tangential strength	Pa
τ_p	Processing time	s
φ_B	Binder mass content	-
ϕ	Solid fraction	-
ψ	Particle sphericity	-
$\omega, \theta_{(x)}, \theta_{(y)}$	Angular velocity	rad/s
$\overline{\omega}_{rel,t}$	Vector of relative rotational velocity between bonded particles in tangential direction	m
$\overline{\omega}_{rel,n}$	Vector of relative rotational velocity between bonded particles in normal direction	m

1.   Introduction

1.1.   Problem Statement

Pellets are macroscopic composites consisting of many small, fine particles. They are joined together due to acting adhesive or capillary forces or by means of solid or liquid bridges [1]. Compared to cohesive powders, materials in pellet form have a lot of advantages like a higher bulk density, a better flow behaviour and lower dust emissions. Thanks to their improved properties, the mechanical treatments, like dosing, transport, storage and handling, are much easier and have lower energy costs. Therefore, pellets are preferred in many industry branches. They find a wide application in almost all manufacturing industries, like chemical, pharmaceutical, food, electrical and recycling. During production, handling transportation or storage, pellets might undergo different mechanical stresses or attritions [2]. Highly damaging are especially impacts during handling between pellets and apparatus walls [3]. Depending on the impact intensity, contact can lead to abrasion or breakage. Particle properties, like size distribution, density and porosity, can change undesirably, which results in a decrease of the product quality [4]. These negative effects increase the financial costs of final products. Hence, studying the nature of attrition and breakage processes in pellets and learning how to prevent them is of crucial importance for the industry and for science.

One of the best ways to avoid any mechanical damages in product pellets is to improve the pellet production and to obtain products with optimised mechanical properties. Pellets are regularly produced by size enlargement processes. These processes are important mechanical operations for the formulation of distributed primary particle populations. The mostly applied and easily implemented size enlargement process is agglomeration (pelletising). The received products from pelletising exhibit mechanical properties, which strongly depend on the process conditions. By modifying the production procedure, one can design tailored products with, e.g., a desired form, porosity, flowability and mechanical strength [5-7]. Due to the wide range of properties of feed materials, which need to be pelletised, of those used as binders in the process and the diversity of equipment for performing the size enlargement, the product design cannot be generalised, and prediction of the final product-mechanical characteristics is problematic. Despite of the large number of scientific works completed in this field, a lot of questions are still not answered [8, 9]. The role of process parameters in the formation of the pellet properties has still not completely been studied and revealed. Therefore, the analysis of pelletising

processes and their product properties shall contribute to progress in this important industrial field.

Thanks to the increasing computing power and improved programming tools, investigations in the field of particle technology are increasingly performed using simulations. The simulation tools should be selected based on the investigated system. For example, the Finite Element Method (FEM) is commonly used for solving problems in the areas of structural analysis, heat transfer, fluid flow and mass transport [10]. The investigation of physical movements of atoms and molecules can be easily performed using Molecular Dynamics (MD). Computational Fluid Dynamics (CFD) is a method specially developed for a fluid mechanics analysis. The investigation of granular materials is regularly performed using the discrete element method (DEM). Depending on the investigated case, the simulation tools can be combined to solve complicated problems.

Simulations provide a possibility to better analyse the processes of the forming and the breakage of pellets. Using simulation tools, one can investigate the bonding between single particles in a pellet and study the process parameter's influence on their strength and stability.

1.2.   Project Introduction and Main Goals

The main goal of this scientific work is to study the breakage behaviour of small non-spherical pellets produced in a horizontal pan pelletiser. Using microscopical primary particles with studied properties and binders, model pellets were first produced, and, afterwards, their mechanical properties were characterised. The pellets were subjected to strain-controlled quasi-static compression tests to characterise their breakage behaviour. Due to their irregular shape and inhomogeneous structure, the mechanical characteristics could not be evaluated with standard, well-studied contact models. Instead, their behaviour was described and summarised using Weibull statistics and approached with regards to their mass-related breakage energy and the breakage-force distribution. The main problem with the application of standard contact models for pellets with an irregular shape is the unknown force pattern trough the pellet structure. Every single investigated model pellet exhibits unique configurations, which makes the prediction of the force propagation time-consuming and increases the intricacy of the analysing process. In this thesis, a solution to the problem was found by performing DEM simulations of the breakage process of selected pellets. To increase the precision of the calculations, model pellets from experimental batches were selected and scanned using micro (µ)-computed tomography before performing breakage tests. The coordinates of the primary particles in the pellet structure were taken down and rebuilt into the software domain. The inner

assembly of the pellets was carefully studied using image processing and the received information about properties, like the number of primary particles, the mean coordination number, the inner voids and others were used for the improved reconstruction of the simulated pellets. After the rebuilding of the model pellets had been successfully completed, the experimental compression tests were replicated using the simulation software. The received results were evaluated and compared with experimental ones. Based on the results from the performed investigations, important questions about the model pellets characteristics, their breakage behaviour and the description and modelling of processes occurring with irregular pellets under stress could be answered:

1) What influence do the production process parameters have in a horizontally adjusted pan-pelletiser on the mechanical characteristics, the morphology and the structure, the mechanical strength and the breakage behaviour of the received model pellets?

2) Can one investigate compression processes of pellet materials using DEM simulation tools and use the results of the simulations for the improvement of the knowledge on product characterisation and design?

This investigation shall contribute to the improvement of modelling methods and the production technologies of irregular pellets.

2.   Theoretical Framework

2.1.   Size Enlargement

Size enlargement by agglomeration is a main operation in particle technology. Its goal is to join small particles together into larger structures with improved properties [11, 12]. The primary particles are connected to each other due to, e.g., the effect of adhesion forces or by means of an added binder. The final product of the process, pellets of different size and shape, is used in many industries due to its controlled product properties (better flow characteristics, controlled density and porosity). Possibly the most important advantage of agglomerated materials is the reduction of cohesive forces acting between single ingredient particles. Using this method, every undesired agglomeration can be prevented, like "caking", due to the strong reduction of the cohesion and the flowability increase of the material, all of which are of major importance for the transport, handling, and storage of granular materials. Generally, the need of the industry and of science to control product properties, like size, shape or density, is the main reason for performing size enlargement processes. Pellet materials are advantageous and widely applied as chemicals, pigments, pharmaceuticals, food materials, fertilizers and automotive fittings.

Agglomeration is one of the oldest methods for handling solids, and it has a natural origin. A lot of processes, which were separately developed in various industries, are combined under the term size enlargement, such as: briquetting (technique for enlargement of coal powder, salt and others), coating (method of surface modification for achieving a homogeneous properties distribution), compacting (used in powder metallurgy), granulation (technique for the improvement of powder flowability in pharmaceutics and bulk chemical industries), pelletising (for the shaping of animal feed or other extruded materials), sintering (high temperature binding of ores, plastics and powders in powder metallurgy) and others [13]. All these processes have the same fundamentals and follow similar application rules, but simultaneously they differ from each other, mainly in the precision of their execution, and, therefore, in the possibility of final product property design. Due to this fact, the correct choice of a size enlargement process for the material to be handled is of crucial importance [13].

The size enlargement processes can be divided into five main groups according to the forces which influence the binding of the primary particles.

- Thermal methods – heat is used to conduct the binding of the primary particles,
- Pressure methods – the primary particles and the binder are compacted through the application of an external force in a confined space,

- Agitation methods – the primary particles and the binder come into contact due to the admixture in the agglomeration equipment [11].

2.1.1. Thermal Methods (Sintering)

Agglomeration by sintering utilises the effect of heat and mass transfer to accomplish binding forces between the particulates to form larger entities [11]. During high temperature treatment, atoms and molecules migrate across the interface where particles touch each other. The process occurs at certain elevated temperature, which is different for various materials. While still in a solid state, diffused matter forms bridge-like structures between the surfaces, which solidify upon cooling. Depending on the process mechanisms, agglomeration may be achieved through the drying of wet slurry of fine particles, high temperature fusion, high temperature chemical reaction, solidification and/or crystallisation of melted or concentrated slurry during cooling [8, 11]. This technique is used in the pelletisation of iron ores, heat hardening, ceramic and metallurgical industries [8].

2.1.2. Pressure Methods

In pressure agglomeration, pellets are produced by applying external forces to dry particle systems in closed dies, which define the shape of the agglomerated product. Depending on the applied force level, there are low, medium, and high-pressure techniques. The effects that are responsible for the bonding include surface interlocking, mechanical deformation, etc. In low and medium-pressure agglomeration, materials are passed (extruded) through openings in plates; in high-pressure agglomeration, roller presses are used. High pressures are applied to decrease the porous space within the agglomerates and ultimately to increase their density [11]. This technique is widely used in ceramic, plastic processing and pharmaceutical industries.

2.1.3. Agitation (Tumble Agglomeration)

Agitation (tumble agglomeration and mixer agglomeration) has the simplest technical implementation while at the same time being highly efficient compared to the other agglomeration processes [6, 12, 14, 15, 16]. The mechanism of pellet formation during the process is shown in figure 1. First, the particles to be agglomerated are wetted by the liquid binder solution. The introduction of binder droplets may differ depending on the equipment used. The binder forms liquid bridges between the single primary particles, which solidify after

a drying process and turn into solid bridges. Part of the binder in the process can be added to the particle mixture before the start of the process or be fed into the system during pelletising.
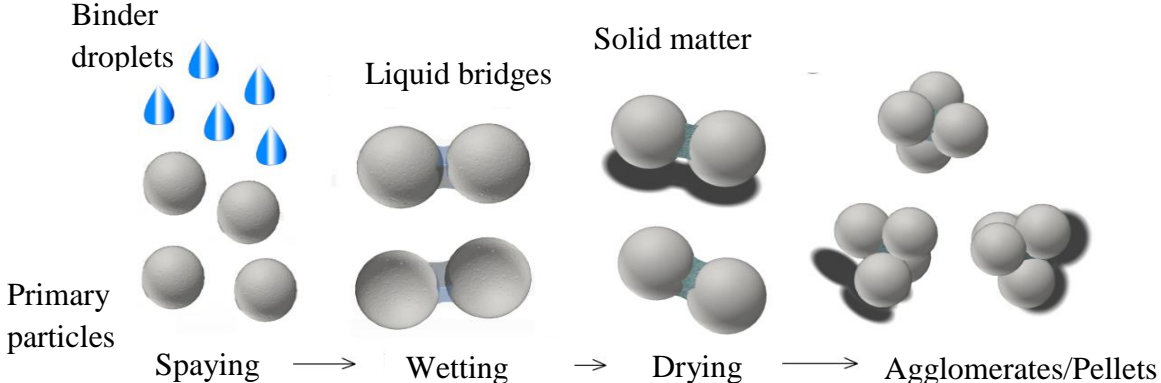
Figure 1: Main principle of the growth agglomeration/pelletising process.

2.2. Agglomeration Equipment

There is a wide variety of tumble agglomeration equipment on the market. The two most common devices are the inclined disc (pan) and the rotary drum (or cylinder). These two apparatuses have many variations, which are adjusted to the needs of the production process.

2.2.1. Inclined Discs (Pans)

The inclined pans consist of a rotating pan, in which the agglomeration charge is filled and a stationary base (figure 2).
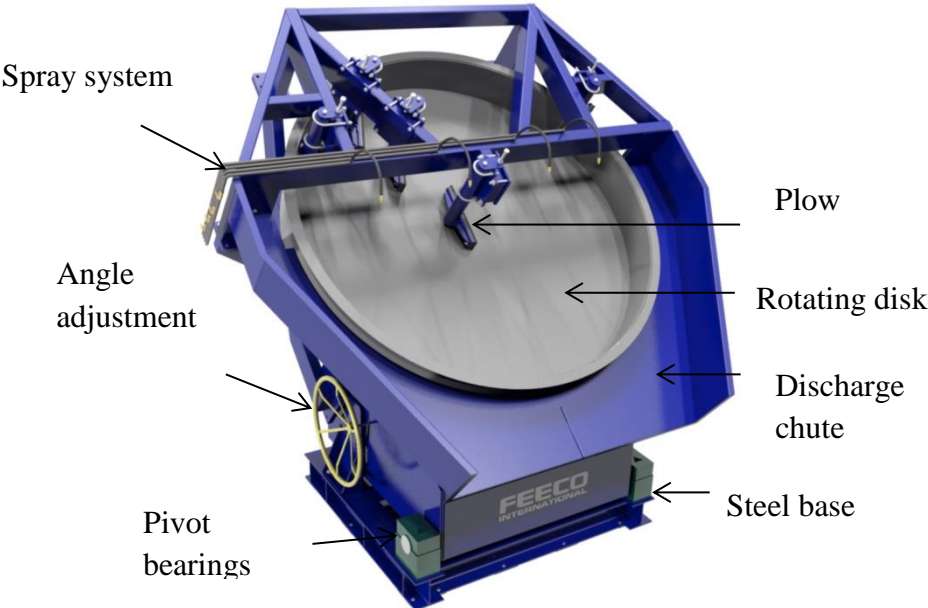
Figure 2: Principal setup of inclined disc (Feeco International Inc.) [17].

These discs are equipped with a spraying system for the adding of binders. The adjustable angle of the discs is between 40º and 70º [11]. Many scientific works have proven that such an angle provides the best pelletisation results for both constant speed and variable speed processes [11]. A dust cover may be added to the apparatus as needed. The most important feature of the inclined disks is the ratio between height and depth, which serves for the trouble-free retaliation of the process. According to Pietsch [6], the optimal ratio between both parameters is 0.2.

2.2.2.   Rotary Drums (Drum Agglomerators)

In drum agglomerators, the bulk material is agglomerated inside of a rotating cylinder (drum) (figure 3).
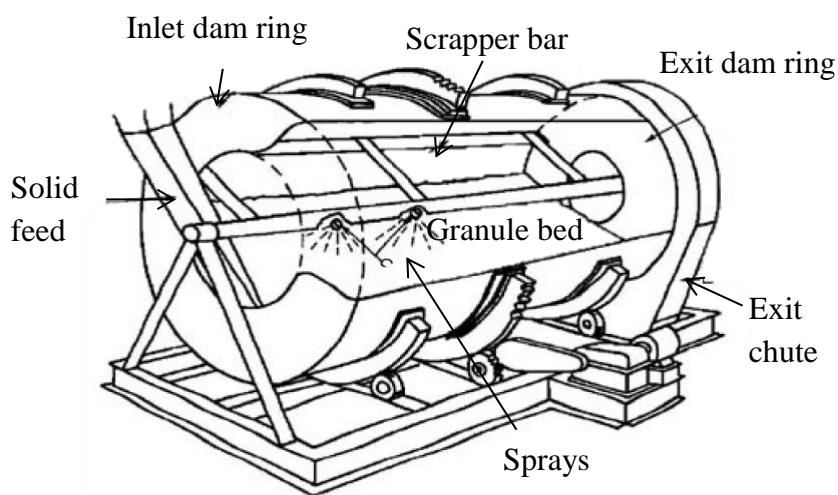
Figure 3:   Rotary drum [20].
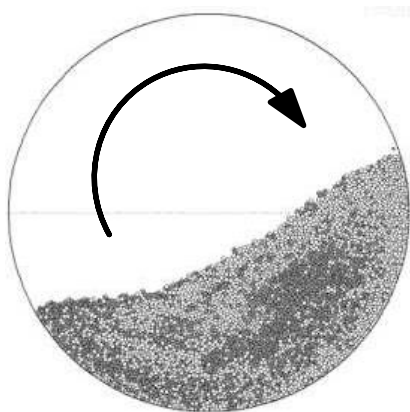
Figure 4:   Material movement inside of a rotary drum [20, 21].

The standard ratio between the length and the diameter of the drum is between 4 to 10 times. The material is introduced into the equipment from the highest point of the apparatus and moves through the machine due to the rotation and the adjusted slope (figure 4).

The binder is normally added progressively from nozzles during the material movement [18]. The main process parameter for these agglomerators is the rotational speed.

A cascading effect of the material is achieved through the rotational motion of the drum [19]. If the drum speed is too low, this will lead to an intermittent sliding of the bed

and a poor tumbling motion. At too high velocity, the material will be pinned to the drum wall, increasing the likelihood of spray blow-through. An eventual spill-back of the material can be prevented by adding retaining rings. These machines are common for fertilizer granulation and iron ore balling [11].

2.3. Binders

The proper choice of a binder is of high importance for a successful pelletising process. The addition of a binder enhances the binding between the primary particles. It provides stability and strength to the agglomerated products. In many cases, the binder also plays the role of a lubricant, which prevents abrasion and breakage of the primary particles during their interaction with the walls of the agglomeration equipment [22]. The selection of the binder depends on the desired properties of the pellets and their further applications. Due to this, no strict definition can be attempted for pelletising binders. However, there are few binder characteristics which can be used for their classification. According to Habenicht [23], the physically bonding adhesives (bonding takes place without a chemical reaction) can be categorised in the following classes: solvent adhesive, contact adhesive, dispersion binders, hot-melt adhesives, plastisols and adhesive tapes. The choice of a matching binder depends on many factors, such as: the physical nature of the primary particles, the production equipment, the atmospheric conditions and many others. The main criterion is the achievement of desired pellet properties which correspond with the needs of industry or science.

In addition, the binders can be organic or inorganic, depending on their chemical composition. Many organic binders are used in the pharmaceutical and food industries due to their non-toxicity and the ability of the human body to tolerate them. Inorganic binders have the advantage to be highly temperature-resistant, which makes them suitable for applications such as metallurgy [23]. Water is also often used as a binder, but then the stability of the received pellets will depend on the moisture content of the environment. At the same time, binders can be divided into film or bridge-forming and matrix-forming. The first group covers the primary particles, builds bridges between them and joins them together. These binders do not drastically change the porosity of the material. Water solutions are often used as film-forming binders. Water soluble chemicals are spread into the water and their molecules penetrate with the water into the structure of the primary particles. After the water has vaporised, only the binder molecules stay on the surface and in the voids, forming films and bridges which hold the particle structure together. Matrix-forming binders close the entire voids between the particles and strongly reduce their porosity. Other binders can react chemically with the primary particles,

which normally leads to the formation of a strong inter-particular bonding [6]. The usage of different binders leads to significant differences in the pellet properties and is the basis of product design.

2.4. Pellets

2.4.1. Bonding

The properties of the received pellets can differ strongly due to the influence of the production methods, the properties of the feed material and the binder. The main reason is the difference in bonding between the single primary particles, which is caused by means of different bonding forces. In figure 5, one can see an overview of the most common bonding types in agglomerates.
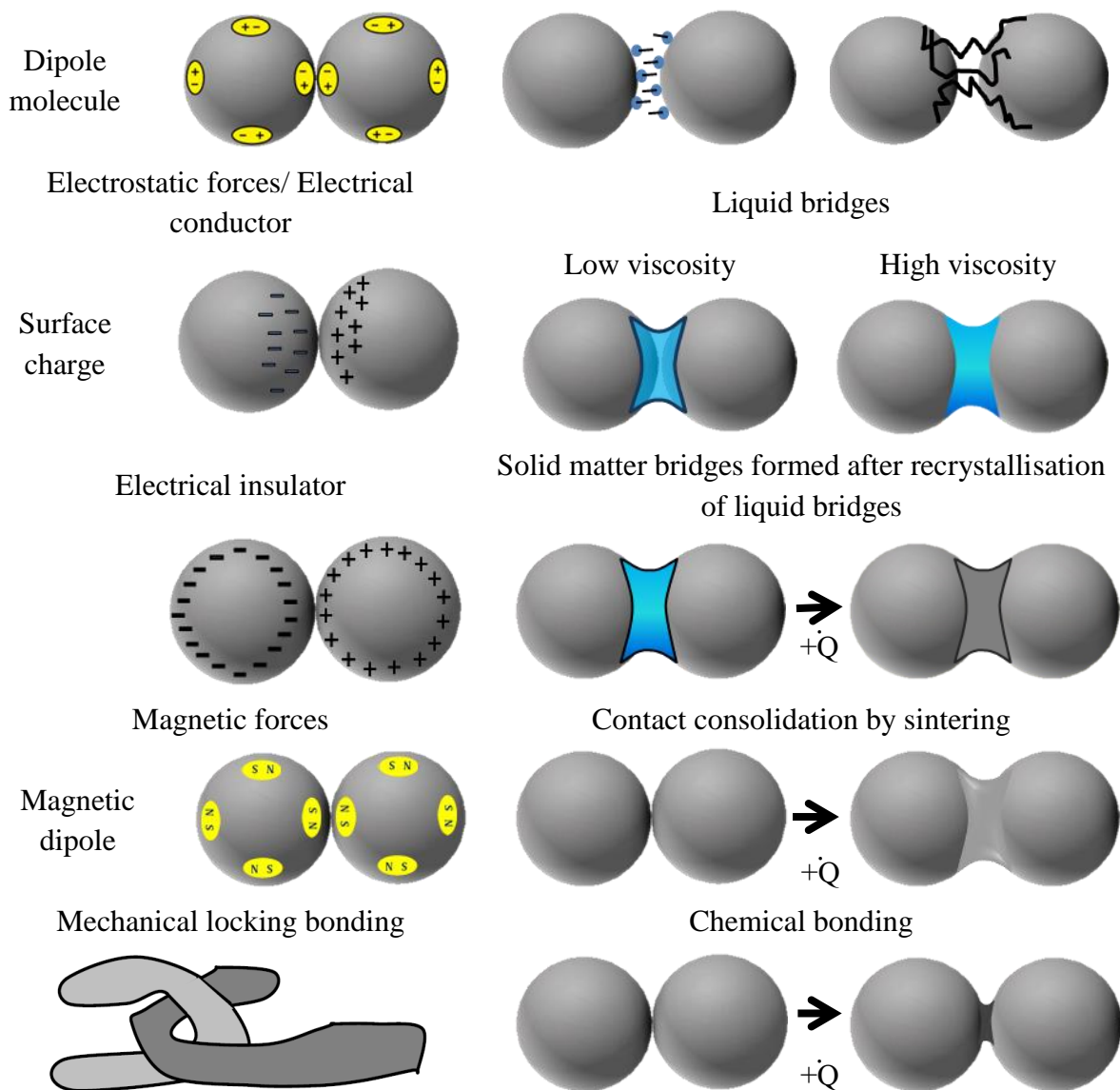
Figure 5: Types of bonds between primary particles [24].

For small particles, the influence of inter-particle forces (Van-der-Waal forces) is quite strong and they may agglomerate without the need to add any additional binder agent. This effect may also be undesired and can lead to many problems during the handling, storage and transport of fine particles. Typical is the caking of particles, the building of "dead zones" and arching in silos and hoppers, particle hydration etc. [24]. Electrical or magnetic forces acting on the particles may also lead to agglomeration, for example the agglomeration of ferromagnetic particles [25]. If the surface of particles is rough, an assembly can be formed due to mechanical interlocking. Normally, when the primary particles are large, the agglomeration needs to be carried out using a binding agent. Its role in the process is to form liquid bridges between the primary particles and to join them together. Depending on the viscosity of the used binder, there are different mechanisms through which the bonding can occur. Low-viscosity liquids (e.g. water) are normally used to bind small, light particles and the acting inter-molecular forces are strong enough in this case to join the primary ingredients. Bonding with high-viscosity liquids (e.g. solution of polymers) regularly leads to the formation of solid bonds after a drying process. The bridges consist of long chain molecules, which interlock and hold the agglomerate structure together.

If the agglomeration occurs under thermal influence, then the thin outer layer of a primary particle may melt and get consolidated with the outer layer of a neighbour particle. The consolidation of the outer layers may also occur as the result of a chemical reaction, taking place on the surface of the particles. Especially interesting for science and industry are agglomerates which form tough bonds due to solid bridges. The solid bridges do not deform the primary particles (like in the case of sintering) and do not change their mechanical or chemical properties. Typically, the binder can be extracted when no longer needed. The main question that remains is the choice of binder matching the type of primary particles that need to be agglomerated.

2.4.2.   Pellet Properties

Without sufficient knowledge about the interactions between the primary particles in pellets, their product design would not be possible. In addition, defining the properties of powders and granulated products may be a difficult task due to their complex nature. Most of these systems are not homogeneous, which means that different parts of the system have different properties. The only proper way to characterise them is to use property distributions, which gives an overview of the presented system characteristics. Another problem is the dependence of the

particle properties on their morphology, the influence of which cannot be predicted empirically and must be measured for every single system. This requires a proper method for the determination of those properties, which leads to an extra effort in the particle characterisation. Nevertheless, depending on the needs of their application, different particle properties may be more or less important in different cases, and this does not allow the establishment of a universal particle characterisation method.

Litster and Ennis [26] classified the particle properties in three different categories: properties which are defined by the particle morphology, those which designate the long-range interaction with other particles or external forces, and contact mechanic properties. Morphology is defined by asperities and roughness, by constituents, or by size and aspect ratio. Interactions with other particles may be influenced by surface-active agents or their coating. They are also affected by surface energy and electrical or magnetic properties. Contact mechanic properties are, e.g., the mechanical strength, hardness, modulus of elasticity and others. Also, there is no strict division between the different groups of properties. Impurities, for instance, can, at the same time, influence the long-range interaction between the particles and their contact mechanic properties. Inner defects and flaws can strongly influence the properties of particles. The friction with other objects and charge transfer from the particle surface may also have a strong effect.

2.4.2.1. Pellet Size

One of the most important properties of any particle, agglomerate or pellet is its size. It determines many of the other physical properties and can influence them strongly [27]. For example, particle size reduction normally leads to an increase of the specific surface and mechanical strength. For small particles, the adhesion forces dominate over the inertial forces and the particles are more likely to agglomerate [28]. Because of its importance for powder technology, large priority has been placed on the need to find a proper way to determine and describe the particle size. In spite of this, there is no universal definition of particle size. Only particles with a standard form have clearly defined size (spherical, cubic and others) [19]. In real cases, pellets and agglomerates often have irregular shapes, and this makes the definition of size complicated. The most common method for describing the size of such particles is the equivalent diameter [29]. The equivalent diameter is the diameter of a sphere having the same characteristics as the investigated irregularly shaped particle. Depending on the already known particle properties, one can use different equivalent diameters. Maybe most well-known is the

volume equivalent diameter $d_{eq,Volume}$. It gives the diameter of a sphere having the same volume V_P as the considered particle [29]

$$d_{eq,Volume} = \sqrt[3]{\frac{6}{\pi} V_P}. \tag{2.1}$$

Another commonly used measurement is the equivalent surface diameter $d_{eq,Surface}$, which gives the diameter of a sphere having the same surface area A_s as the particle [30]

$$d_{eq,\ Surface} = \sqrt{\frac{A_s}{\pi}}. \tag{2.2}$$

The Stokes diameter $d_{eq,Stokes}$ finds application in the study of polymer and macro-molecular systems [31]. It gives the diameter of a sphere having the same sedimentation velocity v_S as the particle

$$d_{eq,Stokes} = \sqrt{\frac{18\eta v_S}{(\rho - \rho_L)g}}, \tag{2.3}$$

where η is the fluid viscosity, g is gravitational acceleration, ρ is specific density of the particle and ρ_L is density of the fluid.

Of huge importance in particle technology is the projected area equivalent diameter

$$d_{eq,Pa} = \sqrt{\frac{4A}{\pi}}. \tag{2.4}$$

This is the diameter of a cycle with an area corresponding to the projected area A of the particle (figure 6). The equivalent diameter can also be defined as the maximum length ($x_{c,\ max}$) of lines parallel to some fixed direction - $d_{c,max}$ (figure 6) [32].

Nevertheless, for assemblies consisting of particles with different sizes, the usage of just one equivalent diameter is no longer appropriate. In such cases, it is more reliable to use particle size distribution functions. One can distinguish between two types of distributions: cumulative and frequency functions [29]. The cumulative distribution gives the fraction of particles ΔQ_x having a diameter less than x. If the measured value of Q is a number, one then speaks of a cumulative number distribution $Q_{0(x)}$. One can also have length $Q_{1(x)}$, area $Q_{2(x)}$, volume or mass $Q_{3(x)}$ distributions. The mass and the volume distributions relate to each other by means of the

specific density ρ [19]. The frequency distribution (distribution density curve) defines, for example, the number of particles between the sizes of x and x + dx.
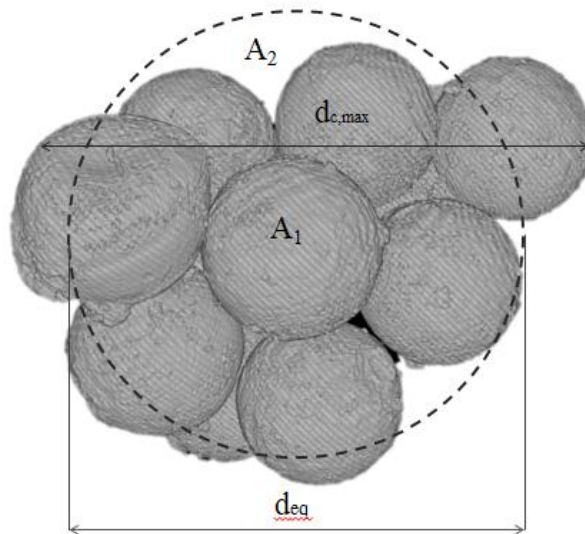
Figure 6: Particle size as maximum length ($x_{c,\,max}$) of lines parallel to a fixed direction - $d_{c,max}$ or as equivalent area diameter (d_{eq}), A_1 – area of the pellet, A_2 – circular area corresponding to the size of the projected area of the pellet, $A_1 = A_2$.

Both distributions are related and can be transformed one to the other. If one normalises the fraction ΔQ to the size of the corresponding interval, one obtains the density of the distribution. Size distributions can be mono-modal, bi-modal or multi-modal. The most common mathematical model for fitting mono-modal size distributions is the logarithmic normal distribution (logarithmic normal probability functions). Other models used are the normal distribution (Laplace-Gauss), the Gates-Gaudin-Schuhmann distribution (bi-logarithmic) and the Weibull distributions [19, 26]. Important characteristics of size distributions are their moments. With the help of moments, one can calculate the average particle size or other mean values from the particle size distribution [19]. One of the most substantial values in distributions is the mode, which correspond to the distribution's peak and gives the value at which the frequency is at its maximum. The median shows half of the size of the cumulative curve and divides the distribution in two equal parts [33]. An influential characteristic of the size distribution is also its spread, which shows the difference between the minimum and the maximum size of the particles.

2.4.2.2. Pellet Shape

Another decisive particle parameter is shape. It has an enormous influence when it comes to the flow and the breakage behaviour. Similar to the particle size, there is no universal way to

define the particle shape. Due to this fact, different shape factors have been introduced, like the volume shape factor, the surface shape factor and the particle sphericity ψ. The sphericity shows the deviation from the ideal spherical shape [29]. There are also different ways to evaluate the sphericity, e.g. using the ratio between the surface area of the ideal sphere and the one of the particle. In scattering analysis, the sphericity can be given as

$$\psi = \frac{4A}{P_p^2},$$ (2.5)

where P_p is the measured perimeter/circumference of a particle projection and A is the measured area covered by the particle projection. It has values between 0 and 1, where 1 is the sphericity of an ideal sphere. The value for the sphericity can be used to transform one equivalent diameter into another.

2.4.2.3. Particle Density and Porosity

Density and porosity play a huge role in determining pellet properties. Very often, the main goal of size enlargement is to increase or to decrease the density of some material [19, 26]. By definition, the density is the ratio between the mass and the volume of an object. So, while the interpretation of mass is rather easy for particle assemblies, it is not the same with their volume. Based on the different ways of bulk solid volume description, there are three different types of density, which are mainly used in particle technology. These are: the tap (bulk) density ρ_t (which is based on the volume of the bulk solid with all voids in it), the particle (apparent) density ρ_p (defined by the volume of a single particle with the voids in it) and the skeletal (true) density ρ_s (the true solid density of the material itself). As is clear from their definition, the bulk and the apparent densities strongly depend on the particle morphology and cannot be tabulated. The skeletal density is inversely related to the porosity of the material: the more pore spaces, the lower the value for skeletal density. The porosity ε of a material is defined as the volume fraction of voids over the total volume. Particle porosity can be calculated from the skeletal and apparent densities:

$$\rho_s = \rho_p(1-\varepsilon).$$ (2.6)

Porosity has a very strong influence on the mechanical strength of the pellets. Many scientific works have proved the strong relationship between particle porosity and particle strength [34]. The presence of voids and defects in the agglomerate structure makes them unstable and decreases their strength. The particle breakage resistance decreases for large agglomerates, due

to the increased possibility of a defect, which may cause a breakage. Subero and Ghadiri [34] investigated the influence of size and distribution of the voids in agglomerates and found that the increased size leads to a weakening of the structures. They also found that for agglomerates with the same porosity but different sizes of the voids, those having larger voids are less stable [34]. Müller et al. [35] found out that water that has condensed and been stored in the pores of the pellets may significantly contribute to particle breakage upon impact.

2.4.2.4. Mechanical Strength of Pellets

Since mechanical strength is one of the most significant particle characteristics in particle technology, it is important to investigate the factors which have an influence on it. The first theory about agglomerate strength was developed by Rumpf [36-38]. He assumed that the most relevant parameter for describing the failure events of particle assemblies is their tensile strength. The base of his approach is the fact that breakage normally occurs as a result of the impact at the highest tension. According to Rumpf [37], the breakage occurs in a brittle manner and takes place in a tension regime rather than in compression or shearing regime. He evaluated the tensile strength as the force causing the failure divided by the cross-section of the particle assembly. The agglomerate is considered as a bonded chain of single particles. Rumpf [37] made the following assumptions on which he based his theory. Firstly, the single particles and bonds should be homogeneously distributed in the agglomerate. The cross-section should contain enough bonds so it can be taken as a representation of the whole pellet. All bonds must have approximately the same value for their mechanical strength and all the single particles must have the same diameter. In addition, the failure should be approximately ideal, which means that all bonds break simultaneously. Hence, he received the following expression for the tensile strength

$$\gamma = \frac{9(1-\varepsilon)k}{8\pi d^2}\overline{F} \tag{2.7}$$

where ε is the porosity, k is coordination number, d is the diameter of the single particle and $\overline{F}$ is the mean breakage force. Rumpf also presented a formula for calculating tensile strength as a function of the type of bonds – capillary forces, van der Waals and electrostatic force or solid bridges [37].

Meissner et al. [39] calculated the crushing strength of agglomerates by using the tensile strength introduced by Rumpf [38]. For their investigation, they also used a correlation for tensile strength and crushing strength proposed by Hertz [40]. The effective elastic modulus of

the agglomerate used is assumed to be approximately proportional to the solid volume fraction. Based on this assumption, they propose that the crushing strength of agglomerates is a function of primary particle size, agglomerate size and packing fraction.

Griffith [41] investigated the brittle failure of materials, which is characterised by crack propagation without the presence of a plastic zone. He firstly proposed that the strength of brittle solids is controlled by the presence of defects (voids, impurities, micro-cracks). These defects act as stress concentrators, generating in their vicinity local stresses above the theoretical material strength, and, therefore, causing crack propagation and material failure. Furthermore, Griffith [41] postulates that the propagation of a crack takes place if it is energetically favourable. Later, Rumpf [42] and Schönert [43] characterised the force-displacement behaviour of limestone, cement and quartz particles and proved that the material strength under compression is strongly influenced by the presence of structural inhomogeneities such as pores, micro-cracks, voids and hollow spaces throughout the granular volume. These inhomogeneities affect the mechanical behaviour of the granular material and increase its fracture probability.

Kendall [44] used Griffith's theory [41] to calculate the fracture toughness of agglomerates. Fracture toughness is the resistance presented by a material to crack propagation and can, therefore, be used on its own as a description of the material strength. Kendall [44, 45] also used this theory to calculate the stress necessary to fracture an agglomerate. This involves the assumption that the primary particles are so small that the agglomerate behaves like a solid body.

Rice [46] used the model of a minimum solid area to characterise agglomerate strength, fracture energy, fracture toughness, compressive strength, flexural strength and tensile strength.

Kapur and Fuerstenau [47] attempted a completely different approach to agglomerate strength. Their theory is based on the theory of strength of homogeneous materials [40, 48]. They combined the theory of elastic strength [49] with some concepts from Rumpf's theory to calculate tensile strength for spherical agglomerates.

In 1998, Denny et al. [50] proposed a combination of Griffith's brittle theory and Rumpf's theory for an explanation of the combined effect of porosity and crack length.

Again in 1998, Iveson and Litster [51] investigated the deformation of macroscopic glass particle granules. They showed that the micro-yield stress increases with increasing binder surface tension and viscosity. A similar investigation was reported by Salman and Gorham [8],

who performed compression tests to investigate the fracture characteristics of glass spheres. In later works, Iveson and Litster [9] recommended an improvement in the design and scale up of granulation processes by in-depth analysis of the formulation properties, characterisation of the process and calculation of key parameters. A similar explanation towards the inhomogeneity of the strength distribution over the granular volume was reported by Kirsch et al. [52] for coarse granules composed of millimeter size primary particles. The authors pointed out the diversity in the consolidation of solidified binder bridges with time. In their reviews, Mörl et al. [53] and Peglow et al. [54] also stressed the influence of various parameters involved in nucleation, growth and attrition on the mechanical strength of granules. Khanal et al. [55] studied the cracking mechanisms of aggregate matrix composite. They found an important correlation between the diameters of contact areas and the loading velocity. They also discovered a similarity in cracking mechanisms, crack patterns and size of fragments between granules broken by impact and under compression.

In 2009, Aman et al. [56] investigated the breakage probability of irregularly shaped particles. They found a linear dependency between the breakage energy and the breakage force for all investigated materials. Antonyuk et al. [57] also studied the breakage behaviour of granules and crystals. They compared experimental and numerical simulation results and proved the capability of the simulation tools to describe the breakage behaviour. Important results for quasi-static compression tests and dynamic impact of zeolite granules have been reported by Müller and Tomas [58]. They concluded that increasing particle size causes an enhancement of the breakage probability due to the larger heterogeneity of the particle and the higher number of defects and micro-cracks within its structure. They also found a negative effect of increased moisture content on the mechanical properties of the granules.

The practical determination of pellet strength in science and industry is accomplished using different testing procedures. These include compression, impact and shear tests, developed to determine the breakage, impact and shear strength as well as the resistance to bending and cutting of the agglomerates. The most common strength testers are shown in figure 7. Possibly the most commonly used method for the strength testing of pellets is compression. There is a huge variety of compression testers, for example: mechanical presses, simple point-load testers, sophisticated presses, and large-scale hydraulic presses [42].

The choice of the compression testing machine depends mostly on particle size. The biggest advantage of compression tests over the other testing methods is the possibility to record the evolution of the applied force and the deformation. Thus, the load-deformation profile can be

determined, and, hence, the particle's fracture energy. One of the most important issues about compression testing is the way the deformation of the particle is measured.

For materials with a low elastic modulus and stiffness, the deformation can be easily found using the movement velocity of the compressing pistons. This method requires the deformations of the pistons to be neglected, which is not possible for very stiff and hard materials. In the case of materials with a moderate to high stiffness, the direct measurement of the deformation is no longer feasible, and this increases the cost and the effort of the analysis.

Despite of the large number of scientific works accomplished in this special field of fracture mechanics, there are still unsolved problems and questions [51]. A better understanding of the connection between product properties and process parameters should contribute to improving product design.
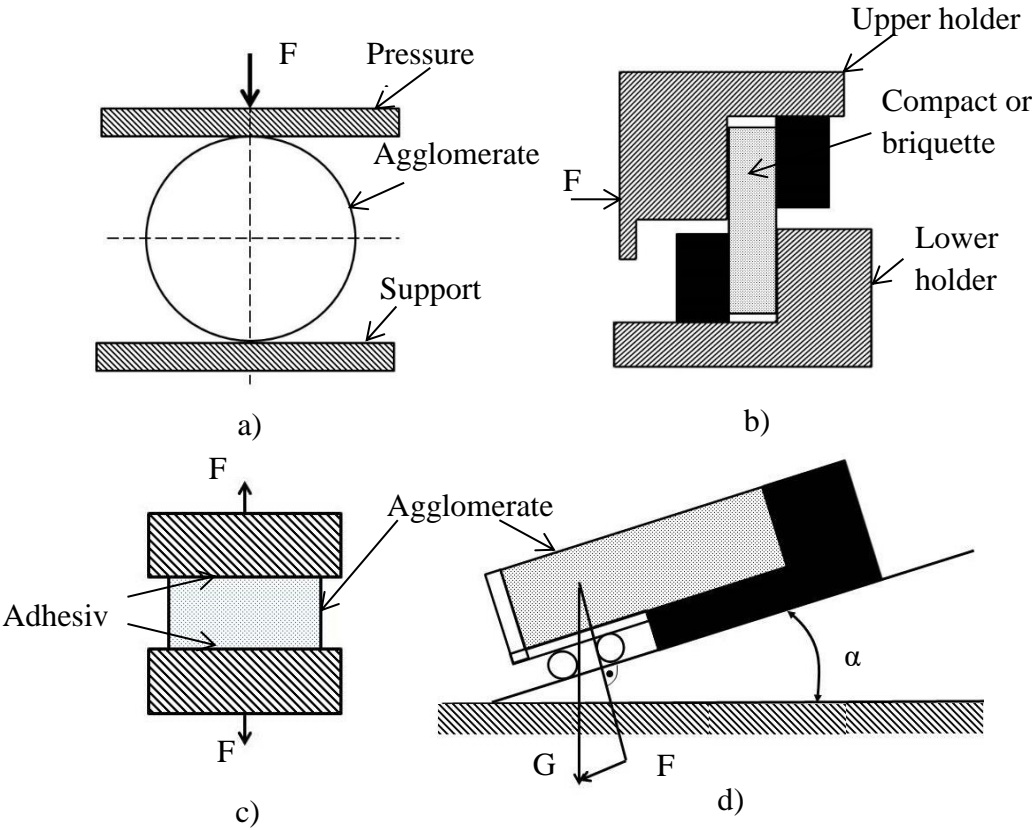
Figure 7:   Main working principles of agglomerate strength testers: a) Compression tester, b) Shear strength tester, c) Tensile strength tester for strongly bonded agglomerates, d) Tensile strength tester for loosely bonded agglomerates [6].

2.5.   Contact Mechanics

As long as the mechanical characteristics of product pellets are of importance for science and industry, one should take a deeper look in particle behaviour under compression. Respective

properties are especially relevant for transport and storage, where the particles are often stressed due to the contact with neighbour particles or the walls of an apparatus or storage tanks. The stressing forces in these cases have a compression nature, due to consolidation during storage which induces stress accumulation in the underlying pellets. Therefore, it is necessary to further characterise and understand the compression behaviour of pellets. Depending on their reaction to stress, one can differentiate between elastic, elastic-plastic and plastic bodies.

2.5.1. Elastic Contact Behaviour

The first studies in this field were performed by Hertz [40]. Based upon his approach to elliptical stress distribution in the contact area, he formulated the normal direction, non-linear, elastic force-displacement law for smooth, isotropic spheres

$$(\frac{P_{el}}{P_{max}})^2 = 1 - \left(\frac{r_k}{r_{k,el}}\right)^2 \ , \ r_k \leq r_{k,el}, \tag{2.8}$$

where r_k is the contact radius. The maximal stress P_{max} that appears in the centre of the contact area is

$$P_{max} = \frac{3F_{el}}{2\pi r_{k,el}^2}, \tag{2.9}$$

where F_{el} is the elastic contact force. The average radius of the contact partners R^* for a sphere-wall contact can be found using the following equation:

$$R^* = (\frac{1}{R_1} + \frac{1}{R_2})^{-1} \approx R_1 \text{ when } R_2 \rightarrow \infty. \tag{2.10}$$

R_1 is the radius of the particle in contact and R_2 is the radius of the contact partner. It should be noted that Hertz assumed that the contact radius r_k is much smaller than the radius of the sphere R_1.

One can calculate the average modulus of elasticity for the contact partners by:

$$E^* = 2(\frac{1-v_1^2}{E_1} + \frac{1-v_2^2}{E_2})^{-1} \approx \frac{2E_1}{1-v_1^2}, \tag{2.11}$$

,

19

where E_1 and E_2 are the moduli of elasticity of the contacting objects and ν is Poisson's ratio. Due to the resulting deflection, the deformation radius is larger than the contact radius $r_{k,max} \geq r_{k,el}$ [60]. An overview of the elastic pressure distribution for particle-wall contact is given in figure 8.
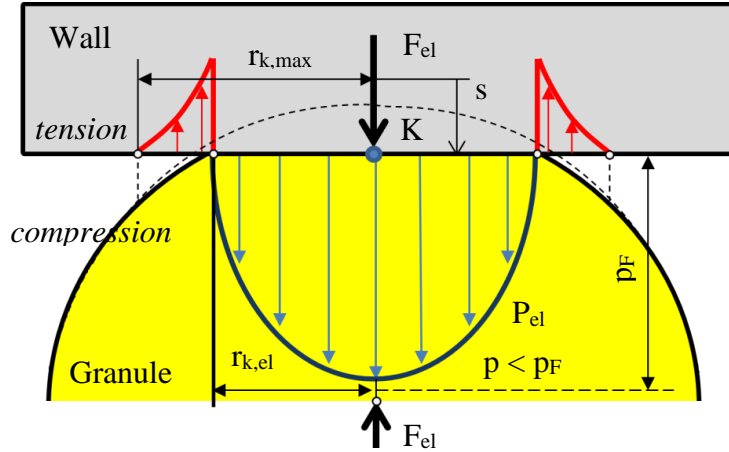
Figure 8: Schematic pressure distribution within wall-particle contact during an elastic deformation [57, 61].

The total elastic deformation is sum from the contact deformations (flattening) of both contact partners

$$s = \frac{r_{k,el}^2}{R^*}.$$

(2.12)

Due to elliptical force distribution during the particle wall contact, the contact stiffness in the normal direction increases with increasing deformation and particle size

$$k_{el}^* = \frac{dF_{el}}{ds} = E^* \sqrt{R^* s} = \left(\frac{F_{el} d}{4D^2}\right)^{\frac{1}{3}}.$$

(2.13)

One can assume that the stiffness of the walls is much larger than the stiffness of the compressed particle. The overall contact stiffness can be evaluated from the spring constants of two spring elements, connected in series:

$$k_{p-w} = \left(\frac{1}{k_p} + \frac{1}{k_w}\right)^{-1} \approx k_p = \frac{2E_1}{1 - v_1^2} \sqrt{R_1 s},$$

(2.14)

The regular method for the characterisation of the particle mechanical behaviour is the accomplishment of uniaxial compression tests. In the experimental setup, the particle is stressed

from two contacting plates. Therefore, it comes to a wall-particle-wall contact and elastic stiffness can be given as a result of the four spring constants of the contacts:

$$k_{w\text{-}p\text{-}w} = \left(\frac{1}{k_{p1}} + \frac{1}{k_{w1}} + \frac{1}{k_{p2}} + \frac{1}{k_{w2}}\right)^{-1} \approx \frac{k_p}{2} = \frac{k_{p\text{-}w}}{2}. \tag{2.15}$$

The contact force for the wall-particle-wall contact according to Hertz [40] will be:

$$F_{el,w\text{-}p\text{-}w} = \frac{2}{3} E^* \sqrt{\frac{d_1}{2}}^* \left(\frac{s}{2}\right)^3 = \frac{1}{6}\frac{E_1}{(1\text{-}v_1^2)}\sqrt{d_1 s^3} = \frac{1}{3}\frac{E_1}{(1\text{-}v_1^2)}\sqrt{d_1 s^3}. \tag{2.16}$$

In this equation, s is the contact deformation and can be expressed with the following relation:

$$s = s_{k,1} + s_{k,2} = \frac{r_{k,el}^2}{R^*} + \frac{r_{k,el}^2}{R^*} = \frac{2r_{k,el}^2}{R_1}. \tag{2.17}$$

After differentiation, one can find the overall stiffness for the wall-particle-wall contact to be:

$$k_{el,w\text{-}p\text{-}w} = \frac{dF_{el,w\text{-}p\text{-}w}}{ds} = \frac{1}{4}E^* \sqrt{d_1 s} \approx \frac{1}{2}\frac{E_1}{(1\text{-}v_1^2)}\sqrt{d_1 s}. \tag{2.18}$$

The axial stress in a cross-section of the stressed particle can be found from the resultant acting force. For homogeneously distributed strain it is:

$$\sigma = \frac{F_{el,w\text{-}p\text{-}w}}{\pi R_1^2}. \tag{2.19}$$

From equations (2.14), (2.17) and (2.18) one can express the stress-strain relation for wall-particle-wall contact:

$$\sigma = \frac{4}{3}\frac{E_1}{\pi(1\text{-}v_1^2)}\sqrt{D^3}. \tag{2.20}$$

2.5.2.   Elastic-Plastic Contact Behaviour

When external force stresses a particle, it first starts to deform elastically, as already described in section 2.5.1. Although in reality, there are no ideal elastic materials, but for stressed objects there is an elastic limit (yield strength). After reaching its yield limit, the material starts to

deform plastically. An example of a force-displacement curve from compression test is given in figure 9.
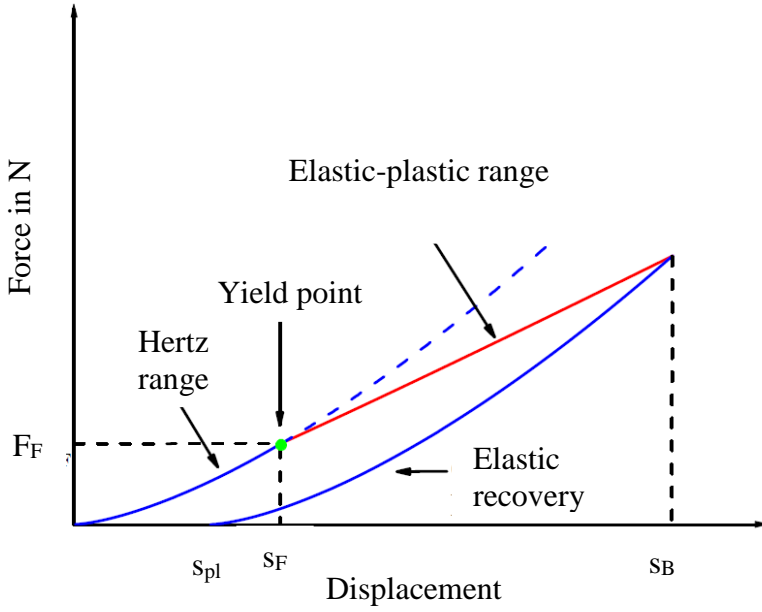
Figure 9:   Force-displacement diagram [62].

As soon as the yield limit of the material is reached $(F > F_F)$, a plastic behaviour appears, which distinguishes the force-displacement curve from the Hertz curve. The contact pressure is inversely related to the particle diameter. Therefore, at a constant acting force, particles with smaller diameters should show a softer behaviour in comparison to larger ones.

It can be seen from figure 10a that the whole elastic-plastic deformation structure can be represented by a superimposed spring and a slider element. The resulting contact force (figure 10b) is the accumulation of plastic deformation affected by the continuous acting elastic $F_{el,1}$ and plastic force F_{pl} as:

$$F = F_{el,1} + F_{pl} = F_{el}. \tag{2.21}$$

According to the compression conditions, both elastic and plastic deformation should be taken into consideration. The force and stress distribution within elastic-plastic compression is shown in figure 9b. It should be noticed that not the whole material immediately deforms plastically. It builds a circular flattening contact with a plastically deformed area in the centre $(r_k \leq r_{k,pl})$. The outside range of the contact will still be deformed elastically because there, the stress is still less than the yield pressure.

During the particle compression process, it is assumed that the yield pressure P_F within the plastic contact area is constant. [61].

The force F_F, at which the yielding of the material starts, can be given as:

$$F_F = \frac{\pi^3 R_1^2 (1-v_1^2)^2}{6E_1^2} A_v^3 \sigma_F^3, \tag{2.22}$$

where A_v is a function of Poisson's ratio [61, 63, 64].

Figure 10: Schematic pressure distribution within wall-particle contact during an elastic-plastic deformation [57].

The normal acting force during elastic-plastic deformation between a wall and a particle can be given with the following equation [65]:

$$F_{el-pl} = F_{el} + F_{pl} = \pi r_k^2 p_F \kappa_A, \qquad (2.23)$$

where κ_A is the ratio of the contact surfaces, having values between 0 to 1. Value of 0 means ideal elastic deformation and of 1 ideal plastic. In the elastic range, the contact surface ratio has the value of 2/3

Similarly to the elastic stiffness, the elastic-plastic stiffness can be found by differentiating the contact force [66]:

$$k_{el-pl} = \frac{dF_{el-pl}}{ds} = \pi R_1 p_F \left(1 - \frac{2}{9}\sqrt[3]{\frac{s_F}{s}}\right). \qquad (2.24)$$

Elastic-plastic stiffness is a function of deformation; the more the particle is deformed, the more the stiffness increases.

2.5.3. Plastic Contact Behaviour

There are also materials the elastic deformation of which is negligibly small, and, thus, they can be described as dominantly plastic. It can be assumed that the whole contact area deforms plastically and that there is no surface deformation outside of it.

The pressure distribution of the pure plastic deformation of a spherical particle in compression is shown in figure 11. This type of mechanical behaviour can be represented as a series of elastic spring and plastic friction elements [67].
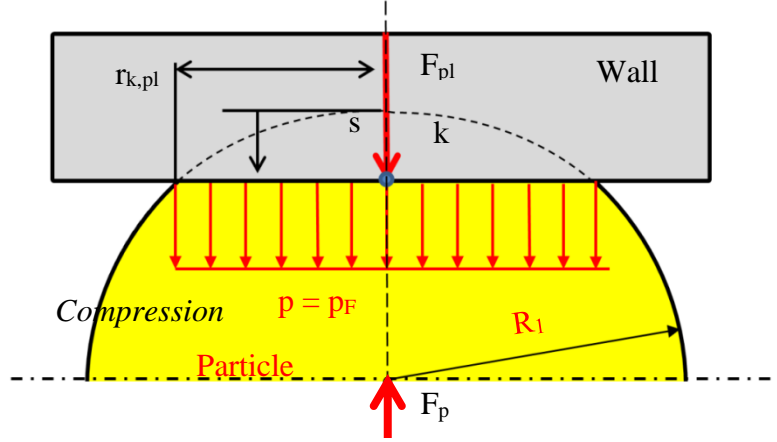
Figure 11:   Schematic pressure distribution within wall-particle-wall contact during a plastic deformation [66].

The ideal plastic deformation starts when an average contact pressure of

$$p \approx 3\sigma_F \tag{2.25}$$

is reached [61]. During the stressing, the whole contact area is plastically deformed. The repulsive force, which acts against the plastic displacement of the compressed particle in the contact area, can be given in terms of yield pressure p_F

$$F_{pl,w\text{-}p\text{-}w} = p_F A_K = \pi r_{k,pl}^2 p_F = \pi R_1 p_F s. \tag{2.26}$$

The contact stiffness is constant for perfectly plastic-yielding material, and can be calculated using the following equation:

$$k_{pl,w\text{-}p\text{-}w} = \frac{dF_{pl,w\text{-}g\text{-}w}}{ds} = \pi R_1 p_F. \tag{2.27}$$

In summary, the Hertz theory and all associated theories have restrictions, which do not allow them to apply in all cases. For example, the objects in the Hertz theory are taken as ideally homogeneous, which makes the theory inapt for the investigation of agglomerates having large voids [68]. Secondly, the contact between the bodies is assumed to occur in only a small area of the surface and to be negligibly small compared to particle diameter [69]. The investigated objects are ideally spherical, and this makes the application of the theory for the cases of stressing of particles with irregular shapes improper. The main problem for investigating the

breakage behaviour of pellets with irregular shapes is the unknown force distribution through the structure, which depends on factors which are not taken into account in the frame of the Hertz model.

2.5.4. Bonded-particle model - Elastic Deformation of Solid Bonds

When one simulates particle assemblies in which the particles are connected to each other with bonds, one needs a matching tool to describe and evaluate their breakage characteristics. Using different mathematical models in the DEM simulations, one can calculate pellet breakage characteristics depending on the properties of their solid bridges. The simplest model is the linear-elastic beam theory (also known as Euler-Bernoulli beam). The solid bonds are considered as cylindrical as shown at the schema in figure 12 [70]. By applying the linear-elastic beam theory [71] one can calculate the forces and moments acting on the bonds.
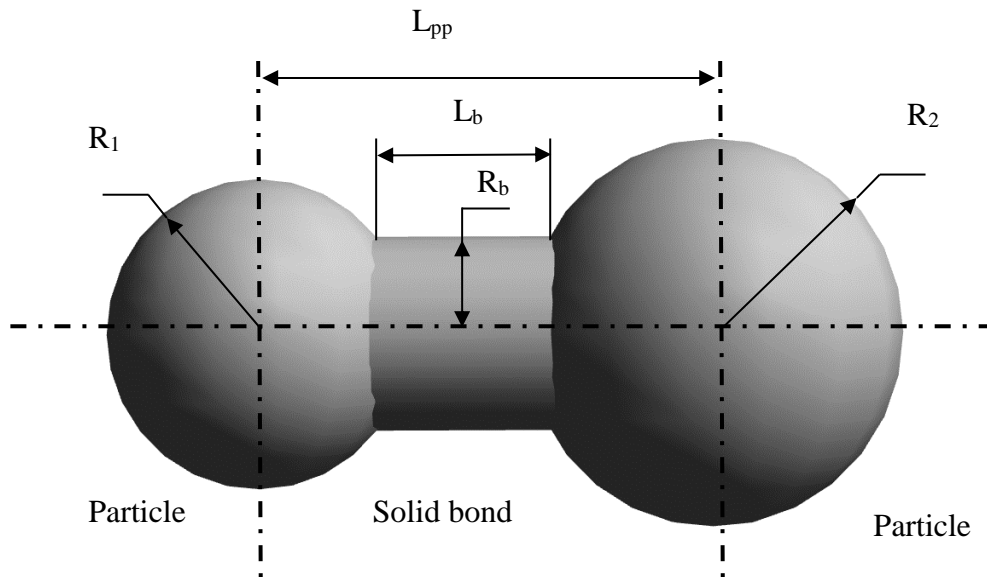
Figure 12:   Structure of a solid bond between primary particles [70].

Due to the different length of solid bonds between the primary particles within the pellet, individual length of bond L_b is defined by the distance between the two particles L_{PP}, bond radius R_b and the radii of the two connected particles R_1 and R_2 [70]

$$L_b = L_{pp} - \sqrt{R_1^2 - R_b^2} - \sqrt{R_2^2 - R_b^2}. \qquad (2.28)$$

It should be noticed that the bond radius R_b is not supposed to exceed the smallest radius of bonded particles. During the compression process, the current length $L_{b,cur}$ should be tracked and compared with the recovery length of the bond $L_{b,rec}$, which defines the length of the bond

when external forces acting on the bonded particles have been removed. The deformation of the bond ξ_B combines the recovery length and the current length of the bond

$$\xi_B = L_{b,rec} - L_{b,cur}. \tag{2.29}$$

From this equation, it can be deduced that ξ_B has a positive value. For ideal elastic behaviour, the bond should return to the initial position, which makes the recovery length constant and equal to the initial length of bond $L_{b,in}$. The calculation of forces and moments in the bond at the point of time $(t + \Delta t)$ is fulfilled by incremental changes of values at the previous time point t

$$\overline{F}_{b,t}^{t+\Delta t} = T \cdot \overline{F}_{b,t}^{t} - \overline{V}_{rel,t} \cdot \Delta t \cdot A_b \cdot \frac{E_b(1+\nu_b)}{2 \cdot L_{b,rec}}, \tag{2.30}$$

$$\overline{F}_{b,n}^{t+\Delta t} = \frac{A_b \cdot E_b \cdot \xi_B \cdot \overline{r_n}}{L_{b,rec}}, \tag{2.31}$$

where $\overline{F}_{b,t}^{t+\Delta t}$ and $\overline{F}_{b,n}^{t+\Delta t}$ are forces in tangential and normal direction and $\overline{V}_{rel,t}$ - tangential component of the relative velocity vector.

If the tangential component of the relative velocity vector $\overline{V}_{rel,t}$ is positive, the tangential force increases with the increment of the bond cross-sectional area A_b and Young's modulus of bond E_b, while the normal force decreases. T represents the transformation matrix, which records the movements of contacting particles. The tangential and normal moments $\overline{M}_{b,t}^{t+\Delta t}$, $\overline{M}_{b,n}^{t+\Delta t}$ are both proportional to E_b, A_b, and time step Δt. They can be defined also by using increments

$$\overline{M}_{b,t}^{t+\Delta t} = T \cdot \overline{M}_{b,t}^{t} - \overline{\omega}_{rel,t} \cdot \Delta t \cdot A_b \cdot \frac{E_b}{L_{b,rec}} \cdot I, \tag{2.32}$$

$$\overline{M}_{b,n}^{t+\Delta t} = T \cdot \overline{M}_{b,n}^{t} - \overline{\omega}_{rel,n} \cdot \Delta t \cdot A_b \cdot \frac{E_b(1+\nu_b)}{2L_{b,rec}} \cdot J, \tag{2.33}$$

where $\overline{\omega}_{rel,t}$ and $\overline{\omega}_{rel,n}$ are the vectors of relative rotational velocities between bonded particles in tangential and normal directions. I and J are the moment of inertia and the polar moment inertia of the solid bond cross-section area [72].

2.6.   Numerical Methods

In recent years, technological progress has shed new light on the investigation of stressed irregularly shaped particles. The development of numerical simulations allows one to easily

investigate the behaviour of granular materials. The numerical methods can be differentiated into discrete and continuous simulations. A typical example for continuous simulation is the finite element method (FEM).

2.6.1. FEM

The FEM is based on the technique for numerically solving the algebraic equations developed by Courant in 1943. At the beginning, the method was used for clarifying problems in linear elastic fracture mechanics [73]. Nowadays, the FEM is widely used to investigate the stresses acting on both fluids and solids. It has applications for simulations of problems in the field of particle flow mechanics [74-86], compression and the breakage behaviour of particle systems [80 – 83], and fluidised bed and heat transfer processes [87-94]. The FEM considers the materials to be simulated as homogeneous. The volume of the investigated object is divided into individual finite elements before the start of the simulation. The simulation system is presented as a grid, which can be 2D or 3D [95]. These elements are connected to each other through contact points on the nodes of the grid (finite element mesh) (figure 13).
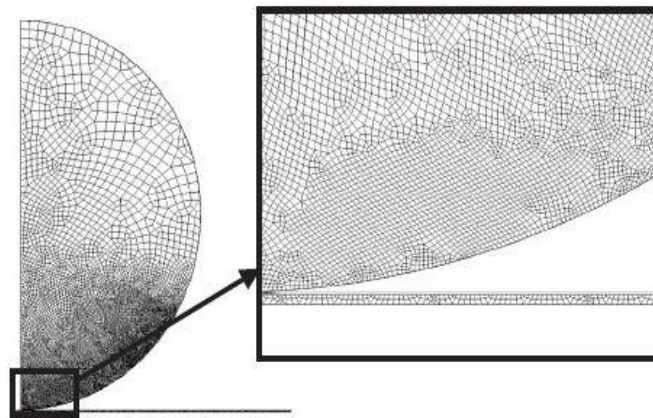
Figure 13:   Example of the finite element mesh of a ball in contact stress [97].

During simulation, the stresses, forces and displacements can only be transmitted via these nodes, according to the specified stress-strain law. The finer the division of the elements, the more precise are the results and the better is the approximation between numerical solution and experiments [96]. In general, the contact zone of the simulated particle is meshed finer than its inner section. The investigated particles may exhibit elastic or elastic-plastic properties. To reflect such behaviour, different contact models of linear and non-linear continuum mechanics can be implemented into FEM.

The advantages of this method lie in the very efficient solution technique and the lack of limitations regarding continuum structures to be simulated. In addition, applied equations are relatively simple to assemble, and the matrices used to describe the system can easily be handled numericaly [73, 98].

As already mentioned, the accuracy of the calculation depends mostly on the number of finite elements used in the simulation. However, a large number of elements also increases the cost of computation time. Thus, an increase in accuracy is faced with a strongly increasing (computing) effort. In addition, some of the numerical methods may be unusable in special cases [73]. A problem for FEM simulations is the inhomogeneous nature of real granules. Therefore, its application for simulation of porous objects, multiple cracks propagation and breakage is not proper. This limits the usage of FEM when it comes to the modelling of micro-structure and the granules' breakage processes.

2.6.2. DEM

A more suitable method for the analysis of particle systems is called "distinct element method" (nowadays "discrete element method" (DEM)). It was introduced by Cundall and Strack in 1971 for solving problems in rock mechanics [99]. The term DEM was suggested for algorithms describing the movement and the rotation of discrete bodies and the detection of contacts between them [100]. The method considers the interactions between particles in dynamic processes. The representation of the simulated system is not a grid like in FEM, but rather a particle structure [101]. The primary particles are presented as distinct elements (they are assumed to be indestructible) and their behaviour and interactions are calculated using Newton's laws of motion. By repeating the calculations for every discrete step, one can track the complete course of the simulated process. The forces acting on any element of the system, the level of stresses or the state of motion can be tracked at any stage of the simulation. DEM provides the possibility to analyse the degree of deformation occurring in solid bodies under stress, to identify and localise the contacts between the primary particles, to trail the transition from continuums to discontinuous during processes like breakage or fragmentation and to describe the motions of the particles in a particular system [97, 98, 102, 103].

Nowadays, DEM is one of the most widely used computer simulation techniques for investigating processes involving particulate solids. The particle systems can be investigated as two- or three-dimensional. The DEM is used to investigate the behaviour of assemblies formed by a large number of particles, where each particle is considered a distinct entity which interacts with its neighbours at the contact points. Correspondingly, the primary particles are presented as circles (2D) or as spheres (3D). Depending on the applied contact model, the normal and the tangential stiffness may be described as springs at the contact points, as shown in figure 14.
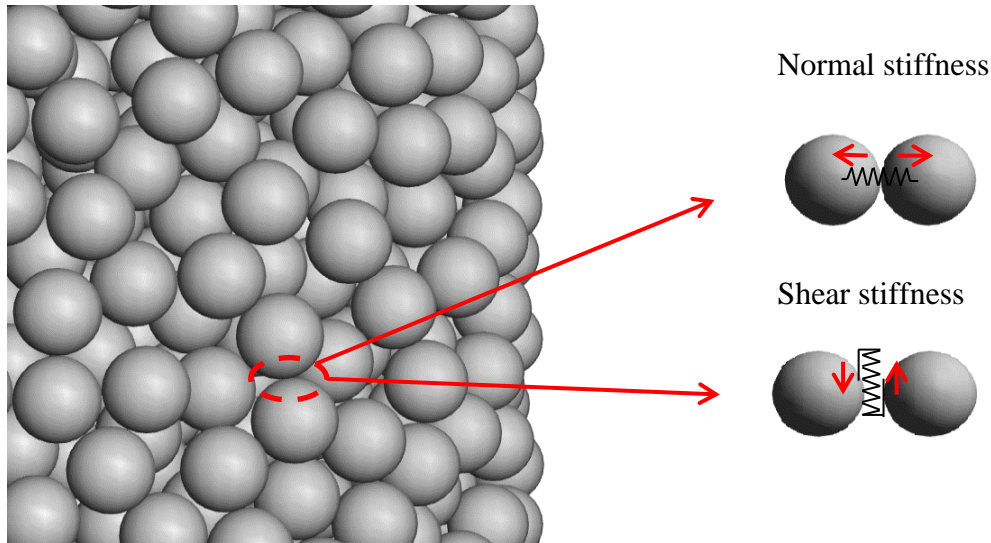
Figure 14: DEM particle assembly.

The opportunity to implement realistic inter-particle contact laws into the DEM codes gives the possibility to investigate different granular assemblies and their response to an applied loading force [104, 105]. The interpretation of objects with complex geometry can be fulfilled by presenting them as a cluster built from small primary spherical particles. In this case, the breakage event is presented as a failure of the bonding between the primary particles inside of the cluster. The focus of the DEM lies on the changing contacts and contact conditions, which should be evaluated for every single discrete step.

The determination of forces and displacement in DEM is illustrated for a 2D system in figure 15. In the given example, two disks are compressed by two rigid walls. The walls are moving with a loading velocity v_l. No contact forces exist in the initial moment t_0. After the next time step Δt the walls have moved in direction to the disks by distance $v_l \Delta t$. Overlaps will appear at the time $t_1 = t_0 + \Delta t$. Their magnitude Δs depends on the time interval and the loading velocity = $v_l \Delta t$. [103]. The contact A is defined as halfway from the point $A_{(D)}$ of the disc and the point $A_{(W)}$ of the wall, lying on the same line from the disc centre. The relative displacement of the contact during the overlap $\Delta s_{(A)t1}$ is defined as the deviation of $A_{(D)}$ and $A_{(W)}$ from their original

positions. The contact forces are calculated using the force-displacement law from the relative displacements and the normal stiffness k_n. After defining the positive direction of the forces acting on both disks, one can use them to calculate the accelerations in the next time step. The cycle of finding the forces corresponding to the displacement through the force-displacement law and substituting the sum of the forces in Newton's law to obtain new displacements can be repeated as often as necessary for the goals of the simulation. In the case of multiple assemblies, the force-displacement law is applied to each contact in the system. Figure 16 shows the main idea behind the force-displacement law for a 2D system. The contacting discs have centre Cartesian coordinates $x_i = (x_1, x_2)$ and $y_i = (y_1, y_2)$. The velocity vectors are $\dot{x}_i$ and $\dot{y}_i$ and the angular velocities $\dot{\theta}_{(x)}$ and $\dot{\theta}_{(y)}$ are positive in a counter-clockwise direction. The radii of the discs are respectively $R_{(x)}$ and $R_{(y)}$ and their masses $m_{(x)}$ and $m_{(y)}$. In Figure 16, the points $P_{(x)}$ and $P_{(y)}$ are the intersections of the line connecting the disc centres with the disc boundaries. It is assumed that the discs are in contact when the distance D between their centres is smaller than the sum of their radii. In this case, one can calculate the relative displacements from the relative velocity. The relative velocities are determined from the velocity vectors at points $P_{(x)}$ and $P_{(y)}$. The increases of the relative displacements are further used to calculate the increase of the normal and the shear forces. The force increments are summed with every time step. The resultant moment acting on each disc is taken as positive in counter-clockwise direction [101]. For 3D systems, the distinct elements x and y will be spheres. The boundaries can be presented as walls.
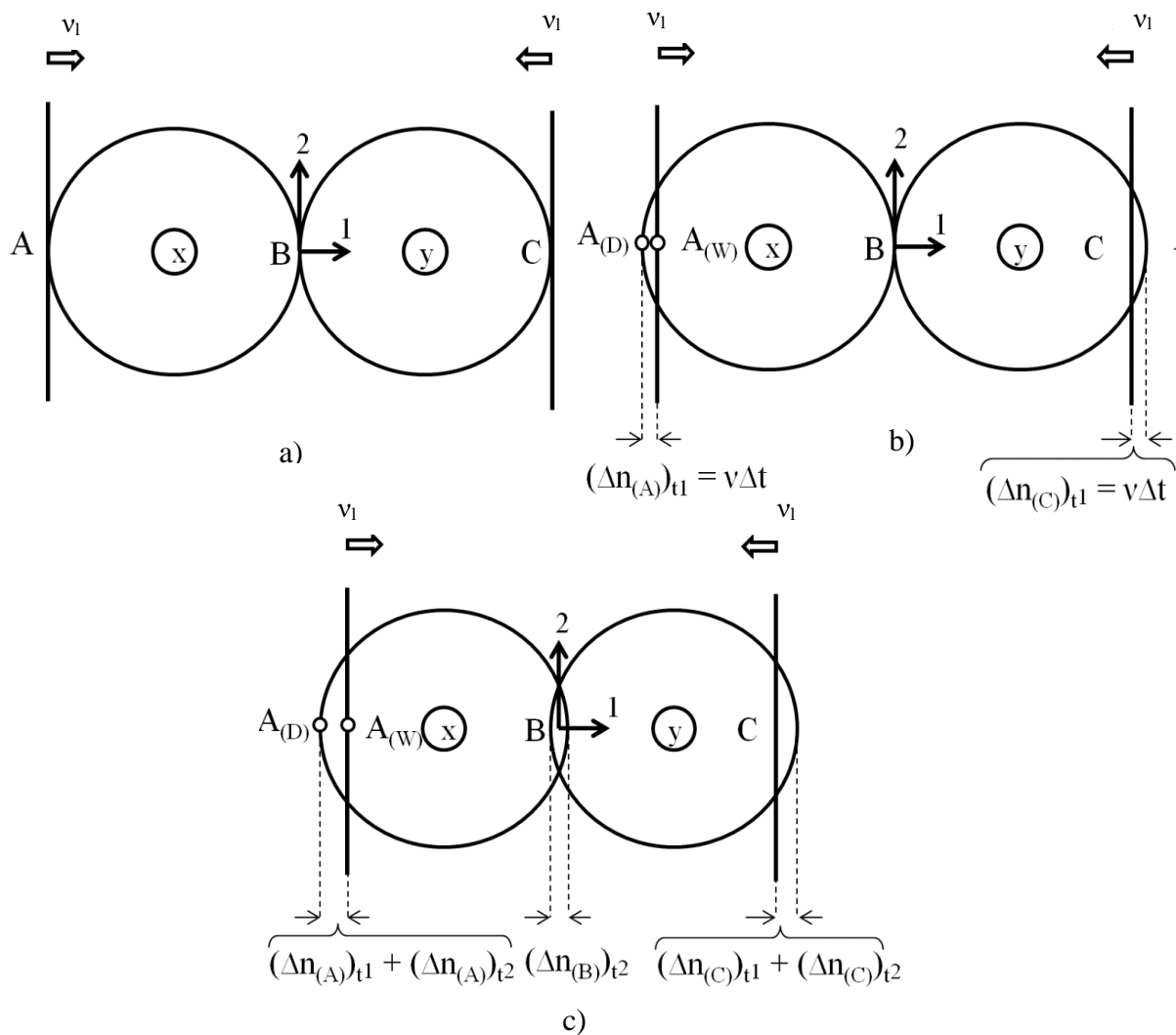
Figure 15: Two discs compressed between rigid walls (the overlaps are exaggerated); a) $t = t_0$: (b) $t = t_1 = t_0 + \Delta t$: c) $t = t_2 = t_0 + 2\Delta t$ [101].
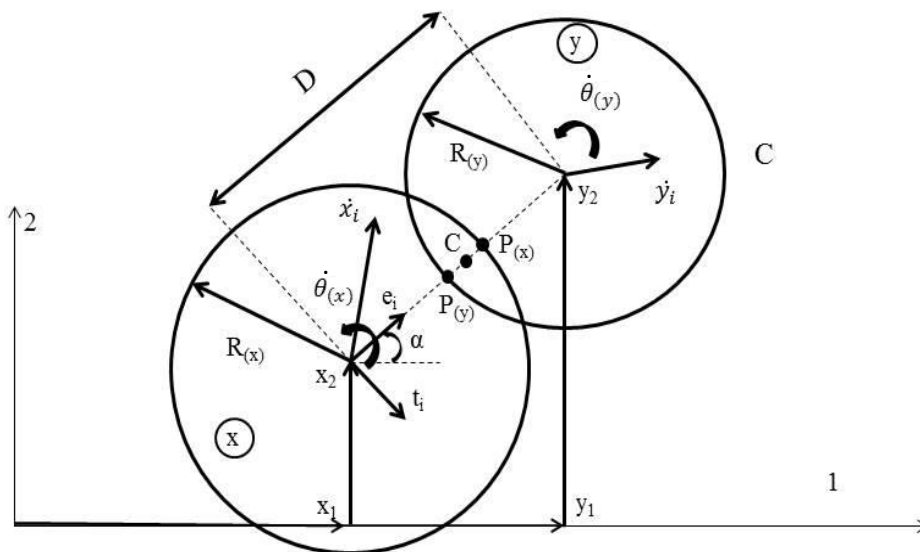
Figure 16: The force-displacement law [103 - 106].

The overlap at the contact point in normal direction $s_n^{(xz)}$ for two spheres, or between a sphere and a wall, can be estimated from the particle centres $\overrightarrow{r_{(x)}}$, $\overrightarrow{r_{(y)}}$ (wall coordinates $\overrightarrow{r_{(w)}}$) and the particle radii ($R_{(x)}$, $R_{(y)}$)

$$s_n^{(xy)} = \begin{cases} R_{(x)} + R_{(y)} - \left| \overrightarrow{r_{(x)}} + \overrightarrow{r_{(y)}} \right| \\ R_{(x)} - \left| \overrightarrow{r_{(x)}} + \overrightarrow{r_{(w)}} \right| \end{cases} . \tag{2.34}$$

Then, the coordinates of the particle centres for a particle-particle contact will be

$$\overrightarrow{r_k^{(xy)}} = \overrightarrow{r_{(x)}} + \left(R_{(x)} - \frac{1}{2} s_n^{(xy)} \right) \overrightarrow{n_{(xy)}} \tag{2.35}$$

and for particle-wall contact

$$\overrightarrow{r_k^{(xw)}} = \overrightarrow{r_{(x)}} + \left(R_{(x)} - \frac{1}{2} s_n^{(x1)} \right) \overrightarrow{n_{(xy)}}. \tag{2.36}$$

The normal vector $\overrightarrow{n_{(xy)}}$ goes through the particle centres perpendicularly to the contact surface

$$\overrightarrow{n_{(xy)}} = \frac{\overrightarrow{r_{(y)}} - \overrightarrow{r_{(x)}}}{\left| \overrightarrow{r_{(y)}} - \overrightarrow{r_{(x)}} \right|}. \tag{2.37}$$

The contact velocity of the elements in the contact area can be found using the following equation:

$$\overrightarrow{v_{(xy)}} = \overrightarrow{v_{(x,k)}} - \overrightarrow{v_{(y,k)}} = \overrightarrow{v_{(x)}} + \overrightarrow{\omega_{(x)}} * \left| \overrightarrow{r_k^{(xy)}} - \overrightarrow{r_{(x)}} \right| * \overrightarrow{n_{(xy)}} - \overrightarrow{v_{(y)}} - \overrightarrow{\omega_{(y)}} * \left| \overrightarrow{r_k^{(xy)}} - \overrightarrow{r_{(y)}} \right| * \overrightarrow{n_{(xy)}}, \tag{2.38}$$

where $\overrightarrow{v_{(x)}}$, $\overrightarrow{v_{(y)}}$, $\overrightarrow{\omega_{(x)}}$ and $\overrightarrow{\omega_{(y)}}$ are resp. the translation and the rotation velocities of the particles x and y. The increment of the overlap in tangential direction can be found from the tangential components of the relative velocity at the contact

$$\Delta s_t^{(xy)} = v_t^{(xy)} \Delta t, \tag{2.39}$$

where Δt is the chosen time step for the simulation.

The main scheme for the calculation cycle of a DEM simulation is given in figure 17. In DEM, one can apply any model for elastic, elastic-plastic, plastic, visco-elastic or visco-plastic contact behaviour. One can also add external forces acting on the particles, like gravitational force, adhesion force, attraction or repulsive forces. They can be implemented as contact restrictions, and, thus, the contact forces result from the imposition of contact restrictions between the solution variables at the contact points. For particle assemblies, the bonding between the single

particles can be also interpreted as contact restrictions. They can be destroyed at previously defined conditions, e.g. when the acting external forces exceed the mechanical strength of the bonding [70].
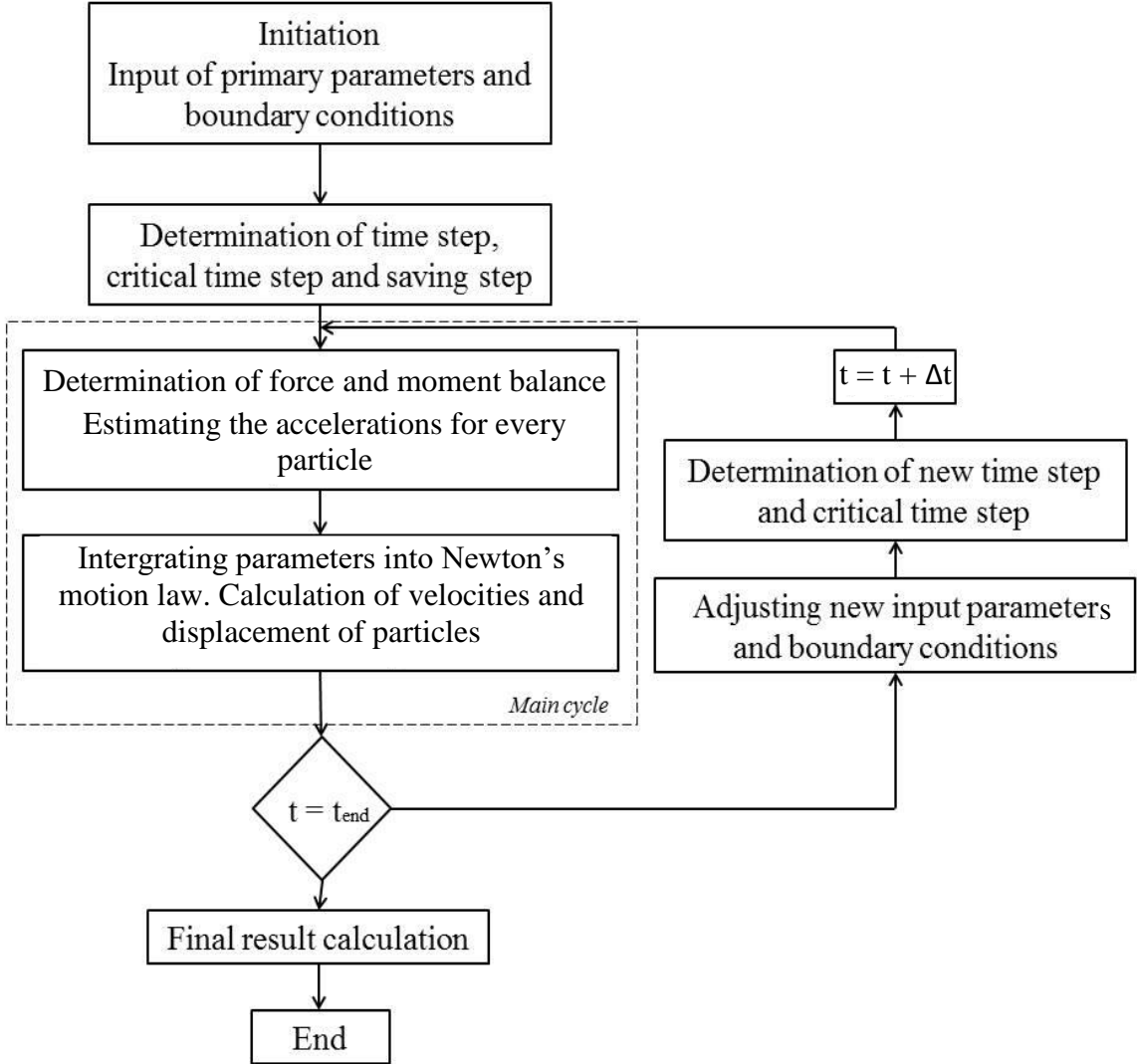
Figure 17:   General workflow of a DEM simulation [62, 107].

3. Pelletising and Methods for Pellet Characterisation

3.1. Experimental Principles and Methods

To investigate the breakage behaviour of irregularly shaped pellets, a series of experiments and DEM simulations were accomplished and analysed in detail. The first step of the analytic procedure was the production of model pellets. In the next step, their characteristics were precisely estimated. The focus was on the compression behaviour of the pellets. Before the compression experiments, selected pellets were scanned using μ-computed tomography and the exact positions of their primary particles were recorded. Using their 3D coordinates, the pellets were rebuilt in a simulated domain and the compression tests were repeated. Results from experimental and simulated compression tests were compared and conclusions about the breakage behaviour of the model pellets and the applicability of the DEM simulations for the investigation of failure events were made.

In this chapter, the methods used for the production and the characterisation of the model pellets will be presented in detail.

3.2. Agglomeration

When it comes to pellet characterisation, too small ingredient particles can cause a lot of difficulties. Pellets can consist of many primary particles and small size of them makes the estimation of the exact number of constituent particles, crack propagation at breakage points and contact behaviour very complicated. Moreover, numerical simulation of particle systems containing many small particles requires high-performance computing resources and long calculation times. Due to this, the primary particles for the model pellets in this work were chosen to have relatively large size. The primary particles should also be light enough so they can be held together by the binder molecules, but at the same time large enough to overcome any cohesion forces between them during production. It was very important that the number of primary particles in the pellets was countable, which allows an easy characterisation of the pellets and makes it possible to trail the force propagation at breakage.

The agglomeration process of the primary particles was accomplished in a laboratory pan pelletiser (figure 18). The equipment consists of a rotation disc with a diameter of 0.2 m and 0.1 m high stationary rim. The pelletiser is horizontally adjusted and is generally used to produce granules within the range of 1 to 20 mm. The provided apparatus is not suitable for

pelletising particles smaller than 250 µm, as they can fall into the gap between the rotational disk and the rim, which leads to losses [15, 72].

The primary particles are fed into the process chamber before the start of the process. To decrease the stirring between the dry primary particles and the pelletiser walls, one third of the total binder amount required should be added to the particles before starting pelletising. This is done to wet the surfaces and the walls of the pelletiser and to avoid primary particle breakage. If a primary particle should break during the pelletising process, its fragments will fall into the gap between the rotating disk and the rim (figure 18). If pieces of these small powder fragments from broken primary particles stay in the processing chamber, they might join the structure of the produced pellets and have a strong influence on their mechanical properties. The fragments might fill the spaces between the primary particles or be dissolved into the binder solution. In both cases, such processes would affect the properties and breakage behaviour of the final product. Allowing these small fragments to pass through the gap ensures that they will not be included in the pellet composition.
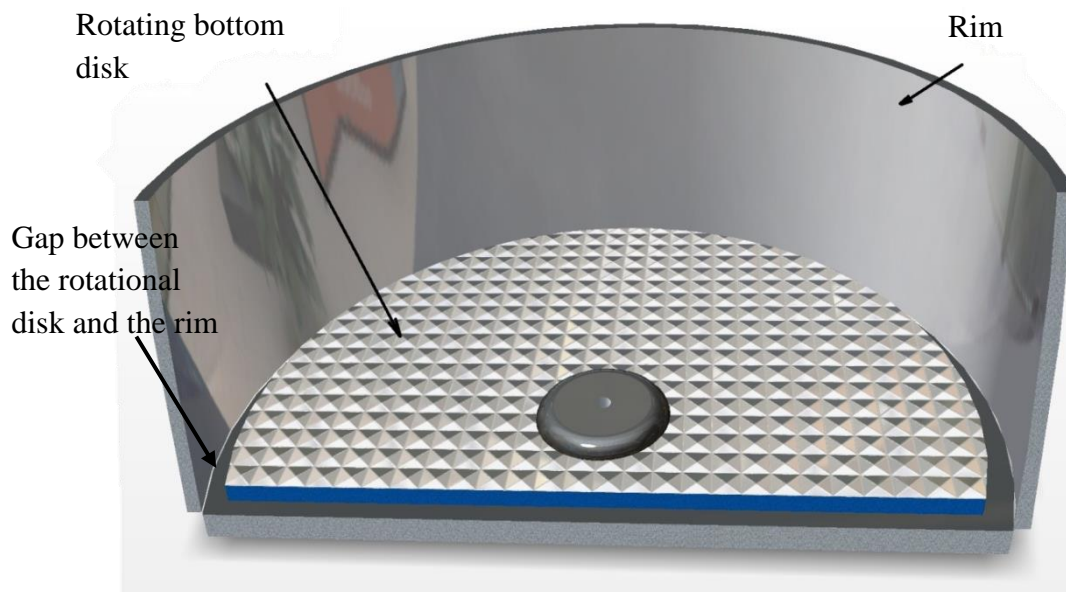
Figure 18:   Horizontally adjusted pan pelletiser.

The basic operation principles of the pelletising machine and the forces acting on the particles are given in figure 19. The granules in the pelletiser perform a torus-like motion [108]. The rotational velocity of the particles depends on their position relative to the bottom disk. The granules are set into motion by the bottom disc's rotation. Therefore, the particles in the lower part of the bed have larger velocities.
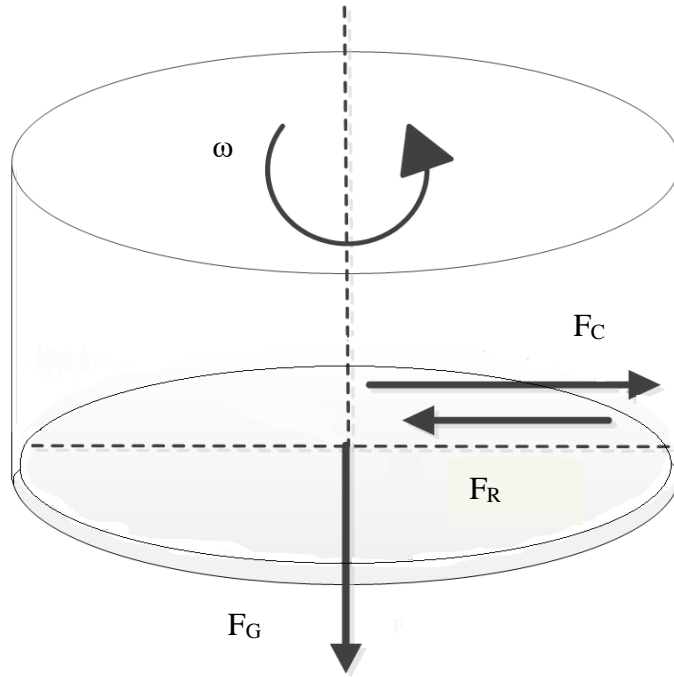
Figure 19:   Principle scheme of rotational pan pelletiser and acting forces.

When the particles are stationary at t = 0, there are no forces governing the process. When the disc begins to rotate with an angular velocity ω, centrifugal forces causing characteristic motion start to act on the particles. The feed in the horizontal pan pelletiser begins to move in a circular direction at a constant velocity. Moreover, there is a movement in a circular direction to the center of the pelletiser of particles caused by particle impact with the pelletizer walls. The centrifugal force F_c is

$$F_c = m_p \cdot r_d \cdot \omega^2, \tag{3.1}$$

where m_p is the mass of the particle, r_d is the radius of the disc and ω is the rotational speed. At the same time, a friction force F_R, acting in opposite direction to the centrifugal force occurs between the particles in the pelletiser and the rotating disk.

$$F_R = \mu_R \cdot F_G, \tag{3.2}$$

where μ_R is the frictional coefficient between the two surfaces and F_G – gravitational force. If the sum of all acting forces in the system is equal to zero, the particles in the pelletiser will be performing stationary motion at a constant velocity:

$$\sum F_n = 0 = F_c - F_R, \tag{3.3}$$

$$F_c = F_R. \tag{3.4}$$

If one substitutes the centrifugal force and the friction force, one arrives at the force balance of the system

$$m_p \cdot r_d \cdot \omega^2 = \mu_R \cdot m_p \cdot g, \tag{3.5}$$

The velocity of the rotating disk at which the particles perform stationary motion can easily be found from the force balance [7]. Hence, one can find the critical angular speed of the process

$$\omega_{crit} = \sqrt{\frac{\mu_R \cdot g}{r_d}}, \tag{3.6}$$

where g is the acceleration of gravity. To avoid uneven built-up and sliding of granules, the operating velocity should provide optimal process conditions [15, 107]. The particles do not move independently, rather the whole particle bed moves. The rotational speed of the horizontal pan pelletiser can be also given in terms of critical number of revolutions n_{cr}

$$n_{cr} = \sqrt{\frac{g \cdot \sin\delta}{2\pi^2 D_d}}, \tag{3.7}$$

where δ is the angle of the disc and D_d is disc diameter. The typical operating range is 50 to 75 percent of the critical number of revolutions n_{cr} [108].

As a result of the motion performed in the pelletiser, the primary particles collide with each other and adhere by means of the added binder. At the same time, some ready formed agglomerates get crushed on the walls of the pelletiser. By controlling the process parameters, it is possible to balance between agglomeration against breakage and to receive in the end a product with the desired properties.

3.3. Microscopy of the Product Pellets

The received pellets were stored under atmospheric conditions for 24 hours in order to achieve complete hardening of the binder and then investigated using a light microscope (LM) and a scanning electron microscope (SEM). The light microscope used was a Binokular 500 produced by the "Carl Zeiss" company. Its maximum magnification is x1600. Through the usage of a lens system, enlarged images of the investigated objects can be acquired and used for their characterisation. The scanning electron microscope uses a focused electron beam to produce images of the scanned object. Compared to the LM, the SEM produces high-resolution images

with more topographical details. The resolution is defined as the minimum distance between two closely located points, at which they can be recognised as separate entities. The best resolution for a LM is about 200 nm, whereas a SEM can provide a resolution of less than 10 nm. The apparatus used was Phenom G2 Pro from the company Phenom-World BV. Principle schemes of a light and a scanning electron microscope are given in figure 20.
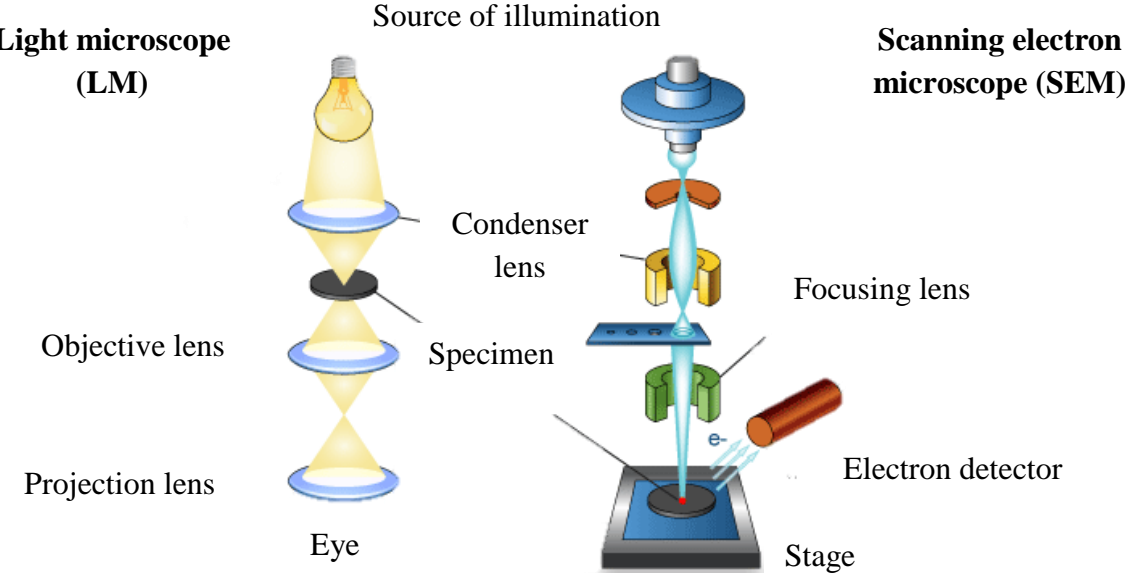
Figure 20:   Basic working principle of light microscope and scanning electron microscope [109].

The main goal of the microscopy was to confirm the presence of solid bridges between the primary particles, like shown in figure 21. This should verify that the binder had successfully joined the particles and was suitable for a pelletisation of the chosen primary particles. The microscopy was also intended to investigate the binder distribution in the pellet to show possible micro-cracks in the structure of the solid bridges or layer formation over the primary particles. Another objective was to indicate any mechanical changes in the primary particles, like breakage or attrition. Possible breakage of the particles and the powder emerging from it can change the properties of the pellets by joining their structure.
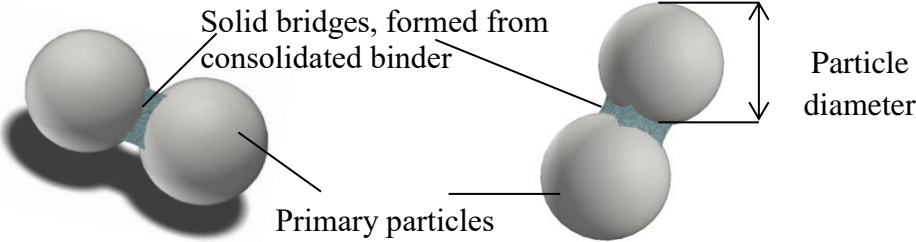
Figure 21:   Primary particles connected through solid bridges.

3.4. Particle Size Analysis

The particle size distribution of the obtained samples and the sphericity of the pellets were analysed using digital image processing. The equipment used for the analysis was the particle analyser Camsizer developed by RETSCH Technology, Germany. The apparatus works on the principal of digital image processing techniques and is used for analysis of the particle size, particle shape and the number of particles in samples [110]. The apparatus consists of two cameras, one basic camera which measures the large particles and another for capturing the small particles at high resolution. The measuring size range is from 30 µm to 30 mm. The operating principle of the Camsizer used is shown in figure 22.

Every pellet sample was fed into the process chamber one by one. A vibratory conveyor transports the particles to the measurement zone. The pellets fall between the light sources and the cameras and their shadows are recorded during the fall. Based on the observed digital images, an analysis of the shape and size distribution was accomplished for every single sample. The investigated agglomerates are not perfectly spherical, and, therefore, different features such as the area equivalent diameter and the shortest chord of the measured set of maximum chords were evaluated. Particle size was finaly characterised by the mean diameter $d_{50,3}$.
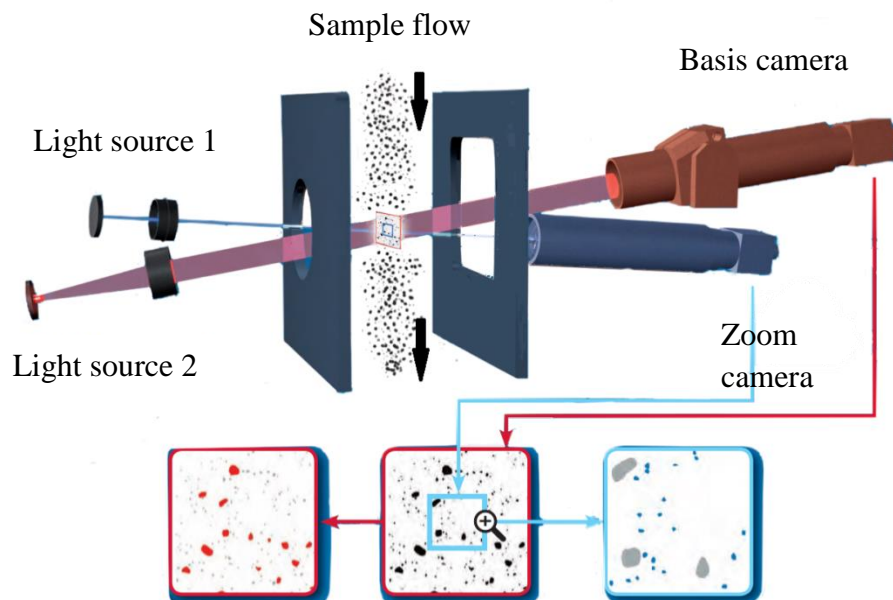
Figure 22:   Camsizer operating principle [110].

3.5. Sieving

Due to technical restrictions of the strength testing equipment used for compression tests of the model pellets, only samples with a size smaller than 3.5 mm could be forward characterised. Therefore, in order to achieve representative results, the produced pellets were separated into different size classes after the characterisation of their size distribution was complited. The used equipment for the separation process was a standard sieving set. For alumina the class sizes were four – pellets with $d_{50,3}$ larger than 4.5 mm, pellets with size $d_{50,3}$ between 4.5 and 3.5 mm, pellets with size $d_{50,3}$ betwenn 3.5 and 1.5 mm and pellets with $d_{50,3}$ smaller than 1.0 mm. For zeolite the size fractions were also four – pellets with $d_{50,3}$ larger than 4.5 mm, pellets with size $d_{50,3}$ between 4.5 and 3.5 mm, pellets with size $d_{50,3}$ betwenn 3.5 and 2.5 mm and pellets with $d_{50,3}$ smaller than 2.5 mm. The last size fraction consists mainly of nonagglomerated primary particles. The size classes were chosen depending on the primary particle diameter. As discussed in section 2.2.2.1, the size is of main importance for the assignment of other particle properties. Therefore, by analysing samples with distinct size we can assume that changes in properties are due to factors like their different structure and distribution and strength of the solid bridges between the primary particles. The density and porosity analysis, X-ray computer tomography, stress analysis and computer simulation were performed only for the size class with $d_{50,3}$ between 3.5 and 1.5 mm for alumina and $d_{50,3}$ between 3.5 and 2.5 for zeolite. The rest of the class sizes were not investigated forward in this work.
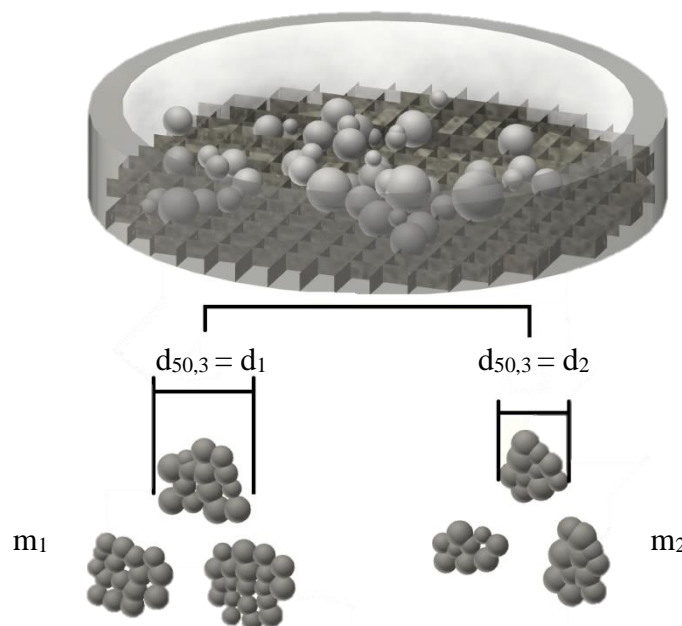
Figure 23:   Standard sieve for separating particles to fractions of sizes d_1 and d_2 [111].

3.6.   Density and Porosity Analysis

As discussed in section 2.2.2.3, the porosity plays an important role in the agglomeration process and is a deciding factor when it comes to the choice of size enlargement process and binder. To ensure that the chosen process conditions are proper for the goals of size enlargement, it is necessary to investigate the difference between the porosity of primary particles and the pellets.

The used primary particles exhibit a high porosity. Their properties have been investigated by Müller et. al. [128] and are given in section 5.1.

At first, one should determinate the skeletal density of the pellets ρ_s and compare it with this of the primary particles. The skeletal denisy is defined as the density of the solid phase obtained when its volume is measured excluding pores, voids and hollow spaces in the sample. Anyway, one should notice that in the investigated case the solid phase of the model pellet consists of two materials – primary particles and binder.

A helium gas pycnometer was used for this measurment (Ultrapyc 1200e, Quantachrome Instruments). This apparatus is used for determination of volume and density of powders, agglomerates, granules, porous materials, chemical mixtures, pastes and liquids [112]. The carrier gas for the measurement is helium due to its small atomic size. Its molecules can reach even the smallest pores into the structure and ensure precise results. The measurement is based on Archimedes' principle of fluid displacement and Boyle's law [113]. The two-cell system of the helium gas pycnometer is shown in figure 24.

a)   Closed valve, measurement of P_1 b) Open valve, measurement of P_2
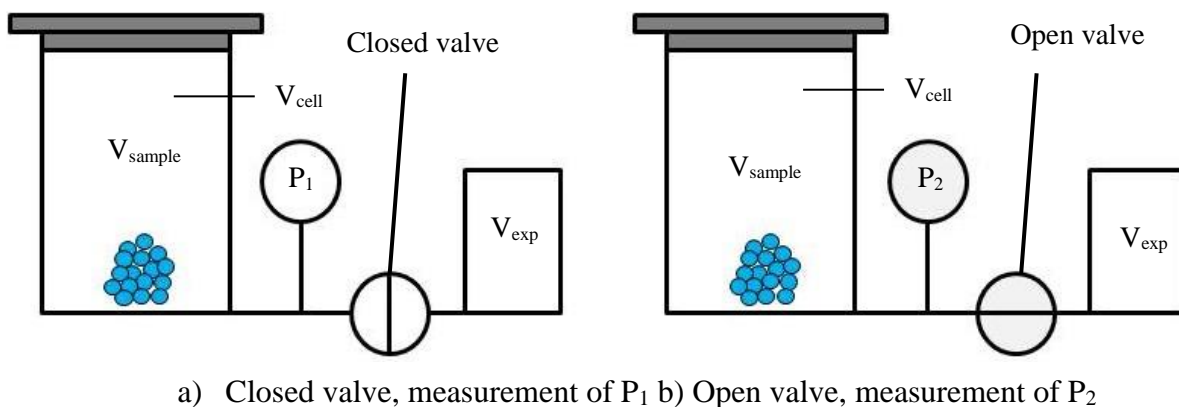
Figure 24:   Operating principle of helium pycnometer.

The helium pycnometer consists of two cells, one for the sample and one reference cell. The two cells are connected by an adjustable control valve. The sample cell is filled with a previously weighed sample of pellets. The chosen measuring cell had a defined volume of V_{cell} = 12.93 cm^3. The reference cell has volume $V_{exp.}$ During the analysis, the cell with the sample is filled with helium gas until the pressure inside has reached a certain constant value. At this point, the helium molecules have penetrated in the pores of the sample including the pores of the primary particles, the micropores of the solid bridges and the voids between primary particles. Then the helium gas is led to the reference cell where its pressure and volume are measured. The volume of the sample V_{sample} is calculated as the difference between the volumes of both cells [114]

$$V_{sample} = V_{cell} - \frac{V_{exp}}{1 - \frac{p_2}{p_1}}, \tag{3.8}$$

where p_1 is the pressure measurement with closed valve and p_2 is the pressure measurement with open valve.

The skeletal density ρ_p is given as a ratio of the mass of the solid pahse m_p and measured solid phase (primary particles and solid bridges) volume V_s

$$\rho_s = \frac{m_p}{V_s}, \tag{3.9}$$

In the further analysis, the apparent density of the produced pellets was characterised using a GeoPyc 1360 Envelope Density Analyser (figure 25).

The equipment consists of a cell and a piston which is filled with fine graphite powder with high pourability. The analysis begins with a calibration measurement. The cell is filled only with the graphite powder. The piston compresses the powder and determines its loaded volume V_B. Then a sample of pellets with mass m is introduced into the cell and the volume is measured again as V_S. The powder penetrates through the voids of the pellets like a fluid. Anyway, due to its large particle size, the powder does not penetrate into the primary particle pores neighter into the micropores of the solid bridges. The volume of the introduced sample is calculated from the difference between the two measurements [115].
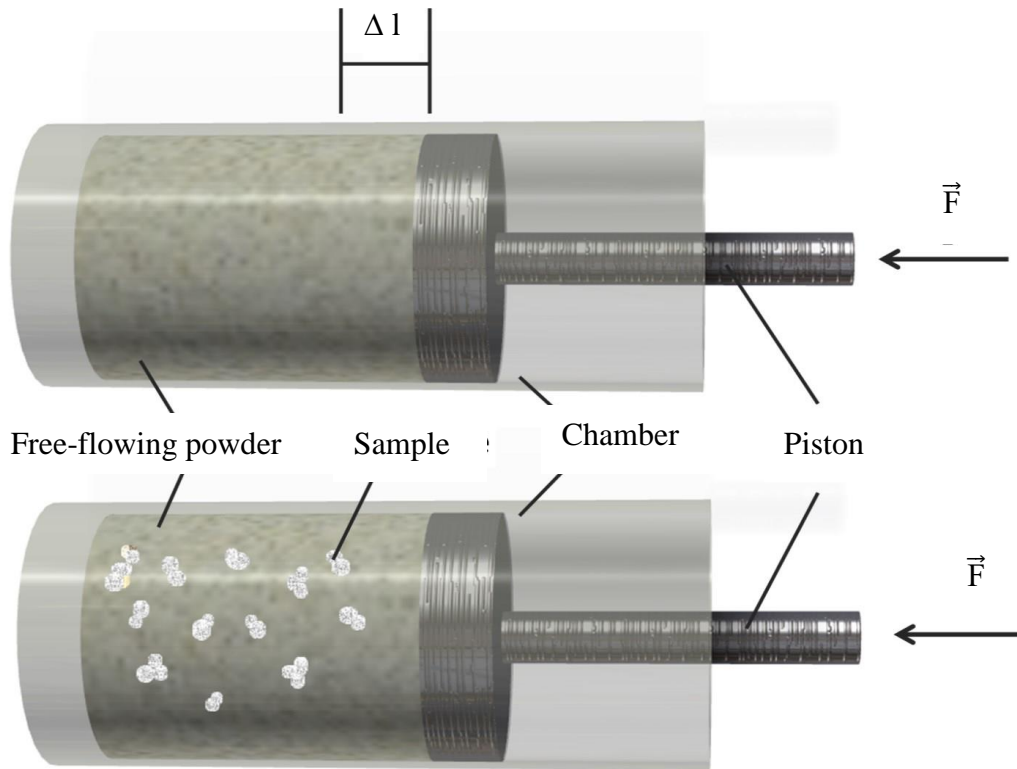
Figure 25:   Operating principle of the Envelope Density Analyser (GeoPyc 1360).

The apparent density of the model pellets is calculated from the difference between the measured volumes of the cell without V_e and with pellets V_f and the weight mass of the introduced sample. (eq. (3.10))

$$\rho_p = \frac{m}{V_f - V_e},$$
(3.10)

The porosity ε can be calculated from the ratio between their skeletal ρ_s and apparent density ρ_p.

$$\varepsilon = 1 - \frac{\rho_p}{\rho_s},$$
(3.11)

3.7.   X-Ray Computer Tomography (CT)

More precise information about the inner structure and assembling of the model pellets could be provided using X-ray computed tomography (CT). CT is a reliable method for structure analysis and an investigation of material morphology. The development of the method was initiated after the Australian mathematician Radon proved in 1917 that a multi-dimensional object can be reconstructed from infinite set of its projections [116]. The process combines spectroscopy and imaging and allows investigating the inner structure of various materials

without taking them apart. The main working principle is shown in figure 26. The chosen sample is put on a sample holder, which rotates around its own axis. The X-ray source irradiates the sample and the detector takes radiographic snapshots of the specimen at different angular positions. From these 2-D images, the CT system creates a full 3-D image for both the interior and exterior of the sample. The 3-D image represents a volumetric density map in grey values based on the composition of the sample. Each grey level offers information about what has been encountered by the X-rays in their paths of travel and their spatial location, thus revealing internal and external structures of an object. The object surfaces are not explicitly defined in this technique, but they can be extracted from the reconstructed volume using a precise surface determination algorithm.
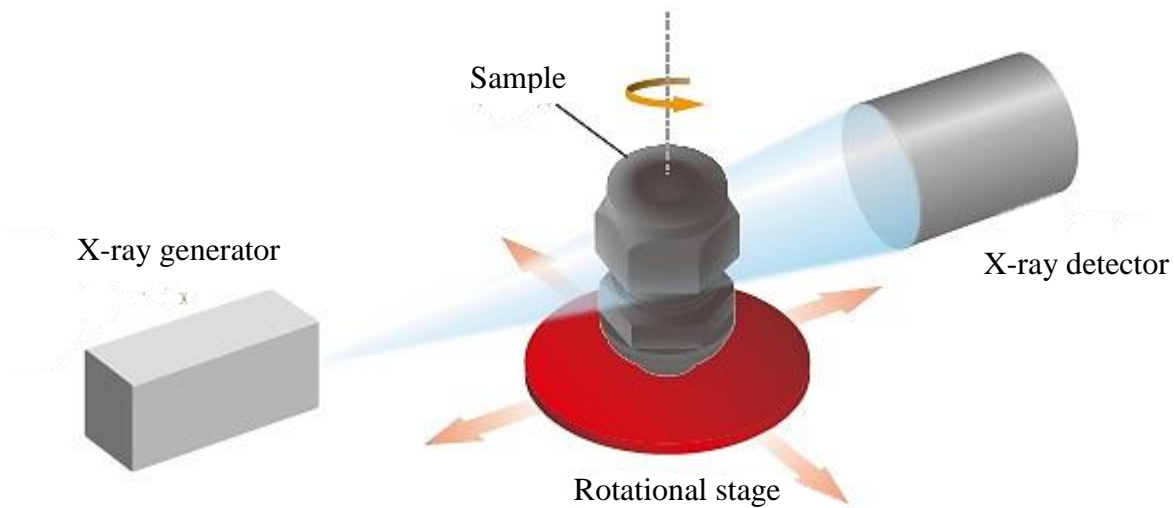
Figure 26:   Basic working principal of X-ray computer tomograph [117].

The reconstruction of the volume images and the measurements of the sample were performed using the software Volex, which was specially developed by the Fraunhofer Institute of Integrated Circuits, IIS, Erlangen, Germany. The image processing, analysis and the data extraction of 3-D images were completed using the same software. Using CT, it is possible to measure volume distributions of pores in the sample and to investigate the concealed micro-structure of individual particles. The apparatus used for the characterisation was CT Alpha, manufactured by the Procon X-ray Company. The maximum tube voltage is 160 kV and the maximum possible resolution of the scanner is limited to 1 μm. Samples of up to 5 cm in each direction of space and up to 5 kg of weight can be measured. The X-ray tube used was a transmission radiator. This offers the advantage of having a large opening angle. The detector had a field size of 10 x 10 cm^2. This is equivalent to 2300 x 2300 pixels, which are assigned with grey levels during the measurement. The rotation of the test sample throughout the

measurement converts two-dimensional information in a set of volume data. Thus, the pixels will also record depth information and are referred to as a voxel. The detector which was used can be classified as an indirect-converting detector. This means that the energy of the X-ray beam is converted into optical light and then detected by photodiodes.

The processing of the 2-D data consists of several steps. Data is firstly transformed to grey-tone images. This allows the displaying of the images without visible gaps. Afterwards, through binarisation, the object image is separated from the background. The next step in the image processing was the application of different filters to remove noise and to clarify the images. During filtering, each voxel value is replaced by the corresponding grey values (depending on the applied filter) of local neighbours to achieve homogeneous structure. The further processing of the images was accomplished by the segmentation of different objects in the images. In this way, one can ensure that every primary particle in the structure of the pellet is recognised as a separate object with its own distinct characteristics. Hence, any small particle fragments or impurities which are present and can lead to mistakes in the analysis can be neglected. Furthermore, different materials on the images were separated through thresholding. This can be performed using different methods, but Otsu's method was chosen for the presented study [116]. This method chooses the optimal threshold by maximizing the repairability of the resultant classes in grey levels. The idea behind the procedure is to find the zeros and the first-order cumulative moments of the grey-level histogram. This is done in two steps – first normalising the grey-level histogram and its presentation as a probability distribution, and afterwards dichotomising the voxels into two classes. A detection of neighbouring objects was also performed, followed by the labelling and identification of the properties of the image objects. Using the CT, it was possible not only to characterise the number of primary particles in a pellet and their centre coordinates, but also parameters like the radius of gyration, the porosity, the fractal dimension, the pre-factor and the coordination angle.

3.8. Particle Coordinates Optimisation

The data received from the CT for the structure of the pellets does not include any information on the binder distribution and the solid bridges connecting the primary particles. The reason for this is the large difference between the density values of primary particles and the binder. Additional processing of the CT data is needed for the characterisation of the binder distribution and the exact positions of the solid bridges. The main goal of the CT scanning was to gather information pertaining to the coordinates of the primary particles and to rebuild them in the simulation software. In any case, using the chosen simulation tool, it is not possible to rebuild

the solid bridges with their exact positions. Moreover, even if it were possible, reconstructing bridges in this way would require much more time and computing resources. However, without data for the solid bridges, the bonding between primary particles could not be detected by the simulation software and in place of the solid bridges, gaps will appear. Additionally, inaccuracy in sphericity or diameter between the real and the simulated particles may appear. This may lead to mistakes in the simulation results. Due to this, the measured coordinates were mathematically optimised to avoid the possibility of particle contact misstatement. Using a self-programmed Matlab script, the coordinates of the primary particles were corrected in a way that enabled the detection of all the contacts in the structure of the pellets and at the same time changed the real positions of the particles as little as possible. Nevertheless, the script also allows preventing any particle overlap errors, which could lead to stress generation through the DEM compression process.

The primary particles are described as ideally spherical with radius r_p and centre coordinates x, y and z. The Eulerian coordinates of the particle can be also given with the space vector V. For the particle i, the space vector will be given as follows:

$$V_i = \{x_i, y_i, z_i\}, \tag{3.12}$$

where $i = [1 \dots N_p]$. The distance between two primary particles i and j can be found by applying the Pythagorean theorem

$$|V_i - V_j| = \sqrt{(x_i - x_j)^2 + (y_i - y_j)^2 + (z_i - z_j)^2}. \tag{3.13}$$

All the primary particles in the pellet have been assumed to have the same radius r_p, which means two particles will be in contact if

$$|V_i - V_j| = 2r_p \tag{3.14}$$

is fulfilled. Correspondingly, through the centre distance, it can be confirmed whether the particles are overlapping or have no contact to each other.

The interval R_{ij} is introduced to identify the particles which are bonded with solid bridges

$$R_{ij} = d_f r_p, \tag{3.15}$$

where d_f is an experimentally determined factor. It is proved for every possible particle pair if the condition

$$\left|V_i - V_j\right| = 2r_p \rightarrow P_K := \{i,j\} \quad \forall i = [1 \ldots N_P\text{-}1] \quad \forall j = [i \ldots N_P] \qquad (3.16)$$

is fulfilled and the number of identified pairs of particles K is determined.

An optimisation function is defined for the adjustment of the particle positions. It consists of an objective function f(x), which can be either minimised or maximised and a series of additional conditions, which are defined as equation constraints ceq(x) = 0 and inequalities c(x) > 0. The new positions of the particles V_i^* must differ as little as possible from the original positions V_i. If the introduced creteria are fullfilled, one can find the cost function of deviations sum from the original coordinates

$$f(V_i^*) = \sum_{i=1}^{N_P} \left|V_i - V_i^*\right|^2. \qquad (3.17)$$

As boundary conditions are included, the particle distance at which the particles are recognised by the simulation tool as a pair decrease. A distance of zero is unsuitable due to numerical inaccuracies that cause a stochastic scattering of particle position. A minimum distance at which a solid bridge can be recognised and in which no overlapping exists is:

$$r_p{}^* = r_p + \frac{\epsilon}{2}. \qquad (3.18)$$

For the equation constraints, the following will be valid

$$ceq(V_i^*): \left|V_{P_{k,i}}^* - V_{P_{k,j}}^*\right| - 2r_p{}^* = 0 \qquad \forall k = [1 \ldots K]. \qquad (3.19)$$

Using the numerical computing programme Matlab, a script was developed for solving the optimisation function. The raw data, consisting of the primary coordinates of the primary particles, was inserted into the programme environment. Additional parameters, like the particle radius r_p, were added manually. Through mathematical iteration, all the combinations of particle pairs are found and checked to see if the condition (eq. (3.18), resp. eq. (3.20)) is fulfilled. The pairs are saved with their particle numbers in a matrix P. The particle distances are also saved in the same matrix. Subsequently, it is verified whether all particles from the assembly appear in the pairing list at least once. If there is a particle without having a contact in the particle assembly, a loop is started, the optimisation function is repeated and new coordinates are adjusted for the solitary particle

.

3.9.   Stress Analysis

The focus of this study was the investigation of breakage behaviour of pellets under compression. The agglomerates produced under different processing conditions were thus subjected to compression tests. To receive reproducible results, the sieved size fractions of pellets with diameters from 1.5 mm to 3.5 mm for alumina and from 2.5 mm to 3.5 mm for zeolite were chosen for the strength testing. 100 pellets from each fraction were tested and their breakage behaviour analysed. The 100 trails were necessary to increase the statistical significance of the results, which were expected to exhibit large standard deviations due to the irregular form and shape of the pellets. The apparatus used for the compression tests is manufactured (GFP) by Etewe, Germany. The measuring zone of the tester is shown in figure 27. The machine consists of two pistons – one moveable and one stationary. Sensors connected to the pistons register the applied force and the deviation of the movable piston from the starting position.

Due to the fact that the primary particles in the structure of the pellets exhibit breakage strength in the range between 30 and 50 N [118, 119], a sensor measuring up to 100 N was used for the compression. The loading velocity can be varied from 0.01 mms^{-1} to 0.05 mms^{-1}. To improve the comparability of the compression results, the loading velocity of the piston was the same for all the experiments: 0.05 mms^{-1}.
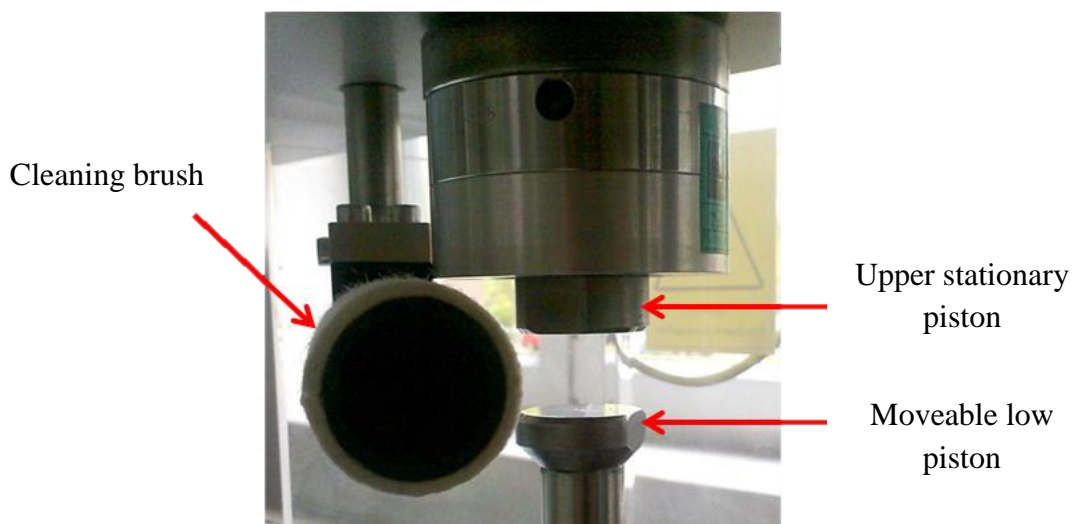
Figure 27:   Measuring zone of breakage testing device.

The pellets were manually placed on the lower piston as shown in figure 28. Each pellet was individually tested. Due to their irregular shape, pellets placement is an issue. The pellets were placed on their longest side in order to achieve maximum stability and to decrease the possibility of rearrangement when the loading begins. This corresponds to the placement of pellets during the CT scans. Therefore, data from the compression tests can be subsequently compared with simulation results, where the primary particles are modelled using coordinates received from the μ-computed tomography.
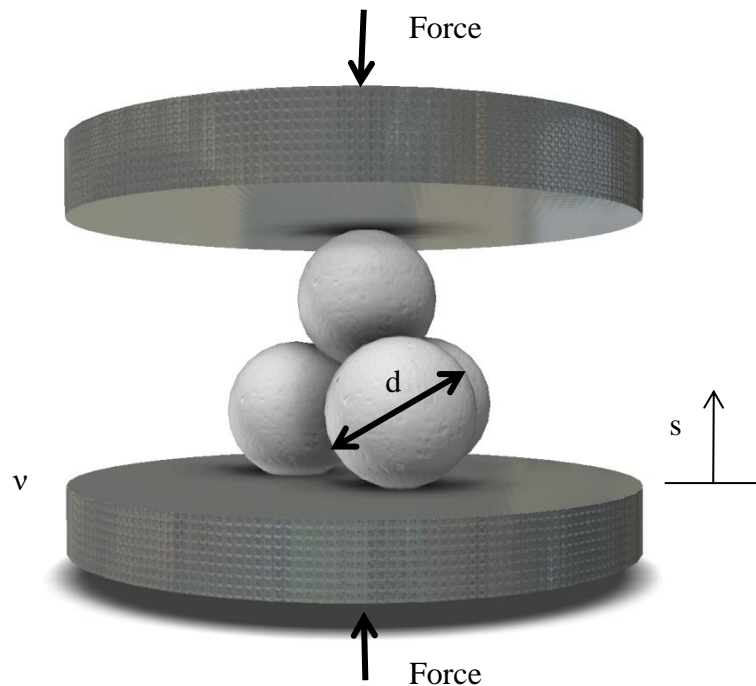
Figure 28:   Pellet with tetrahedron shape during a compression test.

The compression test starts with upward motion of the lower piston with the chosen velocity. The measurement begins when the pellet strikes the upper piston. The applied force F, displacement of the piston s and the time t are recorded using GFP software in force-displacement diagrams (figure 8 in section 2.5.2). The pellets were loaded only until primary breakage. This means the criterion for interruption of the tests was the appearance of the first force peak in the force-displacement diagram. It was assumed that this peak characterises the first failure of the solid bridge network inside of the pellet. The primary particles were not expected to break. This corresponds to the treatment of the primary particles as rigid bodies in the DEM simulation.

However, the model pellets exhibit a large inhomogeneity, especially in the distribution of their solid bridges. Thus, standard deviations are comparatively large. Moreover, undesired effects can occur when the pellets are subjected to compression. Firstly, breakage of primary particles

may occur, due to localy high exposure to stress or if the particles were damaged during the pelletising process. The result is a force-displacement curve with a large breakage force, untypical for the solid bridges. Secondly, primary particles may become rearranged in the pellet when the loading force is applied due to the complicated geometry and the multiple areas of surface contact. After such rearrangement, the contact surfaces to the upper and the lower piston become similar, but primary deformations have already occurred in the pellet. The forces acting during this rearrangement could not be detected properly with the used sensor. Therefore, to obtain significant and statistically representative results, the observed curves were placed into different classes. Only those which represented a regular breakage event of a solid bridge between primary particles were taken into account, and, if necessary, tests were repeated to maintain a sufficient number of force-displacement curves for the probability calculation (100 curves for each pellet batch).

As already discussed in section 2.3, experimental results for spherical particles can be evaluated using models based on the Hertz theory, and properties of the pellets such as elastic modulus, elastic and elastic-plastic stiffness, the coefficient of restitution and many others can be calculated. The pellets investigated in this work exhibit irregular shape, which means that the contact cannot be assumed to be a single point. They are also neither homogeneous nor spherical. Because of this, it is not appropriate to used Hertz-based models for the calculation of the produced pellet breakage characteristics. Instead, their breakage behaviour was characterised based on their specific breakage energy.

The breakage energy E_B, necessary to break a single pellet, can be found as the area under the force-displacement curve until breakage

$$E_B = \int_{s_0}^{s_b} F(s)ds, \tag{3.20}$$

where s_b is displacement at breakage and s_0 the starting position of the piston. The probability of breakage of the model pellets was evaluated using Weibull's statistical analysis [120]. It was given as a function of the mass-related (specific) breakage energy and the required breakage force. The specific breakage energy can be found by dividing the breakage energy by the mass of the model pellet m_{mp}

$$E_m = \frac{E_B}{m_{mp}} = (m_{mp})^{-1} \int_{s_0}^{s_b} F(s)ds. \qquad (3.21)$$

The Weibull distribution is commonly used for describing breakage strength functions due to its flexibility [120, 121].

In order to increase the accuracy of the fit the single values from every test were separated in classes. The number of classes was evaluated based on the variance of the experimental results. As variance σ_V is defined, the average of the squared differences from the mean value of the experimental data μ_V

$$\sigma_V^2 = \frac{\sum_{i=0}^{N} (n_i - \mu_V)^2}{N}. \qquad (3.22)$$

The upper limit of the last class and the lower limit of the first class were respectively the hights and the lowest value of the experimental raw. The upper limit of the lower class is evaluated by adding the variance to the lowest value of the row. All experimental results between the lower and the upper limit or equal to the limits are included in this class. The next class is formed by adding the variance to the upper limit of every formed class until the highst experimental value is reached.

The cumulative probability functions for breakage energy and breakage force can be given as

$$P(E_B, a, b) = 1 - e^{-\left(\frac{E_B}{a}\right)^b}, \qquad (3.23)$$

$$P(F_B, a, b) = 1 - e^{-\left(\frac{F_B}{a}\right)^b}, \qquad (3.24)$$

where a is a scale parameter and b is a shape parameter. The shape parameter is also called slope because its value is equal to the slope of the regressed line in a logarithmic probability plot [122]. The probability distributions $P(E_B)$ for the mass-related breakage energy and $P(F_B)$ for the breakage force were calculated by considering all breakage events occurring before reaching a certain given value E_B or F_B. The corresponding density functions $f(E_B, a, b)$ for the breakage energy or $f(F_B, a, b)$ for the breakage force can be given as

$$f(E_B, a, b) = \frac{b}{a^b} E_B^{b-1} e^{-\left(\frac{E_B}{a}\right)^b}, \qquad (3.25)$$

$$f(F_B, a, b) = \frac{b}{a^b} F_B^{b-1} e^{-\left(\frac{F_B}{a}\right)^b}. \qquad (3.26)$$

If the shape parameter is held constant, the increase of the scale parameter has a stretching out effect on the density function [56]. The optimal scale and shape parameters for the Weibull distributions in this work were estimated using Matlab tool and were assumed for both probability functions. The standart deviation σ_{st} of the cumulative function can be represented as a factorial function (gamma function) Γ of the density function's mean value $\overline{T}$ [122]

$$\sigma_{st} = a. \sqrt{\Gamma\left(\frac{2}{b}+1\right) - \Gamma\left(\frac{1}{b}+1\right)^2} \qquad (3.27)$$

$$\overline{T} = a\Gamma\left(\frac{1}{b}+1\right). \qquad (3.28)$$

The propagation of the force-displacement curves was analysed in detail and correlated with the occurring changes in the structure of the stressed pellet.

4.   DEM Simulations

Using the 3D data from the CT scan of the model pellets, DEM simulations of the compression testing were accomplished. The chosen simulation tool was the MUSEN software, created by Maksym Dosta at the Hamburg University of Technology [123].

4.1.   Reconstruction of Model Pellet and Experimental Set Up

The first step for performing a DEM simulation was to rebuild the model pellet into the software. The 3D coordinates of the primary particles, which were already taken down using the μ-computed-tomography, were inserted into the simulation domain. The positions of the particle centres can be put directly using the MUSEN object editor. The programme recognises three different types of objects – spherical particles, solid bonds and liquid bonds. The primary particles are inserted as spherical particles with given diameter and defined material properties. During the simulation, the programme tracks the change in particle position and velocity with increasing simulation time. The motion state of every single primary particle in a model pellet can be checked in the object editor at any time during the simulation procedure. Both compressing pistons can be easily inserted into the simulation domain from the software-provided list of primary geometries. The programme offers a library consisting of the main basic geometries for performing simulations such as cylindrical walls, different types of plates and hoppers, which can also be expanded if needed.

Two cylindrical plates were chosen for the reconstruction of the experimental set up. Their positions were adjusted according to the position of the pellet to be compressed. A typical simulation domain is shown in figure 29.
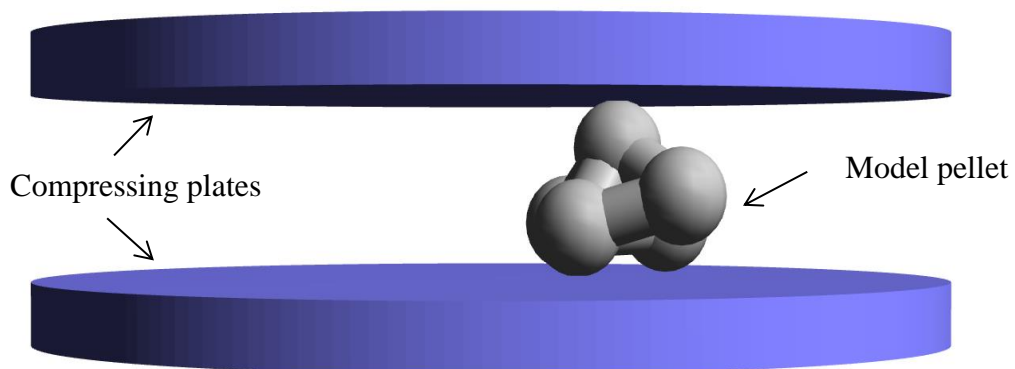
Figure 29:   Simulation domain in MUSEN.

After the pistons had been inserted, their properties were adjusted using the geometry editor. With this programme tool, one can specify the material, the size and the position of the

boundaries. In the geometry editor, the desired loading velocity was also inserted. The used models for describtion of the contact behaviour in DEM were Hertz contact model for the primary particles and Bonded Particles Model for the solid bridges between them. An overview of the equations for the acting forces and moments is given in table A1 (Attachment A)

4.2. Defining Materials

For correctly carrying out a simulation, the properties of the materials have to be described in detail and added into the programme material database. Simulations were performed for model pellets produced from alumina and zeolite primary particles and HPMC as a binder. The material of the compression pistons for stressing the model pellets was high-carbon steel. The required properties for DEM simulation of pellet compression behaviour were the normal and tangential strength of the materials, thier densities, viscosities (only for liquid bodns) and Poisson's ratio. The material properties of the primary particles and of the used binder are specified in section 5.1. (table 1, table 2, table 3 and table 4) and resp. section 5.2 (table 5). The density of the carbon steel pistons was resumed at 7850 kg/m^3 and the Young modulus at 211 GPa. Their normal and tangetial strengths were fixed at 3100 MPa and resp. 810 MPa [124]. An overview of all material data base parameter is given in Attachment A, table A2.

4.3. Solid Bridges Generation

An important part of the model construction is the generation of solid bridges between the primary particles. The DEM software MUSEN provides a bond generator. Using this module of the programme heterogeneous structures of solid or liquid bond can be created. The parameters for each bond class should be specified. The material of the bond is defined by the material data base as described in section 4.2. The second parameter to be added is the diameter of the bond D_b. D_b cannot be larger than smaller diameter of contact partners. Other important parameters are the minimum and maximum allowed length of the bond. They serve as criteria for bond generation between two contact partners as well. Depending on particle radii and their distance the length of possible bond is calculated for each contact partner. A bond will be created if its length is equal to the minimum or maximum given bond length or if its length is in the range between the minimum and maximum allowed bond length. The bond generator gives also the possiblity of overlaying of the bonds. In this way many types of bonds can be inserted at the same time in one simulation object. If overlay is not allowed, then bond will be generated only if there is no bond between these particles. To represent the model pellets as accurately as possible, different series of the experimentaly investigated pellets were rebuilt by varying their maximum allowd bond length and bond thickness. The received results were

compared, and similarities and differences between simulations and compression tests were estimated and discussed. After the bonds between primary particles have been generated, the number of bonds in the model pellet is shown in the bond generator page of the programme.

4.4. Calibration of Pellet and Wall Positions

As mentioned, for successfully carrying out the DEM simulations, the positions of the model pellets must remain the same as in the real experiment. In this way, the force propagation through the simulated pellet will be the same and should provide a valid comparison between the results. If the pellet does not lie stably (figure 30) on the plate, the results will differ and will no longer be comparable. To prevent this and to obtain a stable position of the pellet on the low compression piston, after inserting the coordinates the pellet and the walls can be additionally adjusted using the scene editor of the MUSEN programme.
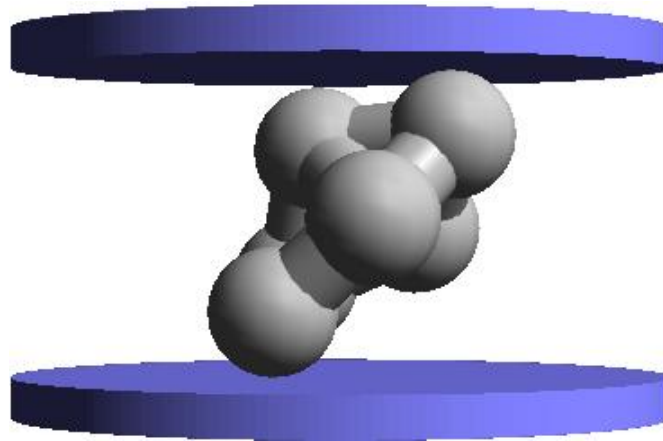
Figure 30:   Unstable agglomerate.

4.5. Time and Saving Steps

The selected time step for the calculation plays a major role in the stability and accuracy of the numerical simulation. Evaluating and adjusting the accuracy in each simulation cycle would be too complicated. For stable solution, the computing time step must not exceed a maximum or critical time step length. The criterion for determining the critical time step is that in the course of time, an elastic wave may pass at most through the smallest particle of the system, so that physical information from a particle cannot be transmitted beyond the particles in contact with it in a time interval. The wave propagation time can be calculated depending on the particle size and material properties. Normally, small particles require smaller critical time steps. The simulation of processes with finely dispersed particle collectives is, therefore, more time-

consuming. The determination of the time step is based on the differential equation for linear vibrations of a massless spring with point attached to it [125].

The modelled particles are considered as a system of mass points connected by elastic springs, each of which has its own mass and spring stiffness. The critical time step can then be calculated for the smallest particle according to [125]:

$$\Delta t_{cr,i} = \begin{cases} \sqrt{\dfrac{m_i}{k_{tran}}} \\ \sqrt{\dfrac{I_i}{k_{rot}}} \end{cases}. \tag{4.2}$$

The second term determines the critical time step for the rotational movement, wherein instead of the mass m, the mass moment of inertia I is a measure of the inertia of the system.

The simulator tool of the MUSEN software calculated the simulation and saving step based on Rayleigh time. Only active existing particles in the simulation domain are considered. If new particles will be generated during simulation or solid bonds existing on the scene, then ther simulation time step should be corrected. Rayleigh time is calculated depending on particle radius R_i, Poisson ratio v, Young's modulus E_i and density ρ_i:

$$\Delta t_{sim,recom} = T_{Rayleigh} = \min \left\{ \frac{\pi . R_i \sqrt{2\rho_i + v_i}}{\sqrt{E_i}(0.163 + 0.8766)} \right\}. \tag{4.3}$$

If scene consisting of primary particles, as well as solid bonds the recommended simulation time step calculated as 10% (factor 0.1) of:

$$\Delta t_{sim,recom} = 0.1 * \min \left\{ T_{Rayleigh}, T_{sim,bond} \right\}. \tag{4.4}$$

where $T_{sim,bond}$ is estimated according following equation [127, 128],

$$T_{sim,bond} = \min \left\{ 2\sqrt{\frac{m_{min}}{K_{b,i,max}}} \right\}, \tag{4.5}$$

where m_{min} is the minimal mass of particles connected with this bond and $K_{b,I,max}$ is the largest bond stiffness calculated for elastic solid beam theory, depending on Young's modulus E_b, Poisson ratio v, initial length L_{init}, cross-cut surface A_b as:

$$K_{b,i,max} = \max \left\{ \frac{E_b . A_b}{L_{init}} , \frac{E_b . A_b}{2 . L_{init} . (1+\upsilon)} \right\}.$$
(4.6)

4.6.   Analysing of the Received Data

After the simulation was complited, a force-displacement curve can be received from the force acting on the cylindrical plate. The data can be exported using the geometry analyser included in the programme. As already discussed in section 3.9, the simulated pellets exhibit a large inhomogeneity, especially in the distribution of their solid bridges and they have irregular shape, which means that the contact cannot be assumed to be a right body. They are also neither homogeneous nor spherical. Because of this, it is not appropriate to used Hertz-based models for the calculation of the produced pellet breakage characteristics. Instead, their breakage behaviour was characterised based on statistical data for their breakage force and specific breakage energy. Using eq. (3.20) and resp. eq. (3.21), the breakage force F_B and the specific breakage energy E_m were found for every simulated pellet. To increase the reproducibility of the results, the simulations were accomplished for 20 to 30 model pellets from every charge and average results were received. The received date was compared with the experimental results.

5.   Used Materials

The model pellets investigated in this thesis were produced using primary particles of two different materials with two different sizes and an organic binder. The feed materials were investigated in previous studies in detail. Their properties were used here in the DEM simulation and for comparison with the properties of the model pellets.

5.1.   Primary Particles

5.1.1.   γ-Aluminum oxide (Alumina)

The first type of primary particles used for the production of the model pellets were alumina granules (produced by Sasol Performance Chemicals, Germany). Aluminum oxide of γ-type is a white powder, water insolvable, but solvable in strong acids and bases [118]. It is highly hygroscopic. Alumina consists of cubic, face-centered packing of oxygen ions in which the aluminum ions are distributed in diverse ways around the octahedron and tetrahedron gaps [4, 118]. The used particles had two different sizes: 1.0 mm and 1.8 mm. These granules were choosen for the experiments because of their well-studied material behaviour. Their properties have already been investigated in detail in many research works [1, 2, 4, 58, 59, 128-133], so that they could be used for comparison base with the properties of the model pellets and in the DEM simulations. The main characteristics of the granules are given in table 1.

Table 1: Properties of alumina primary particles [128].

Property	Mass-median-diameter $d_{50,3}$ in mm	
	1.0	1.8
Sphericity ψ	0.99	0.99
Solid density ρ_{sp} in kg/m^3	3420	3372
Particle density ρ_{pp} in kg/m^3	1172	879
Porosity ε_p in %	65.7	73.9

In the DEM simulation, particle-partice and particle-wall contacts behavior were represented using Hertz contact model. Therefore, the properties needed for simulation are density, normal and tangential strength and Young's modulus. These mechnical characteristics of the primary granules were investigated by Müller et al. [128] and have been directly used for the simulation. Müller et al. [128] used Hertz and Tomas contant models in order to chractirise the properties of the spherical granules. Table 2 shows the mechanical characteristics of the primary particles investigated by Müller [128].

Table 2: Mechanical properties of alumina primary particles [128].

Mean diameter $d_{50,3}$ in mm	Modulus of elasticity E in MPa	Breakage force F_B in N	Normal and tangetial strength σ_B in MPa
1.0	2884 ± 895	37.68 ± 3.65	47.67 ± 4.89
1.8	1223 ± 563	42.49 ± 8.03	17.84 ± 3.56

5.1.2. Zeolite

Zeolites are hydrated aluminosilicate minerals made from interlinked tetrahedra of alumina (AlO_4) and silica (SiO_4). Their name comes from the Greek and means boiling stone [134]. Zeolites have different crystalline structures, which have small open pores with very regular arrangement and roughly the same size. Zeolites are very stable to environmental conditions and highly temperature-resistant (melting point over 1000 °C) [135]. They are used as absorbers for e.g. drying of organic liquids and noble gases [134]. The used zeolites were produced by the German company CWK, Chemiewerk Bad Köstritz GmbH, and have the commercial name Köstrolith 4AK. 4A stays for the size of the pores inside of the particles, which are used as adsorbents. The properties of the zeolite 4A primary particles have been investigated by Müller et al. [35]. In their study, they performed compression tests on zeolite granules and they found their mechanical properties using the Hertz and Tomas models. Analogously to alumina, the properties of zeolite granues needed for performing DEM simulation based on the Hertz contact model are density, normal and tangential strength and Young's modulus. Table 3 gives the properties of the zeolite 4A granules with a diameter of 1.75 mm. As mention in section 5.1.1, particle-partice and particle-wall contact behavior was represented in DEM using Hertz contact model. The mechanical characteristics needed for simulation are density, normal and tangential strength and Young's modulus (table 4).

Table 3: Properties of zeolite primary particles [35].

Propertiy	Mass-median-diameter $d_{50,3}$ in mm
	1.75
Sphericity ψ	0.98
Solid density ρ_{sp} in kg/m^3	2290.7
Bulk density ρ_{pp} in kg/m^3	1127.9
Porosity ε_p in %	50.76

Table 4: Mechanical properties of zeolite primary particles [35].

Mean diameter $d_{50,3}$ in mm	Modulus of elasticity E in MPa	Breakage force F_B in N	Normal and tangetial strength σ_B in MPa
1.75	5391.7 ± 1566.4	23.8 ± 7.7	11.72 ± 3.98

5.2. Binder

The pelletising of the primary particles was accomplished using aqueous HPMC solutions with different concentrations as a binder. The binder solution was prepared by directly dissolving the required amount of HPMC (produced by Thermo Fisher Scientific, Germany) in water. Its role in the process is to form "liquid to solid bridges" between the particles, and to join them thus. The liquid binder also decreases the stirring resistance (friction) between the particles and the walls of the pelletiser, which reduces the probability of primary particle breakage. Hydroxypropyl methylcellulose (HPMC) was used in this investigation, due to its non-toxic nature and large adhesive binding force (chemical formula shown in figure 40). Hypromellose, short for hydroxypropyl methylcellulose, is a semi-synthetic and hydrophilic polymer. HPMC is widely used for hydrophilic gel formation, crystal growth control, as thickener and emulsifier or additive in the food industry [136-141]. According to Habenicht [23], the water solution of HPMC can be classified as a disperse binder. This type of binder is especially used for bonding of porous particles and surfaces. The binder solution penetrates in the structure of the porous material. After the pelletisation process had been accomplished the pellets were allowed to dry under atmospheric conditions. Hence, the water molecules evaporated, and in the pores remained only polymer, which built a binder layer over the particles as well. The used contact model for the solid bridges of HPMC in the DEM simulation was Bonded-particle model [71] and the mechanical characteristics of HPMC binder, investigated from Spettl et al. [142] were direcly implemented into the simulation software (table 5).

Table 5. Mechanical properties of HPMC solid bridges [142, 143].

Young's modulus E_{SB} in MPa [142]	Normal and tangential strength in MPa [142]	Density ρ_B in kg/cm^3 [143]
400	50	700

$$R = -H, -CH_3, -CH_2-CHOH-CH_3$$
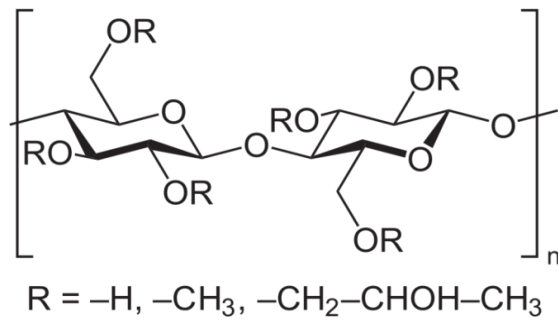
Figure 40:   Chemical structure of HPMC monomer molecule [142].

6.   Results and Discussion

6.1.   Overview of the Pelletising Charges

The model pellets, the properties of which were investigated in the frame of this thesis, were produced using a horizontally adjusted pan pelletiser. The rotational velocity was calibrated using high speed camera which captured the revolutions per minute of the bottom plate (rpm). The linear velocity in m/s was calculated from the received rpm and the radius of the bottom plate. The weight of primary particles was 150 g for all batches. The binder used for the pelletising was Hypromellose (HPMC) as a water solution. The added amount of binder solution with concentrations of 2 %, 4 %, 6 %, 12 % and 25% was 60 g. The binder content φ_B in the pellets was calculated as grams binder (solid phase) per grams primary particles. The binder solution was manually added using a spray flakon to the primary particle bed. The addition was performed step-by-step on 10 g portions during the process into the formed torus-like particle bed. The first portion of binder (around ¼ of the whole amount) was given to the particle bed before the start of the pelletisation in order to prevent dry stirring between the primary particles and the walls of the pelletiser. The rest of the binder was given in equal portions every 1/3 of the processing time. Different process parameters were varied in order to investigate their influence on the final product characteristics. Two types of granules were used as primary particles, alumina and zeolite, the properties of which were well-defined and thoroughly investigated in previous research.

After the pelletisation process had been accomplished, the pellets were placed as thin layer (in order to prevent overlaying of the pellets) on a canvas (2 x 2m) and stored for 24 hours under atmospheric conditions in order to achieve complete hardening of the binder. The results of the pelletising experiments, the characterisation of pellet properties and the simulations of pellet breakage behaviour are summarised and discussed in this chapter.

The experimental investigation started with the formulation of the model pellets. Anyway, not all the pelletising experiments were successful and the reasons for that should be discussed. The first series of experiments were carried out using alumina oxide as primary particles and HPMC as binder solution. The process parameters of the batches were varied to investigate their influence on the produced pellets. Firstly, the concentration of the binder solutions was varied while the processing time and rotational velocity were constant. During the first experiments it was noticed that the model pellet batches consists of tetrahedron shaped and irregular shaped pellets. In the first series with binder content of 0.009 g/g, 0.018 g/g and 0.027 g/g the

tetrahedron shaped pellets were prevailing. On the other hand, the received irregular shaped pellets from the batches with binder content of 0.009 g/g and 0.018 g/g were unstable and therefore they were not further investigated. Tetrahedron shaped and irregular shaped pellets were separated right after the drying process was completed. Due to their simple geometry and stable construction [143], the tetrahedron shaped pellets were seen as pellets of "regular" structure and were analysed firstly. From the received alumina pellets those having tetrahedron shape were separated manually. The received results from the investigation of regularly shaped pellets were then used for the analysis and comparison with the rest of the pellets. Overview of the first experimental batches gives table 6.

In the next experiments, the binder content in the pellets was increased in order to receive stable irregular pellets (table 7). Successful formation of stable irregular pellets was acchieved with binder content of 0.027 g/g, 0.053 g/g and 0.109 g/g. Further binder content increasement was not possible due to the high viscosity of the binder which leads to problematic dosage. Subsequently, the rotational velocity of the pelletiser's bottom disk was varied in order to investigate its influence on the pellet properties, while the other process parameters were held constant. The received alumina pellets were with various shapes and due to their complex geometry, these pellets and their properties cannot be specified in a simple way. They were investigated and analysed using statistical methods. An overview of the successful experimental batches for irregularly shaped model pellets is given in table 7.

One important observation was made during the pelletising, the received pellets with primary particle size of 1.8 mm were rather unstable. Only a small fraction of pellets with tetrahedron shape were stable enough for performing a forward characterisation. Due to this reason, the rest of the experiments were focused on the characterisation of the pellets with primary particles with $d_{50,3} = 1.0$ mm. The small primary particles have less mass, and the structure is casier held together by means of the formed solid bridges (the polymer molecules of the binder are strong enough to carry the weight of the primary particles). Possible explanations for the instability of the pellets made of larger primary particles are the larger weight of such primary particles and their large surface curvature.

The second series of experiments were performed using zeolite granules as primary particles. The successful experiments are listed in table 8. No regularly shaped pellets were found in the zeolite batches. Experiments with zeolite primary particles with diameter of 2.05 mm were not successful due to the large size and mass of the granules.

Table 6: Overview of processing parameters for production of regular (tetrahedron shaped) model pellets from HPMC binder and alumina primary particles.

Type of primary particles	Size $d_{50,3}$ in mm	Binder content φ_B	Rotational velocity v_r in m/s	Processing time τ_p in min.
Alumina	1.0	0.009	0.37	15
Alumina	1.0	0.018	0.37	15
Alumina	1.0	0.027	0.37	15
Alumina	1.8	0.009	0.37	15
Alumina	1.8	0.018	0.37	15
Alumina	1.8	0.027	0.37	15

Table 7: Overview of processing parameters for production of irregular model pellets from HPMC binder and alumina primary particles.

Type of primary particles	Size $d_{50,3}$ in mm	Binder content φ_B	Rotational velocity v_r in m/s	Processing time τ_p in min.
Alumina	1.0	0.009	0.37	15
Alumina	1.0	0.018	0.37	15
Alumina	1.0	0.027	0.37	15
Alumina	1.8	0.009	0.37	15
Alumina	1.8	0.018	0.37	15
Alumina	1.8	0.027	0.37	15
Alumina	1.0	0.027	0.17	10
Alumina	1.0	0.027	0.17	15
Alumina	1.0	0.027	0.17	20
Alumina	1.0	0.027	0.17	30
Alumina	1.0	0.027	0.17	60
Alumina	1.0	0.053	0.37	20
Alumina	1.0	0.053	0.37	20
Alumina	1.0	0.109	0.74	20
Alumina	1.0	0.053	0.17	15
Alumina	1.0	0.053	0.74	15
Alumina	1.0	0.109	0.17	15

Alumina	1.0	0.109	0.74	15
Alumina	1.0	0.053	0.17	30
Alumina	1.0	0.053	0.74	30
Alumina	1.0	0.109	0.17	30
Alumina	1.0	0.109	0.74	30

Table 8: Overview of processing parameters for production of model pellets from HPMC binder and zeolite primary particles.

Type of primary particles	Size $d_{50,3}$ in mm	Binder content φ_B in g/g	Rotational velocity v_r in m/s	Processing time τ_p in min.
Zeolite	1.75	0.053	0.17	10
Zeolite	1.75	0.053	0.17	15
Zeolite	1.75	0.053	0.17	20
Zeolite	1.75	0.053	0.37	10
Zeolite	1.75	0.053	0.37	15
Zeolite	1.75	0.053	0.37	20
Zeolite	1.75	0.053	0.74	10
Zeolite	1.75	0.053	0.74	15
Zeolite	1.75	0.053	0.74	20
Zeolite	1.75	0.053	0.74	30
Zeolite	1.75	0.109	0.17	30
Zeolite	1.75	0.109	0.17	15
Zeolite	1.75	0.109	0.74	15
Zeolite	1.75	0.109	0.17	30
Zeolite	1.75	0.109	0.37	20
Zeolite	1.75	0.053	0.17	30

6.2. Image Analysis of the Received Pellets

The structure and morphology of the received pellets were characterised using light microscopy (LM) and scanning electron microscopy (SEM) images.

6.2.1. Regularly Shaped Pellets

The regular tetrahedron shaped pellets consist of four primary particles, three of which serve as a base for the pellet and one is positioned at the top (figure 41).
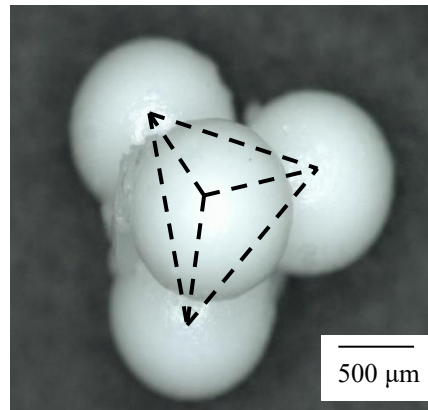
Figure 41:   Light microscopy image of tetrahedron shaped pellet from alumina primary particles with a diameter of 1.0 mm.

The tetrahedra can be assumed as regular due to the comparable distances between the particle centres of all primary particles. These types of structures are well-known for their stability and are widely used in architecture [143]. The tetrahedra from all the batches have similar shapes and morphology. The main difference lies in the larger amount of broken or damaged pellets in the batches with increased rotational velocity (figure 42). This effect can be explained with the increased amount of contact collisions with the rigid walls of the pelletiser, which leads to damages on the primary particles.

a)   b)
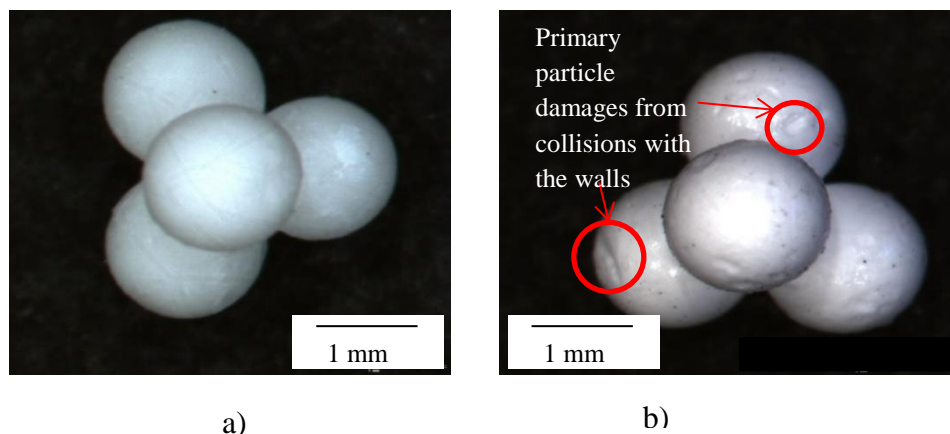
Figure 42:   Light microscopy images of tetrahedron-shaped alumina pellets produced with a binder mass content of 0.109 g/g, at a processing time of 15 min. and a) Rotational velocity of 0.17 m/s b) Rotational velocity of 0.74 m/s.

6.2.2. Irregularly Shaped Pellets

The irregularly shaped pellets were also analysed using LM and SEM images. All investigated pellets have an irregular (blackberry) shape (figure 43). The pellets exhibit a high surface roughness.
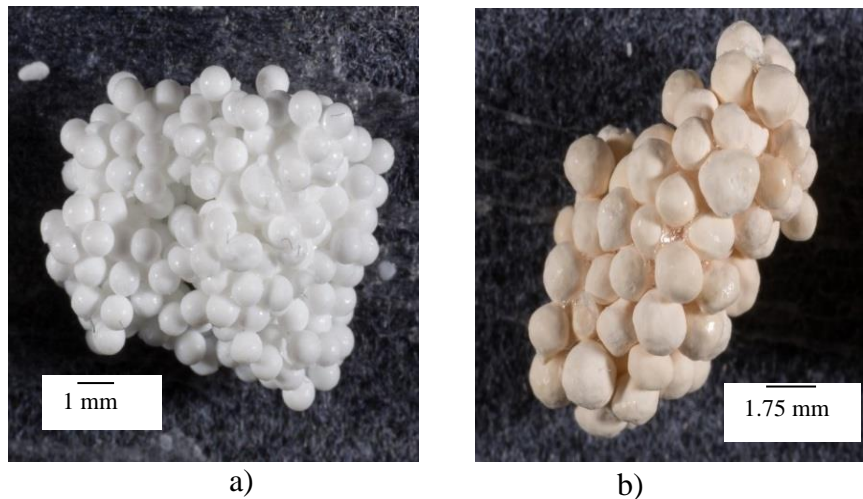
Figure 43: Irregularly shaped pellets produced at processing time of 15 min., a binder content of 0.053 g/g rotational speed 0.17 m/s a) With alumina primary particles with $d_{50,3}$ = 1.0 mm b) Zeolite primary particles with $d_{50,3}$ = 1.75 mm.

In most of the pellets, the primary particles can be easily recognised from the entire structure. Few exceptions were noticed. For a small number of pellets, the primary particles were covered by a layer of binder (figure 44).

Figure 44: Irregularly shaped pellets produced at processing time of 15 min., a binder content of 0.053 g/g , a) Rotational speed 0.17 m/s and alumina primary particles with $d_{50,3}$ = 1.0 mm, b) Rotational speed 0.74 m/s and zeolite primary particles with $d_{50,3}$ = 1.75 mm.

This effect was observed for both alumina and zeolite pellets. Such structures were present in all the pelletising batches. A possible explanation is the irregular binder dispersion in the

pelletiser. Hence, the binder did not disperse uniformly among the primary particles and some of the pellets developed into having more binder than others.

Breakage and attrition of the primary particles occurred during pelletising. Due to the collisions with the pelletiser walls, some of the primary particles were broken. Rests of these broken particles can be joined into the structure of a pellet (figure 45), and thus influence its behaviour. This effect was especially noticeable for batches with zeolite primary particles due to their lower breakage resistance (table 4).

1.75 mm

Broken primary particle fragments
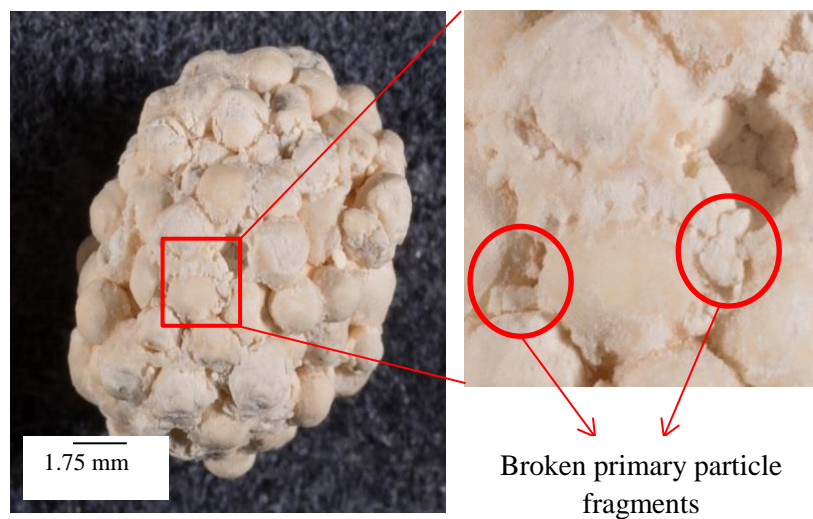
Figure 45:   Irregularly shaped zeolite pellets produced at a processing time of 15 min., a binder content of 0.053 g/g and a rotational speed of 0.74 m/s.

6.2.3.   Solid Bridges Characterisation

The solid bridges shape and distribution were another important aspect to investigate. By increasing the resolution, one can see the contact points between the primary particles and verify if the used binder was able to build solid bridges between them. Figure 46 shows alumina primary particles connected with solid bridges of solidified binder. The binder content in the model pellets was 0.027 g/g. The solid bridges are located at the contact points between the primary particles and join them together as desired. In figure 47, one can see solid bridges between particles in a pellet produced with a binder content of 0.053 g/g. The particles are layered with binder, which solidified on their surface and encapsulated the particles into the structure of the pellet. The binder seems to be spread over the whole particle surface.

A further investigation of the solid bridges between the particles showed that certain part of them seems to be disrupted and hollow in the inside (figure 48). In the bridges structure, micro-voids (micro porosity) are formed, which may be responsible for the pellet instability.

The macroscopic and microscopic porosity of solid bridges in agglomerates produced in fluidised beds has already been investigated by Dadkhah et al. [116, 144]. They proved that for pellets produced in fluidised beds, the applied gas temperature and drying rate have decisive roles for the solid bridges properties.

On the other hand, part of the bridges in the batches produced at high rotational velocity and long processing time were broken. This can be seen in figure 49, where the most common kinds of broken bridges are shown. In figure 49a a solid bridge that was broken from the side is shown.

a)   b)
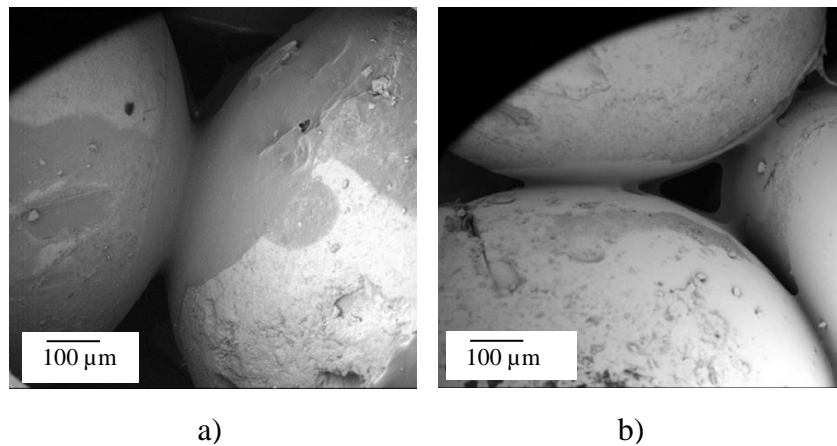
Figure 46:   SEM images of solid bridges between alumina primary particles a) Solid bridge between two primary particles, b) Solid bridges between three primary particles.
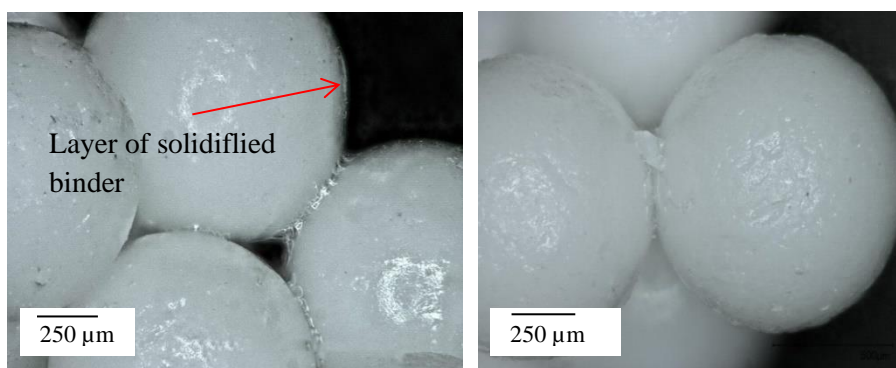
Figure 47:   SEM images of HPMC solid bridges between alumina primary particles (binder content $\varphi_B = 0.053\,g/g$).
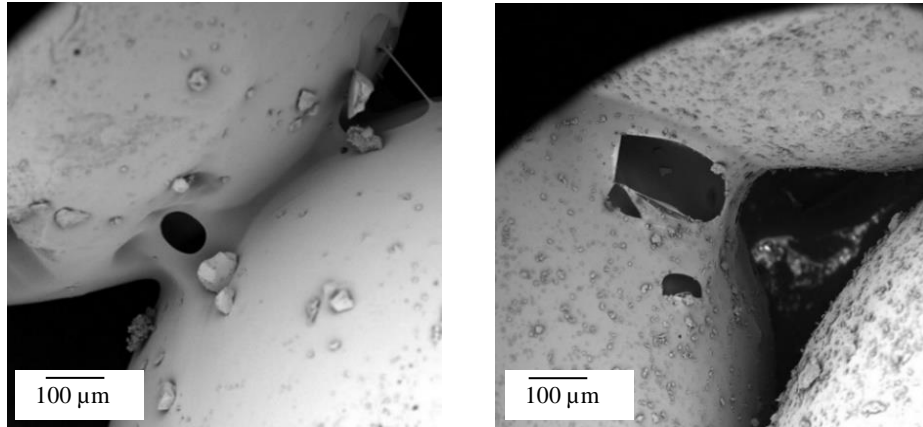
Figure 48:   SEM images of solid bridges in pellets produced with a 0.053g/g binder
content consisting of visible hollowness and micro-voids.
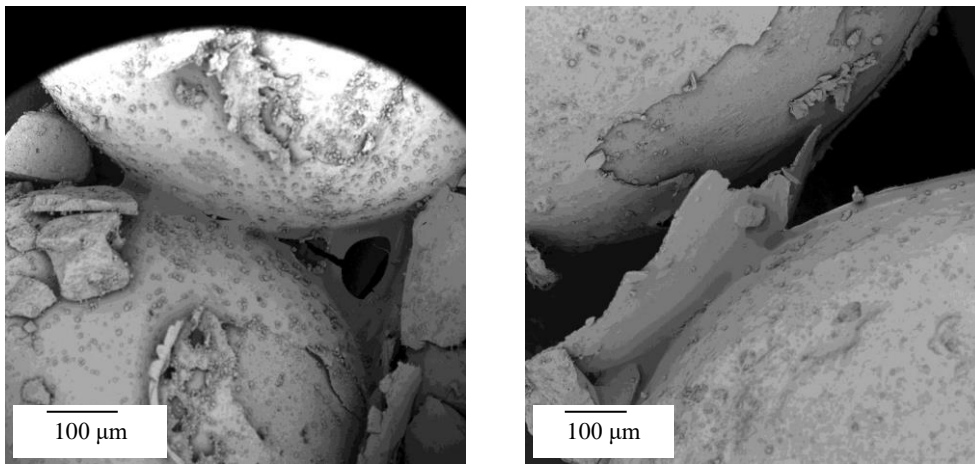
a)

b)
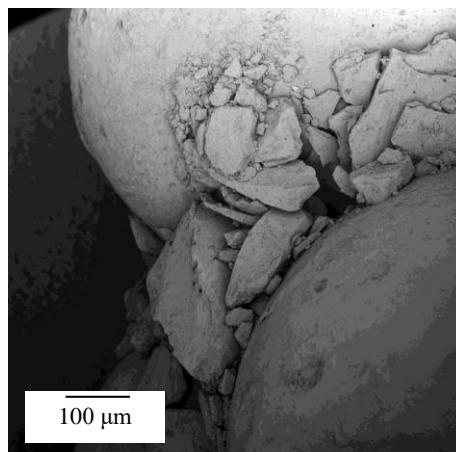
c)

Figure 49:   a) Broken from the side solid bridge between primary particles in a pellet with
binder mass content of 0.053 g/g, b) Torn surface layer between primary particles
in a pellet produced with rotational speed 0.74 m/s, c) Broken primary particle
fragments included in the structure of a solid bridge between primary particles in
a pellet.

This type of breakage was observed mostly in the batches with binder content between 0.027 g/g and 0.053 g/g. The possible reason may be not enough binder solution to fill the gaps between the primary particles.

In figure 49b, one can see a broken bridge the surface layer of which was torn from one of the primary particles. Such solid bridge breakages were common for charges with increased velocity and may result from contact collisions with the pelletiser walls. The next picture, figure 49c, shows a solid bridge that includes in its structure many broken primary particle fragments. In this way, the structure becomes instable due to the inhomogeneity of the bridge.

6.3. Size Distribution

The next step of the pellet analysis was the characterisation of their size distribution. The purpose of this investigation step was to verify any changes in the pellet size as a result of the changing pelletising parameters.

6.3.1. Regular Structures

The regular pellets (tetrahedra) with the same primary particles, from all the pelletising charges, exhibit similar size distributions. The results from the size investigations are summarised in table 9. The change of the binder content, the processing time and the rotational velocity has no influence on the structures due to their similar formation. The average size $d_{50,3}$ of the tetrahedron pellets with a primary particle size of 1.0 mm varies from 2.1 mm to 2.3 mm depending on the measuring method. For the pellets with a primary particle size of 1.80 mm, the measured diameter $d_{50,3}$ is from 3.3 mm to 3.7 mm. The sphericity values for all the charges are similar as well. In figure 50 is shown an example of the size distribution Q_3 (d_{eq}) function of tetrahedron-shaped pellets produced with a binder content of 0.027 g/g, a rotational velocity of 0.17 m/s and a processing time of 15 min. As expected, they exhibit a narrow size distribution.
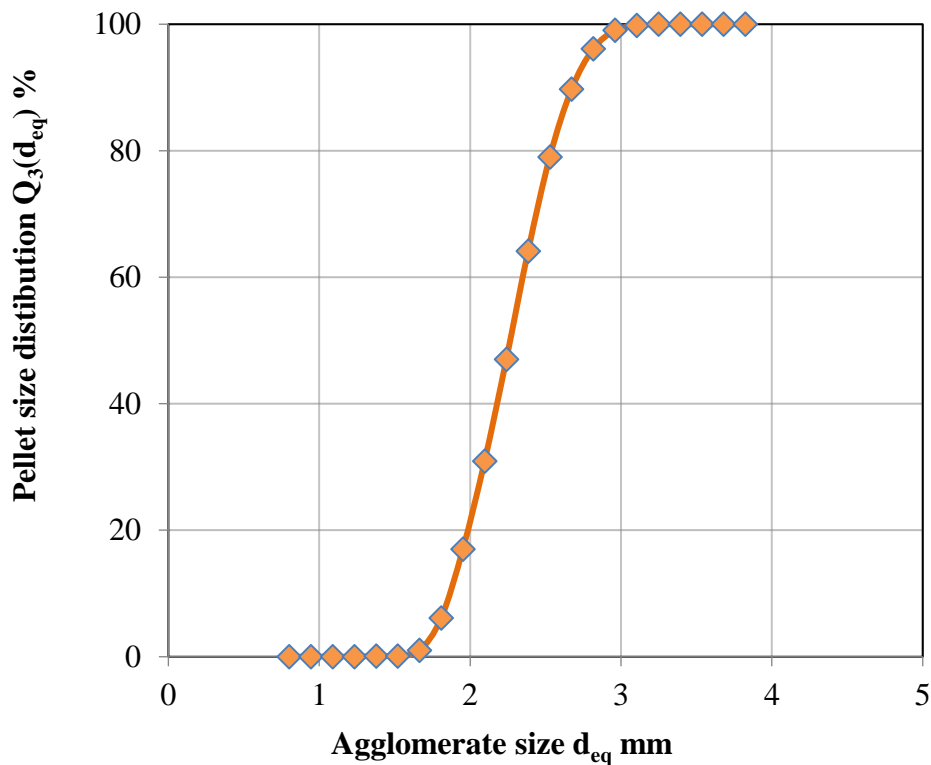
Figure 50: Size distribution Q_3 of tetrahedron shaped pellets produced with binder content of 0.027 g/g, rotational velocity of 0.17 m/s and processing time of 15 min.

It is important to mention that despite of the similar size and shape of all the tetrahedra, they exhibit different coordination angles. This may lead to a slight variation of the size and the sphericity. The values for average size in table 9 are shown with their standart deviation (labeled with "±"). The standard deviations are calculated as

$$\sigma_{st} = \sqrt{\frac{\sum_{i=1}^{N} (y_i - \bar{y})^2}{N-1}}, \qquad (6.1)$$

where y_i is a single value, $\bar{y}$ is mean value and N is the number of values. The same equation is applied for the calculation of all the standard deviations of measured or computed parameters in this thesis.

Table 9: Average size and sphericity of tetrahedron-shaped alumina pellets.

Primary particle size $d_{50,3}$ in mm	Binder content φ_B	Rotational velocity v_r in m/s	Processing time τ_p in min.	Sphericity ψ	Average pellet size $d_{50,3}$ in mm	
					$d_{c,max}$	d_{eq}
1.0	0.009	0.37	15	0.870	2.1 ± 0.9	2.3 ± 0.5
1.0	0.018	0.37	15	0.873	2.2 ± 0.3	2.3 ± 0.7
1.0	0.053	0.37	15	0.828	2.1 ± 0.4	2.3 ± 0.9
1.8	0.009	0.37	15	0.892	3.3 ± 0.7	3.7 ± 0.1
1.8	0.018	0.37	15	0.855	3.3 ± 0.2	3.5 ± 0.8
1.8	0.053	0.37	15	0.876	3.4 ± 0.2	3.7 ± 0.4

6.3.2.   Irregular Structures

6.3.2.1. Alumina

The size distribution of the irregular pellets was tested for the entire pelletising batch (before the removel of the tetrahedra). Table 10 shows the results for size and sphericity for pellets with a binder content of 0.027 g/g and a processing time of 20 min as a function of the rotational velocity. As it gets clear also from the size distribution functions of the pellets produced at different rotational speeds shown in figure 51, increase in velocity leads to the formation of larger pellets. This effect is a result of the intensified contact collisions between the primary particles. The sphericity does not change at higher velocity.

In table 11, the diameters and the sphericity values for pellets are shown as a function of the binder content. As expected, increased binder content leads to formation of larger pellets (figure

52). The added binder stiches more primary particles and joins them. The sphericity also increases due to the deformability of the polymer binder.

Table 10. Diameter ($d_{50,3}$) and sphericity values as functions of the rotational tip velocity for γ-Al_2O_3 pellets, produced with binder content φ_B of 0.027 g/g and at processing time 20 min.

Tip velocity v_r in m/s		0.17	0.37	0.74
Pellet size $d_{50,3}$ in mm	$d_{c, max}$	4.89 ± 2.9	8.0 ± 4.4	10.2 ± 4.7
	d_{eq}	4.87 ± 1.7	8.2 ± 2.8	10.5 ± 3.4
Sphericity ψ		0.75 ± 0.07	0.75 ± 0.30	0.77 ± 0.08
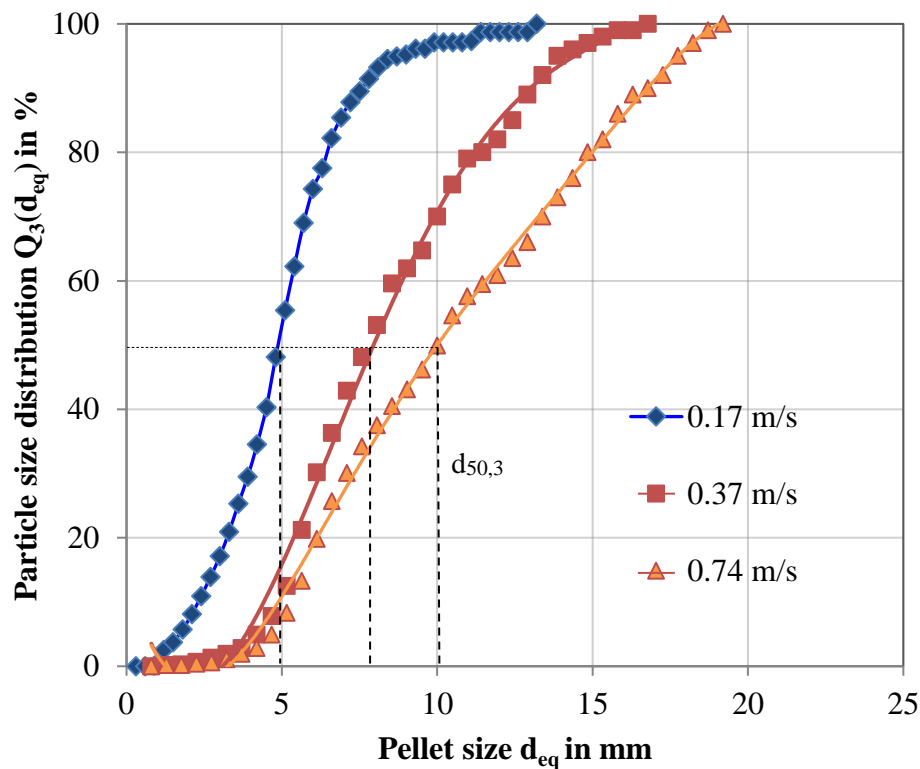
Figure 51: Effect of rotation velocity v_r on the size distribution $Q_3(d_{eq})$ of γ-Al_2O_3 pellets with irregular shape.

Table 11: Diameter ($d_{50,3}$) and sphericity values as functions of the binder content φ_B for γ-Al_2O_3 pellets, produced with a rotational tip velocity 0.17 m/s at processing time of 20 min.

Binder content φ_B in g/g		0.027	0.053	0.109
Pellet size $d_{50,3}$ in mm	$d_{c,\,max}$	5.0 ± 3.5	9.3 ± 6.4	10.0 ± 6.5
	d_{eq}	5.2 ± 1.5	9.2 ± 4.1	9.2 ± 3.7
Sphericity ψ		0.79 ± 0.05	0.81 ± 0.10	0.84 ± 0.08
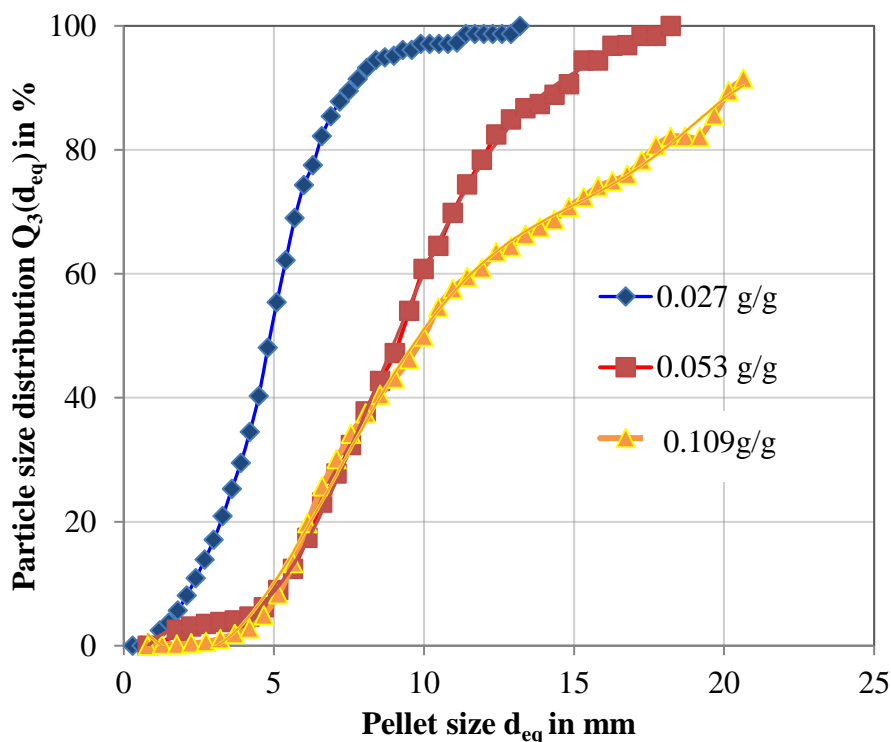
Figure 52:   Effect of binder mass content φ_B on the size distribution $Q_3(d_{eq})$ of irregularly shaped γ-Al_2O_3 pellets.

6.3.2.2. Zeolite

Figure 53 shows the particle size distribution $Q_3(d_{eq})$ as a function of the rotational tip velocity of the pelletiser's bottom disk for zeolite pellets. It is obvious that the increase of rotational velocity from 0.17 m/s to 0.74 m/s does not lead to any significant changes in the pellet size. It should be noticed that the high rotational velocity causes higher losses of zeolite primary particles. At high velocities, primary particles are more likely to get crushed in the process and leave through the gap between the plate and the wall. The sphericity of the obtained pellets does

not change significantly with the increase in rotational velocity. The results are summarised in table 12
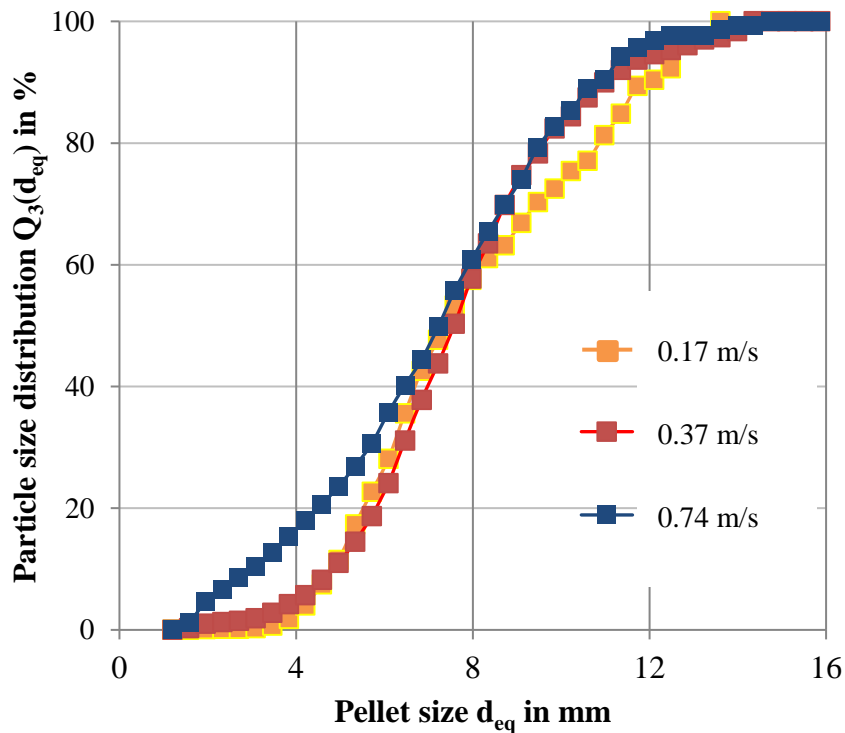
Figure 53:   Effect of rotational velocity v_r on pellet size distribution $Q_3(d_{eq})$.

Table 12: Diameter ($d_{50,3}$) and sphericity values as functions of the rotational tip velocity for zeolite pellets, produced with binder content 0.053 g/g and at processing time 10 min.

Tip velocity v_r in m/s		0.17	0.37	0.74
Pellet size $d_{50,3}$ in mm	$d_{c,max}$	7.87 ± 1.15	7.90 ± 1.02	7.91 ± 0.52
	d_{eq}	7.71 ± 1.07	7.870 ± 1.10	7.95 ± 0.60
Sphericity ψ		0.76 ± 0.12	0.79 ± 0.08	0.74 ± 0.05

Moreover, the size distribution of pellets produced with binder contents of 0.053 g/g and 0.109 g/g is given in figure 54. The mean diameter of the pellets produced with a binder content of 0.053 g/g is larger than that of those produced with a binder content of 0.109 g/g. At the same time, the pellets with larger binder content are more spherical. These differences in the size distribution and sphericity of the pellets with alumina and zeolite can be explained firstly with the larger primary particle diameter of the zeolites, and secondly with their different mechanical

strength. Due to these reasons, the granules behave differently during pelletising. The results are summarised in table 13.

Table 13: Diameter ($d_{50,3}$) and sphericity values as functions of the binder content for alumina pellets, produced with a rotational tip velocity of 0.17 m/s and processing time of 20 min.

Binder content φ_B		0.053	0.109
Pellet size $d_{50,3}$ in mm	$d_{c,max}$	5.6 ± 1.5	4.8 ± 2.4
	d_{eq}	5.8 ± 1.2	4.9 ± 1.7
Sphericity ψ		0.81 ± 0.10	0.84 ± 0.08
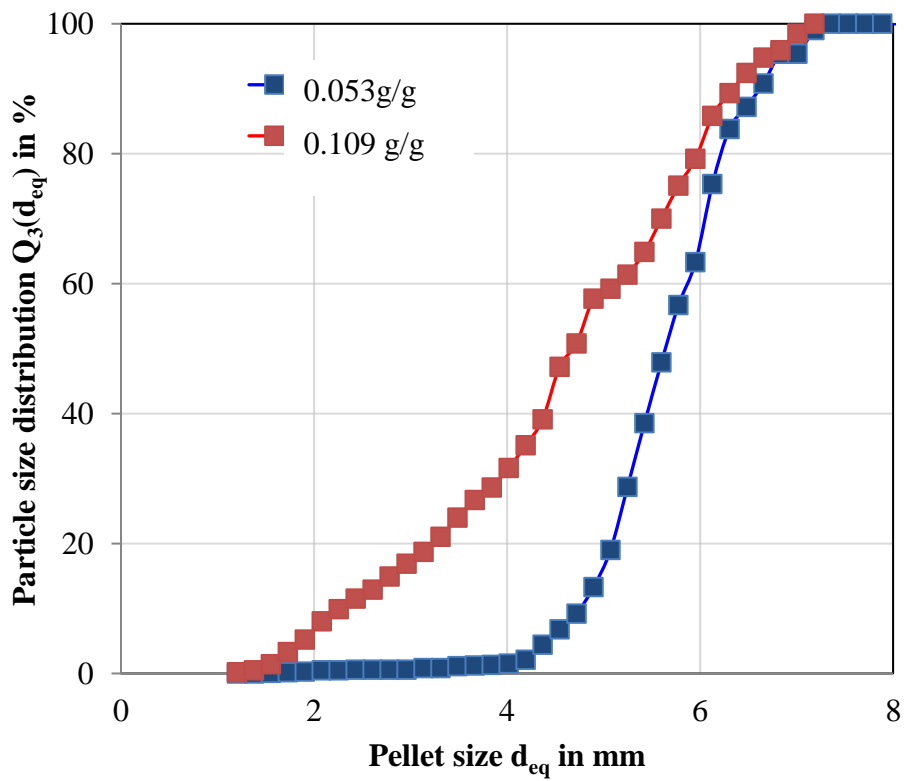
Figure 54: Effect of binder mass content φ_B on the pellet size distribution $Q_3(d_{eq})$ for irregularly shaped alumina pellets.

6.4.   Density and Porosity

6.4.1.   Regular Structures

The density and the porosity of the regularly shaped pellets were investigated for batches produced with different binder content as discribed in section 3.6. The skeletal density was measured using He-pycnometer and the apparent density – using envelope density analyser. The porosity was calculated from the skeletal and apparent densities using eq. (3.11). The results are listed in table 14. The pellets consist of two materials – primary particles (langre density) and binder (low denisity) and therefore the measured skeletal density is lower than skeletal denisity of pure alumina primary particles. The density of the pellets decreased with the increased binder content from 3209.5 kg/m^3 for $\varphi_B = 0.009$ to 3155 kg/m^3 $\varphi_B = 0.027$.

During the apparent density measurement graphite powder fills the voids of the pellets; however, the pores of the primary particles and of the solid brigdes are too small and the powder cannot penetrate into them. The volume increases compare to primary particles due to the solid bridges volume. The mass also increases because the pellet consits of primay particles and solid bridges. If the denisity of the binder was equal to the denisity of the primary particles, then the denisity of the pellet was about to increase as well. Anyway, the binder has much lower denisity compared to the primary particles ($\rho_b \rightarrow 0$) (see table 5) and therefore the apparent density of the pellet ρ_P (consisting of primary particles and binder) decreases.

Accroding to eq. (3.11) the porosity of the pellets depends on the ratio between the skeletal density ρ_s and the apparent denisity ρ_P. As shown in table 14, the skeletal density ρ_s and the apparent denisity ρ_P decrease due to the binder addition, compared to the primary particles denisities (table 1). For the pellets with a primary particle size 1.0 mm, the porosity is between 62.18 and 63.97 % (primary particles' porosity 65.7 % [128]) and for those with primary particle size of 1.8 mm, between 68.95 and 69.82 % (primary particles' porosity 73.9 % [128]). One can conclude that the slight decrease of the porosity is due to the large decreasment of the pellet skeletal density ρ_s as a result of the low-density binder to the primary particles.

Table 14: Skeletal density, apparent density and porosity of regularly shaped pellets produced with different binder content.

Primary particle size $d_{50,3}$ in mm	Binder content φ_B	Rotational velocity v_r in m/s	Processing time τ_P in min	Skeletal density ρ_s in kg/m^3	Apparent density ρ_p in kg/m^3	Porosity ε in %
1.0	0.009	0.37	15	3209.5 ± 8.5	1166.0 ± 6.0	63.67
1.0	0.018	0.37	15	3202.1 ± 9.3	1156.9 ± 1.8	63.95
1.0	0.027	0.37	15	3155.0 ± 10.1	1193.2 ± 1.9	62.18
1.8	0.009	0.37	15	3119.0 ± 9.6	953.1 ± 3.0	69.44
1.8	0.018	0.37	15	3059.3 ± 12.2	949.8 ± 4.9	68.95
1.8	0.027	0.37	15	3046.0 ± 9.3	919.3 ± 0.8	69.82

6.4.2. Irregular Structures

6.4.2.1. Alumina

Using the same analytic procedure for irregularly shaped pellets, the difference in their porosity was analysed for batches produced at different rotational velocity and binder content. The results are summarised in table 15 and table 16 and compared with the porosity of the primary particles. Table 15 shows the porosity values for pellets produced with three different rotational velocities. The increased speed has no significant influence on the porosity of the received pellets. In all cases, the values are slightly lower than the porosity of primary particles as a result of the skeletal and apparent density decreasment due to binder addition. The same effect has the increased amount of binder in the structures (table 16).

Table 15: Porosity of the alumina model pellets as a function of the rotational tip velocity in comparison with the porosity of the primary particles.

Porosity of the primary particles in % [128]	65.7		
Rotational tip velocity v_r in m/s	0.17	0.37	0.74
Porosity ε in %	59 ± 2.4	63 ± 3.1	59 ± 1.5

Table 16: Porosity of the alumina model pellets as a function of the binder content in comparison with the porosity of the primary particles.

Porosity of the primary particles in % [128]	65.7		
Binder content φ_B in g/g	0.027	0.053	0.109
Porosity ε in %	59 ± 3.3	63 ± 3.0	61 ± 2.8

6.4.2.2. Zeolite

The results of the porosity investigation of the zeolite model pellets are given in tables 17 and 18. The results of all the investigated cases are similar, and there is no noticeable influence of the velocity (table 17) and the binder content (table 18). By comparing the results of the model pellets with those of the primary particles and alumina, it can be seen that the differences are larger than in the case of alumina model pellets. This could be explained with the smaller difference between the skeletall denisity of zeolite (2290 kg/m^3) and the used binder in comparison to the alumina (3420 kg/m^3).

Table 17: Porosity of zeolite model pellets as a function of the tip velocity in comparison with the porosity of the primary particles

Porosity of the primary particles in % [35]	50.76		
Rotational tip velocity v_r in m/s	0.17	0.37	0.74
Porosity ε in %	45 ± 1.1	45 ± 1.0	43 ± 1.1

Table 18: Porosity of zeolite model pellets as a function of the binder content in comparison with the porosity of the primary particles.

Porosity of the primary particles in % [35]	50.76	
Binder content φ_B in g/g	0.053	0.109
Porosity of ε %	42 ± 1.3	45 ± 1.4

6.5. Computed Tomographic Investigation of the Model Pellets

The accomplishment of realistic DEM simulations requires a detailed investigation of the model pellets. Such an investigation is available using X-ray micro-computed tomography. Selected batches with largest process parameter variations (for which model pellets, the property differences were expected to be largest) were subjected to a further analysis (table 19). Irregular pellets with similar sizes were chosen for the tomographic investigation. Due to the very large difference between the densities of the primary particles and the solid bridges it was not possible to analyse them simulraneously. Therefore, the X-ray micro-computed tomographcal analysis was focused only on the primary particles in the pellets. The binder was not taken into consideration. By analysing the pellet morphology and structure, one can better understand the influence of the processing conditions and how they change the product pellets.

Table 19. Overview of alumina and zeolite pellet charges scanned with μ-CT.

	Processing time τ_p in min	Rotational velocity v_r in m/s	Binder content φ_B
Alumina Charge 1	15	0.17	0.053
Alumina Charge 2	15	0.74	0.053
Alumina Charge 3	15	0.17	0.109
Alumina Charge 4	15	0.74	0.109
Alumina Charge 5	30	0.17	0.109
Alumina Charge 6	30	0.74	0.109
Alumina Charge 7	30	0.17	0.053
Alumina Charge 8	30	0.74	0.053
Zeolite Charge 1	15	0.17	0.053
Zeolite Charge 2	15	0.74	0.053
Zeolite Charge 3	15	0.17	0.109
Zeolite Charge 4	15	0.74	0.109
Zeolite Charge 5	30	0.17	0.109
Zeolite Charge 6	30	0.74	0.109
Zeolite Charge 7	30	0.17	0.053
Zeolite Charge 8	30	0.74	0.053

The 3D reconstruction of the pellets is a result from the combination of grey scale images. An example of grey scale images and a 3D reconstruction of randon pellet are shown in figure 55. The 3D central ccoordinates of the primary particles were taken down using the software Volex (Fraunhofer Institute of Integrated Circuits, IIS, Erlangen, Germany). On the one hand, the coordinates were used for the post-liminary reconstruction of the model pellets in the simulation software and on the other to characterise the structure in detail. Using proper calculation methods, important spatial characteristics were evaluated.

a)   b)

c)   d)
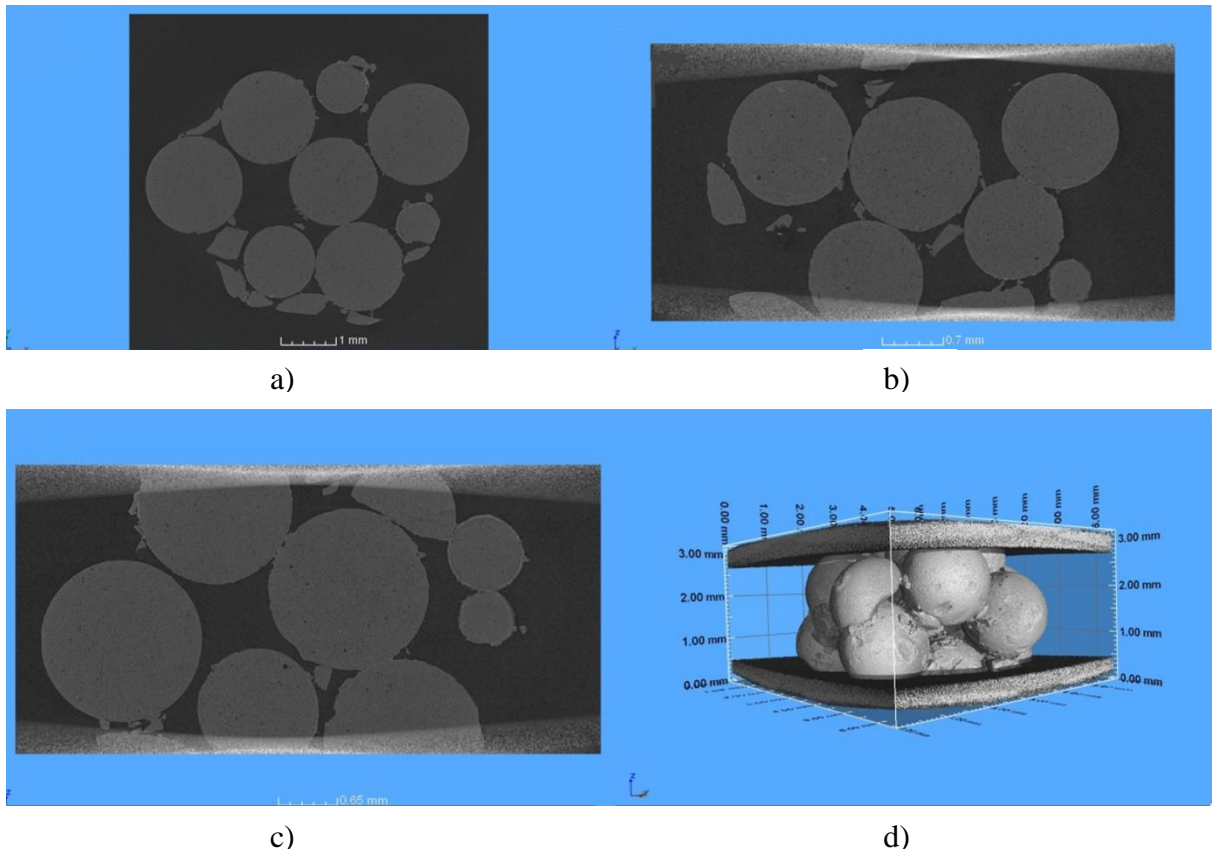
Figure 55:   Example of high-resolution computed tomographs of irregular alumina pellet, taken in the axial (a), coronal (b) and sagittal (c) planes, respectively; d) 3D reconstruction of model pellet.

6.5.1. Number of primary particles

From every pelletising batch, 10 pellets were chosen for the 3D scan and the coordinates of their primary particles were taken down. The average numbers of primary particles were estimated for the investigated pellet types alumina and zeolite. The analysed pellets had diameters of around 3 mm. The tested alumina pellets have an average number of primary particles $N_p = 22$ (attachment B, tables B1 to B8). For the zeolite, due to the larger diameter of the primary particles ($d_{50,3} = 1.75$ mm), the pellets have an average number of primary particles

$N_p = 10$. No significant differences were found between the numbers of primary particles for the pellets from batches carried out at different processing conditions. The average number of primary particles contained in model pellets was not changed at increased rotational velocity, processing time or binder content. The results show that the densification of the structures discussed in section 6.2 is not due to increased number of primary particles in the model pellets, but results because of changes in the binder distribution, solid bridges build-up and primary particle fragmentation.

6.5.2. Center of gravity

The centre of gravity of the pellets had to be found for a further analysis of the topographical data. The received pellets are not spherical, and, therefore, their centre of gravity differs from the centre of geometry. One can find the coordinates of the centre of gravity for an irregular model pellet in a three-dimensional Cartesian system using the projections of the distance vectors v_{xi}, v_{yi}, v_{zi} of its primary particles along the coordinate axes x, y and z:

$$M = \sum_{i=1}^{N_P} M_i, \tag{6.2}$$

$$x_{GC} = \frac{\sum_{i=1}^{N_P} M_i v_{xi}}{M}, \tag{6.3}$$

$$y_{GC} = \frac{\sum_{i=1}^{N_P} M_i v_{yi}}{M}, \tag{6.4}$$

$$z_{GC} = \frac{\sum_{i=1}^{N_P} M_i v_{zi}}{M}, \tag{6.5}$$

where M_i is the mass of the primary particle i and M is the total mass of a model pellet.
The received data about the centre of gravity (table 20, attachment B: tables B1 to B7) is used forward for calculation of the radius of gyration (eq. (6.7)).

Table 20. Results from μ-CT data evaluation received for alumina pellets produced at rotational velocity 0.17 m/s, processing time of 15 minutes and with binder content φ_B of 0.053 g/g.

N_p	r_p in mm	R_g in mm	$d_{c,max}$ in mm	$d_{c,max}$ /$2R_g$	Porosity			Coordination number	Coordination angle in °
					From R_g	From CH*	From dilation		
22	0.5	1.46	5.00	1.72	0.59	0.56	0.54	1.62	63.63
22	0.5	1.36	5.21	1.92	0.49	0.51	0.54	2.14	61.50
20	0.5	1.35	4.56	1.69	0.53	0.53	0.60	1.74	69.71
18	0.5	1.47	4.98	1.69	0.67	0.54	0.51	1.76	68.44
18	0.5	1.64	4.62	1.41	0.76	0.53	0.54	1.59	78.56
15	0.5	1.23	4.01	1.63	0.53	0.48	0.35	2.50	60.10
14	0.5	1.14	3.65	1.60	0.45	0.41	0.52	2.71	61.84
14	0.5	1.12	3.58	1.59	0.43	0.47	0.39	2.46	52.05
9	0.5	1.03	3.21	1.56	0.52	0.51	0.51	1.50	72.50
8	0.5	0.86	2.55	1.48	0.28	0.35	0.59	2.29	64.29

* CH– Convex hull

6.5.3. Radius of gyration

The radius of gyration is a main characteristic for agglomerate or pellet structures. It is correlated with the distribution of different parts of any irregularly shaped pellet from the centre of the mass. It is a size characteristic, but also gives information on the mass distribution around the gravity centre [116]. The radius of gyration can be defined as follows:

$$R_g = \sqrt{\frac{I}{M}} = \sqrt{\frac{1}{N_P}\sum_{i=1}^{N_P} R_i^2}. \tag{6.6}$$

I is the moment of inertia; R_i is the distance of each primary particle from the centre of mass, and NP the number of primary particles in a model pellet. Apart from the possibility of expressing the radius of gyration as a root mean square of the distance of all the primary particles from the centre of the mass it can also be computed as the root mean squared distance between all pairs of primary particles [144]:

$$R_g = \sqrt{\frac{1}{2N_P^2}\sum_i^{N_P}\sum_j^{N_P}(R_i - R_j)^2}. \tag{6.7}$$

The radius of gyration of the model pellets was found using eq. (6.7).

The radius of gyration is used in technical mechanics to describe the breakage mechanism of a column [145]. It is very useful for the characterisation of irregularly shaped objects like polymer chains and agglomerates. The interpretation of its values can be accomplished by comparsion with the maximum projected length of the pellet $d_{c,max}$. The values of $d_{c,max}$ are also evaluated and given in table 20 for alumina pellets produced at rotational velocity 0.17 m/s, processing time of 15 minutes and with binder content of 0.053 g/g. The average radius of gyration for the alumina pellets exhibits a value of 1.36 mm. Individual values are given in attachment B, tables B 1 to B 7. The ratio $d_{c,max}/2R_g$ is for alumina 1.71. For the zeolite pellets, the radius of gyration and the ratio $d_{c,max}/2R_g$ are resp. 1.44 and 1.58. There are no noticeable differences between the radii of gyration for pellets from different batches. This shows that the changes of pelletising process parameters do not influence the overall fragmentation of the pellets.

6.5.4. Porosity

Using the received data from the μ-CT it is possible to determine the volumetric porosity ε of the pellets. It can be defined as:

$$\varepsilon = 1 - \frac{1}{V}\sum_{i=1}^{N_P} V_i, \tag{6.8}$$

where V_i is the volume of one primary particle and V is the total volume of the pellet including inside voides and pores.

There are three main methods for performing a porosity analysis: calculating porosity from the radius of gyration, from the convex hull around the pellet or by dilation of the pellet. The first method for porosity determination is from the radius of gyration. The central moment of inertia of a spherical pellet (figure 56a) having equivalent radius R_e can be found using the following equation:

$$I = \int_0^{R_e} R^2 dm = \int_0^{R_e} R^2 \rho_p dV = \int_0^{R_e} 4\pi R^4 \rho_p dR = \frac{4\pi R_e^5 \rho_p}{5}, \tag{6.9}$$

where ρ_p is the apparent density.

a)　　　　　　　　　　b)　　　　　　　　　　c)
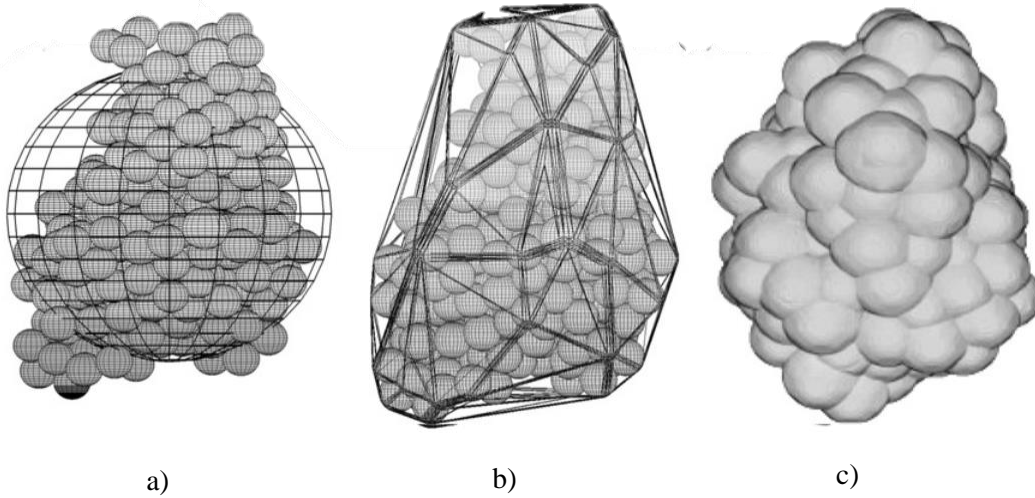
Figure 56:　Procedures to evaluate pellet porosity a) Equivalent radius from gyration radius b) Convex hull c) Dilation [111].

Taking the definition of the radius of gyration from eq. (6.6) and inserting volume and mass one can receive the following function for equivalent radius:

$$R_e = \sqrt{\frac{5}{3}} R_{g.} \tag{6.10}$$

Afterwards one can calculate the total volume of the pellet and insert it in eq. (6.8). Thus, one can receive its porosity.

The second possibility is to use the smallest convex region containing the pellet to receive its volumetric porosity (figure 56b). The coordinates and the radii of the primary particles were used as an input of a Matlab code to create a convex hull over the pellet. The volume within was evaluated and used for the porosity calculation.

The third method is the usage of a dilation operator. By knowing the voxel size and the average void sizes within a pellet, one can use dilation to close all internal voids. By setting the volume of the dilated pellet equal to the total volume, it is possible to evaluate the porosity with eq (6.8).
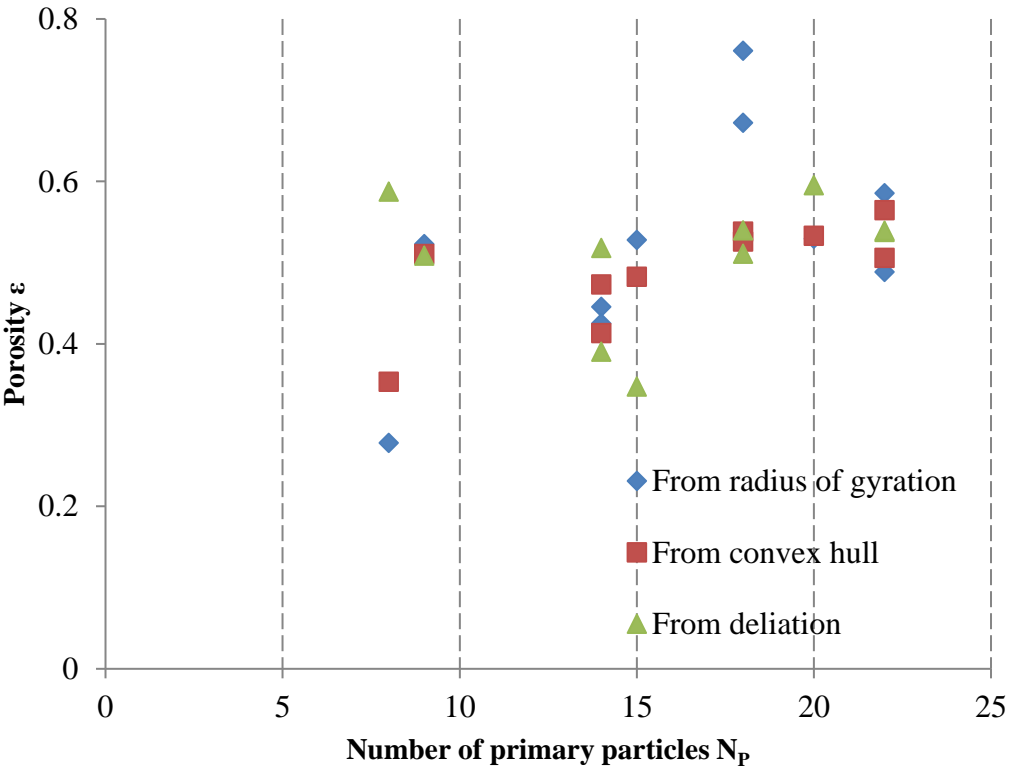
Figure 57: Comparison between porosities calculated by three different methods for alumina pellets produced at rotational speed of 0.17 m/s, processing time of 15 min and with binder content of 0.053 g/g.

The volumetric porosity was calculated for the model pellets through all three methods and results are listed in attachment B. Example results are given in table 20 for alumina pellets produced at a rotational velocity 0.17 m/s, a processing time of 15 minutes and with a binder content of 0.053 g/g. The average values of the porosity of these pellets, calculated from the

equivalent radius, the convex hull and dilation are resp. 0.489, 0.457 and 0.509. There is a good agreement between the porosity measured with different methods. A comparison is shown in figure 57. There was no trend among pellet porosities from different batches.

For zeolite model pellets produced at rotational speed of 0.17 m/s, processing time of 15 min and with binder content of 0.053 g/g, the calculated average volumetric porosities are reps. 0.414, 0.349 and 0.394 depending on the used calculation method (figure 58). Like in the case of alumina pellets, the agreement between the results is good and there is a lack of trend among the values for the different pellet batches. The values are listed in attchment B, tables from B 1 to B 8.
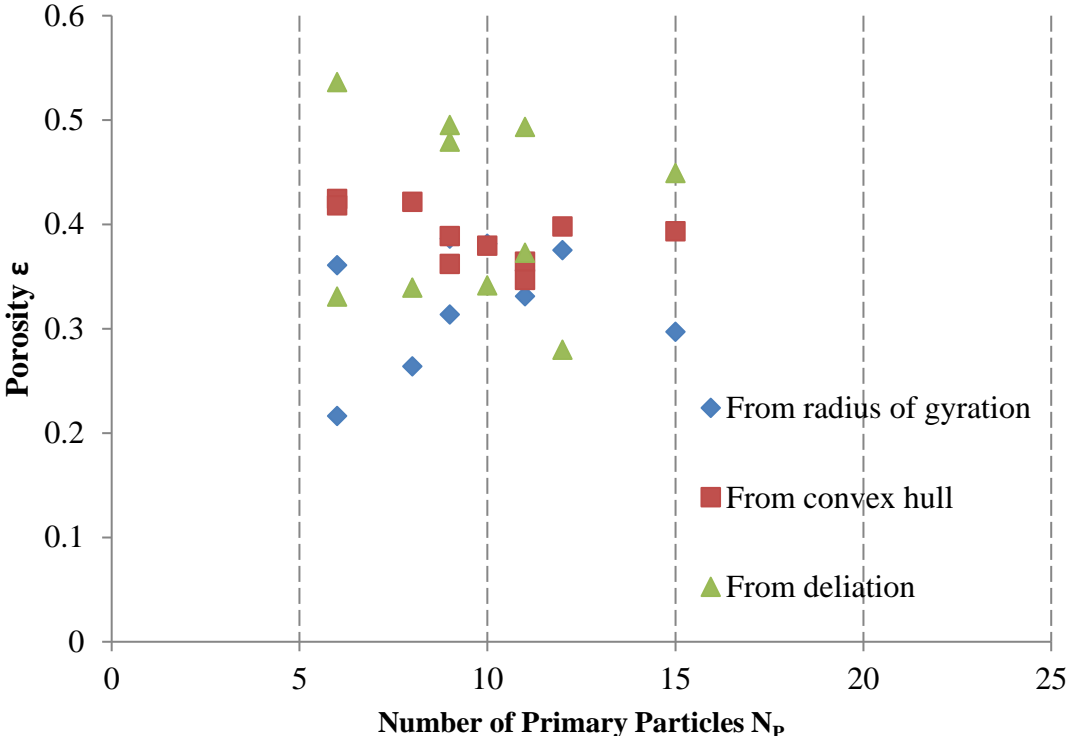
Figure 58: Comparison between porosities calculated by three different methods for zeolite pellets produced at rotational speed of 0.17 m/s, processing time of 15 min and with binder content of 0.053 g/g.

6.5.5. Fractal dimension and pre-factor

For irregular structures like the investigated model pellets in this work, an important characteristic is the fractal dimension D_f [111]. Fractal dimension describes statistically the structural compactness of an object. It is related to the number of primary particles N_p, the radius of gyration R_g, the radius of the primary particles r_i and the fractal pre-factor K_g according to

Graphically the fractal dimension can be found by plotting the number of primary particles

$$N_P = K_g \left(\frac{R_g}{r_i}\right)^{D_f}. \tag{6.11}$$

versus the ratio of the radius of gyration R_g to primary particle radius (figure 59). The slope of
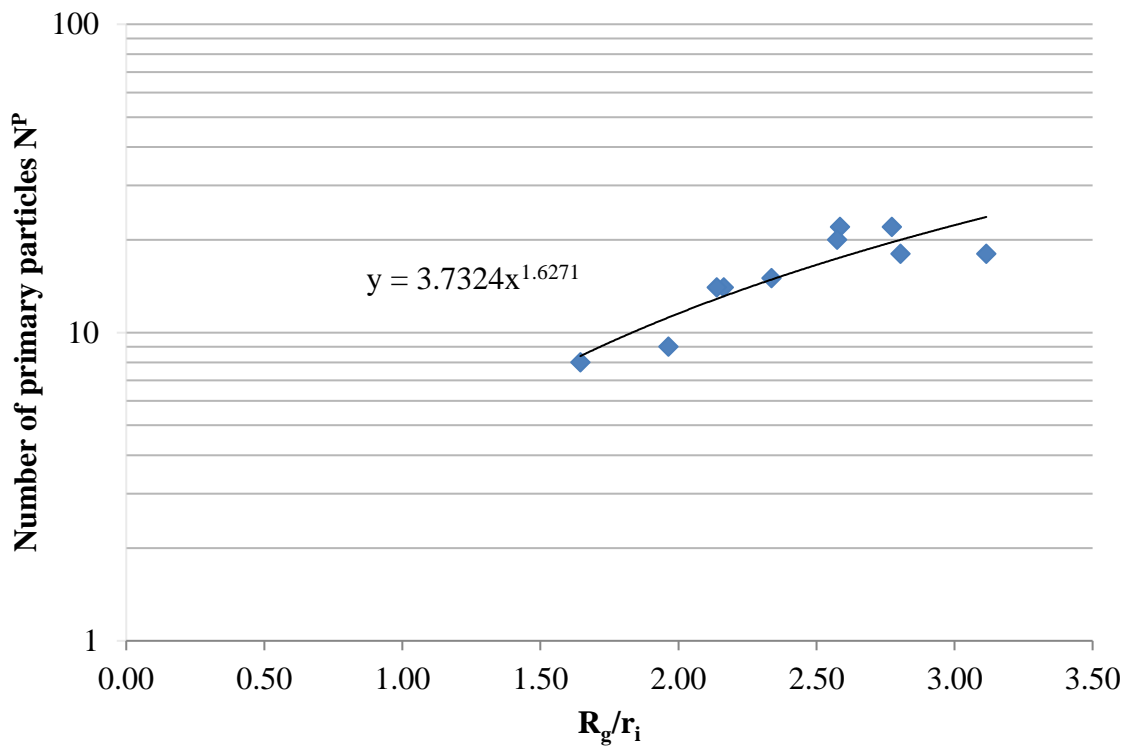
Figure 59: Normalized radius of gyration as a function of the primary particle number for alumina pellets produced at rotational speed of 0.17 m/s, processing time of 15 min and with binder content of 0.053 g/g.

the received trend line is the fractal dimension and the intersection is the pre-factor.

The pre-factor gives information about the structure of pores within the pellet and indicates structural heterogeneity. Both parameters were estimated for the entire sample of irregular pellets investigated for each production batch. The results for alumina pellets are summarized in Table 21.

Table 21. Fractal dimension and pre-factor of alumina pellets produced at different processing conditions.

	Charge 1	Charge 2	Charge 3	Charge 4	Charge 5	Charge 6	Charge 7	Charge 8
Fractal dimension D_f	1.63	2.26	2.22	1.08	2.19	2.32	1.48	2.32
Pre-factor K_g	3.73	2.36	2.26	5.75	2.31	2.24	4.81	2.25

The values of the fractal dimension are between 1.08 and 2.63 for the alumina pellets and the pre-factors from 2.24 to 5.75. For the zeolite pellets, the values are more widely spread and are between 1.85 and 9.52 for the pre-factors and from 0.07 to 2.60 for the fractal dimension (table C 1 to table C 8 in attachment C). Fractal dimension lower than unity are unphysical, because D_f can only assume values betwenn 1 and 3 for threedimentional objects. The low values are resulting from too narrow and/or too sparsely occupied variation range of R_g/r_i, especially for zeolite pellets that have been extracred from a fractional sieved between 2.5 and 3.5 (section 3.5)

6.5.6.   Coordination number

The coordination number (CN) of primary particles in a pellet shows the number of contacts with neighbour primary particles. The coordination number can be determined by calculating the distance between the centres of neighbor particles. If the distance is equal or smaller than the sum of the particle radii then one contact is counted to the coordination number of the particle. The minimum path connecting two primary particles was calculated by the equation

$$\sqrt{\left(x_i - x_j\right)^2 + \left(y_i - y_j\right)^2 + \left(z_i - z_j\right)^2} = \left|R_i - R_j\right|, \qquad (6.12)$$

where x, y and z are the centre coordinates of every sphere. The mean coordination numbers for alumina pellets produced with a rotational velocity of 0.17 m/s, a processing time of 15 min, binder content of 0.053 g/g and different primary particle numbers is shown in figure 60. The values vary between 1.5 and 2.7, but no specific trend can be noticed for pellets with different sizes. Similar are the results for zeolite model pellets, summarised in tables B1 to B8 in attachment B. The values of mean coordination number are between 1.0 and 5.4. They do not

follow any specific trend and do not show any clear dependency on processing conditions or the size of the pellets.
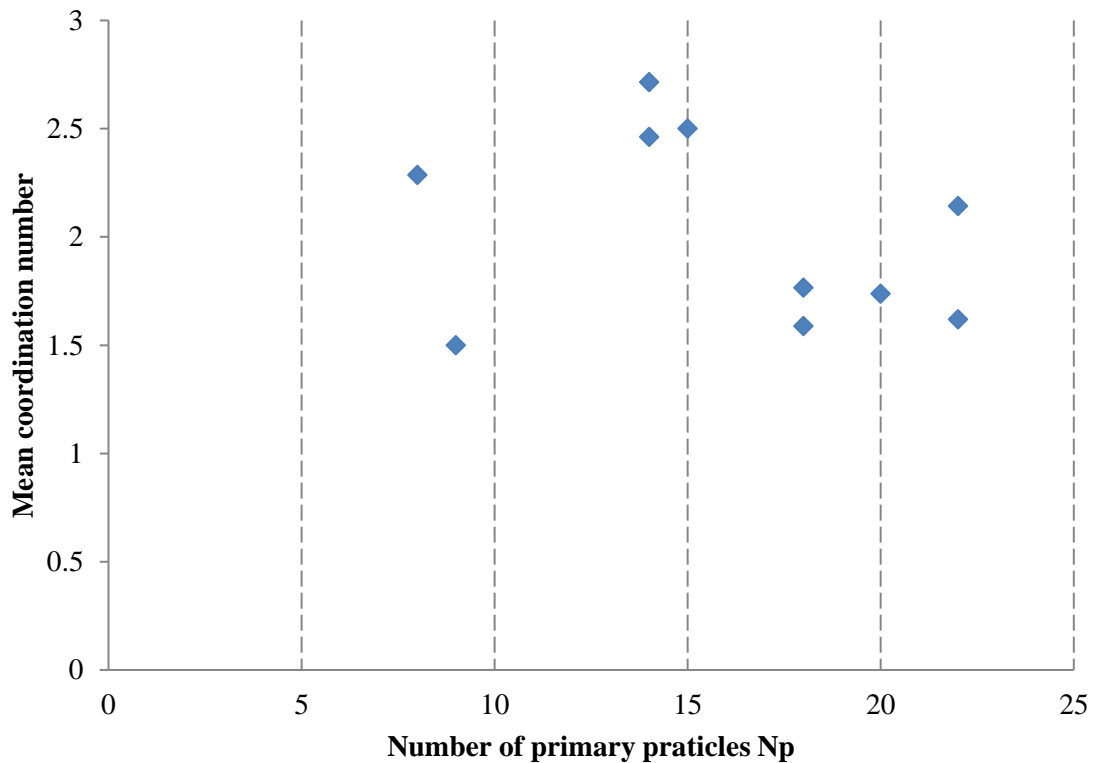
Figure 60:   Mean coordination number as a function of primary particles number for alumina pellets produced at rotational velocity of 0.17 m/s, processing time of 15 min and binder content of 0.053 g/g.

6.5.7.   Coordination angle

The coordination angle is defined as the angle between the vectors connecting the center of each primary particle to the centers of two of its contact neighbors [116]. For example, pellets with the same contact partners may behave differently due to the different angle between them. The number of coordination angles is the same as the coordination number. The average coordination angle for a pellet is found by deviding 2π on the coordination number. It is important to characterise the distribution of coordinate angles within pellet charges due to its deciding role for pellet stability. In figure 61 the coordination angles for alumina pellets produced at a rotational velocity of 0.17 m/s, a processing time of 15 min. and a binder content of 0.053 g/g are shown.
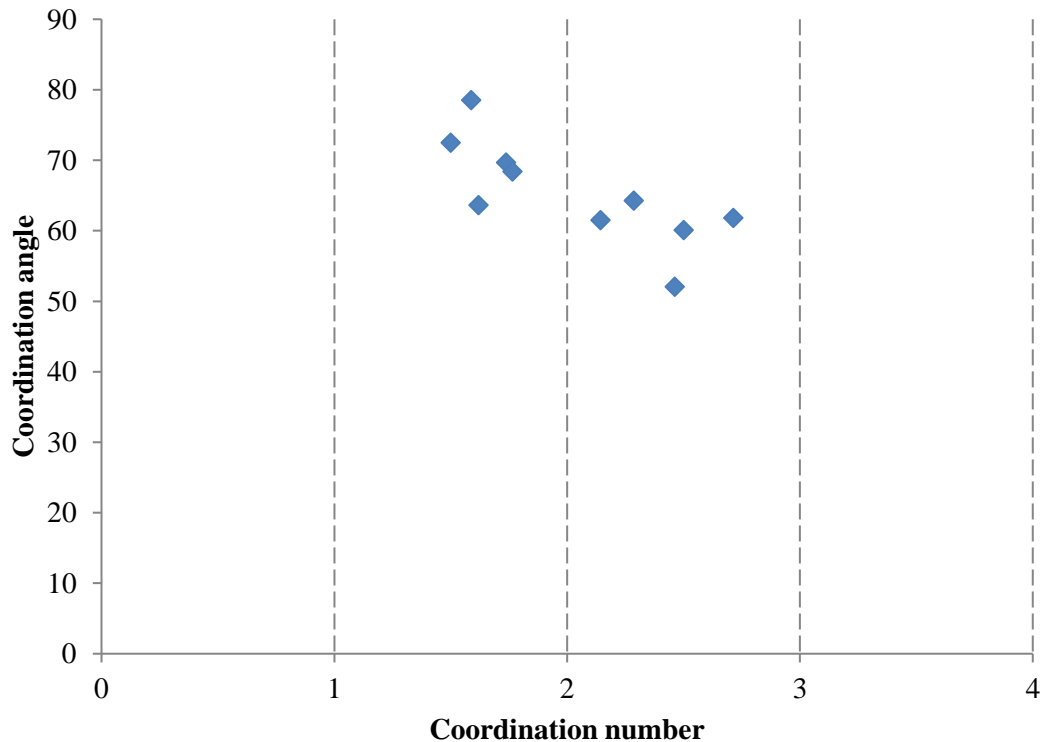
Figure 61:   Mean coordination angle as a function of the coordination number for alumina pellets produced at rotational velocity of 0.17 m/s, processing time of 15 min and binder content of 0.053 g/g.

One can see that the most frequent coordination angles for the model pellets are 60º and 70º. The average coordination angle for all alumina charges is 59°, which is less than for zeolite pellets. They have an average coordination angle of 65° due to their larger diameter, and, therefore, a lower coordination number.

6.5.8.   Overview of computed tomographic investigation of the model pellets

The investigations of the topographical characteristics of alumina and zeolite model pellets show no correlation between the arrangement and structuring of the primary particles in pellets and the processing condition during the production process. In both cases, the primary particles are spread similarly through the pellet, and the distances between them are not influenced by changing process parameters. This result is very important because it proves that the process parameters influence the mechanical behaviour of the investigated system by changing the binder distribution and propagation among the primary particles. They do not change the primary particle number, distribution or packing. These results are of crucial importance for DEM simulations of the model pellets. Based on the received data, one can rebuild and study the behaviour of particular systems produced at different processing conditions by changing their solid bridges (binder) distribution.

6.6.   Compression Tests

Quasi-static compression tests were performed to investigate the behaviour of the produced pellets under stress. The term "quasi-static" means that the loading is applied so slowly that the structure also deforms very smoothly (very low strain rate), and, therefore, any inertia forces are small enough to be neglected [87]. Due to technical restrictions of the used compression equipment, the maximal size of pellets that could be investigated is 3.5 mm. As already pointed out, investigated alumina pellets were either tetrahedral or selected from the sieve fraction 1.5 to 3.5 mm. Zeolite pellets were from the sieve fraction 2.5 o 3.5 mm. In the focus of the study were the differences between the pellets produced at various processing conditions.

6.6.1.   Breakage Behaviour of Regular Structures – Tetrahedra

6.6.1.1. Tetrahedra with a Primary Particle Diameter of 1.0 mm

As already mentioned, the produced pellets are not spherical and due to this fact, conventional models of particles in contact for calculating their mechanical properties cannot be applied. Hence, the breakage behaviour of the pellets was analysed based on their mass-related breakage energy and breakage force. After the pelletising, hardening of the binder and sorting of the received structures, tetrahedron shaped pellets were separated manually from the alumina charges. These pellets were investigated separately and the results were used as a comparison for the rest of the pellets. No tetrahedron pellets were found in the zeolite batches. The reason for the lack of tetrahedron pellets in the zeolite batches needs to be investigated further. One of the possible explanations is the larger primary particle size combined with the brittle structure of the zeolite.

The breakage probability of alumina tetrahedra produced at different processing conditions was evaluated using the received force-displacement curves. From every batch, 100 pellets were tested individually and the breakage probability was calculated from the breakage force and mass-related breakage energy. In figures 62 and 63, the probability distribution versus the classified breakage force resp. the breakage energy for tetrahedron pellets produced with three different binder amounts is shown: 0.009 g/g, 0.018 g/g and 0.027 g/g. The used binder was HPMC and the primary particle size 1.0 mm. The results are tabulated in table 22. A clear upward trend can be noticed for the required breakage force and the breakage energy with increased binder amount in the pellets. The additionally added binder increased the strength of the received pellets. The parameters of the Weibull distributions for the breakage force and the specific breakage energy are given in table 23.
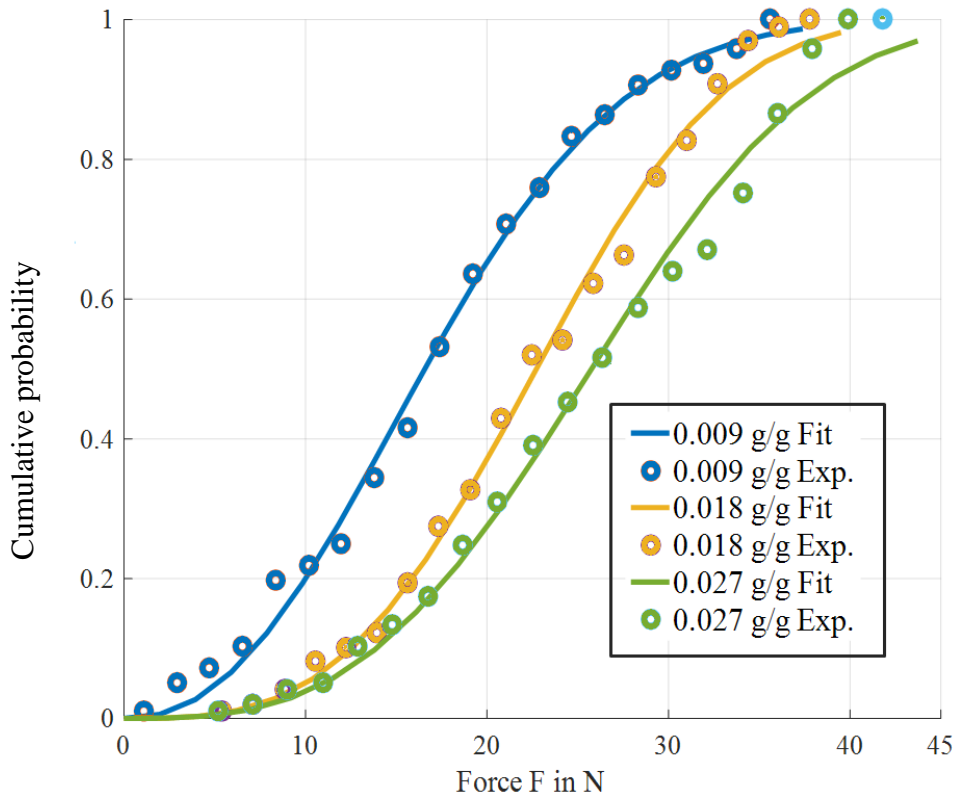
Figure 62:   Cumulative probability distribution as a function of breakage force for tetrahedron-shaped pellets with a primary particle diameter of 1.0 mm produced with different binder amounts.
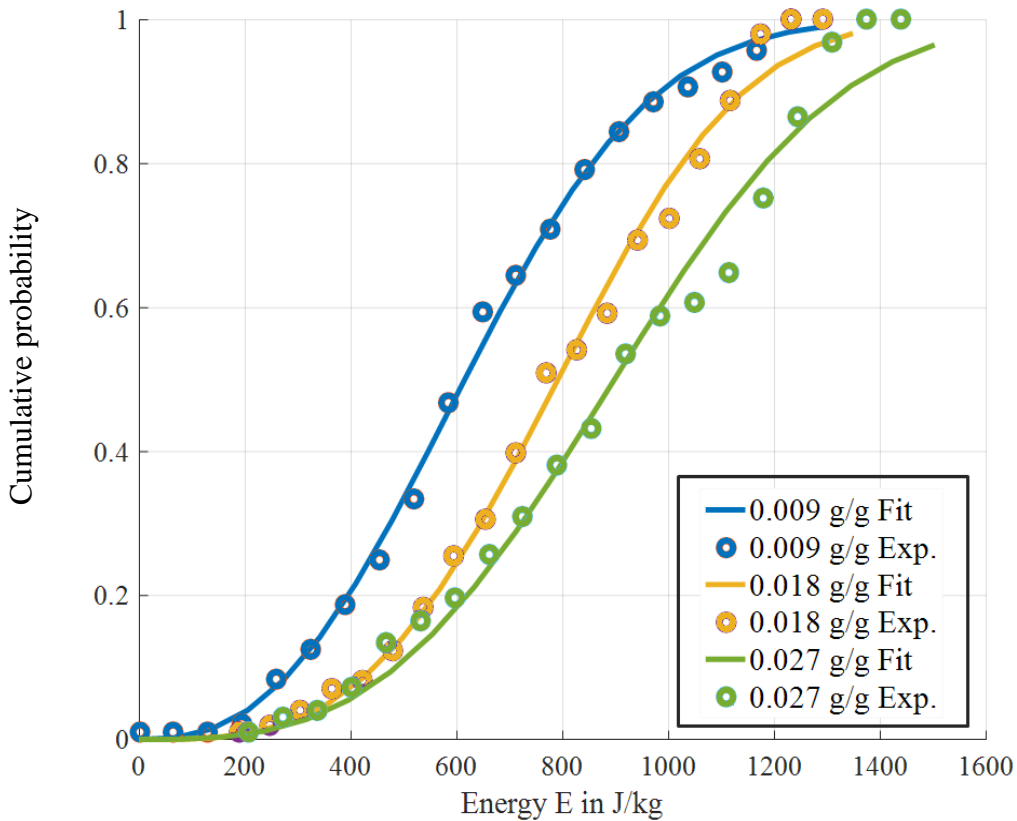
Figure 63:   Cumulative probability distribution as a function of breakage energy for tetrahedron-shaped pellets with a primary particle diameter of 1.0 mm produced with different binder content.

The coefficients of determination R^2 of all the distributions have values around 1, which points at a good agreement with the experiment results.

Another important aspect is illustrated in figure 64. It shows typical force-displacement curves for pellets produced with different binder contents. It can be noticed that the breakage of the pellets produced with the larger binder content does not occur in a brittle way like in the cases of pellets with less binder. The reason is the dominant plastic behaviour of the binder. In the case of increased binder content, the force propagates mainly through the binder, which leads to less plastic breakages.

Table 22: Breakage characteristics of tetrahedron-shaped pellets with a primary particle diameter of 1.0 mm produced with different binder contents.

Binder content C_B in g/g	Mass-related breakage energy E_m in J/kg	Average breakage force F_B in N	Displacement s_B in mm	Mech. Strength σ_B in MPa
Primary particles [128]	1286.7 ± 209.9	37.68 ± 3.65	0.039 ± 0.037	47.67 ± 4.89
0.009	622.47 ± 263.68	19.17 ± 8.41	0.059 ± 0.028	24.35 ± 10.48
0.018	751.05 ± 245.18	22.90 ± 7.82	0.065 ± 0.030	29.12 ± 10.05
0.027	902.18 ± 298.78	26.17 ± 9.27	0.069 ± 0.034	33.27 ± 11.91

Table 23: Shape parameter a, slope b and coefficient of determination R^2 of Weibull distribution for tetrahedron-shaped pellets with a primary particle diameter of 1.0 mm produced with different binder contents.

Binder content φ_B in g/g	a in $(kg/J)^z \, m^{-2}$	b [-]	R^2 [-]
0.009	$8.115 * 10^{-3}$	2.416	0.9900
0.018	$7.122 * 10^{-3}$	1.874	0.9842
0.027	$9.571 * 10^{-3}$	2.147	0.9911

Compared to the primary particles, the pellets exhibit lower breakage force and resp. breakage energy. Due to the small size, the bonding in the primary particle is stronger. Structure defects, like pores and voids in the primary particle, are comparatively small and homogeneously distributed. The nearly ideal spherical form of the primary particles also contributes to their mechanical stability.
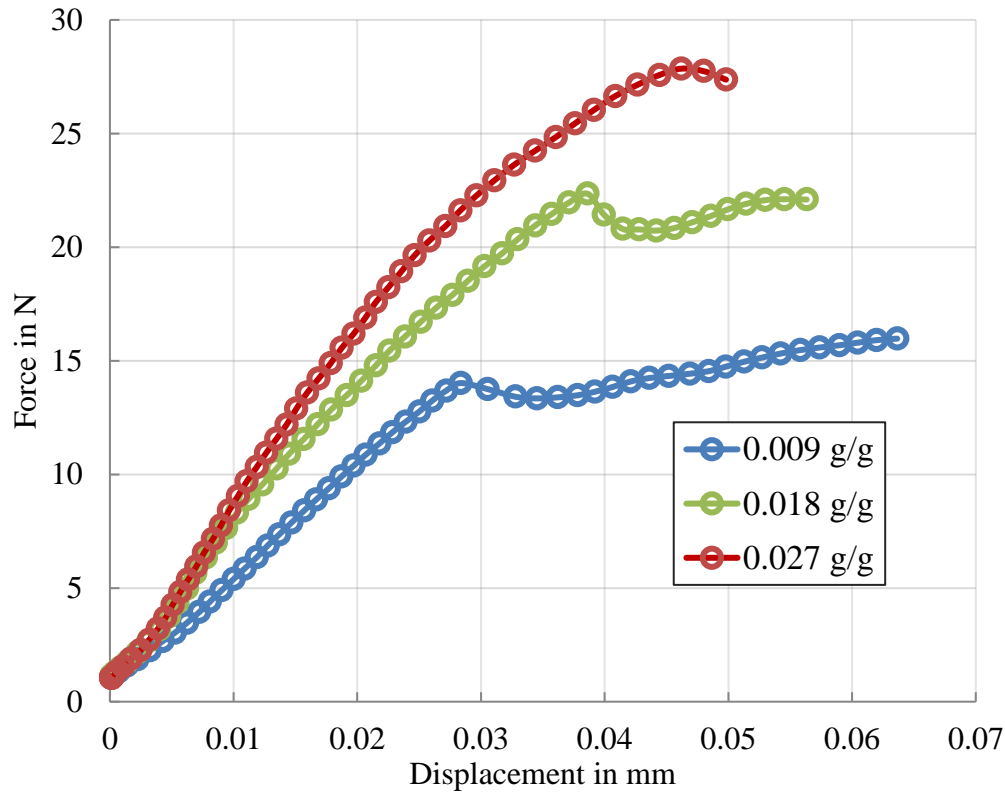
Figure 64: Typical force displacement curves for tetrahedron-shaped pellets with a primary particle diameter of 1.0 mm produced with different binder amounts.

6.6.1.2. Tetrahedra with a Primary Particle Size of 1.8 mm

The next step of the investigation was to analyse the behaviour of the tetrahedra with a primary particles size of 1.8 mm. In figures 65 and 66 are shown the breakage probability of the pellets as a function of the classified breakage force, resp. of the breakage energy. The results of the investigation of binder content influence on the produced tetrahedron mechanical properties are summarized in table 24. The pellets produced with a binder content of 0.018 g/g have the highest breakage force, resp. they need the largest specific energy for failure. It seems that there is an optimum binder content and after reaching it, binder addition does not lead to an increase of the breakage strength anymore. Such an optimum was not observed for the pellet with a primary particle diameter of 1.0 mm. Table 25 shows the Weibull distribution parameters.

Similar to the distributions of the pellets with smaller primary particles, slope is between 1.211 and 2.113 and R^2 has values over 0.90. It is important to notice that for unstable pellets the effect of rearrangement at the beginning of the test is strong. This may influence the results and leads to breakage event at the beginning of the loading.

Table 24. Breakage characteristics of tetrahedron-shaped pellets with a primary particle diameter of 1.8 mm produced with different binder contents.

Binder content φ_B in g/g	Mass-related breakage energy E_m in J/kg	Average breakage force F_B in N	Displcement s_B in mm	Mech. strength σ_B in MPa
Primary particles [128]	503.4 ± 146.4	42.49 ± 8.03	0.058 ±0.011	17.84 ± 3.56
0.009	642.59 ± 215.98	35.89 ± 9.11	0.097 ± 0.029	14.27 ± 3.58
0.018	714.13 ± 165.25	40.29 ± 8.03	0.101 ± 0.031	15.83 ± 3.15
0.027	553.18 ± 250.89	31.04 ± 10.64	0.096 ± 0.040	12.20 ± 4.18
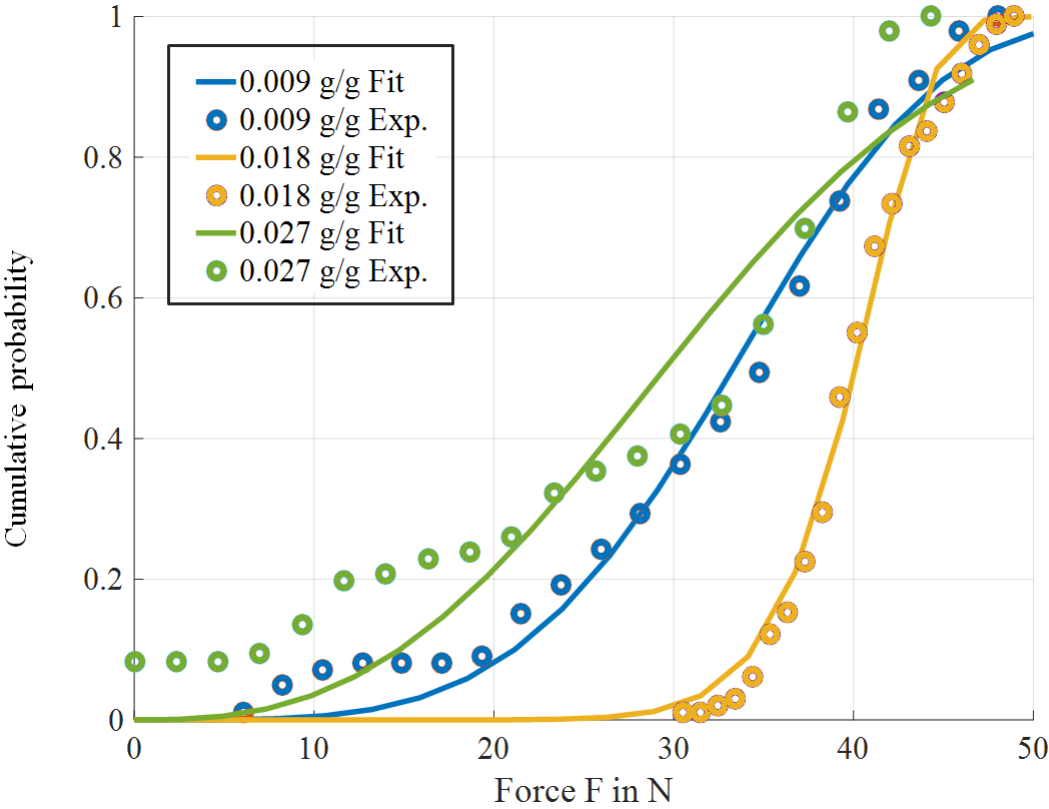
Figure 65: Cumulative probability distribution as a function of the breakage force for tetrahedron-shaped pellets with a primary particle diameter of 1.8 mm produced with different binder amounts.

All the pellets exhibit narrow breakage peaks and the primary breakage is followed by a drop down of the force, as shown in figure 67. Compared to the pellets with a primary particle diameter of 1.0 mm, these pellets require more force to break.
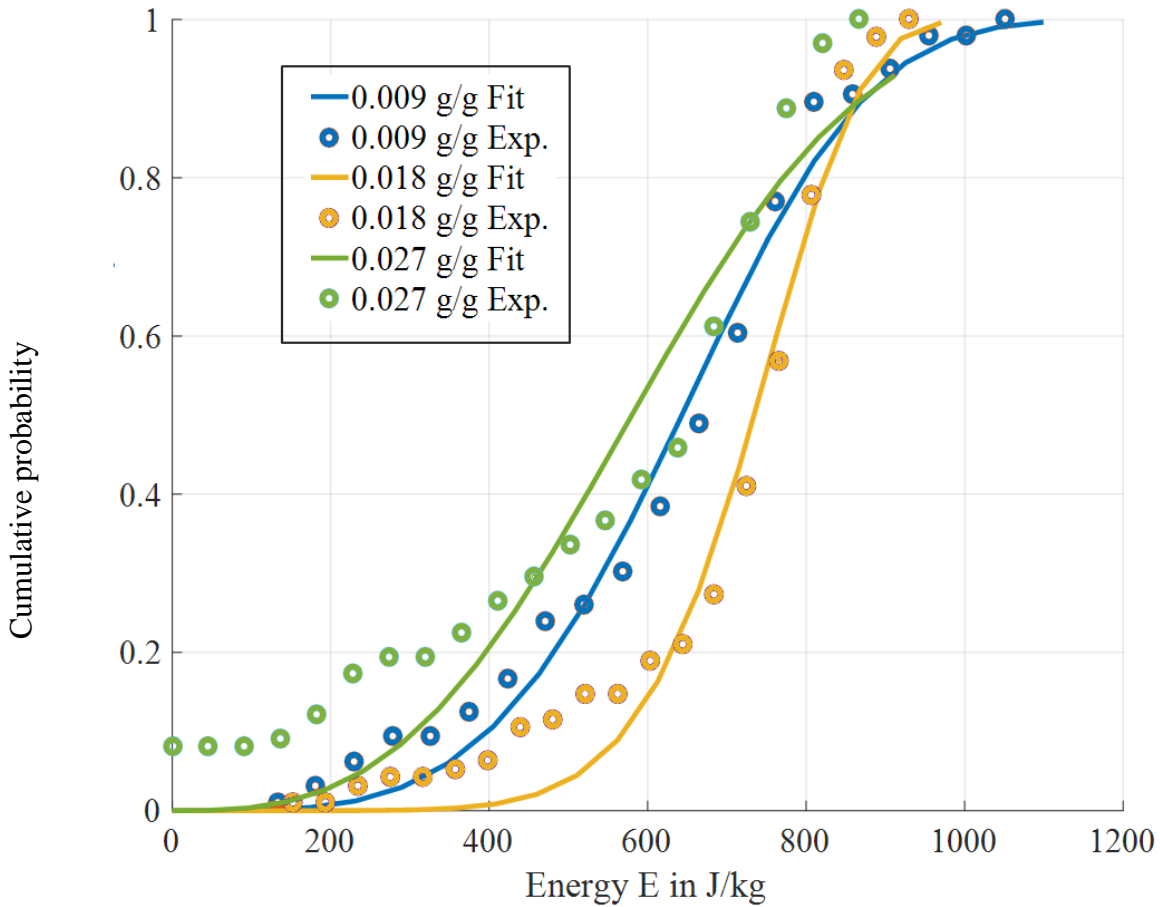
Figure 66:   Cumulative probability distribution as a function of the breakage energy for tetrahedron-shaped pellets with a primary particle diameter of 1.8 mm produced with different binder contents.

Table 25: Shape parameter a, slope b and coefficient of determination R^2 of Weibull distribution for tetrahedron-shaped pellets with a primary particle diameter of 1.8 mm produced with different binder contents.

Binder content φ_B in g/g	a in $(kg/J)^z\,m^{-2}$	b [-]	R^2 [-]
0.17	$11.612*10^{-3}$	1.516	0.9229
0.37	$9.544*10^{-3}$	1.211	0.9011
0.74	$10.111*10^{-3}$	2.113	0.9021
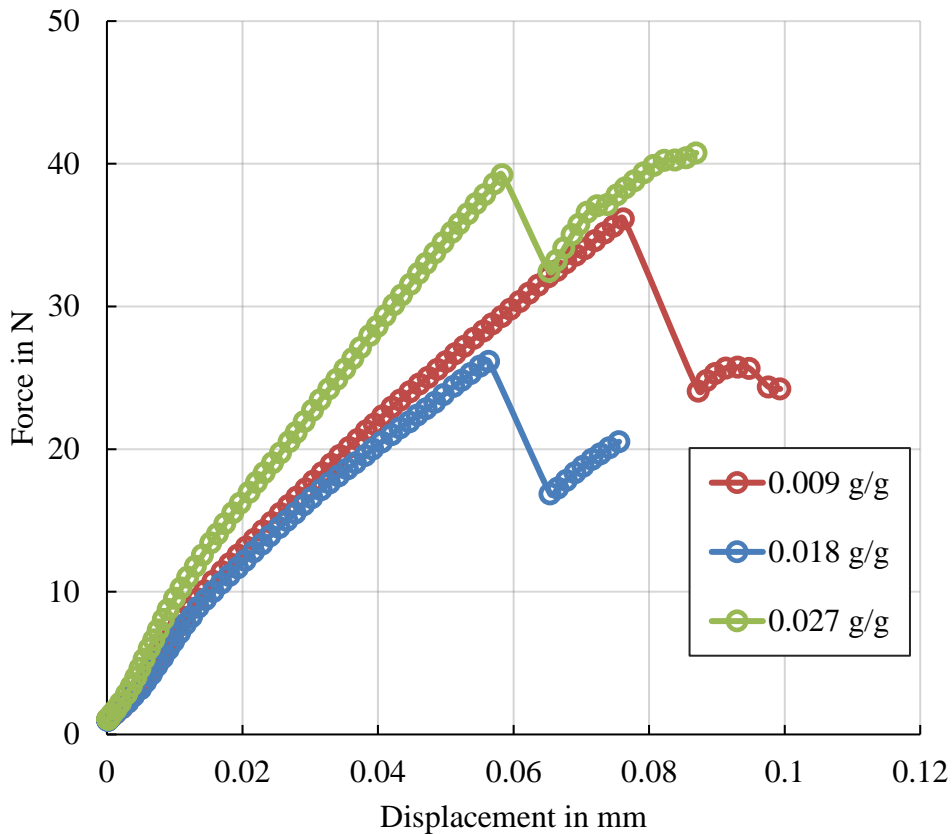
Figure 67: Typical force-displacement curves for tetrahedron-shaped pellets with a primary particle diameter of 1.8 mm produced with different binder contents.

A comparison between the typical breakage patterns of two tetrahedron-shaped pellets with different primary particle diameters is shown in figure 68. The breakage propagation follows a similar way for both pellet types. At the beginning of the compression, the pellet undergoes an elastic deformation. In both cases, the elastic deformation region is comparatively small. After reaching their yield point, the pellets start to deform elastic-plastically until reaching their breakage point. For both pellets with primary particle size of 1.0 mm and 1.8 mm, the primary breakage is followed by secondary breakages.

A comparison between the breakage characteristics of the primary particles and the pellets shows that in the case of primary particles with a diameter of 1.8 mm, the received pellets have breakage strength as high as the primary particles. This result was unexpected due to the fact that the 1.8 mm-based irregularly shaped pellets were unstable and not suitable for further investigation. An explanation for this result may be the force propagation within the structure, occurring through the large primary particles instead of through the easily deformable bridges. Another important observation for both pellet sizes was made during the experimental compression procedure. Independently of the primary particle diameter, the failure of tetrahedron-shaped pellets strongly depends on the angle between their primary particles.

Pellets with obtuse angles break smoothly, whereby the primary particles move away from each other. The bridges between them suffer under tensile stress and break when their maximum mechanical strength is reached. If there are different types of angles between the primary particles, the bridge between those having the most acute angle will break first. Moreover, if the angles in a pellet are acute, the probability of a primary particle breakage increases due to the stress accumulation on the top particle.
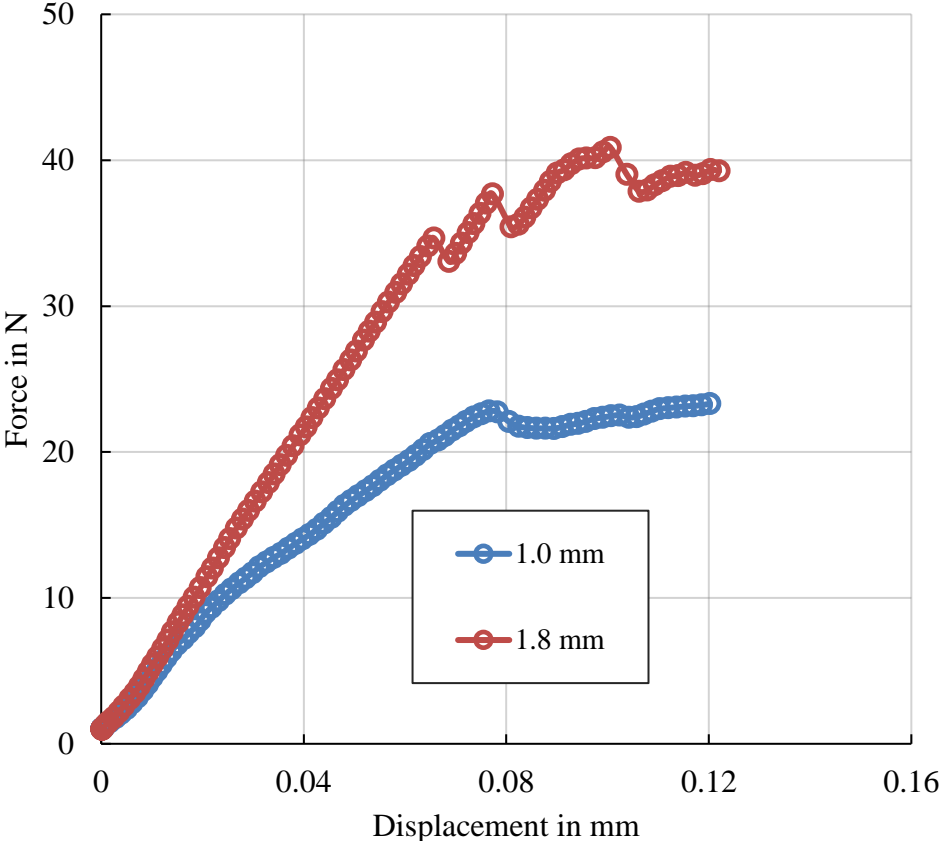
Figure 68:   Comparison between typical breakage patterns of two tetrahedron-shaped pellets with different primary particle diameters.

6.6.2.   Irregular Pellets

The results of the compression tests of irregularly shaped pellets were evaluated and systemised using the same procedure as for regular structures. The main goal was to analyse the influence of the production process parameters on the pellets' breakage behaviour.

6.6.2.1. Influence of the Rotational Velocity on the Irregularly Shaped Alumina Pellets

The influence of the rotational velocity on the breakage behaviour was investigated by comparing the breakage force and the breakage energy probability distributions. The investigated pellets were produced at the same processing time and with the same binder content, but at different rotational velocities. The results are compared with the results for the breakage probability of primary particles introduced by Müller [128] and those received for the regularly structured pellets. As shown in figures 69 and 70, the increase of the rotational velocity leads to formation of more stable pellets, requiring more breakage force, resp. breakage energy, for fracture. In table 26 the results for the breakage probability of alumina pellets at different rotational velocities and a processing time of 15 min are shown.
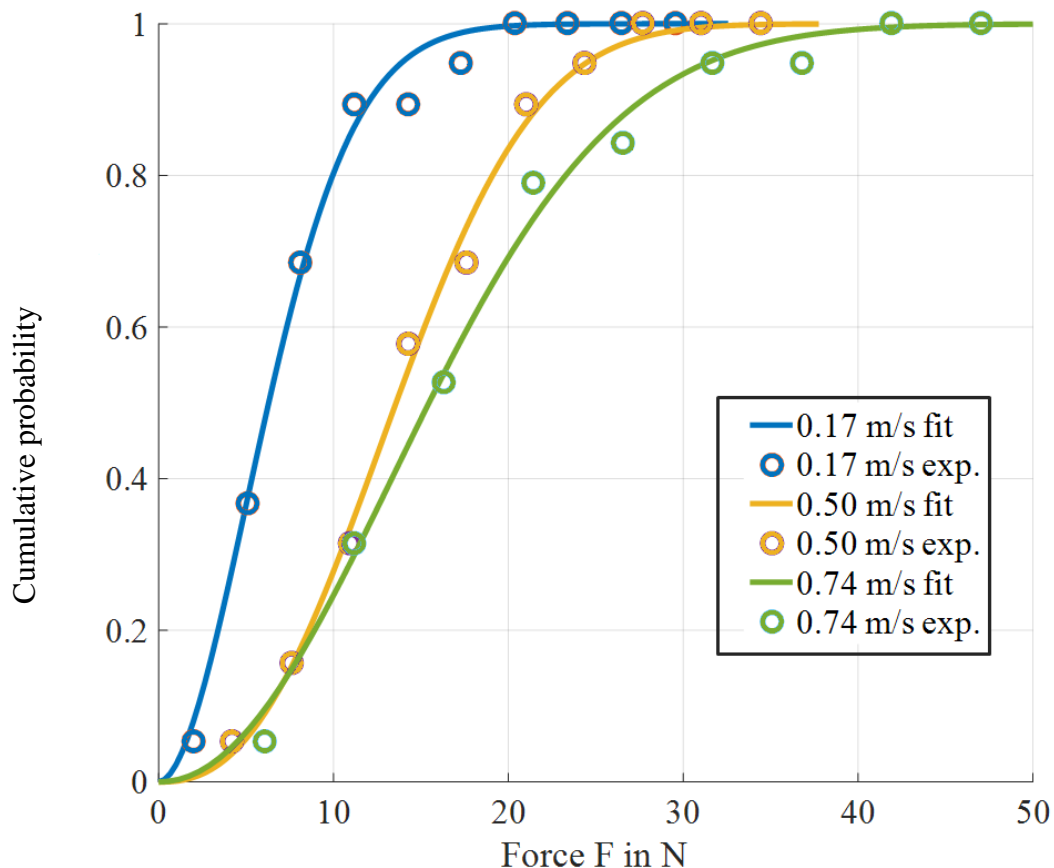
Figure 69:   Cumulative probability distribution of the breakage force for irregularly shaped alumina pellets produced at different rotational speeds.

The breakage force for pellets produced at a rotational velocity of 0.17 m/s is 7.83 N, while at an increased velocity, the needed force for particle breakage grows to 18.10 N. Respectively, the mass-related breakage energy (figure 70) increase from 427.11 J/kg to 875.74 J/kg with increasing velocity. In comparison, the primary particles exhibit larger values (according to Müller [128] alumina primary particles have 37.68 N average breakage force and 1286.7 J/kg average mass-related breakage energy) for both parameters, due to the strong bonding between their fine-powder ingredients.
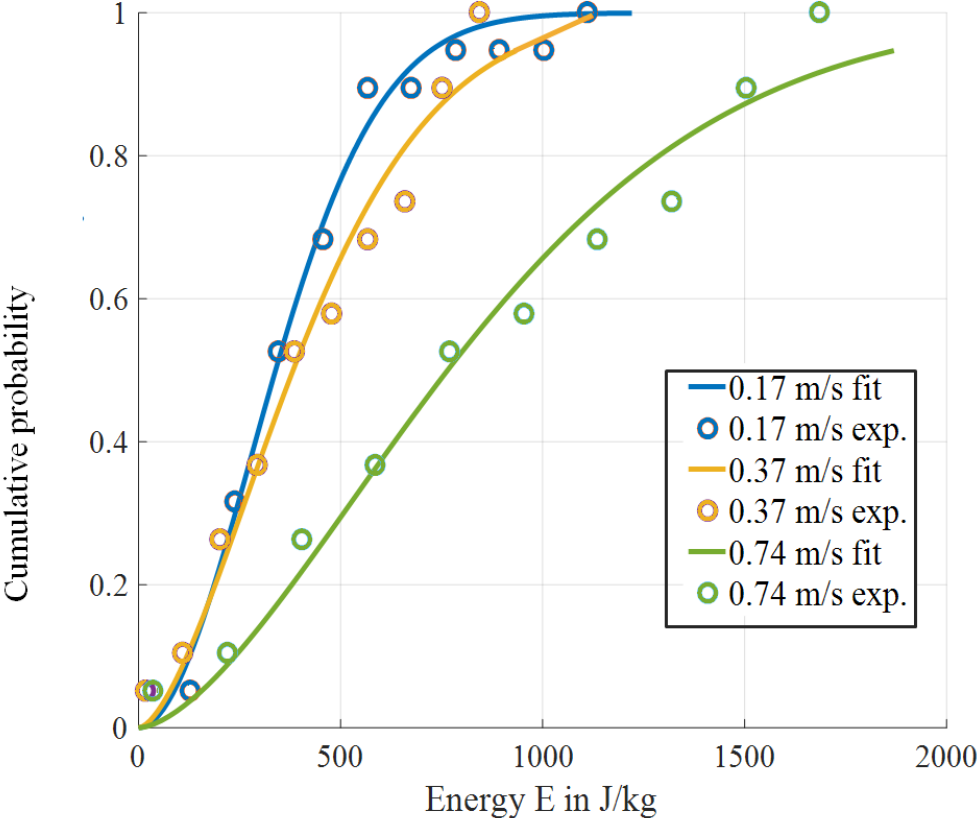
Figure 70: Cumulative probability distribution of the breakage energy for irregularly shaped alumina pellets produced at different rotational speeds.

Figure 71 shows typical force-displacement curves for pellets produced with different rotational speeds. It can be seen that the breakage of pellets produced at a higher velocity is accurately defined and is followed by a large drop of the acting force. The pellets produced at a lower tip velocity start to deform dominantly plastically shortly before the breakage point. In comparison, the pellet produced at a large velocity follows a linear elastic-plastic regime until breakage. The parameters of the Weibull distribution are listed in table 27.
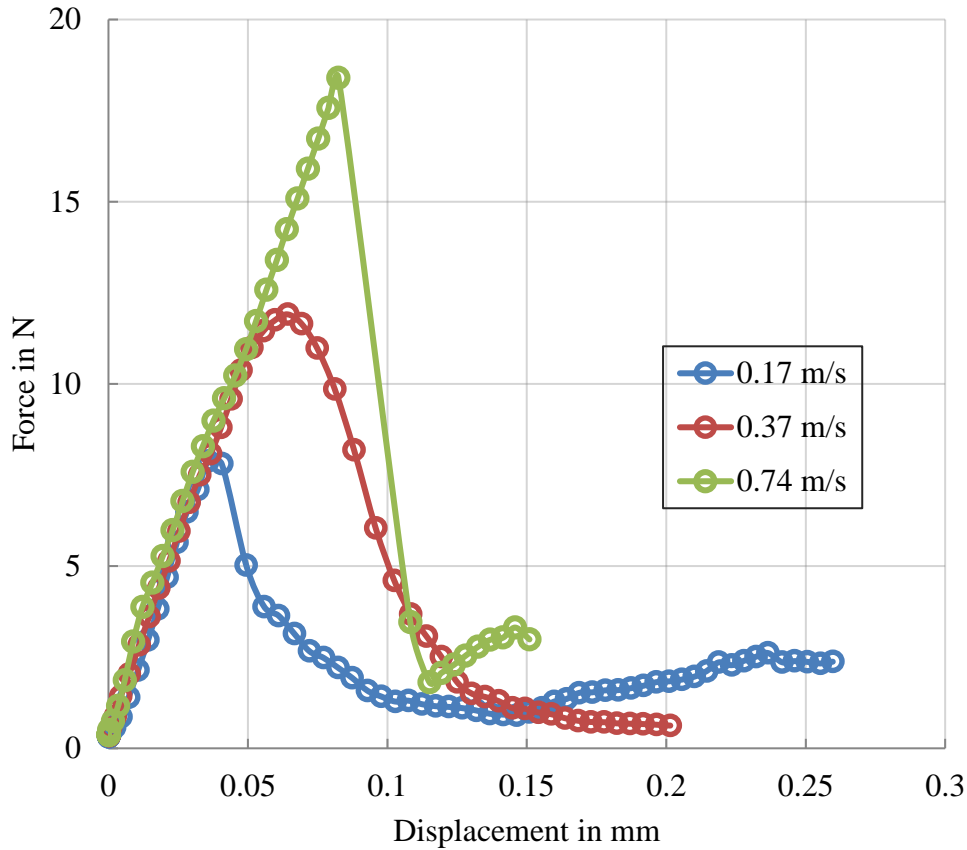
Figure 71:   Typical force-displacement curves for irregularly shaped alumina pellets
              produced at different rotational speeds.

The values of the coefficient of determination R^2, which are significant for the fitting of the experimental data to the statistical method, are closely to 1, showing the accordance of the Weibull distribution and experimental data.

Table 26: Mass-related breakage energy and breakage force for irregular alumina pellets produced with different rotational velocities.

Rotational tip velocity v_r in m/s	Mass related breakage energy E_m in J/kg	Average breakage force F_B in N	Displacement s_B in mm	Mech. strength σ_B in MPa
Primary particles [128]	1286.7 ± 209.9	37.68 ± 3.65	0.039 ± 0.037	47.67 ±4.89
0.17	427.11 ± 272.59	7.83 ± 2.73	0.091 ± 0.048	6.31 ± 2.27
0.37	437.87 ± 268.79	11.07 ± 5.17	0.088. ± 0.015	8.92 ± 2.166
0.74	875.74 ± 537.58	18.10 ± 8.61	0.165 ± 0.012	12.46 ± 3.46

Table 27: Shape parameter a, slope b and coefficient of determination R^2 of Weibull distribution for alumina pellets produced with different rotational velocities.

Rotational tip velocity v_r in m/s	a in $(kg/J)^z\,m^{-2}$	b [-]	R^2 [-]
0.17	7.676*10⁻³	1.836	0.9901
0.37	15.74*10⁻³	2.47	0.9942
0.74	18.47*10⁻³	2.058	0.9908

6.6.2.2. Influence of Binder Content on the Irregularly Shaped Alumina Pellets

To study the effect of binder content increase on the breakage behaviour of model pellets, their mechanical characteristics were compared to those of pellets produced at the same processing time and rotational velocity, but with different binder contents. In figure 72, the breakage force distributions for pellets with three different binder contents are shown. The force required for breakage of a pellet decreases with increasing binder content in the pellets.
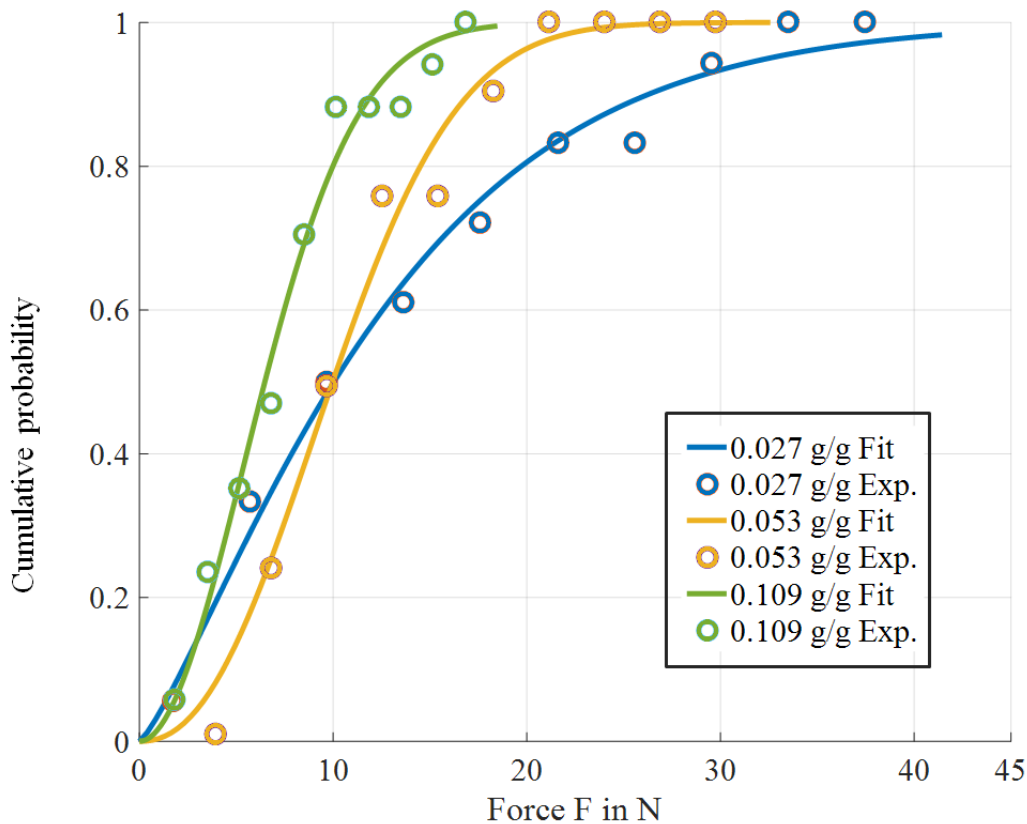
Figure 72: Cumulative probability distribution of the breakage force for irregularly shaped alumina pellets produced with different binder contents.

This result can be explained with breakage pattern propagation whith the increased content of solidified binder having much less breakage strength than the primary particles. This can also be seen in table 28, where the results are listed. With increasing binder content, the breakage force decreased from 11.62 N for 0.027 g/g to 8.66 N for 0.109 g/g.

Table 28: Mass-related breakage energy and breakage force for irregular alumina pellets produced with different binder contents.

Binder content φ_B in g/g	Mass related breakage energy E_m in J/kg	Average breakage force F_B in N	s_B in mm	Mech. strenght σ_B in MPa
Primary particles [128]	1286.7 ± 209.9	37.68 ± 3.65	0.039 ± 0.037	47.67 ± 4.89
0.027	591.23 ± 120.33	11.62 ± 6.62	0.069 ± 0.034	8.68 ± 3.06
0.053	414.26 ± 210.58	10.56 ± 12.08	0.071 ± 0.022	7.65 ± 2.52
0.109	46.27 ± 28.46	8.66 ± 5.36	0.088 ± 0.027	6.31 ± 3.76

The same trend is seen in the mass-related breakage energy (figure 73), decreasing dramatically from 591.23 J/kg for pellets with a binder content of 0.027 g/g to 46.27 J/kg for the pellets with a binder content of 0.109 g/g. In figure 74, typical force-displacement curves for pellets produced with different binder amounts are given. The compression starts for all the pellets with a small elastic deformation, followed by an elastic-plastic range. Shortly before the breakage, the pellets exhibit a dominant plastic deformation. The parameters of the Weibull distribution are listed in table 29. The values of the breakage force and the breakage energy for the pellets are much below those reached for alumina primary particles. The breakage characteristics are also lower than those for regularly shaped pellets. While the tetrahedral produced with a binder amount of 0.027 g/g have a breakage force of approximately 26.17 N (table 22), the irregular pellets with the same binder content break at 11.62 N. The almost threefold decrease shows the importance of the pellets' shape when it comes to breakage and compression. During the loading, the force propagates irregularly through the structure, making convex or side parts of the pellet unstable and easily breakable.

Besides the influence of the rotational velocity and the binder content, experiments were made to investigate the effect of different processing times on the properties of the received pellets. Those studies do not show any trend among the results. No effect could be verified for process duration.
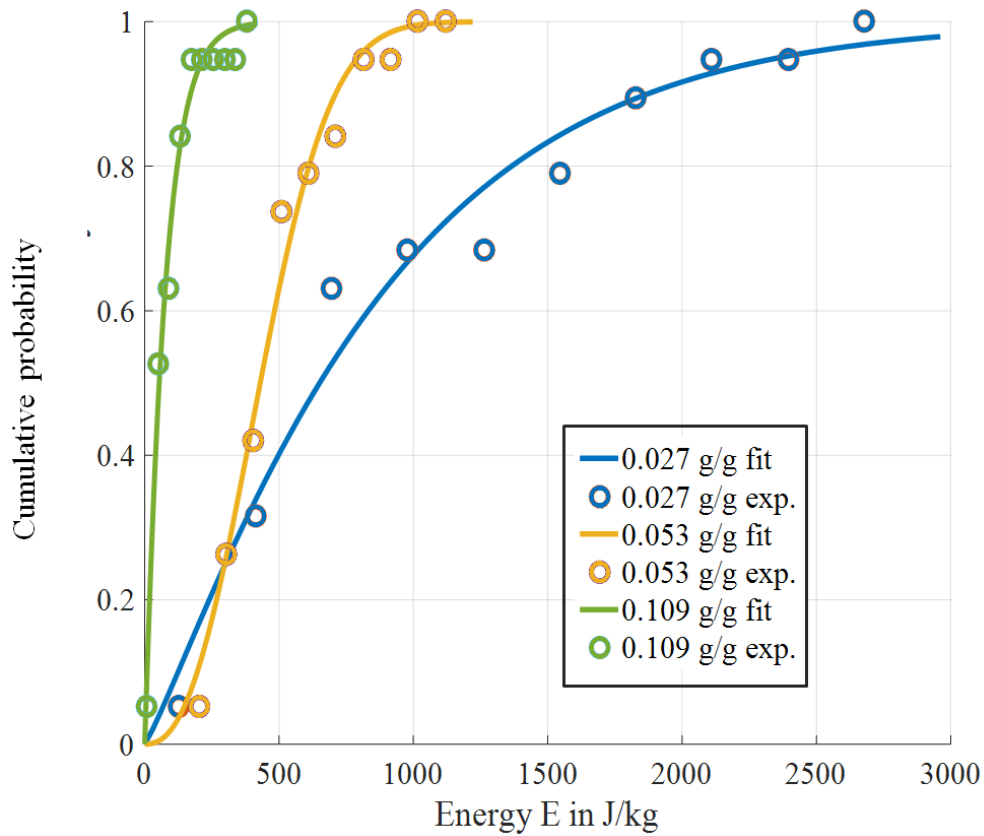
Figure 73: Cumulative probability distribution of the breakage energy for irregularly shaped alumina pellets produced with different binder content.
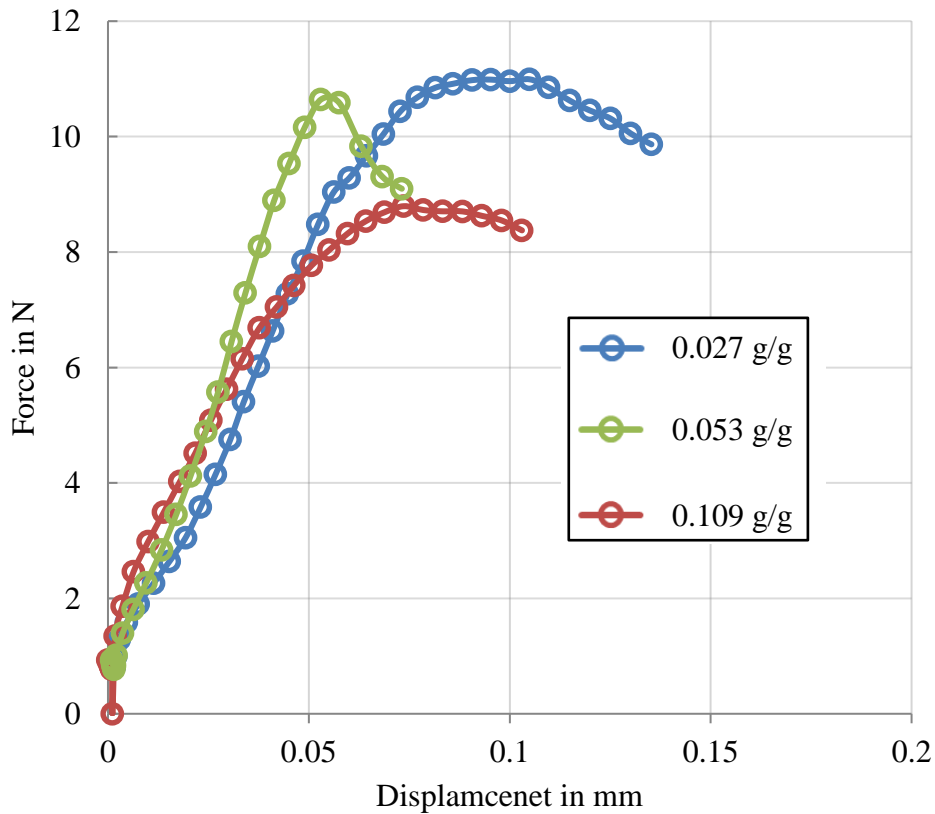
Figure 74: Typical force-displacement curves for irregularly shaped alumina pellets produced with different binder content.

Table 29: Shape parameter a, slope b and coefficient of determination R_2 of the Weibull distribution for alumina pellets produced with different binder contents.

Binder content φ_B in g/g	a in $(kg/J)^z m^{-2}$	b [-]	R^2 [-]
0.027	$14.83*10^{-3}$	1.435	0.9753
0.053	$9.338*10^{-3}$	0.8783	0.9295
0.109	$7.817*10^{-3}$	1.944	0.9608

6.6.2.3. Influence of the Rotational Velocity on the Irregularly Shaped Zeolite Pellets

The compression tests and evaluation methods used for the characterisation of the alumina pellets were also applied to irregularly shaped zeolite model pellets. First, the influence of the rotational velocity was studied while the binder content and the processing time were kept constant. The results are presented as a function of the breakage force, resp. breakage energy, (figures 75 and 76).
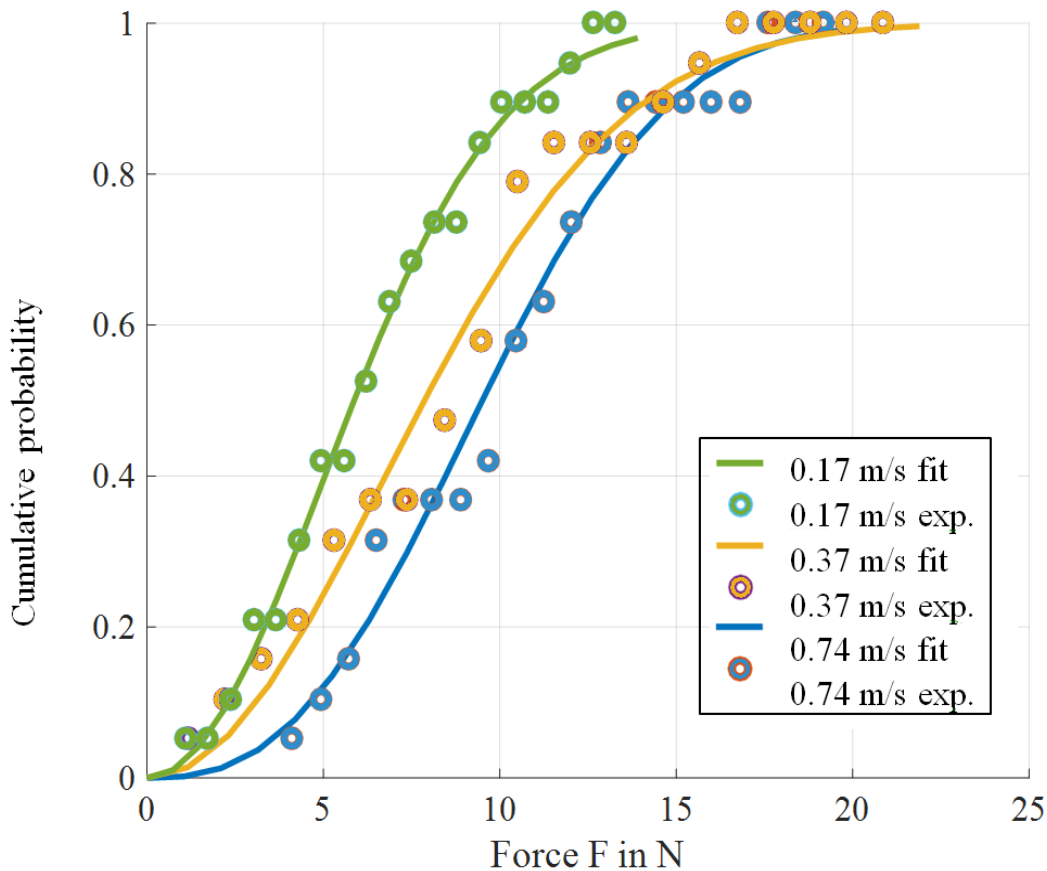
Figure 75:   Cumulative probability distribution of the breakage force for irregularly shaped zeolite pellets produced at different rotational speeds.

Similarly to alumina an increased rotational speed leads to the formation of structures with an improved mechanical strength. This can be seen from the upward trends for the breakage force and for the breakage energy. The force increases from 6.822 N for pellets produced at a speed of 0.17 m/s to 9.084 N for those produced at a velocity of 0.74 m/s. The breakage energy scales up resp. from 89.24 J/kg to 163.90 J/kg. The results are listed in table 30 and the parameters of the force and breakage probability distribution in table 31.

The reason for the increasing mechanical strength of the received pellets at high speed is that the high-energy contact collisions cause a compaction of the pellet, decreasing thus the defects inside of the structure (voids and hollowness between the particles), and, therefore, increasing the breakage resistance of the product.

Table 30: Mass-related breakage energy and breakage force for zeolite pellets produced with different rotational speeds.

Rotational velocity v_r in m/s	Average breakage energy E_m in J/kg	Average breakage force F_B in N	s_B in mm	Mech. strenght σ_B in MPa
Primary particles [35]	241.29 ± 123.25	23.8 ± 7.7	0.0502 ± 0.0127	11.72 ± 3.98
0.17	89.24 ± 28.46	6.822 ± 4.82	0.0457 ± 0.0274	1.62 ± 1.60
0.37	116.51 ± 50.33	8.871 ± 4.47	0.0594 ± 0.0436	3.51 ± 0.90
0.74	163.90 ± 70.58	9.084 ± 4.40	0.0898 ± 0.0158	5.76 ± 1.35

Table 31: Shape parameter a, slope b and coefficient of determination R^2 of the Weibull distribution for zeolite pellets produced at different rotational speeds.

Rotational velocity v_r in m/s	a in $(kg/J)^z\, m^{-2}$	b [-]	R^2 [-]
0.17	$2.125*10^{-3}$	1.548	0.9737
0.37	$10.92*10^{-3}$	2.634	0.9779
0.74	$2.222*10^{-3}$	2.621	0.9839
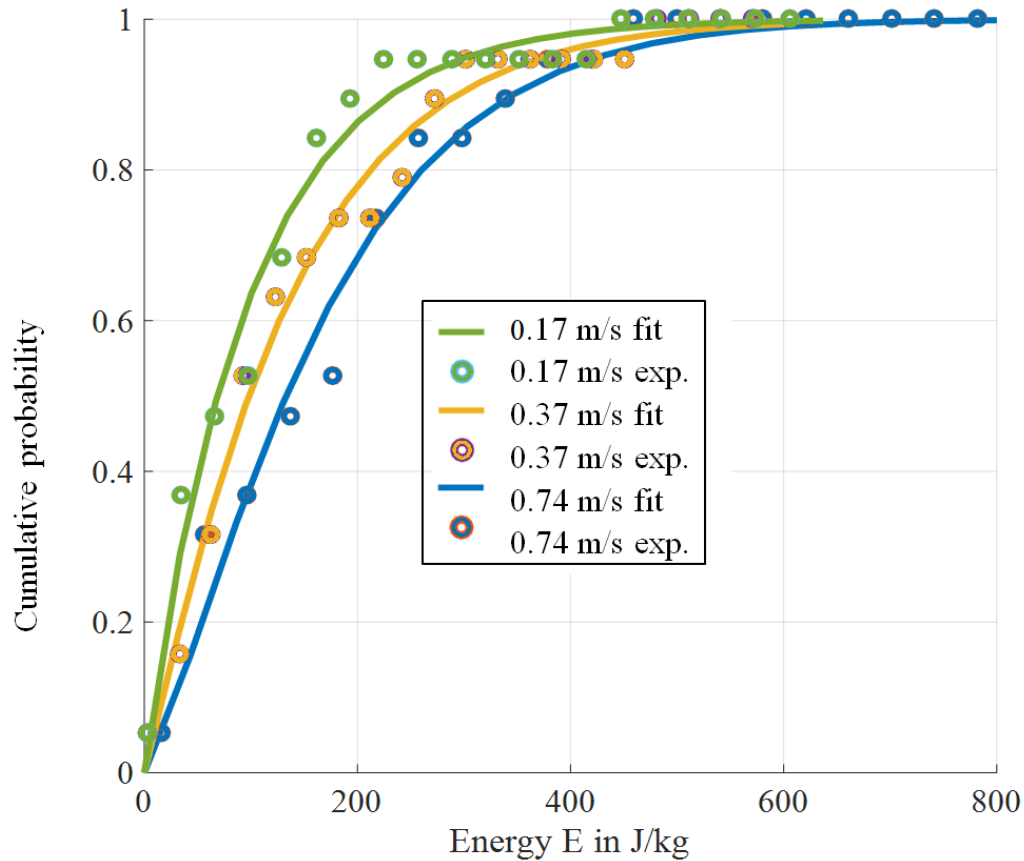
Figure 76:   Cumulative probability distribution of the breakage energy for irregularly shaped zeolite pellets produced at different rotational speeds.

Although the zeolite primary particles have lower mechanical strength compared to aluimina, and, consequently, are more likely to be exposed to undesired breakage, the produced pellets show improved breakage characteristics. This signifies that even for dominantly plastically deformable primary particles like zeolite [34], the added binder successfully joins those together and prevents any breakage during wall-particle collisions. In figure 77, typical force-displacement curves for irregularly shaped zeolite pellets produced at different rotational speeds are shown. It can be noticed that the force-displacement curves of the pellets produced at low rotational speed (0.17 m/s and 0.37 m/s) are not so smooth as for those produced at large rotational speed (0.74 m/s). Such behaviour was typical in this investigation for rather loose pellets. When the particles are weakly joined, there are more voids between them as discussed in section 6.5.4. As a result, when the compression starts, there is more of a chance that the pellets are rearranged. During the rearrangement, the primary particles are slightly moving into the hollow space of the structure and solid bridges are getting elastically deformed.

Due to the multiplicity of the process, it is not possible to only receive data for the elastic deformation of a single bridge. After the compactionm at a high speed, due to fewer defects like voids and hollowness, the pellets show a tendency to break straight off, following mostly elastic paths until the breakage point.
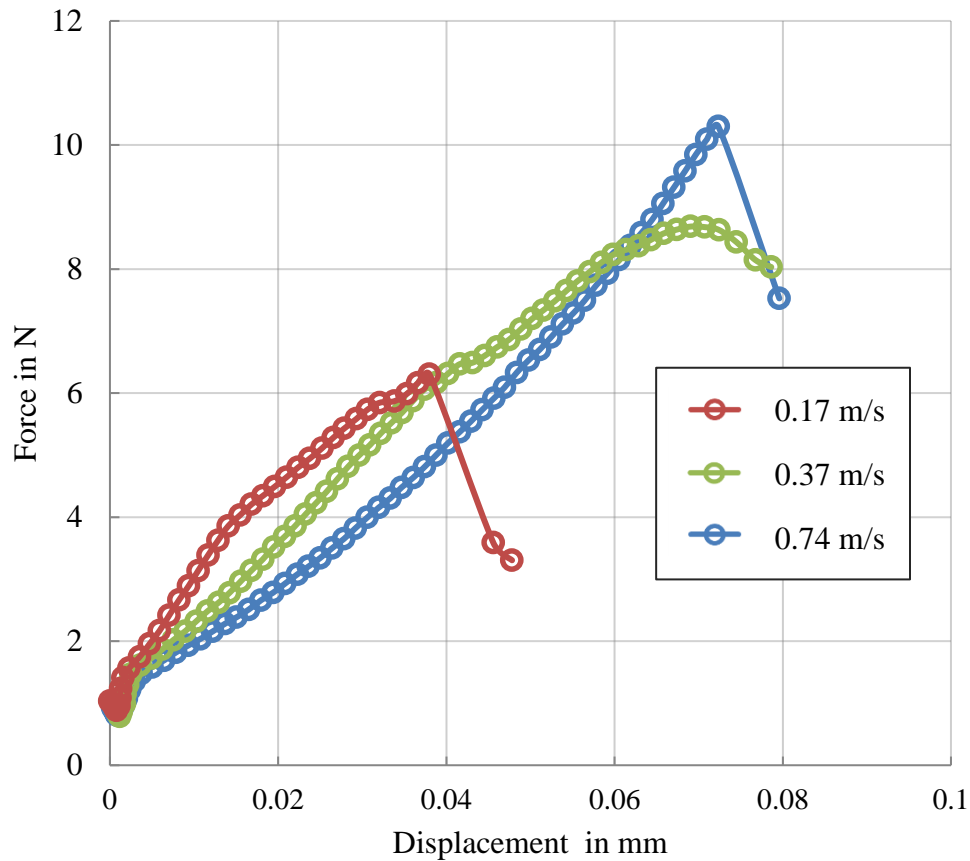
Figure 77:   Typical force-displacement curves for irregularly shaped zeolite pellets produced at different rotational speeds.

6.6.2.4. Influence of Binder Content on the Irregularly Shaped Zeolite Pellets

The next step in the characterisation of the zeolite pellets was to investigate the influence of the binder content on their mechanical strength. In figures 78 and 79, cumulative probability distributions of the breakage force, resp. the breakage energy, are shown for zeolite pellets produced with different binder contents. As already mentioned in section 6.1, the lower concentrated binder solutions were not able to form stable pellets and reliable results were only achieved with a binder amount higher than 0.053 g/g. Binder content over 0.109 g/g was also not suitable for pelletising due to the difficult dosage of the solutions. As shown in figure 78, the required breakage force decreases for pellets with higher binder content. The same trend holds true for the cumulative probability distribution of the breakage energy (figure 79). Table 32 summarises the results of the breakage probability investigation. Similar to the alumina

pellets, the overloading of the pellets with additional binder decreases thier strength. The increased plastic deformation, as a result of binder addition, can also be clearly seen from the typical force-displacement curves shown in figure 80. The typical force-displacement curve for pellets with a binder content of 0.053 g/g starts with an elastic deformation range, followed by a well-defined elastic-plastic region. The breakage is announced by a steep increase of the force.

Table 32: Mass-related breakage energy and breakage force for zeolite pellets produced with different binder contents.

Binder content φ_B in g/g	Average breakage energy E in J/kg	Average breakage force F in N	$s_{B\,in}$ mm	Mech. Strenght σ_B in MPa
Primary particles [35]	241.29 ± 123.25	23.8 ± 7.7	0.0502 ± 0.0127	11.72 ± 3.98
0.053	89.83 ± 120.33	14.33 ± 6.62	0.065 ± 0.030	7.65 ± 2.52
0.109	58.17 ± 110.58	7.46 ± 12.08	0.059 ± 0.028	6.31 ± 0.027

Table 33: Shape parameter a, slope b and coefficient of determination R^2 of the Weibull distribution for zeolite pellets produced with different binder contents.

Binder content φ_B in g/g	a in $(kg/J)^z\,m^{-2}$	b [-]	R^2 [-]
0.053	$11.823*10^{-3}$	1.435	0.9753
0.109	$8.138*10^{-3}$	0.8783	0.9295
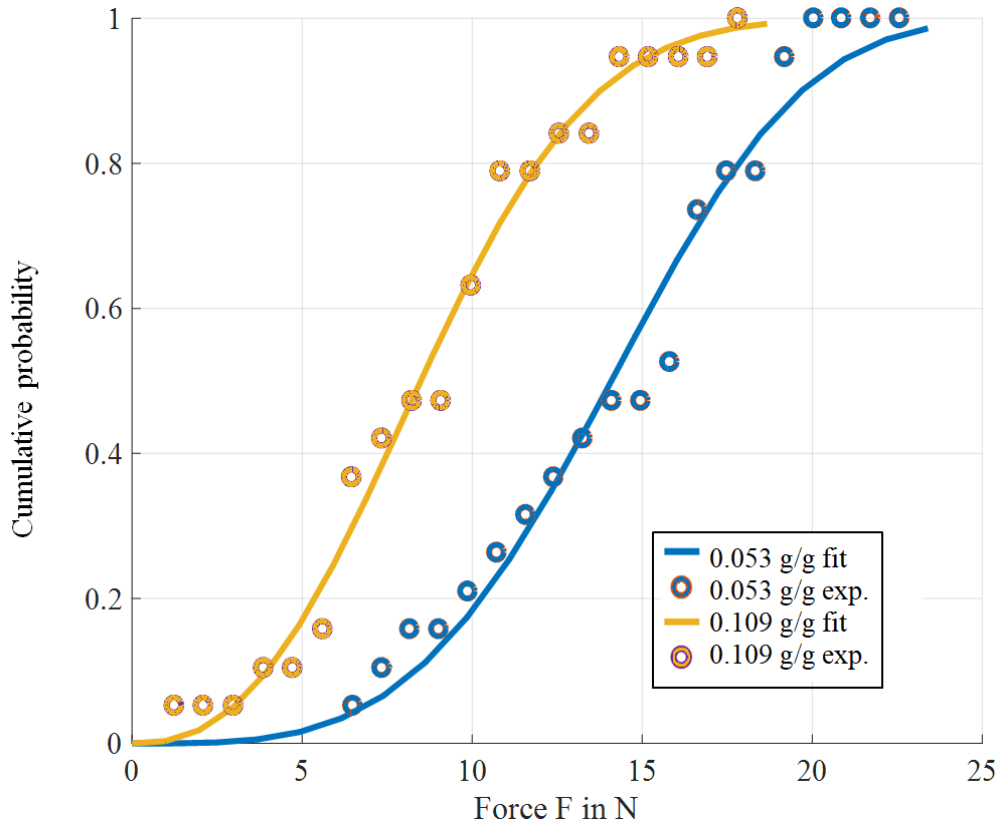
Figure 78: Cumulative probability distribution of the breakage force for irregularly shaped zeolite pellets produced with different binder contents.
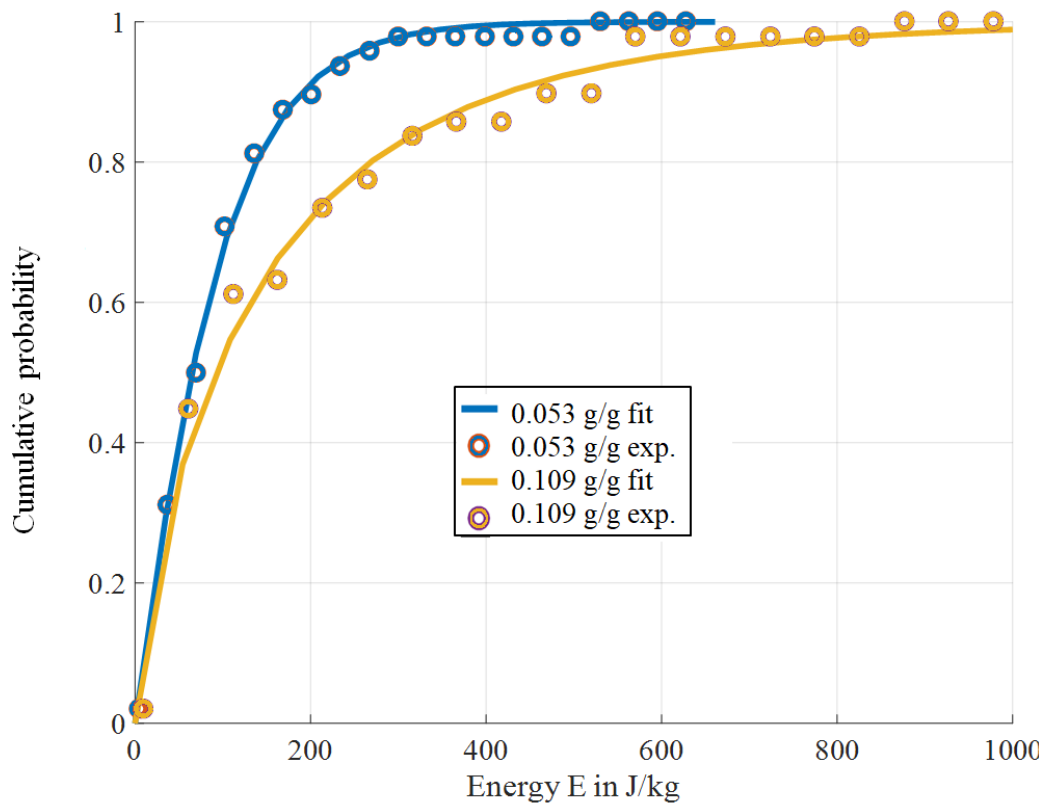
Figure 79: Cumulative probability distribution of the breakage energy for irregularly shaped zeolite pellets produced with different binder contents.
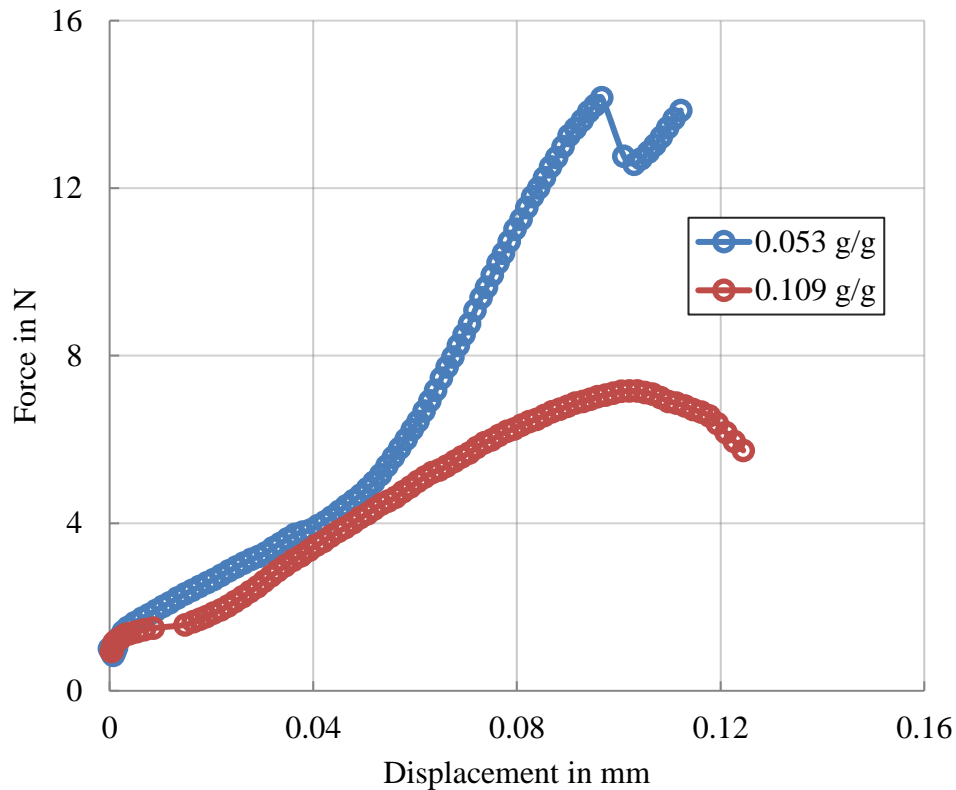
Figure 80:   Typical force-displacement curves for irregularly shaped zeolite
              pellets produced with different binder contents.

The overloading with binder of the pellets leads to decrease of the required breakage force and breakage resistance due to larger amount of easily plastically deformable binder in the pellets. As shown in figure 80, the breakage of pellets with larger binder content occurs not immediately but gradually. The reason for this behaviour is that the bridges do not break at once during the compression. During the elastic deformation, most of the bridges deform reversibly. Due to their low mechanical strength, the elastic deformation range is very small and soon after the loading force is applied, the single bridges start to yield. At that point, micro-cracks start to propagate through the bridges and even if there is no complete breakage, the occurring deformations are not reversible. If the loading continues to act, the bridge which is most closely positioned to the pellet's centre of mass (where the loading force has its maximum) is going to break.

The force does not drop down immediately because the rest of the bridges still counteract to the acting force. The average breakage force does not increase in the case of much added binder because it is a function of the elastic deformation of the primary particles and the plastic deformation of the bridges. When the binder fraction in the pellet increases, the plasticity of the pellet increases too and the pellet breaks more easily.

6.7. DEM Simulations of Irregular Pellet Compression Tests

A compaction of the model pellets at a large rotational velocity and a decrease of the surface roughness were reported by the image analysis in section 6.2 of this thesis. The experimental results show that pellets produced at large rotational velocities have larger mechanical strength as a result of the intensified and increased number of contact collisions. At the same time, increased binder content proved itself as a factor leading to a mechanical strength decrease due to an over-flooding of primary particles with an easily deformable binder. In both cases, the results are explained with changes in the model pellets caused by different solid bridges distribution through the primary particles. Despite of a detailed image and computer-tomographic analysis and because of the structures' variety, it was not possible to verify how exactly the pellet changes and which deformation within it is responsible for the mechanical properties variation.

It was, however, proved that the mechanical behaviour changes of model pellets are not caused by allocation of the primary particles in the pellet. The reasons for it should be searched in the changes of the formation of the solid bridges structures and in their distribution. To investigate this issue in detail DEM simulations were performed with the received and optimised primary particle coordinates of the CT-scans. The experimental compression tests were repeated using DEM for 20 to 30 various pellets from every batch (table 19), and experimental and simulated results were compared and thoroughly analysed. Different properties of the solid bridges were varied to investigate their influence and to compare them with the experiment results.

The input parameters for the particles and bonds are their densities, their strength and their modulus of elasticity (Table 2, Table 4 and Table 5 in chapter 5). The Possions ratio was fixed at 0.3. Detailed overview of the input data is given Attachment A, table A2 to table 4.

6.7.1. DEM Simulation of Irregular Pellets Compression with Two Different Maximal Bond Lengths

The first series of simulations was accomplished by varying the maximum allowed bond length between the primary particles. The increase of the maximal bond length leads to generation of more solid bridges between the primary particles. The experimental pellets were rebuilt in the simulation domain with the same number of primary particles and the same Euler-coordinates as known from the μ-CT results. The coorditates were added manualy and the system was adjusted to lie perpendicular to the stressing direction. The used maximal allowd bond lengths were 0.8 mm and 1.0 mm. The bond thickness was fixed at 0.8 mm. The received data from

simulated compression tests was represented in form of force-displacement curves. The simulated curves were compared with the experimental results. The statistic data for brekage force and specific breakage energy received from the simulations was compared with the results of the experimental studies.

6.7.1.1. DEM Simulations with Alumina Pellets and Two Different Bond Lengths

The first pellets rebuilt in the DEM software had alumina primary particles with a diameter of 1.0 mm. Their properties were previously specified as well as those of the used binder and the compression pistons as described in chapter 5. In figure 81 are given examples of simulated force-displacement curves of rebuilt pellets (18 primary particles) once with maximum bond length of 0.8 mm and once of 1.0 mm. The given maximum length of a solid bond between primary particles influences the pellets behaviour through the number of bonds created in a pellet during its rebuilding in the simulation programme. The solid bonds between the primary particles are 80 in the case of maximum bond length of 0.8 mm and 106 for maximum bond length 1.0mm. As is becomes clear from the graph, the increased number of the solid bonds leads to increase of the breakage force needed for pellet fracture. The limitation of bond length to 0.8 mm accumulates short solid bridges between all pellets having a centre distance less than 1.8 mm (particle diameter d + maximum bond length l_{b_max}). Overlapping of the bonds was allowed in order to take into account the influence of irregularly shaped solid bridges connecting more than two particles at the same time. Such structures have already been investigated by Dadkhah et al. [116]. They studied the morphology of the solid bridges in agglomerates and found that binder forms various structures between the primary particles, which are very different from the ideal solid bond. It was also proved that for agglomerates with large sizes, the binder spreads through the particles, forming a binder cluster. Because diverse bonds between the particles are merged, one can conclude that the binder distribution reminds of a bond network. By allowing an overlap between the bonds, the differentiation between the theoretical models presenting the solid bridges as ideal cylindrical connections and the real particle bonds should be minimised. In the case of maximum bond length 1.0 mm solid bonds are accumulated between all pellets having a centre distance less than 2.0 mm. One practically allows the simulation software to create connections between distant particles. Hence, the network of solid bridges connecting the single particles in the pellets gets denser, and, subsequently, the mechanical strength of the structure increases. The summarised results are given in table 34. The average breakage force for simulated pellets with a maximum bond

length 0.8 mm is 7.84 N. The received value for pellets with an increased maximum bond length is 18.51 N.
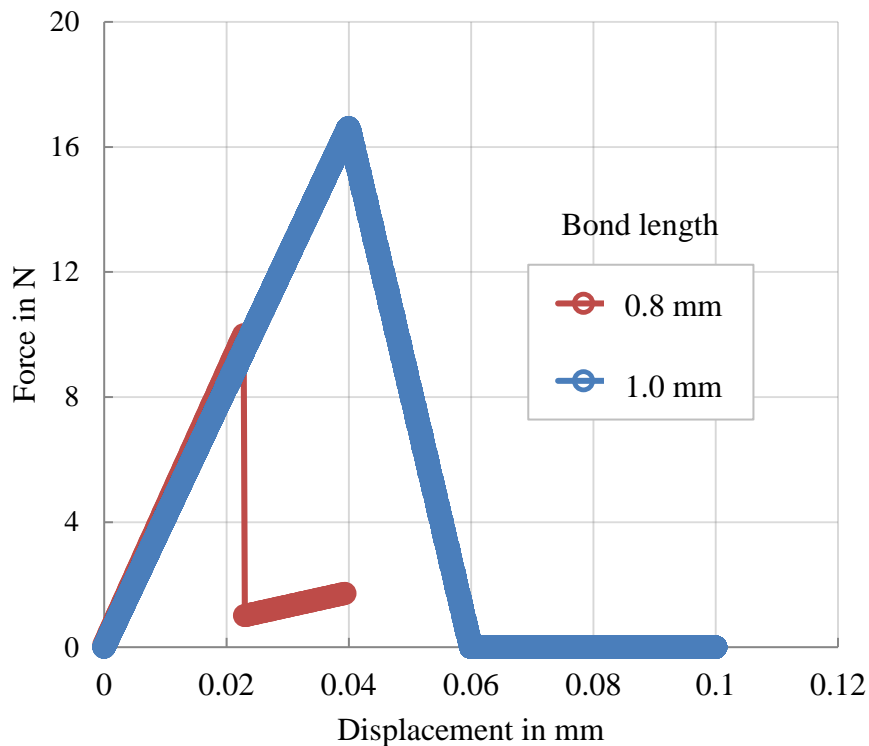
Figure 81:   Examples of simulated force-displacement curves for pellets with bond lengths of 0.8 mm and 1.0 mm.

Based on the approach that the densification of the solid bridge network in the DEM simulation leads to formation of stable pellets, one can compare the simulated results with the experimental ones received from the rotational velocity investigation, where the compaction of the structures as a result of intensified contact collisions also delivers more stable structures.

Figure 82 shows exemplarity experimental force-displacement curves of two pellets having also 18 primary particles, same as the pellet the coordinates of which were rebuilt in the simulation software. The pellets are from two different charges produced with two different rotational velocities. As already discussed in section 6.6.2.1, the structures produced with a higher rotational speed exhibit an increased mechanical strength and require more energy input for a breakage. The comparison between the average values of experimental and simulated results is given in table 34. The values of required breakage force for experimental pellets are 7.83 N for those produced at a rotational speed of 0.17 m/s and 18.10 N for those produced at a speed of 0.74 m/s. These values accord very well with the simulated results also listed in table 34. The slightly lower values of the experimental results can be explained with defects in the structures

of the real pellets, which cannot be anticipated before the experimental compression test and cannot be considered in the simulations.

Another important aspect is the comparison of force-displacement curves between simulations and experiments. As it gets clear from figure 81, the simulation curves exhibit mostly linear elastic-plastic behaviour. The primary breakage occurs spontaneously and is followed by a large drop of the applied force. The breakage of the experimental pellets also takes place in the elastic-plastic range, but the curves exhibit a much larger elastic deformation part (see figure 82). The curves also flatter more, which may be explained by local defects. The drop after primary breakage is not as drastic as in the simulations, which is justified by the different breakage progresses. While in the simulation the solid bridge practically "disappears" after its maximum breakage strength has been reached, the real solid bridges remain in the pellet structure after the breakage. These remnants are forward compressed and influence the further behaviour of the pellet.
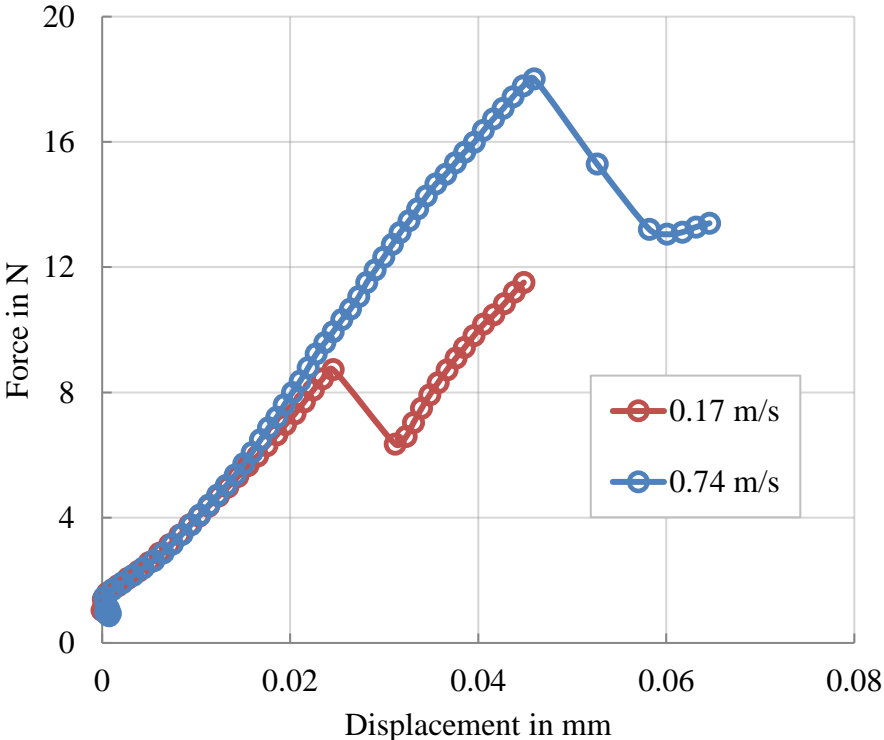
Figure 82: Examples of experimental force-displacement curve for pellets produced at a rotational speed of 0.17 m/s and 0.74 m/s.

Table 34: Comparison between breakage parameters for alumina primary particles, experimental pellets produced with different rotational speeds and simulated pellets with different bond lengths.

Mech. Parameter		Mass-related breakage energy E_{m50} in J/kg	Average breakage force F_{B50} in N	s_B in mm	Mech. strength σ_B in MPa
Primary particles [128]		1286.7 ± 209.9	37.68 ± 3.65	0.039 ± 0.037	47.67 ± 4.89
Solid bond length l_b in mm	0.8	586.78 ± 141.83	7.84 ± 4.66	0.037 ± 0.023	5.93 ± 3.22
	1.0	1170.01 ± 404.60	18.51 ± 10.25	0.0695 ± 0.088	9.45 ± 5.04
Rotational tip velocity v_r in m/s	0.17	427.11 ± 272.59	7.83 ± 2.73	0.091 ± 0.048	6.31 ± 2.27
	0.74	875.74 ± 537.58	18.10 ± 8.61	0.165 ± 0.012	12.46 ± 3.46

6.7.1.2. DEM Simulations with Zeolite Pellets and Two Maximum Bond Lengths

A further investigation of the maximum bond length influence on the mechanical characteristics is performed by rebuilding experimental pellets with zeolite primary particles. These primary particles are larger than the alumina particles, exhibit less porosity and have dominant plastic compression behaviour. The used maximum bond lengths were 0.8 mm and 1.0 mm. Bond thickness was 1.0 mm. In figure 83, two examples of force-displacement curves from simulated compression tests with zeolite pellet with 11 primary particles are shown. The blue curve represents a force-displacement distribution for zeolite pellet with a maximum bond length of 0.8 mm. The generated bonds between the primary particles are 31. As listed in table 41, the average breakage force for the pellets with maximum bond length of 0.8 mm is about 6.83 N. Increased maximum bond length leads to formation of more solid bridges (in the showed case – 38 solid bridges) and the pellet breakage strength increases – for pellets with maximum bond length of 1.0 mm, the breakage force increases to 9.12 N. The red distribution in figure 83 shows the force-displacement curve of a pellet with 1.0 mm maximum bond length. Similar to the alumina particles, the increased density of the bond network increases the pellet strength. Therefore, the results are compared with experiments about the influence of rotational velocity on the properties of the model pellets. In figure 84, force-displacement curves from the experimentally tested pellets with the 11 primary particles are given.
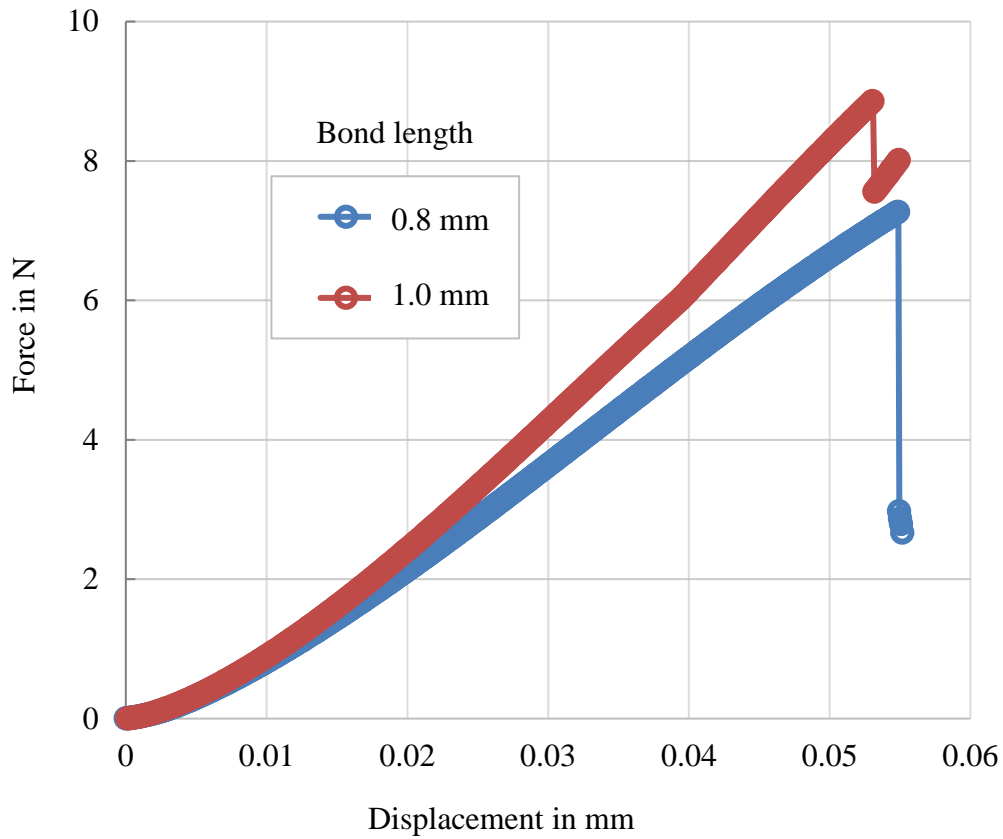
Figure 83:   Examples for simulated force-displacement curve for zeolite pellets with
              two bond lengths.
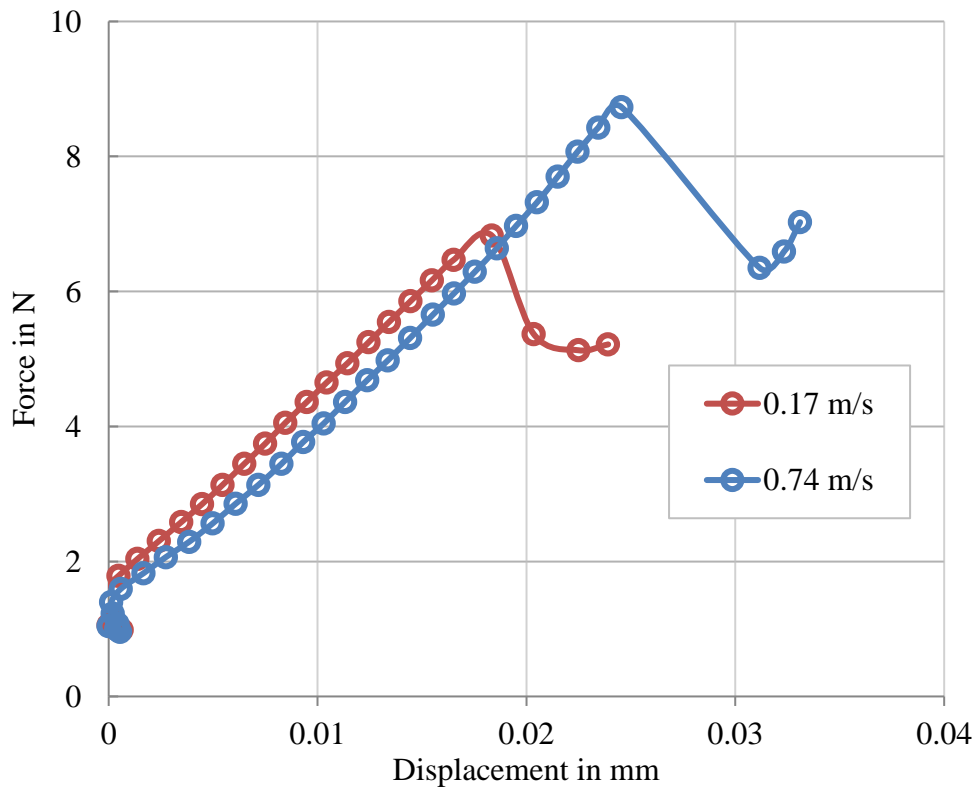
Figure 84:   Examples for experimental force-displacement curve for zeolite pellets with
              two different maximum allowed bond lengths.

As already reported in section 6.6.2.3 the breakage force required for pellet fracture increases with the increase of the rotational speed. The values from simulations and experiments are summarised and compared in table 35. As one can see, the values received from simulations and experimental force-displacement propagations are very similar.

The received simulation curves are smooth. They have a defined elastic range followed by an elastic-plastic part where the primary breakage takes place. The curve representing the breakage pattern of pellets with increased maximum bond length exhibits a larger elastic range. The experimental curves follow similar propagations. In the case of pellets produced with a rotational speed of 0.74 m/s, the distribution has a large elastic deformation part followed by an elastic-plastic range and a primary breakage. The distribution of the pellets produced with 0.17 m/s has a more elastic-plastic character, similar to the simulation curve.

Table 35: Comparison between breakage parameters for zeolite primary particles, experimental pellets produced with different rotational speed and simulated pellets with two bond lengths.

Mech. Parameter		Mass-related breakage energy E_{m50} in J/kg	Average breakage force F_{B50} in N	s_B in mm	Mech. strength σ_B in MPa
Primary particles [35]		241.29 ± 123.25	23.8 ± 7.7	0.0502 ± 0.0127	11.72 ± 3.98
Solid bond length l_b in mm	0.8	86.78 ± 41.83	6.83 ± 1.56	0.0386 ± 0.013	1.76 ± 0.405
	1.0	140.85 ± 53.65	9.12 ± 4.84	0.0544 ± 0.017	2.87 ± 1.523
Rotational tip v_r velocity in m/s	0.17	89.24 ± 28.46	6.822 ± 4.82	0.0457 ± 0.0274	1.62 ± 1.60
	0.74	163.90 ± 70.58	9.084 ± 4.40	0.0898 ± 0.0158	2.76 ± 1.35

6.7.2. DEM Simulation of Irregular Pellets Compression with Two Different Bond Thicknesses

Another possibility to investigate the influence of the bond properties on the pellet behaviour is to vary the bond thickness and to see how this parameter changes the pellet compression characteristics. The next two simulation cycles were conducted using the same primary particle coordinates (for alumina resp. zeolite charges) and primary particle number but with two different bond thicknesses: 0.8 mm and 1.0 mm bond diameter. A precise measurement of the contact surface between particle and binder was not possible, so values were chosen which are partially arbitrary and partialy supported by results from image analysis. In the cases of increased binder content in the experimental batches, alumina primary particles were covered with binder and no longer recognisable from the complete structure of the pellet. This effect was achieved in the simulation for alumina with a bond diameter of 1.0 mm. Hence, the alumina particles are completely captured by the binder as shown by the image analysis (figure 44). Such an effect was not observed for zeolite, but due to the same binder content in the pellets the bond thickness was kept constant. Like in the previous simulation cycles, the received data was summarised and represented in the form of force-displacement curves. The statistical data for breakage force and specific breakage energy was compared with experimental results. Exampe of simulated alumina model pellet once with bond diameter of 0.8 mm and once with bond diameter of 1.0 mm is shown in figure 85.

a)

b)
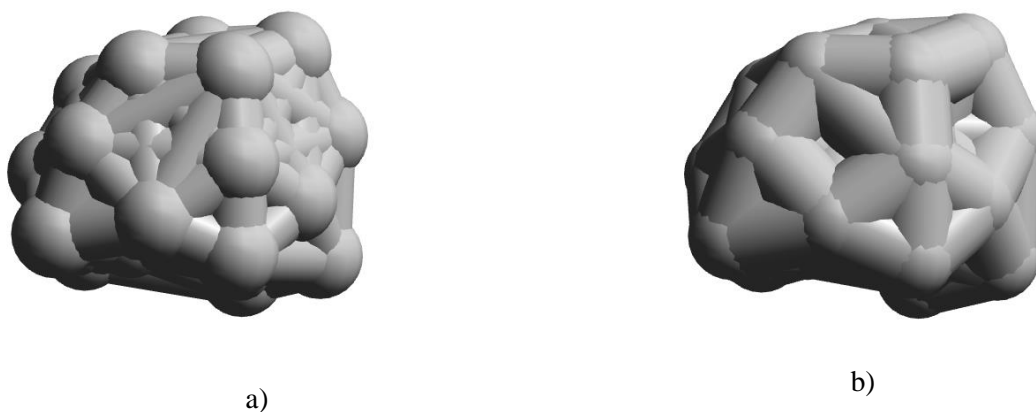
Figure 85: Example of simulated alumina pellets with 22 primary particles with diameter of 1.0 mm and bond diameterc of a) 0.8 mm and b) 1.0 mm.

6.7.2.1. DEM Simulations with Alumina Pellets and Two Different Bond Thicknesses

Alumina pellets with a primary particle diameter of 1.0 mm, maximum allows bond length of 0.8 mm, average primary particle number N_p of 22, average 88 solid bonds and two different

bond thicknesses – 0.8 mm and 1.0 mm were simulated in the second cycle of DEM investigation. Figure 86 shows examples for force-displacement distributions for simulated pellets with two different bond thicknesses. There is very little variation between the values for the primary breakage as summarised in table 36: pellets with a bond diameter of 0.8 mm break at 9.72 N and those with a bond diameter of 1.0 mm at 10.56 N. The values for pellets with larger bond diameters are slightly larger. The increased bond diameter is directly correlated with the bond strength [70] and, therefore, with an increased bond diameter, the pellets' strength increases as well. The main difference between the simulated curves is their form, where the 0.8 mm bond curve has a larger elastic range. As described in section 6.6, the behaviour of the pellet is a result of the mechanical behaviour of the primary particles and the binder. In the experimental results with less binder, the behaviour of the pellet is dominated by the elastic deformation of the primary particles. By increasing the binder, the elastic-plastic range enlarges due to the plastic deformation of the binder. Corresponding experimental curves from model pellets with 22 primary particles are given in figure 87. They exhibit the same trend of elastic-plastic range as the simulated curves, although the curve for the pellet with a binder content of 0.109 g/g differs from the typical force-displacement propagation for those pellet batches (figure 81). The experimental curves show different trendes for an increased amount of solidified binder.
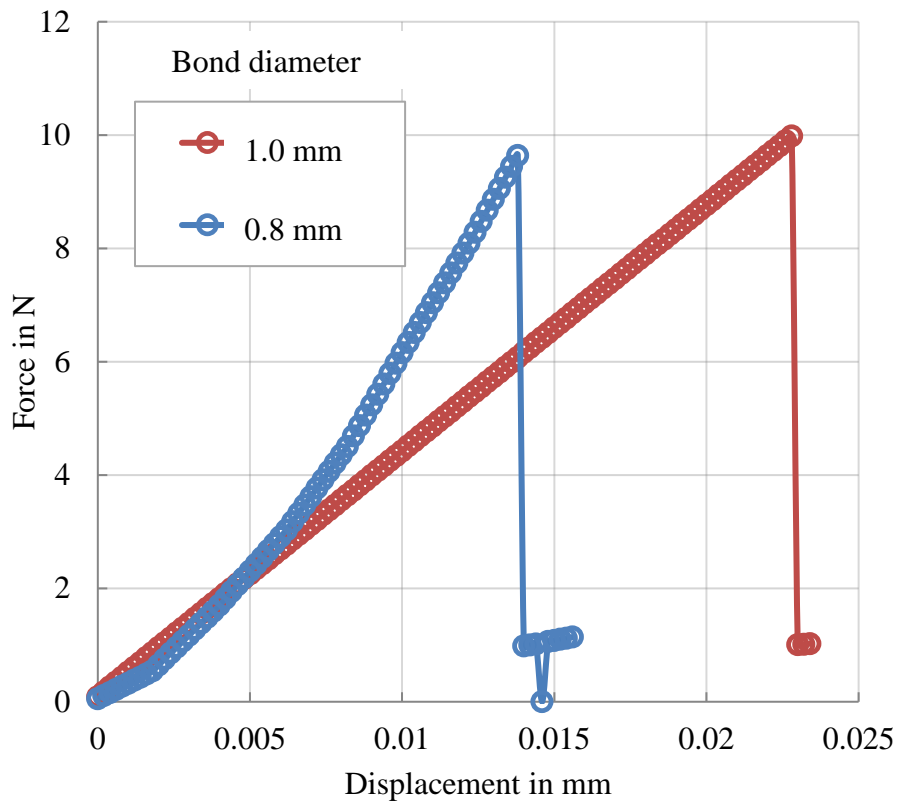
Figure 86:   Examples of simulated force-displacement curves for alumina pellets with a bond thickness of 0.8 mm and 1.0 mm.
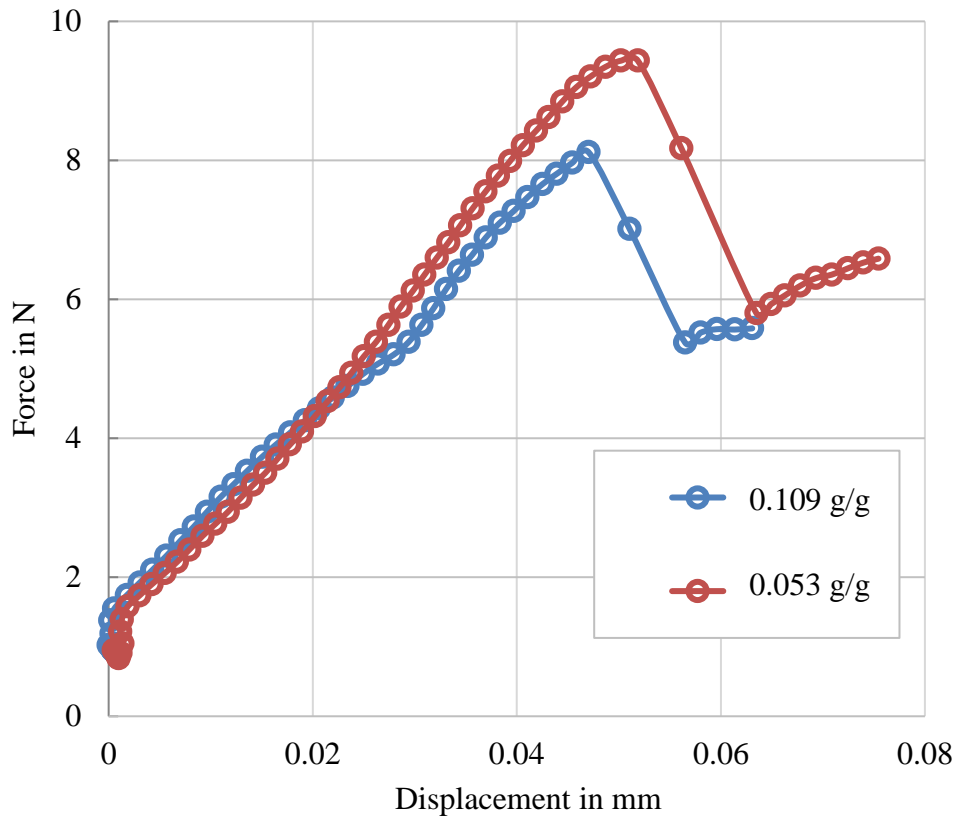
Figure 87:   Examples of force-displacement curves for alumina pellets produced with binder content of 0.109 g/g and 0.053 g/g

Table 36: Comparison between breakage parameters for alumina primary particles, experimental pellets produced with different binder contents and simulated pellets with two bond thicknesses.

Mech. Parameter		Mass-related breakage energy E_{m50} in J/kg	Average breakage force F_{B50} in N	s_B in mm	Mech. strength σ_B in MPa
Primary particles [128]		1286.7 ± 209.9	37.68 ± 3.65	0.039 ± 0.037	47.67 ±4.89
Solid bond thickness in mm	0.8	257.24 ± 154.76	9.72 ± 2.48	0.042 ± 0.034	5.79 ± 1.19
	1.0	844.92 ± 166.39	10.56 ± 2.70	0.056 ± 0.049	9.28 ± 1.511
Binder content φ_B in g/g	0.027	591.23 ± 120.33	10.56 ± 12.08	0.069 ± 0.034	8.68 ± 3.055
	0.109	46.27 ± 28.46	8.66 ± 5.36	0.088 ± 0.038	6.31 ± 0.027

6.7.2.2. DEM Simulations with Zeolite Pellets and Two Different Bond Thicknesses

The bond thickness influence was also investigated for zeolite pellets with a primary particle diameter of 1.75 mm, maximum allowed bond length of 0.8 mm, average number of primary particles of 10 and 30 solid bonds between the primary particles. In figure 88, examples of force-displacement curves for two pellets with different bond thicknesses are shown. As it becomes clear from the graph, the increased bond diameter leads to an increase of the required breakage force. The form of the force-displacement curves is similar – both have a well-defined elastic range followed by an elastic-plastic part where the primary breakage takes place. The force-displacement curves of experimental pellets with the same primary particle number – 10 are given in figure 89. It can be seen that the force-displacement curves differ a lot from the simulated curves. The presence of defects and voids in the experimental pellets can explain these differences. The overview of average values for simulated and experimental pellets is given in table 37 and compared to those for primary particles. The overloading with binder leads to a reduction of the required breakage force in the experiments. The results show that the increase of the binder content in pellets cannot be represented as a bond with larger diameter, so that a comparison between the simulation results and the experiment is in this case not adequate. The reasons for these different results should be searched in the micro-porosity of the binder brigdes described by Dadkhah et al. [116]. The simulation software takes the bonds as solid material, which differs from the experimental case. The micro-porosity of the bridges reduces their strength and is combined with defects within thier structure, which leads to deviation from the ideal case. The software cannot represent a system with overdosage of

binder, due the software restriction that the bond diameter cannot be larger than the smallerst diameter of a contact partner.
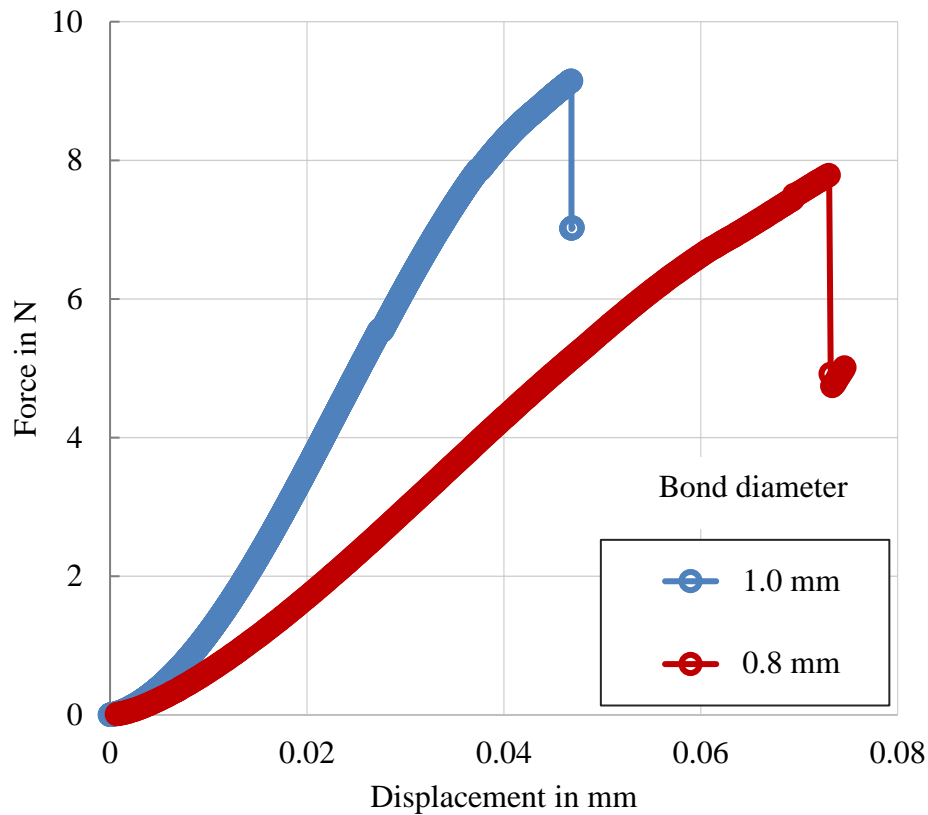
Figure 88: Examples of simulated force-displacement curves for alumina pellets with bond diameter of 1.0 mm and 0.8 mm.

Table 37. Comparison between breakage parameters for zeolite primary particles, experimental pellets produced with different binder contents and simulated pellets with two bond thicknesses.

Mech. Parameter		Mass related breakage energy E in J/kg	Average breakage force F in N	s_B in mm	Mech. strength σ_B in MPa
Primary particles [35]		241.29 ± 23.25	23.8 ± 7.7	0.0502 ± 0.0127	11.72 ± 3.98
Solid bond thickness in mm	0.8	166.39 ± 144.92	7.72 ± 2.48	0.038 ± 0.032	5.28 ± 1.511
	1.0	257.24 ± 154.76	9.56 ± 1.97	0.042 ± 0.032	6.79 ± 1.19
Binder content φ_B in g/g	0.053	211.83 ± 120.33	14.33 ± 6.62	0.065 ± 0.030	7.65 ± 2.52
	0.109	158.17 ± 110.58	7.46 ± 12.08	0.059 ± 0.028	6.31 ± 0.027
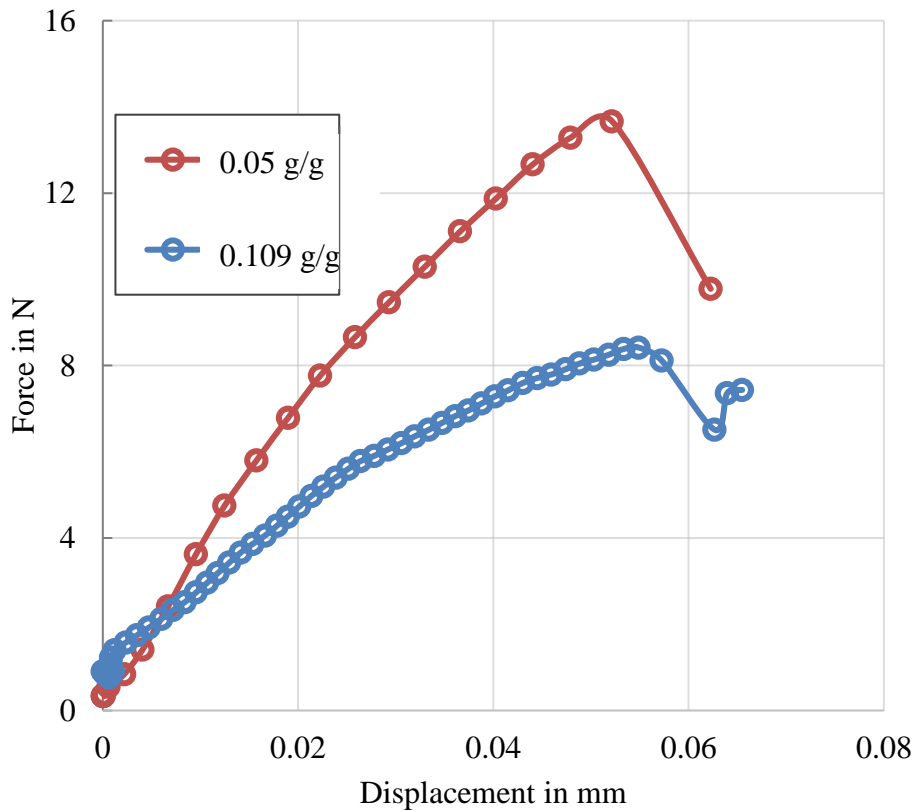
Figure 89:   Examples of experimental force-displacement curves for alumina pellets produced with binder content of 0.05 g/g and 0.109 g/g m/s.

6.7.3.   Overview of Simulation Results

Results from the simulations performed in the frame of this thesis show a good agreement with the experimental results. The investigation of the influence of the bond length between primary particles showed that an increased maximum length contributes to the formation of stable pellets by adding more bonds between the primary particles and by densifying the bond network within the pellet. The comparison with pellets produced with two different velocities, where the pellets are densified due to the increased contact collisions, showed a very good agreement. These results were confirmed for both investigated types of pellets with alumina and with zeolite primary particles.

The bond diameter is directly correlated to the breakage strength of the pellet, and its increase leads to formation of stable pellets. Increasing the maximum diameter of the bond, one practically adds more binder material to the pellets. Thus, the results on bond thickness influence were compared to experimental results of pellets with increased binder content. The comparison showed a different trend for simulated and experimental results. The reasons for this are the micro-porosity of the solid bridges and the lack of possibility to represent an over-

dosage of binder in the simulations. No simulations of the breakage behaviour of tetrahedra we made. Their breakage behaviour was investigated and simulated by Müller et al. [146].

7. Conclusion

Two experimental pelletisation series were accomplished in the frame of this thesis. The first series was performed using single alumina granules as primary particles and the second one with zeolite granules. Three main parameters were varied during the size enlargement to investigate their influence on the pellet breakage behaviour, the rotational speed, the binder content and the processing time. After pelletising and drying at atmospheric conditions, the produced alumina pellets were separated in two fractions, tetrahedron-shaped and irregularly shaped. They were analysed separately and the results were compared to investigate the influence of the pellet shape on the mechanical behaviour. Tetrahedron-shaped pellets in the zeolite batches were either very few or unstable, and, therefore, unsuitable for a further analysis. The reason for the lack of tetrahedra may be the small fracture strength of the primary particles. This fact was not investigated in detail and should be analysed in future research.

Using image analysis, light and electron scanning microscopy, the morphology of the pellets was investigated. No visible changes were found between the regularly shaped pellets of different batches. The increased rotational velocity increases the primary particle breakage due to stronger contact collisions. The binder content seems to have no influence on the pellet condition. All irregular pellets are blackberry-shaped exhibiting a large surface roughness.

The pellet size distribution was also characterised to find differences among pellets produced with different process parameters. The regular pellets (tetrahedra) with the same primary particles from all the pelletising charges exhibit similar size distributions. The change of the binder content and the rotational velocity has no influence on the structures due to their similar formation. The sphericity values for all the charges are similar as well. The main difference between the tetrahedra is their coordination angle.

The size distribution of irregular alumina pellets showed that increase in the rotational velocity of the pelletiser bottom plate and larger binder content enhance the formation of large alumina pellets. The rotational velocity has no influence on pellet sphericity. Pellets with larger binder content have higher sphericity due to the deformability of the polymer binder.

For zeolite pellets, increase of the rotational velocity from 0.17 m/s to 0.74 m/s does not lead to any significant changes in pellet size. The high rotational velocity causes higher losses of zeolite primary particles. At high velocities, the primary particles are more likely to get crushed in the pelletization and fall into the gap between the plate and the wall. The sphericity of the

obtained pellets does not change significantly with the increase of the rotational velocity. The mean diameter of pellets produced with a binder content of 0.053 g/g is larger than that the pellets produced with a binder content of 0.109 g/g. In addition, the particle size of the pellets that are produced with 0.109 g/g binder content exhibits a narrower distribution. At the same time, pellets with larger binder content are more spherical. These differences in the size distribution and sphericity between pellets of alumina and zeolite can be explained firstly with the larger primary particle diameter of the zeolites and secondly with their different mechanical strength. Due to these reasons, the granules behave differently during pelletising.

The density and porosity of the regularly shaped pellets was investigated for batches produced with different binder contents. No significant changes were found between the batches despite of the increased fraction of binder in the pellet structure. This result can be explained with the relative low density of the binder compared to primary particles.

For irregularly shaped pellets, the difference in porosity was analysed for batches produced at different rotational velocities and binder contents. It was found that increased speed has no influence on the porosity. In all of these cases, the values are slightly lower than the porosity of the primary particles. The same effect has the increased binder content in the structures.

The next step in pellet analysis was to conduct µ-CT scans of pellets with similar size from various batches. The coordinates of their primary particles were extracted and topographical characteristics were investigated. Average numbers of primary particles were estimated for both investigated pellet types, alumina and zeolite. The analysed size fraction was from 1.5 mm to 3.5 mm. It was found that for the zeolite, due to the larger diameter of the primary particles ($d_{50,3} = 1.75$ mm), the pellets have a smaller average number of primary particles. No significant differences were found in primary particle number for pellets from batches carried out at different processing conditions. The average number of primary particles in the pellets did not change at increased rotational velocity, processing time or binder content.

The results show that the densification of the structures is not due to an increased number of primary particles in the pellets, but results from changes in binder distribution, solid bridges build-up and primary particle fragmentation. The estimation of the radius of gyration showed than there are no noticeable differences among pellets from different batches. This underlines that changes in pelletising process parameters do not influence the overall fragmentation of the pellets. The volumetric porosity was calculated for the pellets by three methods, from an equivalent radius, convex hull and dilation. There is a good agreement of porosities measured

with different methods for both alumina and zeolite pellets. There was no trend testified among pellet porosities from different batches. Besides, the fractal dimension D_f, the pre-factor K_g, the average coordination number and the coordination angle were calculated for alumina and zeolite pellets. In none of the investigated cases was an influence of the pelletising process parameters noticed.

The conclusion from the topographical investigation is that process parameters do not influence the coordination and the arrangement of the primary particles in a pellet. Their influence is introduced by the interaction between primary particles and the binder.

Produced pellets were subsequently subjected to a quasi-static compression test to investigate their behaviour under stress. Firstly, the regular tetrahedra were compressed until breakage and their breakage behaviour was analysed. For the pellets with a primary particle size of 1.0 mm, a clear upward trend was noticed for the required breakage force and breakage energy with increasing binder content. It was also testified that the breakage of pellets produced with small binder content occurs in a brittle way. In case of high binder content, the force propagates mainly through the binder, which leads to plastic breakage. Compared with the primary particles, the pellets exhibit a lower breakage force, and resp. breakage energy. Primary particles are fine-grained and strongly bonded. They have less, smaller and uniformly distributed structural defects so that they are stronger. The almost ideally spherical shape of the primary particles also contributes to their mechanical stability.

The next step was to analyse the behaviour of the tetrahedra with larger primary particle size of 1.8 mm. There, pellets produced with a binder content of 0.053 g/g have the highest breakage force, resp. they need the largest specific energy to fail. It seems that after reaching optimum binder content, the following binder addition does not lead to an increase of breakage strength. Compared to the pellets with a primary particle diameter of 1.0 mm, these pellets require more force to break. An explanation of this result may be force propagation occurring through the large primary particles instead of through the easily deformable bridges.

Another important observation was made during the experimental compression procedure. Independently of the primary particle diameter, the failure of tetrahedron-shaped pellets strongly depends on the angle between their primary particles. Pellets with obtuse angles break smoothly, whereby the primary particles move away from each other. The bridges between them suffer under tensile stress and break when their maximum mechanical strength is reached. If there are different types of angles between the primary particles, the bridge between those having the most acute angle will break first. Moreover, if the angles in a pellet are acute, the

probability of primary particle breakage increases due to the stress accumulation on the top particle.

The compression behaviour of the irregularly structured pellets was investigated next. It was proved that increase in the rotational velocity leads to formation of more stable alumina pellets, requiring more breakage force, resp. breakage energy, for a fracture. The single primary particles exhibit again larger values for both parameters.

The force required for breakage of a pellet decreases with increasing binder content in the alumina pellets. This result can be explained with the increased fraction of solidified binder within the structure of the pellet, having much less breakage strength than the primary particles. The values of breakage force and breakage energy of the pellets are much lower than for the alumina primary particles, and also lower than those for regularly shaped pellets (tetrahedra). The strong decrease in breakage force shows the importance of pellet shape when it comes to breakage by compression.

For zeolites, increased rotational speed leads to formation of structures with improved mechanical strength. Fierce collisions cause a compaction of the pellet which decreases defects in the structure (voids and hollowness), so that the breakage resistance of the product increases. The zeolite model pellets show improved breakage characteristics, although the zeolite primary paritlces have low mechanical strength and, consequently, are more likely to break. This signifies that the added binder successfully joins together even dominantly plastically deformable primary particles like zeolite and prevents thier breakage during wall-particle collisions.

The next step in the characterisation of the zeolite pellets was to investigate the influence of binder content on their mechanical strength. The required breakage force decreases with the addition of binder to the zeolite primary particles. More binder leads to a decrease of the required breakage force and breakage resistance due to the larger amount of easily plastically deformable material in the pellets. The average breakage force does not increase in the case of more added binder because it is a function of the elastic deformation of the primary particles and the plastic deformation of the bridges. When the binder fraction in the pellet increases, the plasticity of the pellet increases too and the pellet breaks easily.

To investigate in detail the pellet compression behaviour, DEM simulations were performed with primary particle coordinates from received and optimised CT-scans. Experimental compression tests were repeated using DEM, and experimental and simulated results were compared and analysed. The length and the thickness of the solid bridges were varied to investigate their influence and to compare it with the experiment results.

Simulations were made using two bond lengths: 0.8 mm and 1.0 mm. For both investigated pellets, alumina and zeolite, increased bond length leads to an increase of pellet strength. This result was explained with the overlapping of the bonds. The length of solid bonds between primary particles influences pellet behaviour through the number of bonds created when rebuilding the pellets in the simulation programme. The overlapping of bonds allows to take into account the influence of irregularly shaped solid bridges connecting more than two particles at the same time. By allowing an overlap between the bonds, the difference between the theoretical notion of solid bridges as ideal cylindrical connections and real particle bonds should be minimised. Hence, the network of solid bridges connecting the single particles in the pellets gets denser, and, consequently, the mechanical strength of the structure increases. Based on the approach that densification of the solid bridge network in the DEM simulation leads to formation of stable pellets, the results were compared to experimental ones received from the rotational velocity investigation, where the densification also delivers more stable structures. The comparison between the experimental and the simulated results showed good agreement. Slightly lower values of the experimental results were explained with defects in the structure of real pellets, which cannot be anticipated before the experimental compression test and cannot be considered in the simulations.

The investigation proceeded with analysis of the bond thickness influence on the pellet compression behaviour. Simulations were conductedd using the same primary particle coordinates (for alumina resp. zeolite charges) and primary particle number, but with different bond diameter of 0.8 mm and 1.0 mm. In the simulations for both pellet types, alumina and zeolite, increased bond diameters leads to increased breakage strength. Despite of the attempt to compare the simulation and the experimental results, they showed different trends. The increase of binder content in pellets cannot be represented as a bond with increasing diameter and a comparison between the simulation results and the experiments is not appropriate in this case. The reason for these results is that the simulation software takes the solid bonds as ideal cylindrical bonds without any defect and micro-porosity. The software also cannot represent a system with overdosage of binder because of the restriction that the bond diameter cannot be larger that the diameter of the contact partner.

8. Outlook

One of the main difficulties during the preparation of this thesis was the lack of theoretical models to describe the interactions between the primary particles in irregularly shaped pellets during breakage. The usage of probability distributions can be useful for describing the mechanical properties, but has its flaws. For example, due to the various shapes of the pellets, the results have large standard deviations.

The future of particle breakage behaviour investigations is undoubtedly in the further development of process simulations. Due to the complicated structure of irregularly shaped pellets and agglomerates, the rebuilding procedure of simulated systems is long and time-consuming. Even after a careful study of solid bridges structure and arrangement in the pellets, it was extremely difficult to rebuild those large numbers of bridges in the simulation domain. Future work on simulations should include an improvement of both particle and bond generation.

Using results from this thesis, future work on developing models able to describe inter-particle interactions in pellets should continue and contribute to a better understanding of the pellet breakage.

References

[1]   Müller, P., Antonyuk, S., Tomas, J., Heinrich, S. (2011). Ermittlung der normalen und tangentialen Stoßzahl von Granulaten, Chem. Ing. Tech., Vol. 83(5), 638-642.

[2]   Müller, P., Horbach, S., Antonyuk, S., Heinrich, S., Tomas, J. (2011). Untersuchung des schiefen Stoßes von drei charakteristischen Granulaten, Chem. Ing. Tech., Vol. 83(5), 612-617.

[3]   Bauer, H. (1980). Report on investigations on particle movement in straight horizontal tubes, particle/wall collision and erosion of tubes and tube bends, Powder Bulk Solids Tech., 4, 3-12.

[4]   Antonyuk, S. (2006). Deformations- und Bruchverhalten von kugelförmigen Granulaten bei Druck- und Stoßbeanspruchung, Dissertation, Otto-von-Guericke-Universität Magdeburg, docupoint Verlag.

[5]   Schubert, H. (1984). Aufbereitung fester mineralischer Rohstoffe: Entwässern, Mischen, Lagern, Fördern, Probenahme u. a., Leipzig, VEB Deutscher Verlag für Grundstoffindustrie

[6]   Pietsch, W. (1991). Size enlargement by agglomeration, Chichester, UK, John Wiley & Sons/Salle.

[7]   Rumpf, H. (1972). Haftung und Festigkeit von Agglomeraten, Pharm. Ind., Vol. 34, 270-281.

[8]   Salman, A. D., Gorham, D. A. (2000). The fracture of glass spheres, Powder Technology, Vol. 107, 179-185.

[9]   Iveson, M. S., Litster, J. D., Hapgood, K., Ennis, B. J. (2001). Nucleation, rowth and breakage processes: A review, Powder Technology, Vol. 117, 3-39.

[10]   Reddy, J. N. (2006). An Introduction to the finite element method, Boston, McGraw-Hill, Inc.

[11]   Capes, C. (1980). Particle size enlargement, Baton Rouge, LA, Elsevier Scientific Pub. Co.

[12]   Köster, D. (2012). Spheronization Process - Particle Kinematics and Pellet Formation Mechanisms Dissertation, Düsseldorf, Heinrich Heine Univestiät Düsseldorf.

[13]   Pietsch, W. (2008). Agglomeration Processes, Wiley/VCH.

[14]   Kapur, P. (1977). Role of similarity size spectra in balling and granulation of coarse, liquid deficient powders, Proc. of Symp. on Agglomeration, 156-175.

[15]   Ouchiyama, N., Tanaka, T. (1974). Mathematical model in the kinetics of granulation, Industrial & Engineering Chemistry Process Design and Development, Vol.13, 383-389.

[16]   Ouchiyama, N., Tanaka, T. (1980). Kinetic analysis and simulation, Industrial & Engineering Chemistry Process Design and Development, Vol. 21, 29-35.

[17]   Kozicki, C., Carison, C. (2008). Principles Of Using A Pelletizer, FEECO International, Green Bay, USA, Retrieved from https://feeco.com.

[18] Bhandari, B., Bansal, N., Zhang, M., Schuck, P. (2013). Handbook of Food Powders: Processes and Properties, Elsevier.

[19] Green, D., Perry, R. (2007). Perry's Chemical Engineers' Handbook, 8th Ed. McGraw-Hill.

[20] Sherrington, P. J., Oliver, R. (1981). Granulation, London/Philadelphia/Rheine, Heiden & Son Ltd.

[21] Liu,Y., Gonzalez, M., Wassgren, C. (2018). Modeling granular material blending in a rotating drum using a finite element method and advection-diffusion equation multi-scale model, AIChE Journal, Vol, 64(9), 3277-3292.

[22] Cantor, S., Augsburger, L., Hoag, S., Gerhardt, A. (2008). Pharmaceutical Granulation Processes, Mechanism and the Use of Binders, DOI: 10.1111/bjet.12103.

[23] Habenicht, G. (2009). Kleben: Grundlagen, Technologien, Anwendungen, Berlin, Springer.

[24] Tomas, J. (2009). Mechanical process engineering, Otto-von-Guericke-Universität Magdeburg, Retrieved from http://www.mvt.ovgu.de/.

[25] Hintz, W., Tomas, J. (2012). Influence of process parameters on particle size and morphology of nano-scaled magnetite particles, Prag, Tschechische Republik, 20th International Congress of Chemical Engineering CHISA 2012.

[26] Litster, J., Ennis, B. (2004). The Science and Engineering of Granulation Processes, Dordrecht, Springer Netherlands.

[27] Stieß, M. (2009). Mechanische Verfahrenstechnik - Partikeltechnologie, Berlin/Heidelberg Springer-Verlag.

[28] Tomas, J. (2004). Product design of cohesive powders - mechanical properties, compression and flow behavior, Chem. Eng. Technology, Vol. 27, 605-618.

[29] Abhik, M., Debashish, C., Kousik, B., Arpan, H. (2017). Development of a mass model in estimating weight-wise particle size distribution using digital image processing, International Journal of Mining Science and Technology, Vol. 27, 435-443.

[30] Pabst, W., Gregorová, E., (2007). Characterization of particles and particle systems, Institute of Chemical Technology, Prague, 50-51.

[31] Elliott, C., Goren, H. J. (1984). Adipocyte insulin-binding species: The 40 A Stoke's radius protein, Can. Biochem Cell Biol., Vol. 62(7), 566-70.

[32] Retsch technology (2012). Product prospect - CAMSIZER XT, Retrieved from https://www.retsch-technology.de.

[33] Allen, T. (1997). Particle Size Measurement, Vol. 1, Powder sampling and particle size measurement, Wilmington, Delaware, Dupont de Nemur and Company.

[34] Subero, J., Ghadiri, M. (2001). Breakage patterns of agglomerates, Powder Technology, Vol. 120(3), 232-243.

[35] Müller, P., Aman, S., Tomas, J. (2013). Compression and impact behavior of moist zeolite 4A granules, Proc. of the 13th European Symposium on Comminution and Classification, 332 -335, Sierke Verlag.

[36] Rumpf, H. (1958). Grundlagen und Methoden des Granulierens, Chem. Ing. Tech., Vol. 30, 144-158.

[37] Rumpf, H. (1962). The strength of granules and agglomerates. In Agglomeration, Proc. of the First International Symposium on Agglomeration, New York/London, John Wiley and Sons.

[38] Rumpf, H. (1970). Zur Theorie der Zugfestigkeit von Agglomeraten bei Kraftübertragung an Kontakpunkten, Chem. Ing. Tech., Vol. 42, 538-540.

[39] Meissner, H. P., Michaels, A. S., Kaiser, R. (1964). Crushing strength of zinc oxide agglomerates, I&EC Process Design and Development, Vol. 3(3), 202-205.

[40] Hertz, H. (1981). Über die Berührung fester elastischer Körper. J. reine u. angew. Math. Vol. 92, 156-171.

[41] Griffith, A.A. (1920). The phenomena of rupture and flow in solids. Philosophical Transactions of the Royal Society A (Mathematics and Physics), Vol. 221, 163-198.

[42] Rumpf, H. (1956) Die Einzelkornzerkleinerung als Grundlage einer technischen Zerkleinerungswissenschaft, Chem. Ing. Tech. Vol. 37 (3), 187-202.

[43] Schönert, K. (1966). Einzelkorn-Druckzerkleinerung und Zerkleinerungskinetik, Dissertation, University of Applied Science Karlsruhe.

[44] Kendall, K. (1988). Agglomerate strength, Powder Metallurgy, Vol. 31(1), pp. 28-31, 1988.

[45] Kendall, K., Alford, N., Birchal, J. D. (1986). The strength of green bodies, Inst. Ceram. Proc. Special Ceramics, Vol. 8, 255-265.

[46] Rice, R. W. (1996). Grain size and porosity dependence of ceramic fracture energy and toughness at 22° C, Mater. Sci., Vol. 31, 1969-1998.

[47] Kapur, P. C., Fuerstenau, D.W. (1967). Dry strength of pelletized spheres, J. Am. Ceram. Soc., Vol. 50(1), 14-18.

[48] Timoshenko, S., Goodier, J. N. (1951). Theory of elasticity (3rd Edition), Londong, McGraw-Hill.

[49] Landau, L. D., Lifschitz, E. M. (2001). Theoretische Physik, Band VII: Elastizitätstheorie. Moskau, Fizmatlit.

[50] Denny, P. J., Stanley-Wood, N. G., Wilkes, R. (1998). The dependence of the diameter/thickness ratio and internal structure to compact strength, Proc. of the World Congress of Particle Technology 3, 94.

[51] Iveson, M. S., Litster, J. D. (1998). Liquid-bound granule impact deformation and coefficient of restitution. Powder Technology, Vol. 99, 234-242.

[52] Kirsch, R., Bröckel, U., Brendel,L., Török, J. (2011). Measuring tensile, shear and torsional strength of solid bridges between particles in the millimeter regime, Granul. Matter, Vol. 13, 517-523.

[53] Mörl, L., Heinrich, S., Peglow, M. (2007). Fluidized bed spray granulation. In: Salman, A. D., Hounslow, J. P. K., Seville, J. P. K. (Eds.), Handbook of Powder Technology, Vol. 11. Elsevier, 21-188.

[54] Peglow, M., Antonyuk, S., Jacob, M., Palzer, S., Heinrich, S., Tsotsas, E. (2011) Particle formulation in spray fluidized beds. In: Tsotsas, E., Majumdar, A. S. (Eds.), Modern Drying Technology, Vol. 3, Product Quality and formulation, Weinheim, Wiley-VCH GmbH, 295-378.

[55] Khanal, M., Schubert, W., Tomas, J. (2008). Compression and impact loading experiments of high strength spherical composites, Int. J. Miner. Process. Vol. 86, 104-113.

[56] Aman, S., Tomas, J., Kalman, H. (2010). Breakage probability of irregularly shaped particles, Chemical Engineering Science, Vol. 65(5), 1503-1512.

[57] Antonyuk, S., Palis, S., Heinrich, S. (2011). Breakage behavior of agglomerates and crystals by static loading and impact, Powder Technolgy, Vol. 206(1-2), 88-98.

[58] Müller, P., Tomas, J. (2013). Druckverhalten feuchter kugelförmiger Zeolith 4A-Granulate. Chem. Ing.Tech., Vol. 85, 364-373.

[59] Huber, M. T. (1904). Zur Theorie der Berührung fester elastischer Körper, Annalen der Physik, 153-163.

[60] Fischer-Cripps, A. C. (2000). Introduction to Contact Mechanics, Berlin/Heidelberg/New York, Springer-Verlag.

[61] Johnson, K. L. (1985). Contact Mechanics, Cambridge Univ. Press.

[62] Müller,P. (2011). Druck-, Stoß- und Bruchverhalten feuchter kugelförmiger Granulate, Dissertation, Otto-von-Guericke-Universität Magdeburg.

[63] Castellanos, A. (2005). The relationship between attractive interparticle forces and bulk behaviour in dry and uncharged fine powders, Adv. Phys. Vol. 54(4), 263-376.

[64] Vu-Quoc, L., Zhang, X., Lesburg, L. (2002). A normal force-displacement model for contacting spheres accounting for plastic deformation: Force-driven formulation, J. Appl. Mech. Vol. 67(2), 363-371.

[65] Tomas, J. (2000). Particle Adhesion fundamentals and bulk powder consolidation. In KONA - Powder and Particle Vol. 18, 157-169.

[66] Tomas, J. (2004). Product design of cohesive powders – Mechanical properties, compression and flow behaviour. Chem. Ing. TechnologyVol. 27, 1-14.

[67] Ziegler, F. (1985). Technische Mechanik der festen und flüssigen Körper, Wien/New York Springer-Verlag.

[68] Subero, J., Ning, Z., Ghadiri, M., Thornton, C. (1999). Effect of interface energy on the impact strength of agglomerates, Powder Technology, Vol. 105(1-3), 66-73.

[69] Dosta, M., Dale, S., Antonyuk, S., Wassgren, C., Heinrich, S., Litster, J. D. (2016). Numerical and experimental analysis of influence of granule microstructure on its compression breakage, Powder Technology, Vol. 299, 87-97.

[70] Kozhar, S., Dosta, M., Antonyuk, S., Heinrich, S., Bröckel, U. (2015). DEM simulations of amorphous irregular shaped micrometer-sized titania agglomerates at compression, Adv. Powder Technology, Vol. 26, 767-777.

[71] Potyondy, D., Cundall, P. (2004). A bonded-particle model for rock, Int. J. Rock Mech., Vol. 41, pp. 1329-1364.

[72] Koester, M., García, R., Thommes, M. (2014). Spheronization process particle kinematics determined by discrete element simulations and particle image velocimentry measurements, Int. Journal of Pharmaceutics, Vol. 477(1-2), 81-87.

[73] Bathe, K.-J. (1990). Finite-Elemente-Methoden, Berlin/Heidelberg, Springer-Verlag.

[74] Konietzky, H. (2001). Numerische Simulation in der Geomechanik mittels expliziter Verfahren, Habilitationsschrift, Technische Universität Bergakademie Freiberg.

[75] Balevičius, R., Kačianauskas, R., Mroz, Z., Sielamowicz, I. (2006). Discrete element method applied to multiobjective optimization of discharge flow parameters in hoppers, Struct. Multidisc. Optim., Springer-Verlag.

[76] Kruggel-Emden, H., Wirtz, S., Simsek, E., Scherer, V. (2006). Modeling of granular flow and combined heat transfer in hoppers by the discrete element method (DEM), Journal of Pressure Vessel Technology, Vol. 128, 139-444.

[77] Kleier, A. J., Kleinschrodt, H.-D. (2002). Discontinuous mechanical modeling of granular solids by means of PFC and LS-Dyna, Proc. of the 1st International PFC Symposium Gelsenkirchen, 6-8.

[78] Zhang, Z. P., Liu, L. F., Yuan, Y. D., Yu, A.B. (2001). A simulation study of the effects of dynamic variables on the packing of spheres, Powder Technology. Vol. 116, 23-32.

[79] Kishino, Y. (1988). Disc Model Analysis of Granular Media. In Micromechanics of Granular Materials, ed. by M. Satake and J. T. Jenkins, Amsterdam, Elsevier Science Publishers.

[80] Tykhoniuk, R., Luding, S., Tomas, J. (2004). Simulation der Scherdynamik kohäsiver Pulver, Chem. Ing. Tech. Vol. 76(1-2), 59-62.

[81] Iwashita, K., Oda, M. (2000). Micro-deformation mechanism of shear banding process based on modified distinct element method. Powder Technology, Vol. 109, 192-205.

[82] Luding, S. (2004). Molecular Dynamics Simulations of Granular Materials, Physics of Granular Media, H. Hinrichsen, D. Wolf (Eds.), Berlin, Wiley-VCH.

[83] Gröger, T., Tüzün, U., Heyes, D.M. (2003). Modelling and measuring of cohesion in wet granular materials. Powder Technology, Vol. 133, 203-215.

[84] Iwashita, K., Rarumi, Y., Casaverde, L. Uemura, D., Meguro, K., Hakuno,,M. (1987). Granular Assembly Simulation for Ground Collapse, Micromechanics of Granular Materials, M. Satake, J. T. Jenkins, (Eds.), Elsevier Science Publishers.

[85] Buchholtz, V. (1994). Molekulardynamische Untersuchungen granularer Stoffe, Dissertation, Humboldt-Universität zu Berlin.

[86] Matuttis, H. G., Luding, S., Herrmann, H. J. (2000). Discrete element simulations of dense packings and heaps made of spherical and non-spherical particles, Powder Technology, Vol. 109, 278-292.

[87] Hoomans, B., Kuipers, J., Briels, W., van Swaaij, W. (2002). Discrete particle simulation of bubble and slug formation in a two-dimensional gas-fluidised bed: A hardsphere approach, Chem. Eng. Sci. Vol. 51(1), 99-118.

[88] Link, J., Cuypers, L., Deen, N., Kuipers, J. (2005). Flow regimes in a spout–fluid bed: A combined experimental and simulation study, Chem. Eng. Sci., Vol. 60, 3425-3442.

[89] Ye, M., van der Höf, M., Kuipers, J. (2004). A numerical study of fluidization behavior of particles using a discrete particle model, Powder Technology, Vol. 139, 129-139.

[90] Tsuji, Y., Kawaguchi, T., Tanaka, T. (1993). Discrete particles simulation of 2-dimensional fluidized bed, Powder Technology, Vol. 77, 79-87.

[91] Kafui, K., Thornton, C., Adams, M. (2002). Discrete particle-continuum fluid modeling of gas-solid fluidised beds, Chem. Eng. Sci., Vol. 57, 2395-2410.

[92]   Takeuchi, S., Wang, S., Rhodes, M. (2004). Discrete element simulation of a flat-bottomed spouted bed in the 3-D cylindrical coordinate system, Chem. Eng. Sci., Vol. 59, 3495-3504.

[93]   Zhou, H., Flamant, G., Gauthier, D. (2004). DEM-LES of coal combustion in a bubbling fluidized bed. Part I: Gas-particle turbulent flow structure, Chem. Eng. Sci., Vol. 59, 4193-4203.

[94]   Kaneko, Y., Shiojima, T., Horio, M. (1999). DEM simulation of fluidized beds for gas-phase olefin polymerization, Chem. Eng. Sci., Vol. 54, 5809-5821.

[95]   Weaver, W., Gere, J. M. (1990). Matrix Analysis Framed Structures, Springer-Verlag.

[96]   Ferber, F. (2001). Numerische und experimentelle Untersuchungen rissbehafteter Strukturen, Habilitationsschrift, Universität Paderborn, Shaker Verlag.

[97]   Adams, M. J., Lawrence, C. J., Ursob, M. J. (2004). Rance, Modeling collisions of soft agglomerates at the continuum length scale, Powder Technology, Vol. 140, 268-279.

[98]   Milne, I., Ritchie, R. O., Karihaloo, B. (2003). Comprehensive Structural Integrity, Vol. 2: Fundamental Theories and Mechanisms of Failure, Kidlington, Elsevier Ltd.

[99]   Cundall, P., Strack, O. (1979). A discrete numerical model for granular assemblies, Geotechnique, Vol. 29, 47-65.

[100] Verwey, E., Overbeek, J. (1948). Theory of the stability of lyophobic colloids. The interaction of particles having an electric double layer, New York/Amsterdam, Elsevier.

[101] Wittel, F. (2006). Diskrete Elemente - Modelle zur Bestimmung der Festigkeitsevolution in Verbundwerkstoffen, Dissertation, Universität Stuttgart.

[102] Stein, E., de Borst, R., Hughes, T. (2004). Encyclopedia of Computational Mechanics, Volume 1: Fundamentals, First Edition, Chichester, John Wiley & Sons, LTD.

[103] Hazzar, L. (2015). 3D distinct element modeling of mechanical lab tests for unsaturated granular materials, Department of Civil Engineering, University of Sherbrooke (QC).

[104] Thornton, C., Randall, C. W. (1988). Micromechanics of Granular Materials, M. Satake, J. T. Jenkins (Eds.), Amsterdam, Elsevier, 133-142.

[105] Thornton, C., Yin, K. K. (1991). Impact of elastic spheres With and Without Adhesion, Powder Technology, Vol. 65, 153-166.

[106] Itasca Consulting Group Inc.- (2005). Particle Flow Code in 3 Dimensions, User Manual, Version 3.1.

[107] Obermayr, M., Dressler, K., Vrettos, C., Eberhard, P. (2013). A bonded-particle model for cemented sand, Comput. Geotech., Vol. 49, 299-313.

[108] Radeva, Z., Müller, P., Tomas, J. (2013). Influence of the Pelletizer Rotational Velocity and the Particles Size on the Agglomeration of Alumina Oxide Granules, In: Proc. of 7th International Conference on Micromechanics of Granular Media, Sydney.

[109] Australian Centre for Microscopy & Microanalysis, Retrieved from: http://www.ammrf.org.au/myscope/images/sem/sem-ve-lm.png

[110] Technology review (2013). Optimising the measurement of fine particles, Metal Powder Report, Vol. 68(4), 34-37.

[111] Forney, L. (2018). Sieve Kit - Soil Particle Size Analysis Set, Retrieved from: http://www.forneyonline.com/sieves/soils-particle-size-analysis-kit-sieve-stack-kit-4.html

[112] Heath, T. L. (1987). The works of Archimedes, University Press in Cambridge.

[113] Aligizaki, K. (2014). Pore Structure of Cement-Based Materials: Testing, Interpretation and Requirements, Modern Concrete Technology.

[114] Micromertics (1996). Product prospect - GeoPyc TM 1360, Operators manual V1.01.

[115] Tamari, S. (2004). Optimum design of the constant-volume gas pycnometer for determining the volume of solid particles, Meas. Sci. Technology, Vol. 15, 549-558.

[116] Dadkhah, M., Tsotsas, E. (2014). Study of the morphology of solidified binder in spray fluidized bed agglomerates by X-ray tomography, Powder Technology, Vol. 264, 256-264

[117] Shimadzu corporation (2018). InspeXio SMX-100CT - Micro Focus X-Ray CT System, Retrieved from: http://www.shimadzu.com/an/ndi/ct/smx100ct.html

[118] Puralox Sasol Germany GmbH (2009). Product prospect, Retrieved from: http://www.sasoltechdata.com/alumina_group.asp, PURALOX® - CATALOX® Brochure.

[119] Chemiewerk Bad Köstritz GmbH (2009) Product prospect, Retrieved from: http://www.cwk-bk.de/CWK/pages/ms/ms_tro.html, TKI.

[120] Weibull, W. (1939). A statistical theory of the strength of materials, Ingenjörs Vetensk Akademiens Handlingar 151, Stockholm, Generalstabens Litografiska Anstalts Förlag.

[121] Haidyrah, S., Newkirk, J., Castano, C. (2016). Weibull statistical analysis of Krouse type bending fatigue of nuclear materials, Journal of Nuclear Materials, Vol. 470, 244-250.

[122] Weibull, W. (1951). A statistical distribution function of wide applicability, J. Appl. Mech.-Trans. ASME, Vol. 18(3), 293-297.

[123] Dosta, M., Antonyuk, S., Heinrich, S. (2013). Multiscale simulation of agglomerate breakage in fluidized beds, Ind. Eng. Chem., Vol. 52, 11275-11281.

[124] Brady, S., Clauser, R., Vaccari, A. (1997). Materials Handbook, New York, McGraw-Hill.

[125] Itasca Consulting Group Inc. (2002). Particle Flow Code in 2 Dimensions Manual, Vers. 3.0.

[126] Brown, N. J., Chen, -F., Ooi, J.Y. (2014). A bond model for DEM simulation of cementitious materials and deformable structures, Granular Materials, Vol. 16, 299-311.

[127] O'Sullivan, C., Bray, J.D. (2003). Selecting a suitable time step for discrete element simulations that use the central difference time integration scheme, Engineering Computations, Vol. 21, 278-303.

[128] Müller, P., Russell, A., Bergstedt, J., Tomas, J. (2016). Influence of cyclic moisture loading and unloading on the mechanical properties of alumina oxide granules, Granul. Matter, Vol. 18(4), 1-14.

[129] Müller, P., Antonyuk, S., Tomas, J., Heinrich, S. (2008). Investigations of the restitution coefficient of granules, Micro-Macro Interactions in Structured Media and Particle Systems, Berlin, Springer, 235-241.

[130] Müller, P., Antonyuk, S., Tomas, J., Heinrich, S. (2008). The restitution coefficient of wet granules, In: Proc. of the XXXVI Summer School "Advanced Problems in Mechanics", 446-456.

[131] Müller, P., Antonyuk, S., Tomas, J., Heinrich, S. (2011). Ermittlung der normalen und tangentialen Stoßzahl von Granulaten. Chem. Ing.Tech., Vol. 83, 638-642.

[132] Müller, P., Antonyuk, S., Stasiak, M., Tomas, J., Heinrich, S. (2011). The normal and oblique impact of three types of wet granules, Granul. Matter, Vol. 13(4), 455-463.

[133] Müller, P., Antonyuk, Tomas, J. (2011). Investigation on the influence of moisture content on the compression behavior of granules, Chem. Eng. Technology, Vol. 34 (9), 1543-1550.

[134] Woodford, C. (2018). Zeolites, Retrieved from: http://www.explainthatstuff.com/zeolites.html

[135] Chemiewerk Bad Köstritz GmbH (2013). Product prospect - Köstrolith 4AK, Retrieved from: http://www.cwk-bk.de/de/produkte/molekularsiebe/.

[136] Cao, Q., Choi, Y., Cui, J., Lee, B. (2005). Effect of solvents on physical properties and release characteristics of monolithic hydroxypropylmethylcellulose matrix granules and tablets, Arch. Pharm. Res., Vol. 28, 493-501.

[137] Rajabi-Siahboomi, A., Bowtell, R., Mensfield, P., Davies, M., Melia, C. (1996). Structure and behavior in hydrophilic matrix sustained release dosage forms, Studies of water mobility and diffusion coefficients in the gel layer of HPMC tablets using NMR imaging, Pharmaceutical Research, Vol. 13.

[138] Raghavan, S., Formation and stabilisation of triclosan colloidal suspensions using supersaturated systems, International Journal of Pharmaceutics, Vol. 261, 153-158.

[139] Camposaldrete, M., Villafuerterobles, L. (1997). Influence of the viscosity grade and the particle size of HPMC on metronidazole release from matrix tablets, European Journal of Pharmaceutics and Biopharmaceutics, Vol. 43, 173-178.

[140] Pygall, S. (2009). Mechanisms of drug release in citrate buffered HPMC matrices, International Journal of Pharmaceutics, Vol. 370(1-2), 110-120.

[141] Shah, N., Zhang, G., Apelian, V., Zeng, F., Infeld, M., Malick, A. (1993). Prediction of drug release from hydroxypropyl methylcellulose (HPMC) matrices: effect of polymer concentration, Pharm Res., Vol. 10(11), 1693-1695.

[142] Spettl, A., Dosta, M., Antonyuk, S., Heinrich, S., Schmidt, V. (2015). Statistical investigation of agglomerate breakage based on combined stochastic microstructure modeling and DEM simulations, Adv. Powder Technology, Vol. 26, 1021-1030.

[143] Roussel, M. R. (2009). The conformations of linear polymers. Lecture notes, University of Lethbridge, 1-13.

[144] Dadkhah, M. (2014). Morphological characterization of agglomerates produced in a spray fluidized bed by X-ray tomography, Dissertation, Otto-von-Guericke Universität Magdeburg.

[145] Swokowski, W. (1983). Calculus with analytic geometry, Weber & Schmidt.

[146] Müller, P. (2016). Wechselwirkungen bei Beanspruchung, Bruch und beschleunigter Bewegung von Granulaten und Agglomeraten, Habilitation, docupoint GmbH.

Attachment A: Overview of contact models used for DEM simulation and input simulation parameters

Table A1: Contact models used for DEM simulation of the breakage behavior of the model pellets

Contact model	Hertz model	Solid bond model
Conctact behavior	Elastic contact behavior of spherical particles	Elastic contact behavior of solid bond
Normal force	$\overline{F_n}= -\overline{r_n}*\dfrac{2}{3}*\xi_n*k_n$	$\overline{F_{n,b}}= \overline{r_n}*(L_{init}-L_b)*\dfrac{E}{L_{init}}*A_b$
Tangential (shear) force	$\Delta\overline{F_t}=[k_t*\Delta\overline{\xi_t}]$	$\overline{F_{t,b}}=T*\overline{F_{t,b}}+\Delta\overline{\delta_t}*\dfrac{E}{2L_{init}\,(1+v)}*A_b$
Moments	- Moment due to rolling friction $\overline{M_{ro,i}}= -\mu_{ro}*\lvert\overline{F_n}\rvert*r_1*\dfrac{\overline{\omega_i}}{\lvert\overline{\omega_i}\rvert}$	- In normal direction $\overline{M_{n,b}}=T*\overline{M_{n,b}}+\Delta\overrightarrow{\delta_{\omega n,b}}*\dfrac{E}{2L_{init}\,(1+v)}*J$ - In shear direction $\overline{M_{t,b}}=T*\overline{M_{t,b}}+\Delta\overrightarrow{\delta_{\omega t,b}}*\dfrac{E}{L_{init}}*I$

Table A2: DEM simulation parameters – primary paricles

Type granules	Contact model	Size in mm	Denstiy in kg/cm^3	Young modulus	Normal and tangential strength in Pa	Poisson ratio
Alumina	Hertz contact model - elastic contact behavior	1.0	3420	2884	47.67	0.3
Zeolite		1.75	2290.7	5391.7	47.67	

Table A3: DEM simulation parameters – Solid bridges

Solid brigdes material	Contact model	Max. bond lenght	Bond thickness	Denstiy in kg/cm^3	Young modulus	Normal and tangential strength in Pa	Poisson ratio
HPMC	Solid bond model	0.8	0.8	700	400	50	0.3
		1.0	1.0				

Table A4: DEM simulation parameters – Compression pistons

Piston material	Contact model	Diameter in m	Thickness in m	Denstiy in kg/cm^3	Young modulus	Normal and tangential strength in Pa	Poisson ratio
Hhigh-carbon steel.	Hertz contact model - elastic contact behavior	0.010	0.002	7850	211	3100 / 810	0.3

Attachment B: Tomographic data for alumina model pellets

Tabelle B 1: Results from μ-CT data evaluation received for alumina pellets produced at rotational velocity 0.74 m/s, processing time of 15 minutes and with binder content of 0.053 g/g

N_p	r_i in mm	R_g in mm	$d_{c,max}$ in mm	$d_{c,max}/2R_g$	Porosity From R_g	Porosity From CH	Porosity From dilation	Coordination number	Coordination angle in °
29	0.50	1.46	4.75	1.63	0.46	0.46	0.48	3.14	52.07
25	0.50	1.42	4.99	1.76	0.49	0.48	0.43	2.19	58.16
19	0.50	1.23	4.26	1.74	0.40	0.44	0.37	2.22	60.71
17	0.50	1.20	4.18	1.74	0.43	0.44	0.38	1.94	63.64
17	0.50	1.16	3.85	1.66	0.37	0.43	0.43	2.50	61.13
14	0.50	1.13	3.77	1.67	0.43	0.42	0.37	2.69	49.52
9	0.50	0.92	2.78	1.51	0.33	0.39	0.47	2.13	65.25
30	0.50	1.62	5.68	1.75	0.59	0.29	0.37	3.14	48.80
29	0.50	1.51	5.26	1.75	0.51	0.28	0.47	1.18	94.69
26	0.50	1.44	4.85	1.69	0.49	0.28	0.47	2.29	51.00
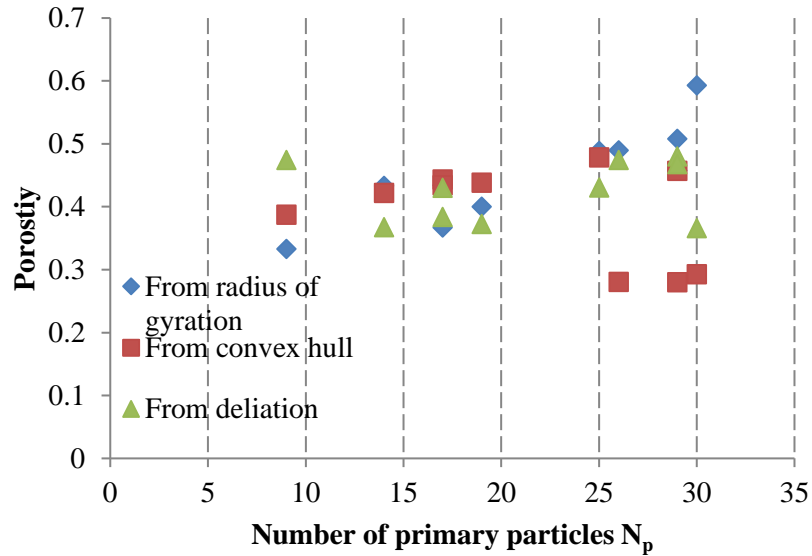
Figure B 1. Comparison between porosities calculated by three different methods for alumina pellets produced at rotational speed of 0.74 m/s, processing time of 15 min and with binder content of 0.053 g/g
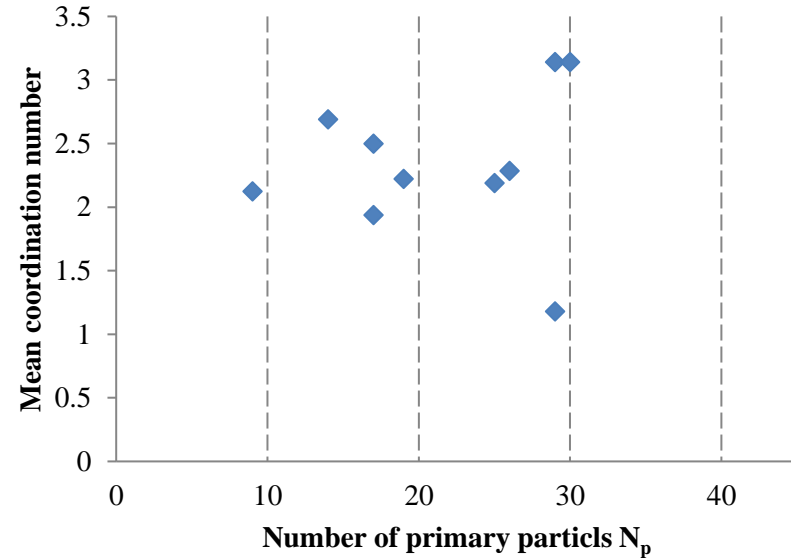
Figure B 2. Mean coordination number as a function of the primary particles number for alumina pellets produced at rotational velocity of 0.74 m/s, processing time of 15 min and binder content of 0.053 g/g
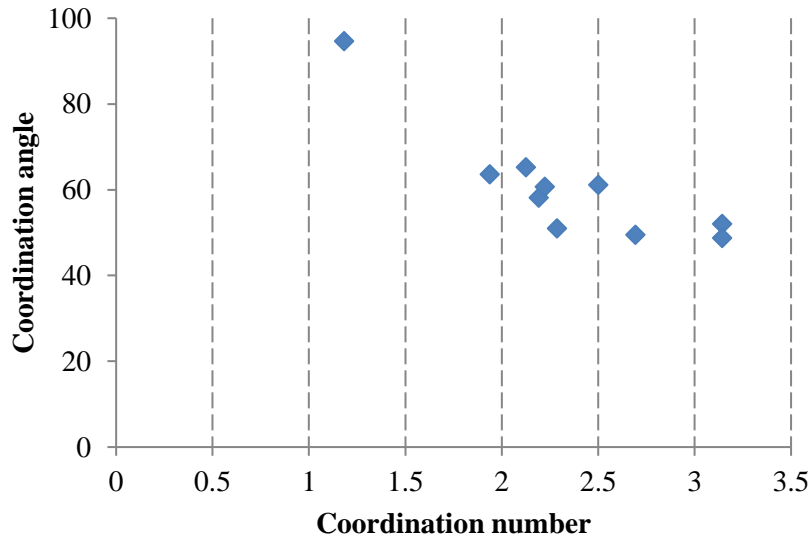
Figure B 3. Coordination angle as a function of the coordination number for alumina pellets produced at rotational velocity of 0.74 m/s, processing time of 15 min and binder content of 0.053 g/g
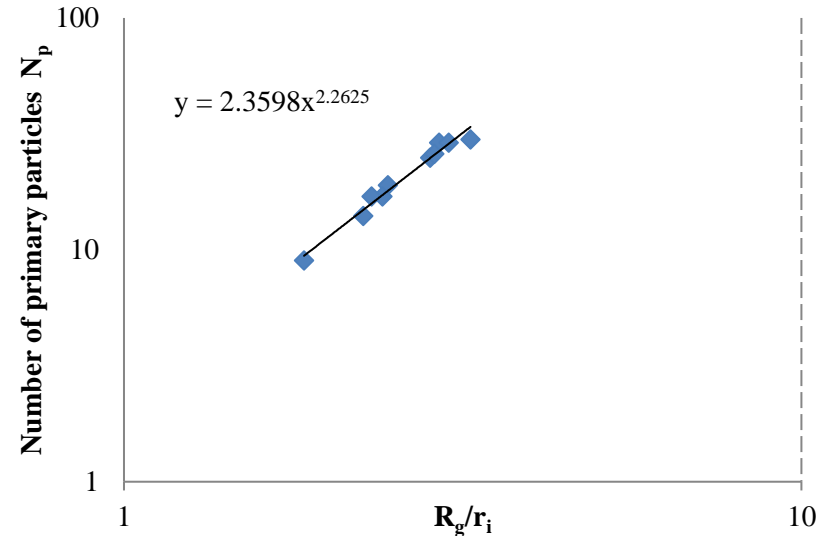
Figure B 4. Primary particle number as a function of normalized radius of gyration for alumina pellets produced at rotational speed of 0.74 m/s, processing time of 15 min and with binder content of 0.053 g/g

Tabelle B 2: Results from μ-CT data evaluation received for alumina pellets produced at rotational velocity 0.17 m/s, processing time of 15 minutes and with binder content of 0.109 g/g

N_p	r_i in mm	R_g in mm	$d_{c,max}$ in mm	$d_{c,max}/2R_g$	Porosity From R_g	Porosity From CH	Porosity From dilation	Coordination number	Coordination angle in °
37	0.50	1.64	6.14	1.88	0.51	0.50	0.62	2.25	49.40
19	0.50	1.36	4.67	1.72	0.56	0.51	0.58	2.28	73.24
36	0.50	1.61	5.83	1.81	0.50	0.55	0.58	2.03	48.83
31	0.50	1.67	5.97	1.79	0.61	0.57	0.61	1.73	52.20
34	0.50	1.75	6.72	1.92	0.63	0.55	0.55	1.58	43.80
30	0.50	1.69	6.59	1.95	0.64	0.51	0.58	2.07	45.00
23	0.50	1.38	5.19	1.87	0.50	0.54	0.42	2.29	53.75
23	0.50	1.44	5.15	1.79	0.55	0.43	0.52	1.90	53.54
18	0.50	1.23	4.15	1.68	0.44	0.45	0.58	1.89	61.07
17	0.50	1.29	4.32	1.68	0.54	0.52	0.58	1.81	65.14
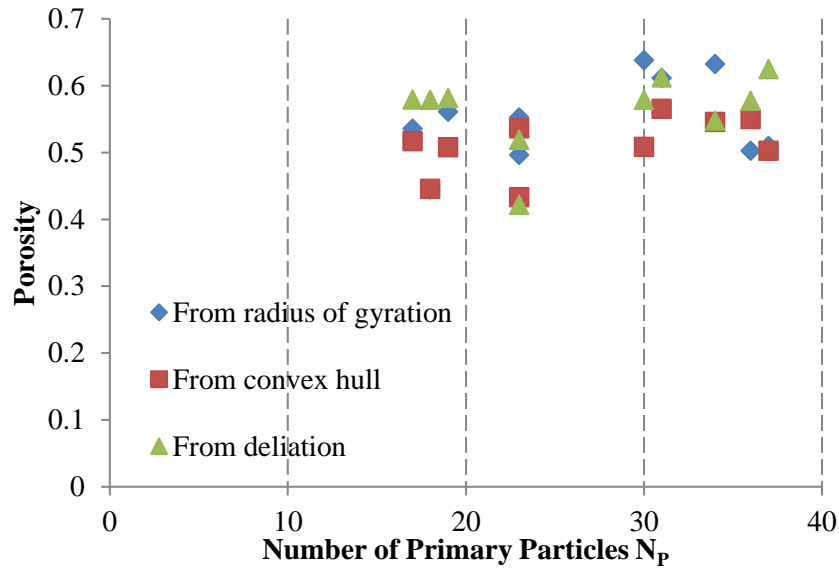
Figure B 5. Comparison between porosities calculated by three different methods for alumina pellets produced at rotational speed of 0.17 m/s, processing time of 15 min and with binder content of 0.109 g/g
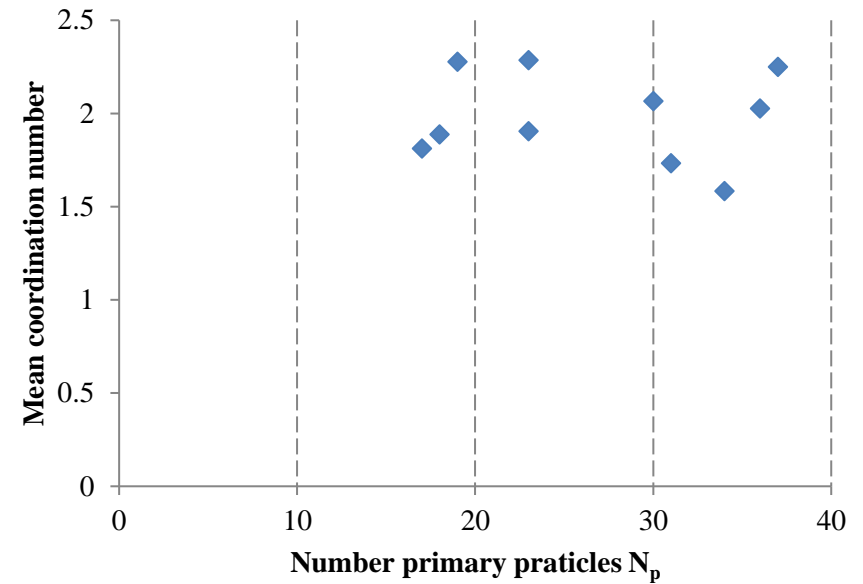
Figure B 6. Mean coordination number as a function of the primary particles number for alumina pellets produced at rotational velocity of 0.17 m/s, processing time of 15 min and binder content of 0.109 g/g
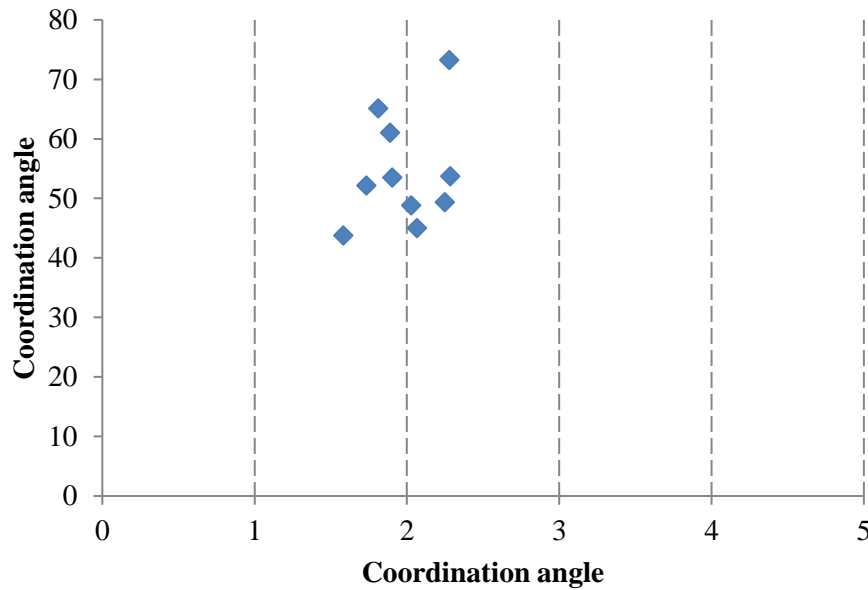
Figure B 7. Coordination angle as a function of the coordination number for alumina pellets produced at rotational velocity of 0.17 m/s, processing time of 15 min and binder content of 0.109 g/g
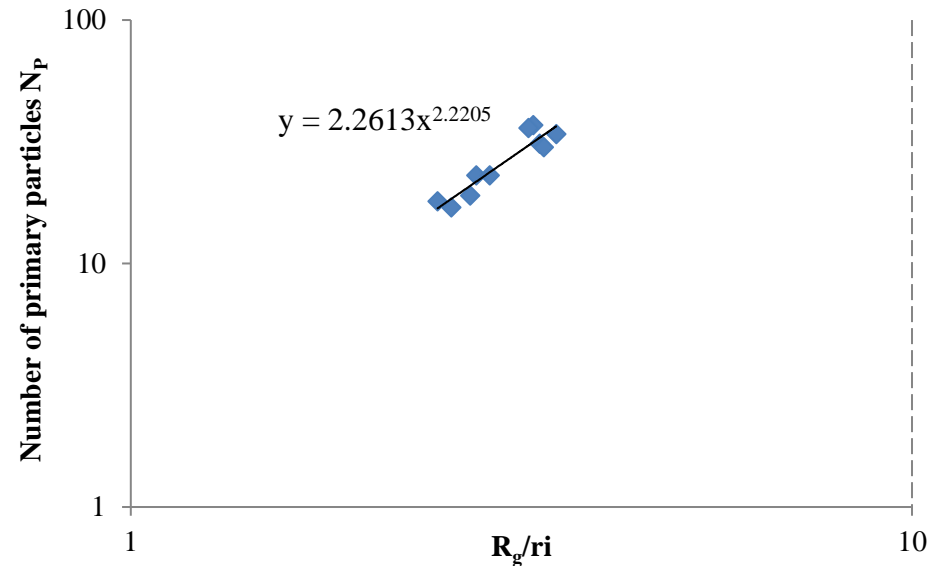
Figure B 8. Primary particle number as a function of normalized radius of gyration for alumina pellets produced at rotational speed of 0.17 m/s, processing time of 15 min and with binder content of 0.109 g/g

Tabelle B 3: Results from µ-CT data evaluation received for alumina pellets produced at rotational velocity 0.74 m/s, processing time of 15 minutes and with binder content of 0.109 g/g

N_p	r_i in mm	R_g in mm	$d_{c,max}$ in mm	$d_{c,max}/2R_g$	Porosity			Coordination number	Coordination angle in °
					From R_g	From CH	From dilation		
31	0.5	1.55	5.78	1.87	0.51	0.49	0.54	2.92	56.91
28	0.5	1.43	5.17	1.81	0.44	0.45	0.58	3.19	51.03
24	0.5	1.40	4.52	1.61	0.49	0.49	0.58	2.05	67.42
24	0.5	1.76	6.57	1.87	0.56	0.49	0.54	1.78	71.17
22	0.5	1.31	4.44	1.70	0.43	0.47	0.55	2.80	53.85
22	0.5	1.38	4.44	1.61	0.51	0.49	0.58	2.56	56.06
20	0.5	1.30	4.55	1.75	0.47	0.48	0.54	2.38	59.63
19	0.5	1.24	4.32	1.74	0.42	0.48	0.51	2.25	63.56
18	0.5	1.22	4.36	1.79	0.42	0.45	0.55	2.71	55.71
18	0.5	1.11	4.01	1.80	0.24	0.46	0.52	2.08	64.75
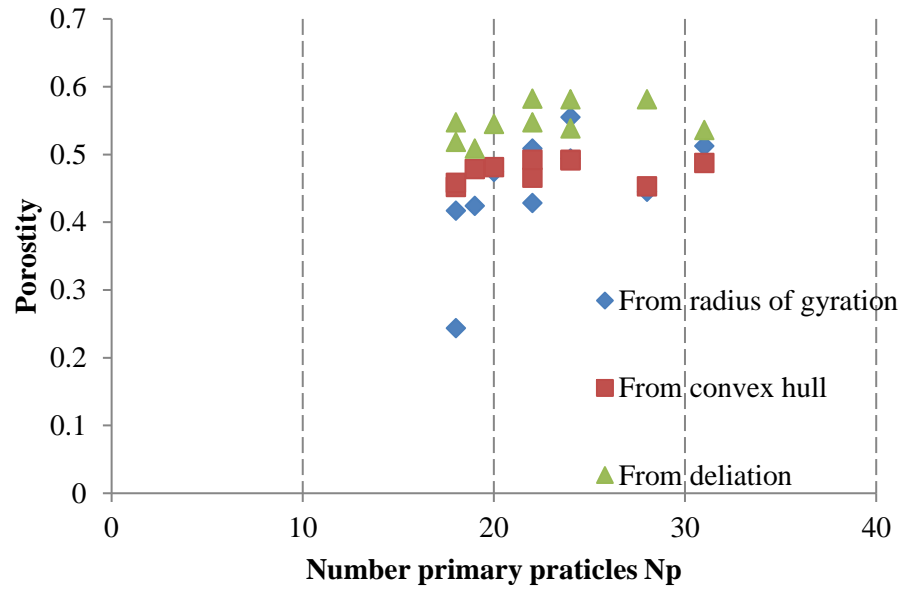
Figure B 9. Comparison between porosities calculated by three different methods for alumina pellets produced at rotational speed of 0.74 m/s, processing time of 15 min and with binder content of 0.109 g/g
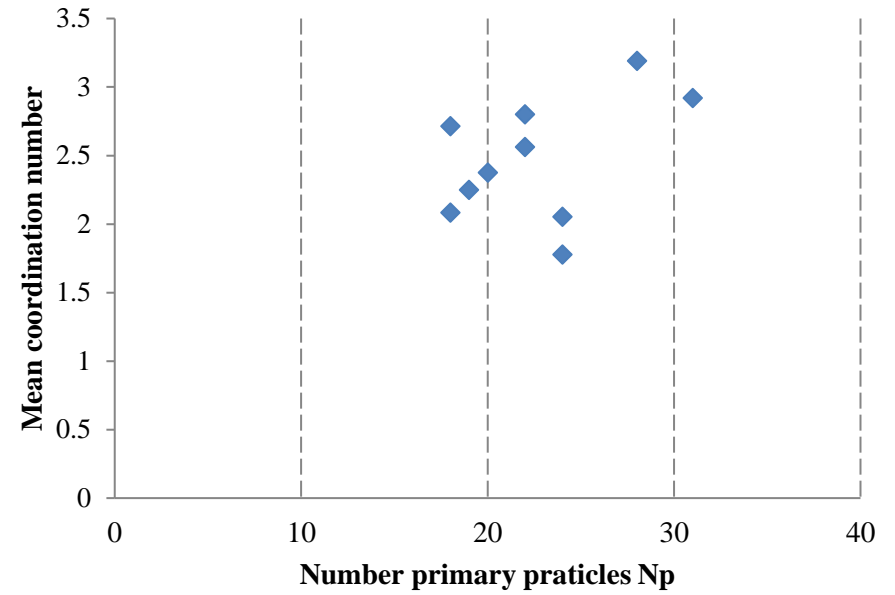
Figure B 10. Mean coordination number as a function of the primary particles number for alumina pellets produced at rotational velocity of 0.74 m/s, processing time of 15 min and binder content of 0.109 g/g
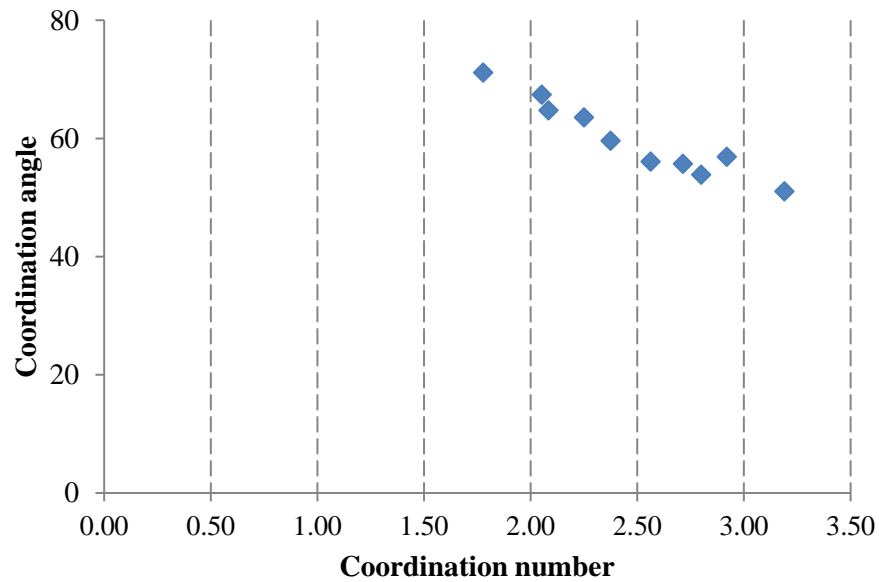
Figure B 11. Coordination angle as a function of the coordination number for alumina pellets produced at rotational velocity of 0.74 m/s, processing time of 15 min and binder content of 0.109 g/g

$y = 5.7453x^{1.0789}$
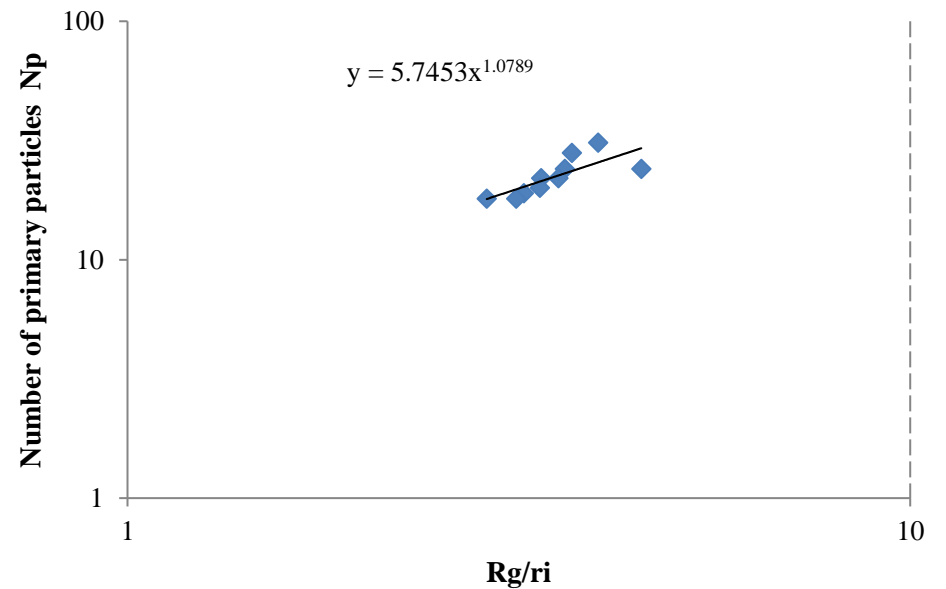
Figure B 12. Primary particle number as a function of normalized radius of gyration for alumina pellets produced at rotational speed of 0.74 m/s, processing time of 15 min and with binder content of 0.109 g/g

Tabelle B 4: Results from μ-CT data evaluation received for alumina pellets produced at rotational velocity 0.17 m/s, processing time of 30 minutes and with binder content of 0.109 g/g

N_p	r_i in mm	R_g in mm	$d_{c,max}$ in mm	$d_{c,max}/2R_g$	Porosity From R_g	From CH	From dilation	Coordination number	Coordination angle in °
36	0.5	1.64	5.83	1.78	0.50	0.51	0.52	2.52	60.62
31	0.5	1.31	5.97	2.27	0.61	0.52	0.54	2.17	65.25
19	0.5	1.35	4.26	1.58	0.40	0.49	0.58	2.35	60.71
17	0.5	1.25	4.18	1.68	0.43	0.47	0.49	2.21	63.64
19	0.5	1.42	4.53	1.59	0.51	0.49	0.54	2.21	62.57
18	0.5	1.12	5.12	2.29	0.65	0.54	0.58	2.64	57.34
16	0.5	1.36	4.08	1.50	0.48	0.46	0.43	2.14	61.07
15	0.5	1.43	3.62	1.27	0.41	0.45	0.45	2.08	68.08
14	0.5	1.57	3.66	1.17	0.48	0.47	0.44	2.70	52.50
12	0.5	1.54	3.56	1.16	0.50	0.47	0.46	1.88	63.75
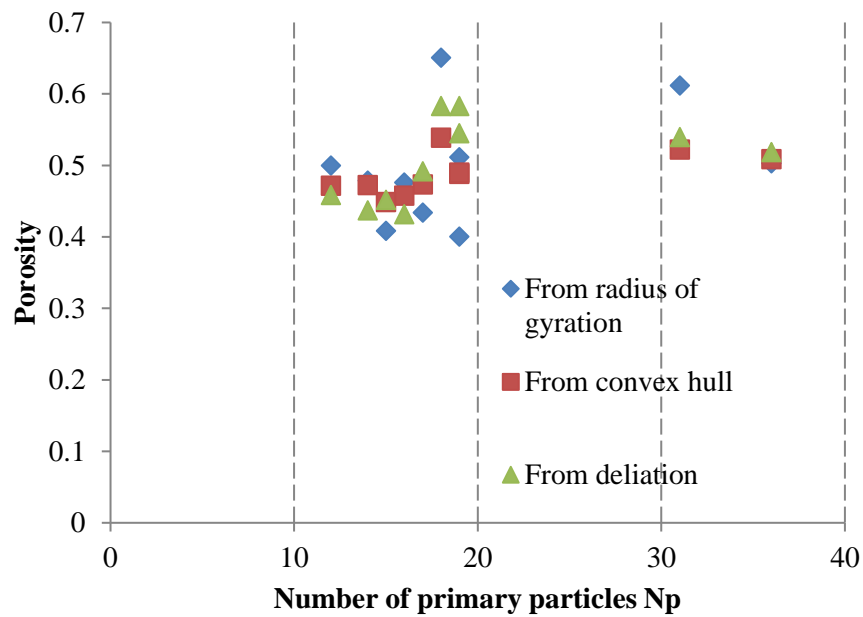
Figure B 13. Comparison between porosities calculated by three different methods for alumina pellets produced at rotational speed of 0.17 m/s, processing time of 30 min and with binder content of 0.109 g/g
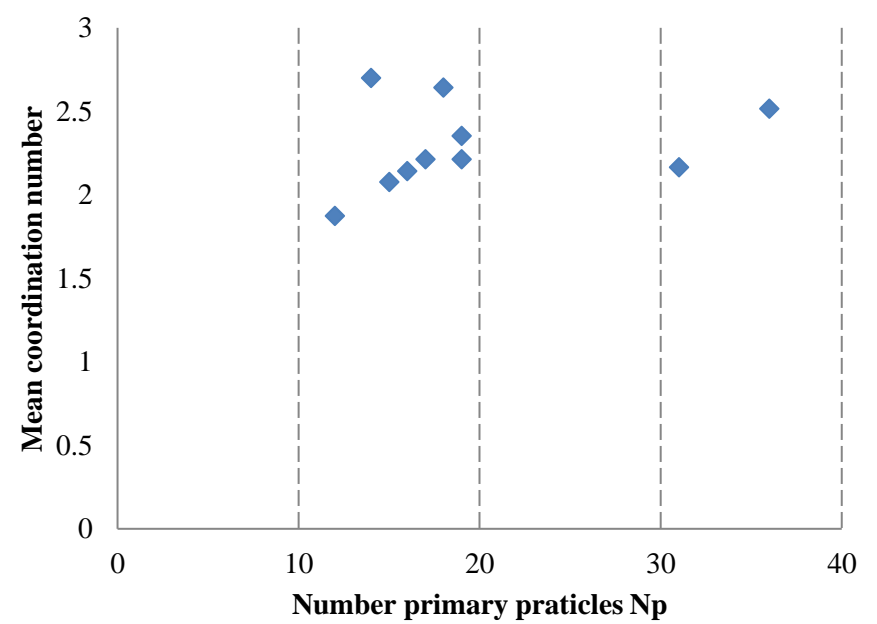
Figure B 14. Mean coordination number as a function of the primary particles number for alumina pellets produced at rotational velocity of 0.17 m/s, processing time of 30 min and binder content of 0.109 g/g
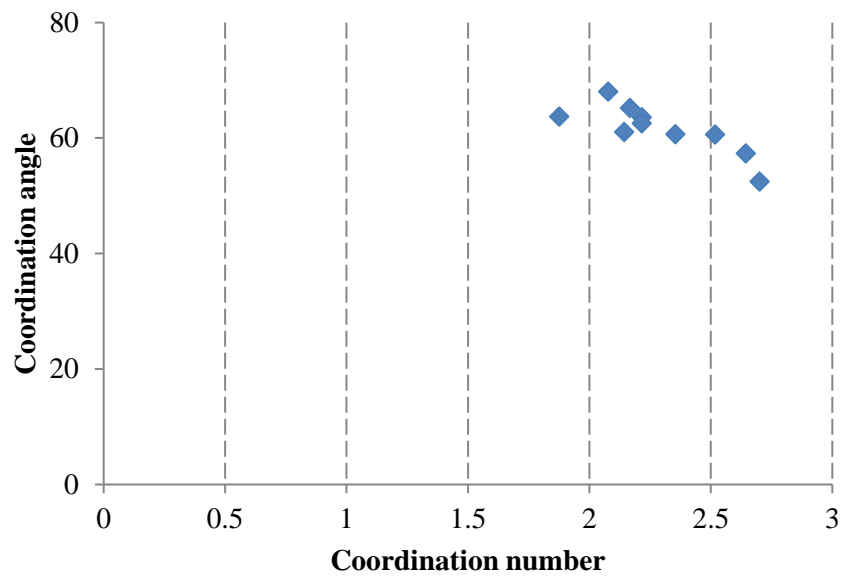
Figure B 15. Coordination angle as a function of the coordination number for alumina pellets produced at rotational velocity of 0.17 m/s, processing time of 30 min and binder content of 0.109 g/g
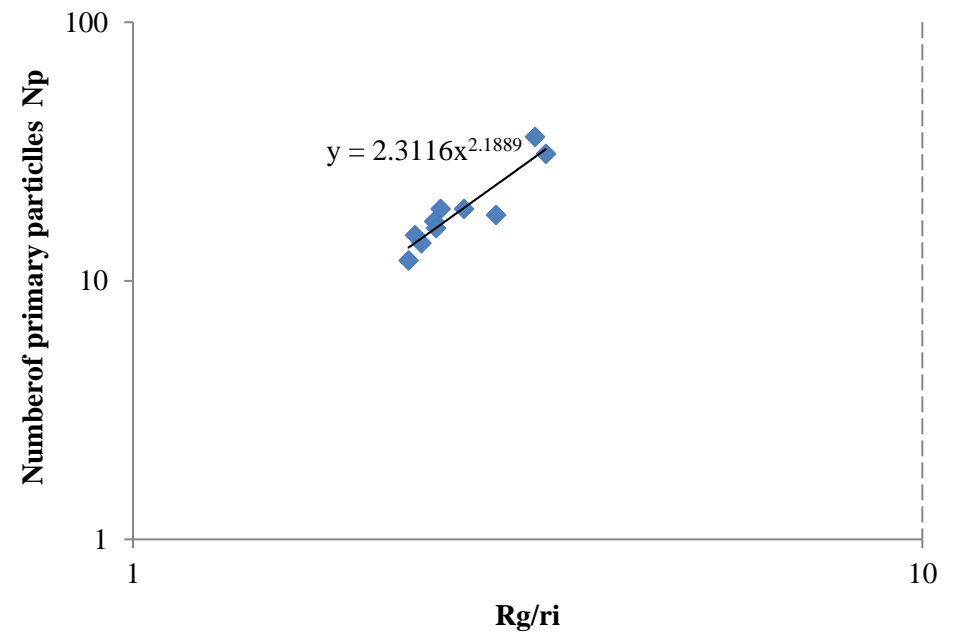
Figure B 16. Primary particle number as a function of normalized radius of gyration for alumina pellets produced at rotational speed of 0.74 m/s, processing time of 30 min and with binder content of 0.109 g/g

Tabelle B 5: Results from μ-CT data evaluation received for alumina pellets produced at rotational velocity 0.74 m/s, processing time of 30 minutes and with binder content of 0.109 g/g

N_p	r_i in mm	R_g in mm	$d_{c,max}$ in mm	$d_{c,max}/2R_g$	Porosity			Coordination number	Coordination angle in °
					From R_g	From CH	From dilation		
32	0.5	1.59	5.57	1.76	0.53	0.37	0.59	2.06	42.73
22	0.5	1.30	4.63	1.78	0.41	0.34	0.45	2.29	59.44
22	0.5	1.30	4.87	1.87	0.42	0.36	0.50	1.95	61.06
24	0.5	1.35	4.74	1.76	0.43	0.38	0.49	2.52	58.50
22	0.5	1.37	4.71	1.72	0.50	0.30	0.49	2.48	60.51
19	0.5	1.27	4.18	1.65	0.46	0.35	0.49	1.78	66.56
17	0.5	1.19	3.99	1.67	0.42	0.40	0.51	2.00	64.71
18	0.5	1.26	4.41	1.75	0.48	0.35	0.50	1.72	65.80
17	0.5	1.18	4.01	1.69	0.41	0.36	0.49	2.19	42.73
15	0.5	1.15	3.94	1.70	0.43	0.40	0.47	1.43	70.00
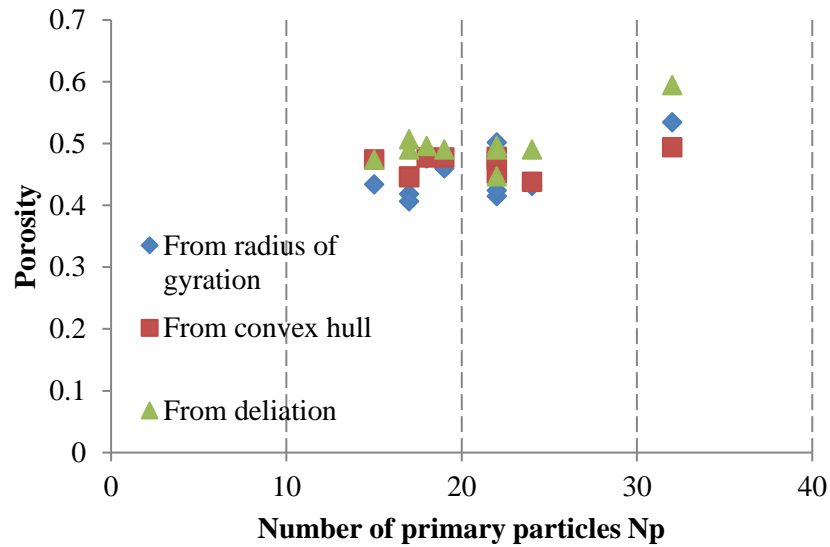
Figure B 17. Comparison between porosities calculated by three different methods for alumina pellets produced at rotational speed of 0.74 m/s, processing time of 30 min and with binder content of 0.109 g/g
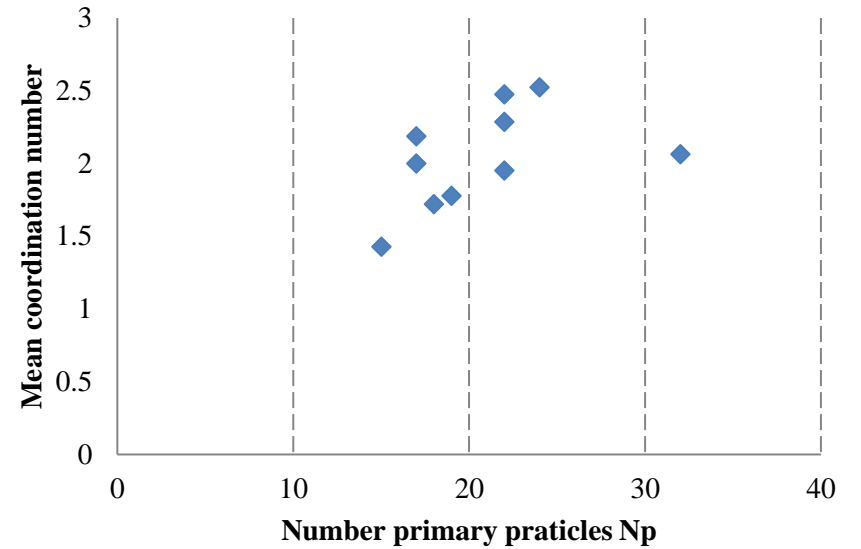
Figure B 18. Mean coordination number as a function of the primary particles number for alumina pellets produced at rotational velocity of 0.74 m/s, processing time of 30 min and binder content of 0.109 g/g
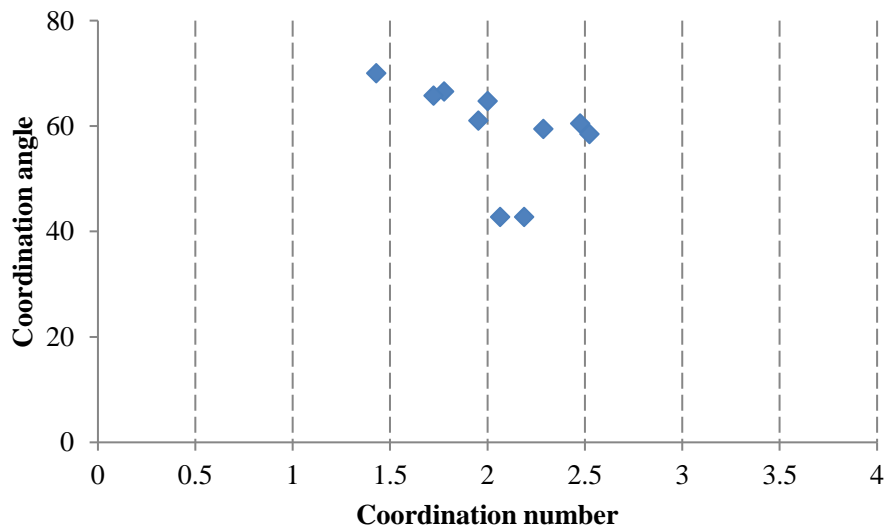
Figure B 19. Coordination angle as a function of the coordination number for alumina pellets produced at rotational velocity of 0.74 m/s, processing time of 30 min and binder content of 0.109 g/g

$$y = 2.2417x^{2.3238}$$
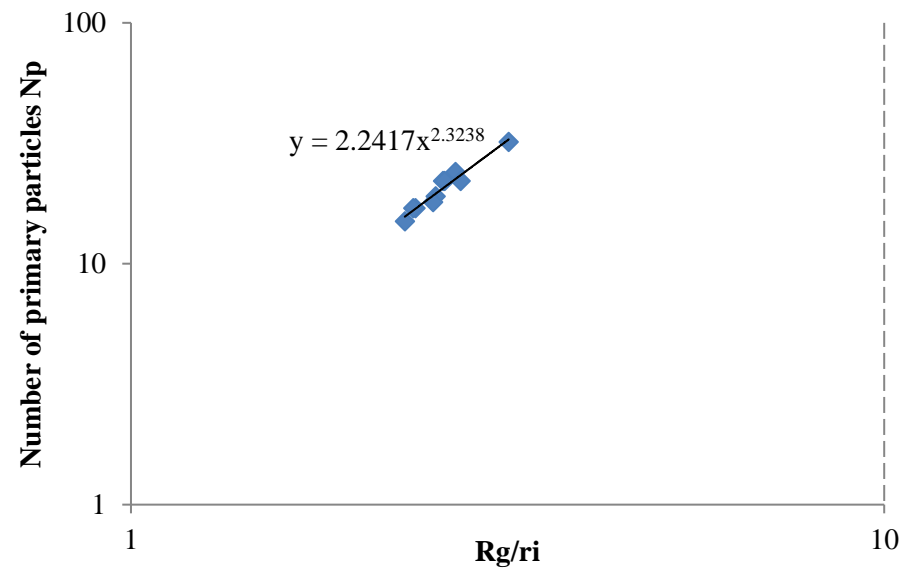
Figure B 20 Primary particle number as a function of normalized radius of gyration for alumina pellets produced at rotational speed of 0.74 m/s, processing time of 30 min and with binder content of 0.109 g/g

Tabelle B 6: Results from μ-CT data evaluation received for alumina pellets produced at rotational velocity 0.17 m/s, processing time of 30 minutes and with binder content of 0.053 g/g

N_p	r_i in mm	R_g in mm	$d_{c,max}$ in mm	$d_{c,max}/2R_g$	Porosity			Coordination number	Coordination angle in °
					From R_g	From CH	From dilation		
31	0.5	1.64	5.31	1.62	0.59	0.51	0.59	2.67	55.88
27	0.5	1.69	5.69	1.68	0.68	0.53	0.54	2.29	62.51
27	0.5	1.48	5.33	1.80	0.52	0.48	0.57	2.73	57.20
25	0.5	1.46	5.13	1.76	0.53	0.50	0.61	2.52	58.94
21	0.5	1.51	5.36	1.78	0.64	0.53	0.60	2.36	62.27
23	0.5	1.40	4.88	1.74	0.51	0.44	0.57	2.95	56.94
21	0.5	1.37	4.78	1.75	0.52	0.47	0.54	2.65	58.44
20	0.5	1.36	4.82	1.77	0.54	0.49	0.60	2.87	51.40
21	0.5	1.39	4.96	1.79	0.54	0.52	0.52	2.33	64.50
21	0.5	1.33	4.84	1.82	0.48	0.47	0.54	2.33	60.17
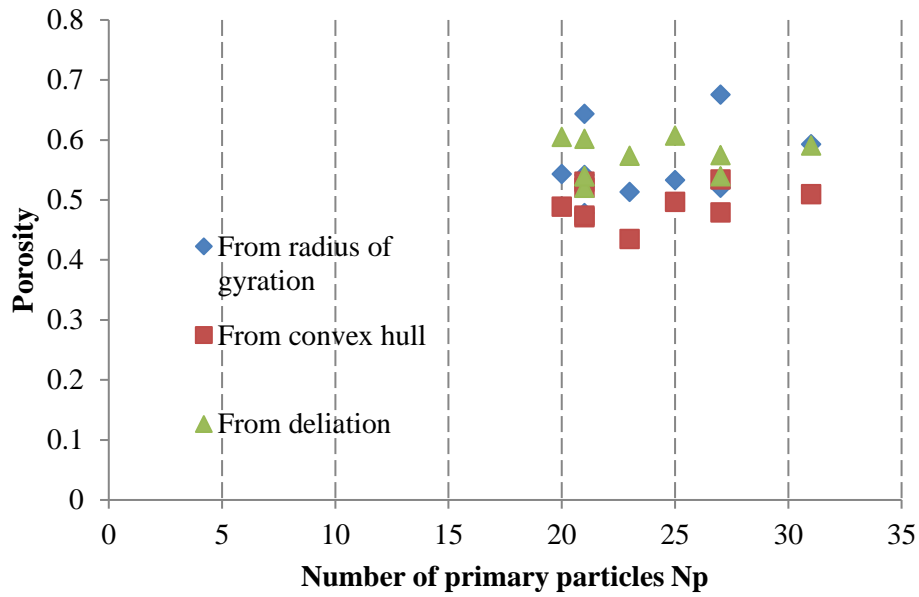
Figure B 21. Comparison between porosities calculated by three different methods for alumina pellets produced at rotational speed of 0.17 m/s, processing time of 30 min and with binder content of 0.053 g/g
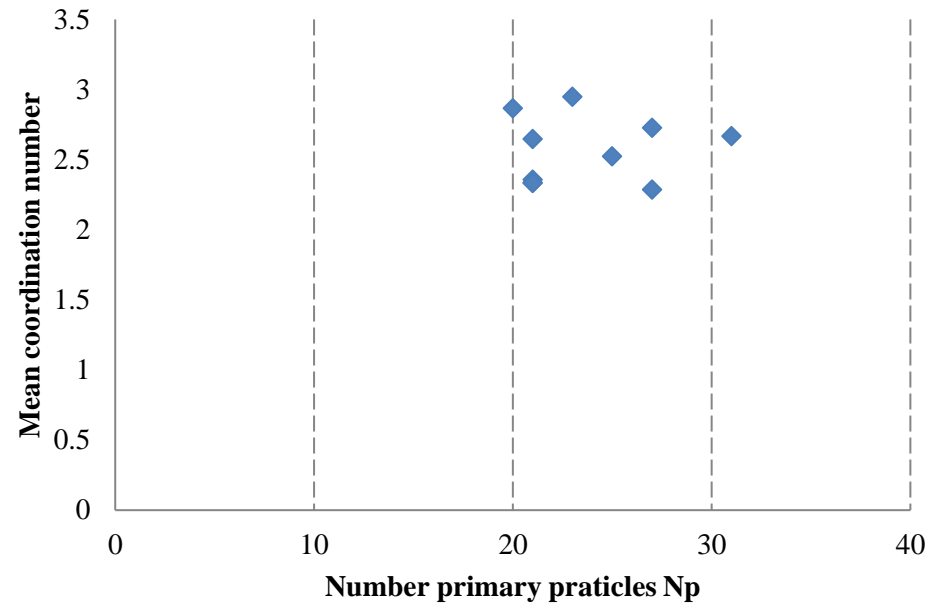
Figure B 22. Mean coordination number as a function of the primary particles number for alumina pellets produced at rotational velocity of 0.17 m/s, processing time of 30 min and binder content of 0.053 g/g
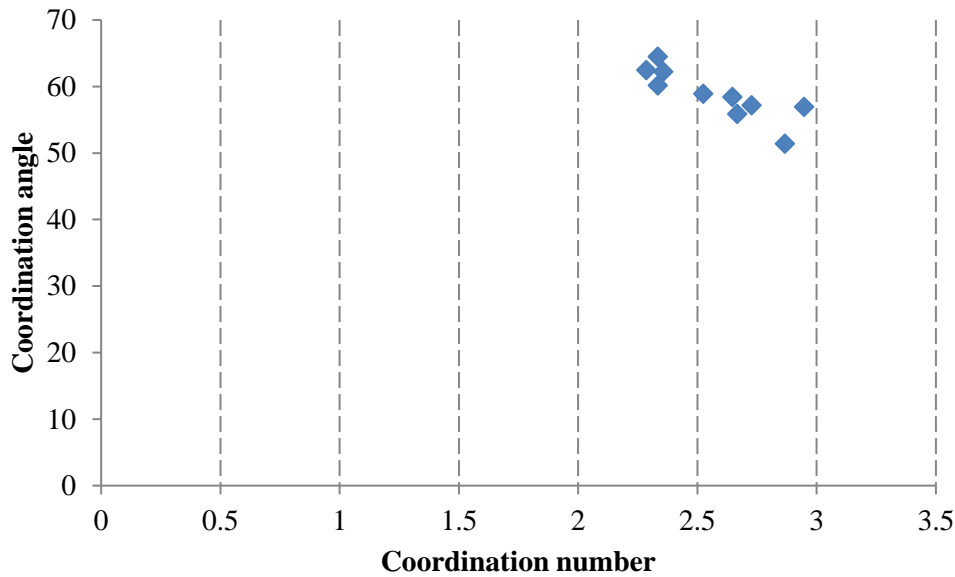
Figure B 23. Coordination angle as a function of the coordination number for alumina pellets produced at rotational velocity of 0.17 m/s, processing time of 30 min and binder content of 0.053 g/g
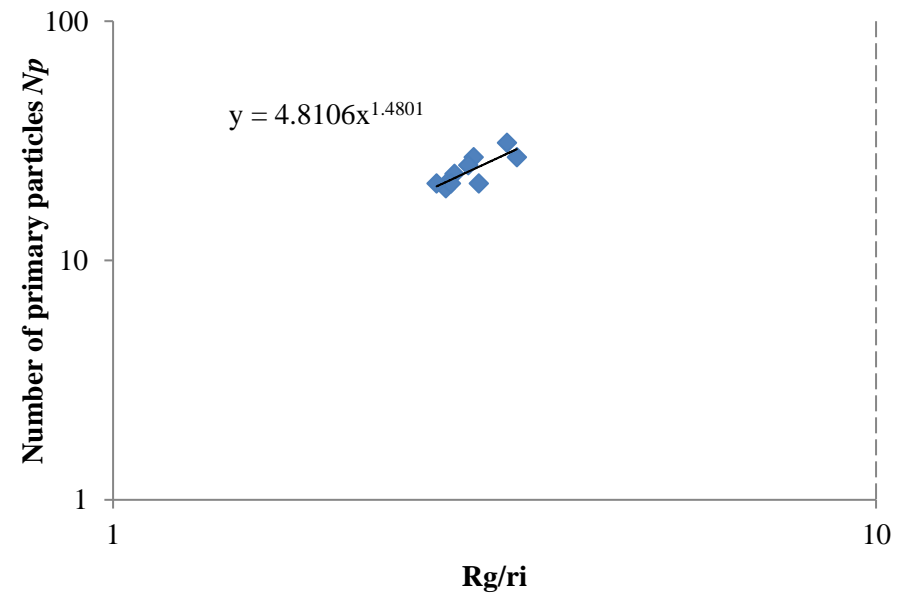
Figure B 24. Primary particle number as a function of normalized radius of gyration for alumina pellets produced at rotational speed of 0.17 m/s, processing time of 30 min and with binder content of 0.053 g/g

Tabelle B 7: Results from μ-CT data evaluation received for alumina pellets produced at rotational velocity 0.74 m/s, processing time of 30 minutes and with binder content of 0.053 g/g

N_p	r_i in mm	R_g in mm	$d_{c,max}$ in mm	$d_{c,max}/2R_g$	Porosity From R_g	Porosity From CH	Porosity From dilation	Coordination number	Coordination angle in °
25	0.5	1.37	4.63	1.69	0.44	0.44	0.49	3.10	53.00
26	0.5	1.38	4.64	1.68	0.42	0.46	0.50	2.71	38.58
21	0.5	1.23	4.12	1.68	0.34	0.42	0.45	3.17	52.61
20	0.5	1.28	4.26	1.66	0.45	0.47	0.42	2.44	56.63
20	0.5	1.28	4.33	1.70	0.44	0.46	0.42	2.63	57.00
21	0.5	1.37	4.77	1.74	0.53	0.45	0.49	2.78	58.85
20	0.5	1.25	4.35	1.74	0.41	0.45	0.51	2.56	57.94
16	0.5	1.29	4.37	1.70	0.56	0.50	0.49	2.45	58.25
15	0.5	1.12	3.45	1.54	0.38	0.42	0.42	2.58	55.64
14	0.5	1.14	3.58	1.58	0.45	0.44	0.42	2.27	66.55
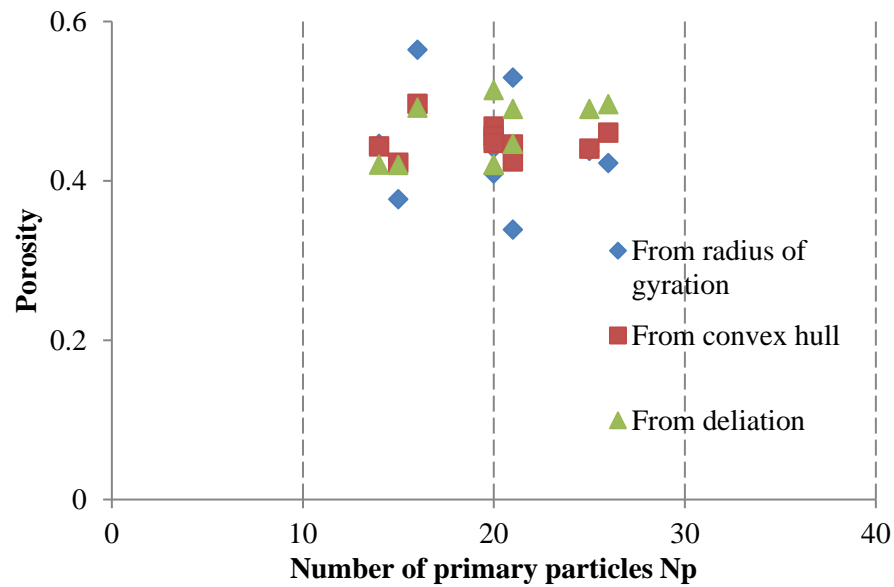
Figure B 25. Comparison between porosities calculated by three different methods for alumina pellets produced at rotational speed of 0.74 m/s, processing time of 30 min and with binder content of 0.053 g/g
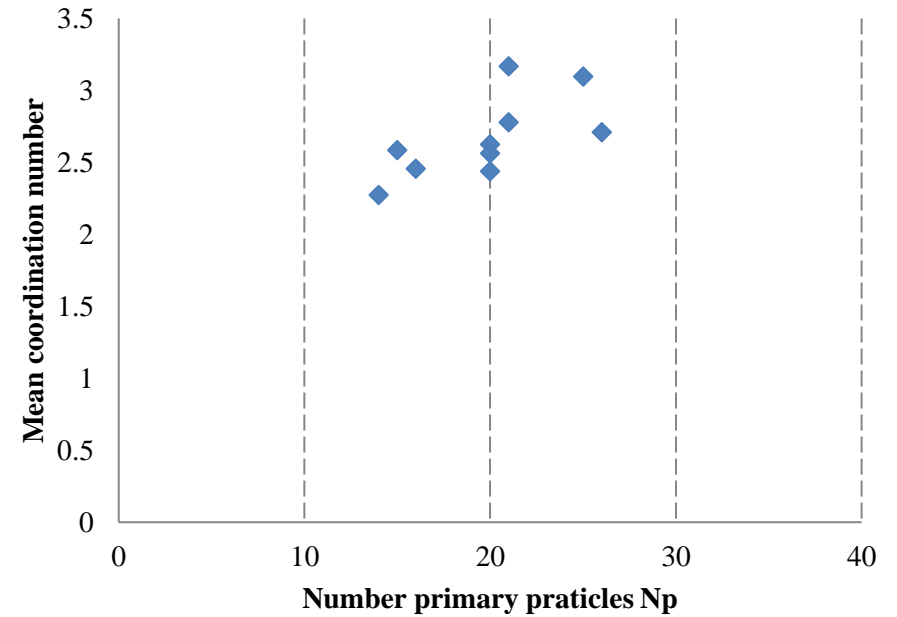
Figure B 26. Mean coordination number as a function of the primary particles number for alumina pellets produced at rotational velocity of 0.74 m/s, processing time of 30 min and binder content of 0.053 g/g
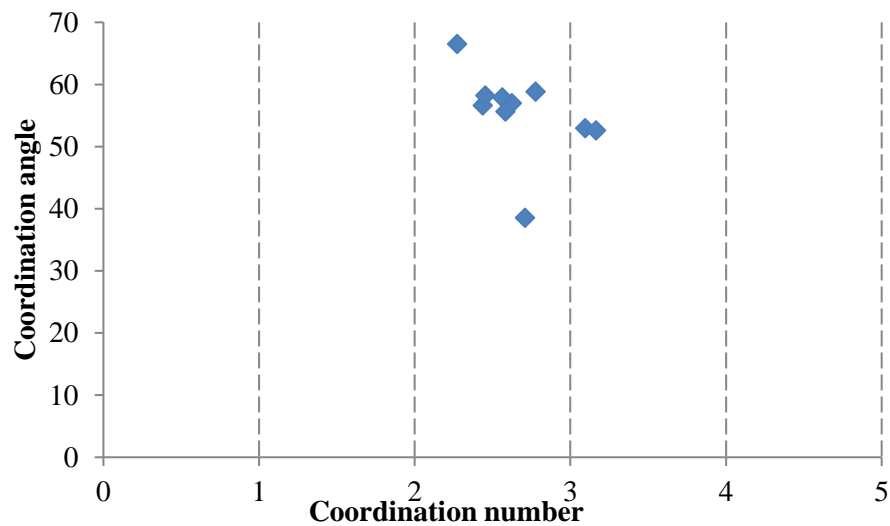
Figure B 27. Coordination angle as a function of the coordination number for alumina pellets produced at rotational velocity of 0.74 m/s, processing time of 30 min and binder content of 0.053 g/g
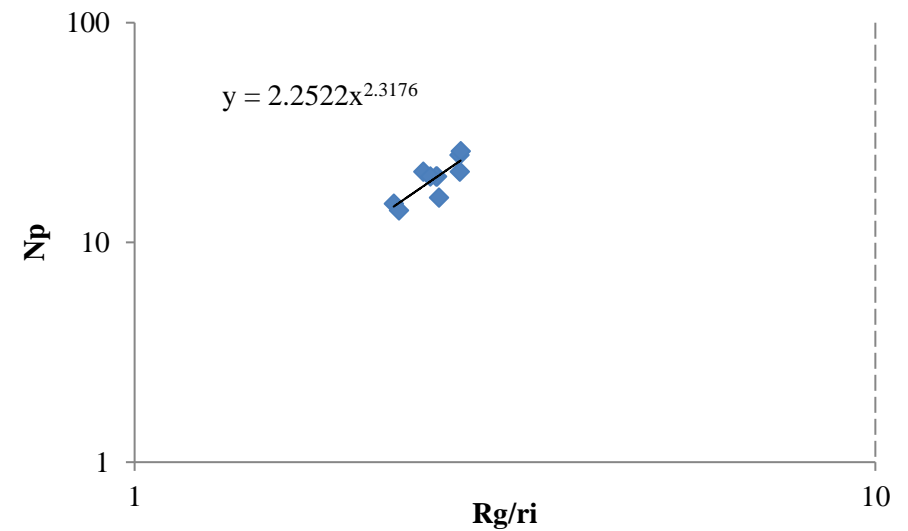
Figure B 28. Primary particle number as a function of normalized radius of gyration for alumina pellets produced at rotational speed of 0.74 m/s, processing time of 30 min and with binder content of 0.053 g/g
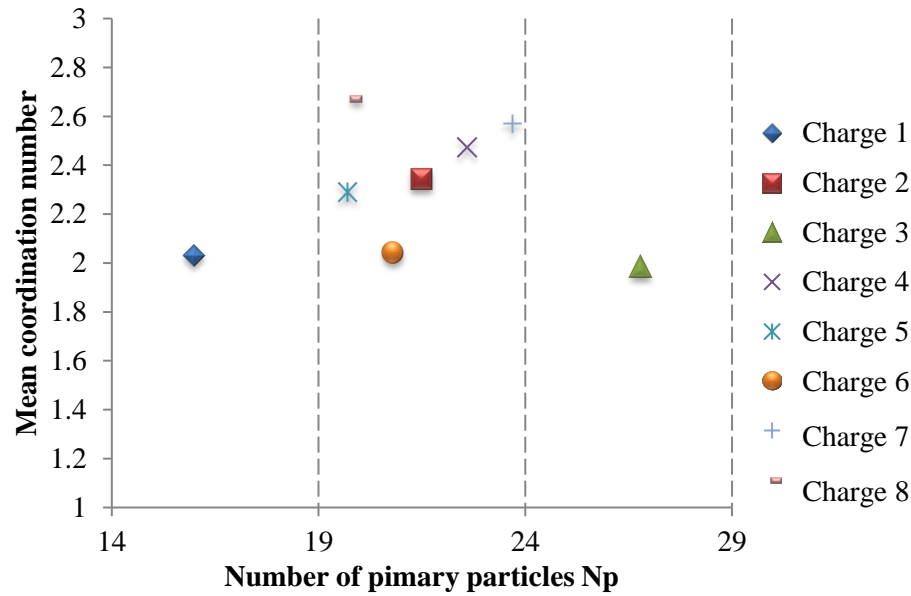
Figure B 29. Mean coordination number as a function of the primary particle number for alumina charges
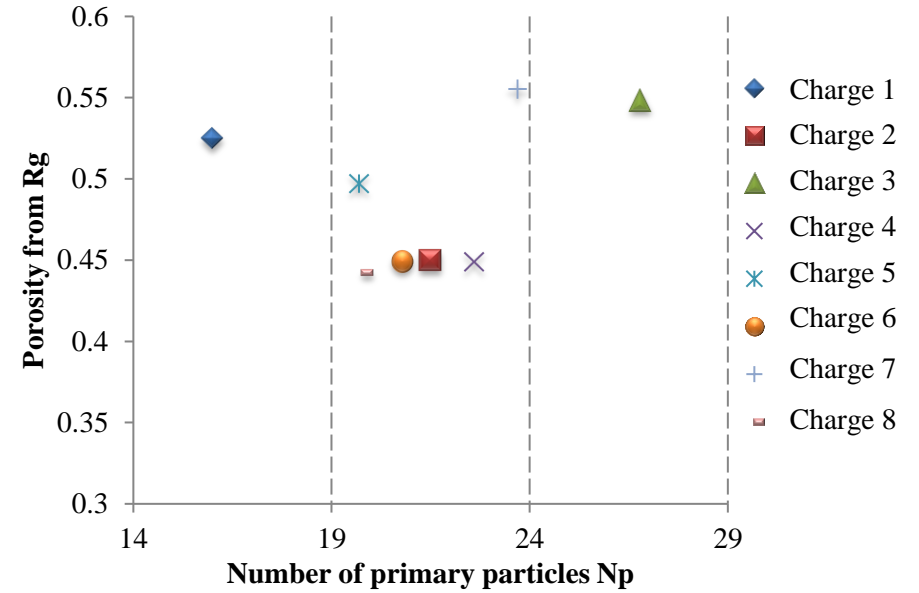
Figure B 30. Comparison of porosity of different alumina charges, calculated from radius of gyration
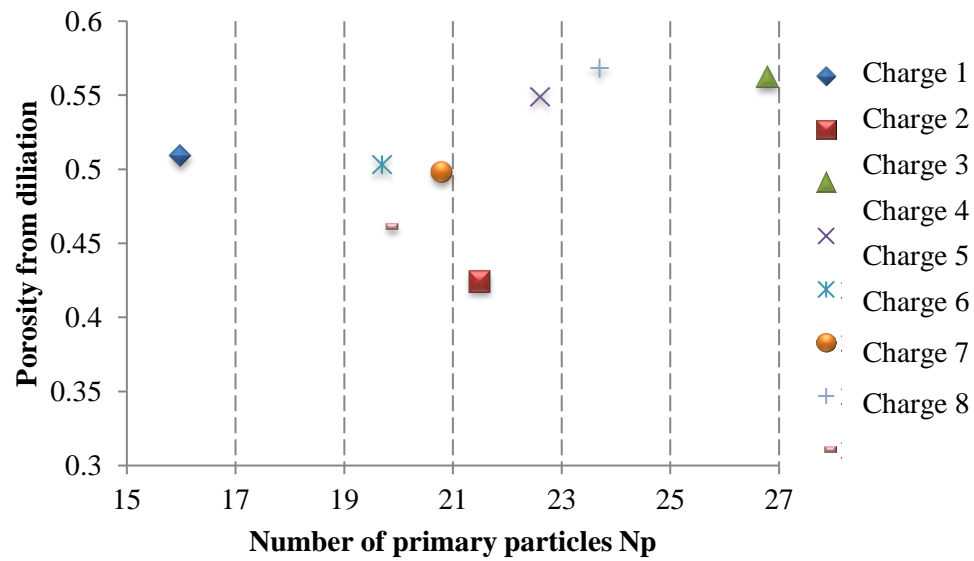
Figure B 31. Comparison of porosity of different alumina charges, calculated by dilation
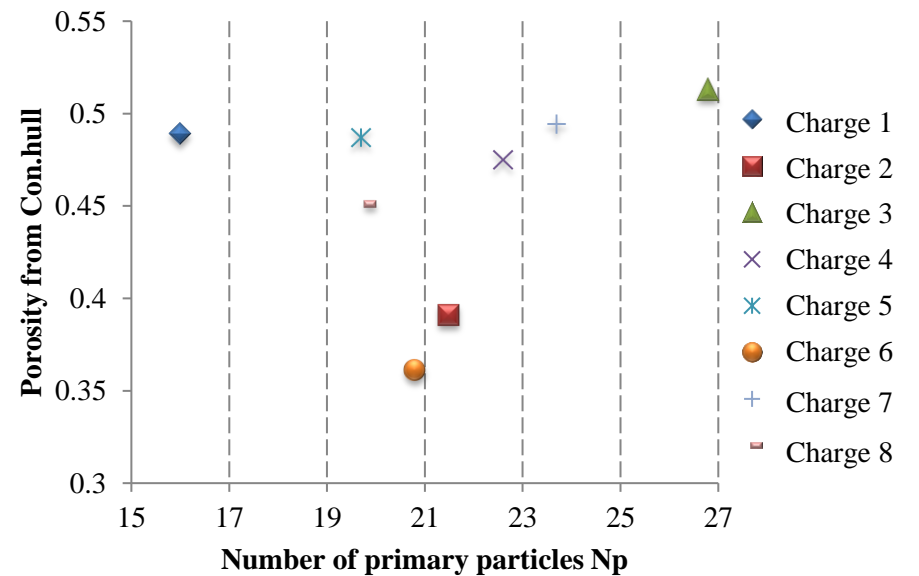
Figure B 32. Comparison of porosity of different alumina charges, calculated from convex hull

Attachment C: Tomographic data for zeolite model pellets

Tabelle C 1: Results from μ-CT data evaluation received for zeolite pellets produced at rotational velocity 0.17 m/s, processing time of 15 minutes and with binder content of 0.053 g/g

N_p	r_i in mm	R_g in mm	$d_{c,max}$ in mm	$d_{c,max}/2R_g$	Porosity			Coordination number	Coordination angle in °
					From R_g	From CH	From dilation		
9	0.825	1.64	2.73	0.83	0.47	0.37	0.51	2.50	55.00
6	0.825	1.31	3.94	1.50	0.31	0.34	0.38	2.00	57.75
6	0.825	1.35	3.84	1.42	0.36	0.36	0.44	2.60	55.20
5	0.825	1.25	3.23	1.29	0.33	0.38	0.48	1.67	90.00
7	0.825	1.42	2.75	0.97	0.37	0.30	0.37	1.67	75.00
4	0.825	1.12	2.91	1.30	0.25	0.35	0.47	1.67	90.00
6	0.825	1.36	3.81	1.40	0.38	0.40	0.50	1.50	90.00
8	0.825	1.43	4.23	1.48	0.28	0.35	0.43	3.14	48.43
10	0.825	1.57	4.74	1.51	0.33	0.36	0.50	1.67	60.00
8	0.825	1.54	5.03	1.63	0.43	0.40	0.52	2.00	70.71
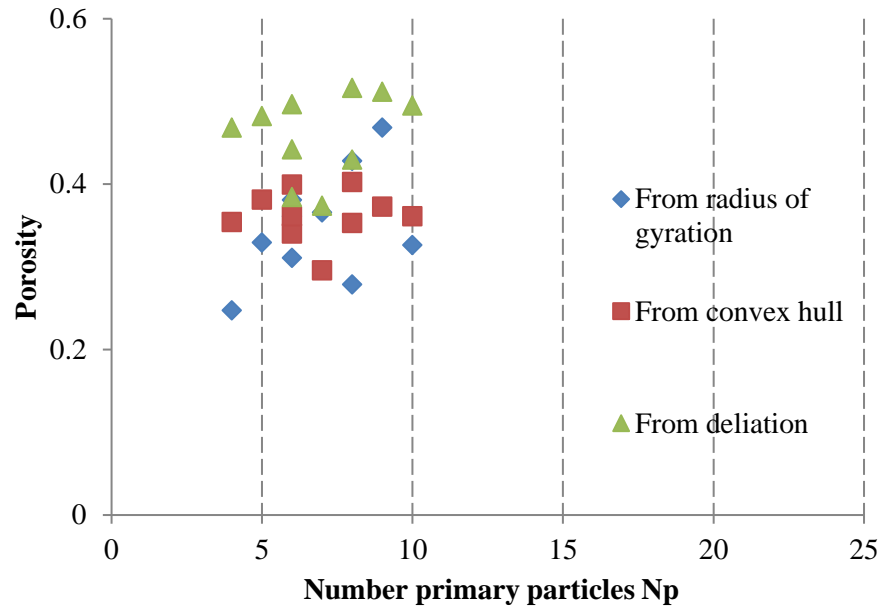
Figure C 1. Comparison between porosities calculated by three different methods for zeolite pellets produced at rotational speed of 0.17 m/s, processing time of 15 min and with binder content of 0.053 g/g
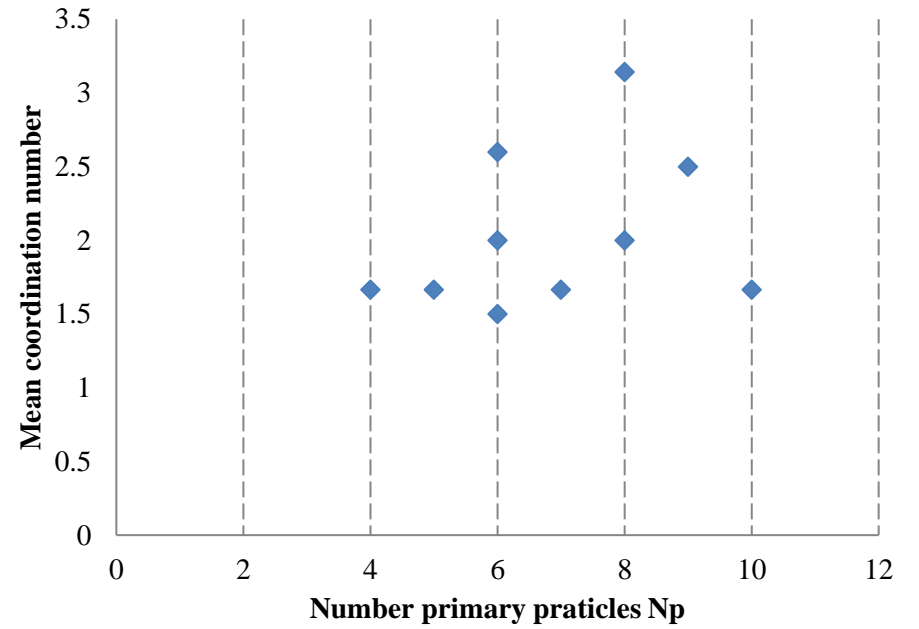
Figure C 2. Mean coordination number as a function of the primary particles number for zeolite pellets produced at rotational velocity of 0.17 m/s, processing time of 15 min and binder content of 0.053 g/g
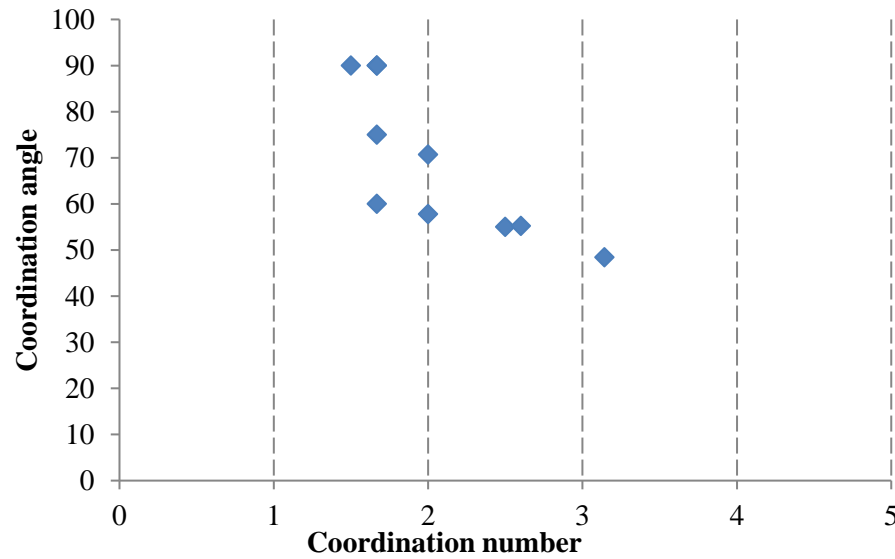
Figure C 3. Coordination angle as a function of the coordination number for zeolite pellets produced at rotational velocity of 0.17 m/s, processing time of 15 min and binder content of 0.053 g/g

$y = 1.9586x^{2.3462}$
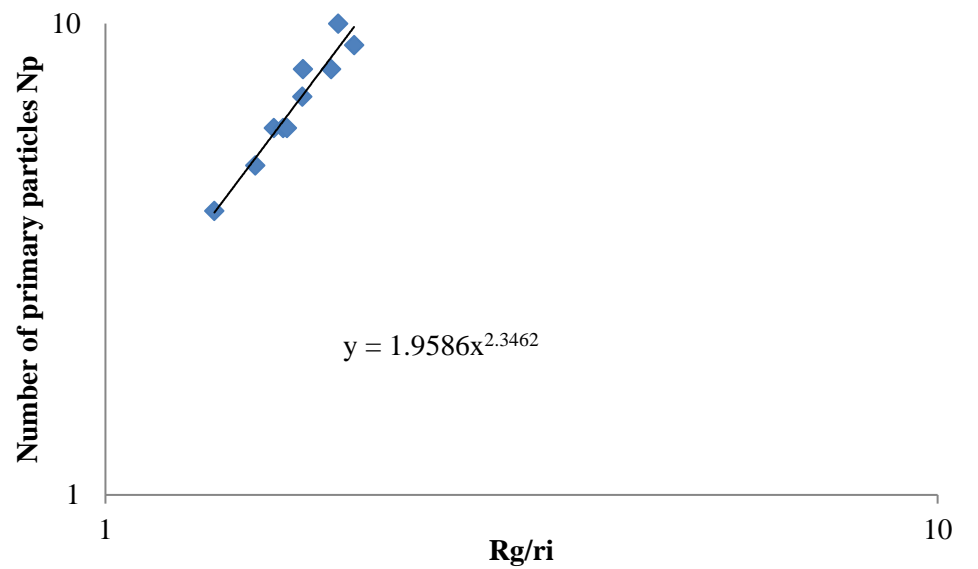
Figure C 4. Primary particle number as a function of normalized radius of gyration for zeolite pellets produced at rotational speed of 0.17 m/s, processing time of 15 min and with binder content of 0.053 g/g

Tabelle C 2: Results from μ-CT data evaluation received for zeolite pellets produced at rotational velocity 0.74 m/s, processing time of 15 minutes and with binder content of 0.053 g/g

N_p	r_i in mm	R_g in mm	$d_{c,max}$ in mm	$d_{c,max}/2R_g$	Porosity			Coordination number	Coordination angle in °
					From R_g	From CH	From dilation		
8	0.825	2.16	4.35	1.01	0.71	0.38	0.39	1.86	60.00
6	0.825	1.36	3.80	1.40	0.37	0.39	0.27	1.20	75.00
6	0.825	1.50	3.84	1.28	0.53	0.34	0.48	1.80	69.00
4	0.825	1.01	2.67	1.32	0.31	0.28	0.36	2.00	65.00
7	0.825	1.42	3.84	1.35	0.37	0.37	0.43	1.60	67.50
9	0.825	1.49	4.67	1.56	0.30	0.38	0.46	2.25	49.29
6	0.825	1.29	3.58	1.39	0.27	0.33	0.40	1.80	72.00
8	0.825	1.50	4.50	1.50	0.38	0.37	0.42	2.14	59.29
10	0.825	1.49	4.82	1.62	0.21	0.35	0.37	2.67	62.71
8	0.825	2.13	5.03	1.18	0.69	0.31	0.37	2.00	70.71
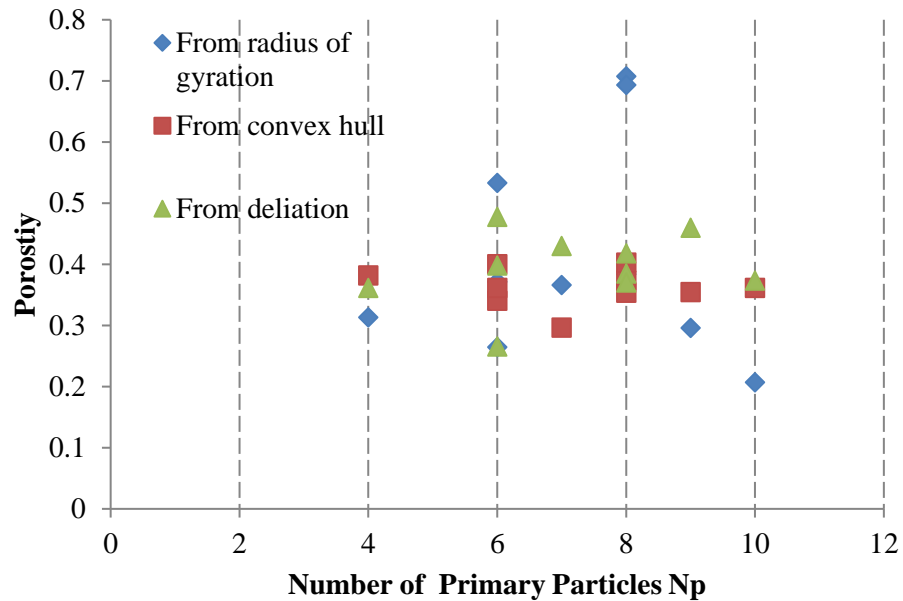
Figure C 5. Comparison between porosities calculated by three different methods for zeolite pellets produced at rotational speed of 0.74 m/s, processing time of 15 min and with binder content of 0.053 g/g
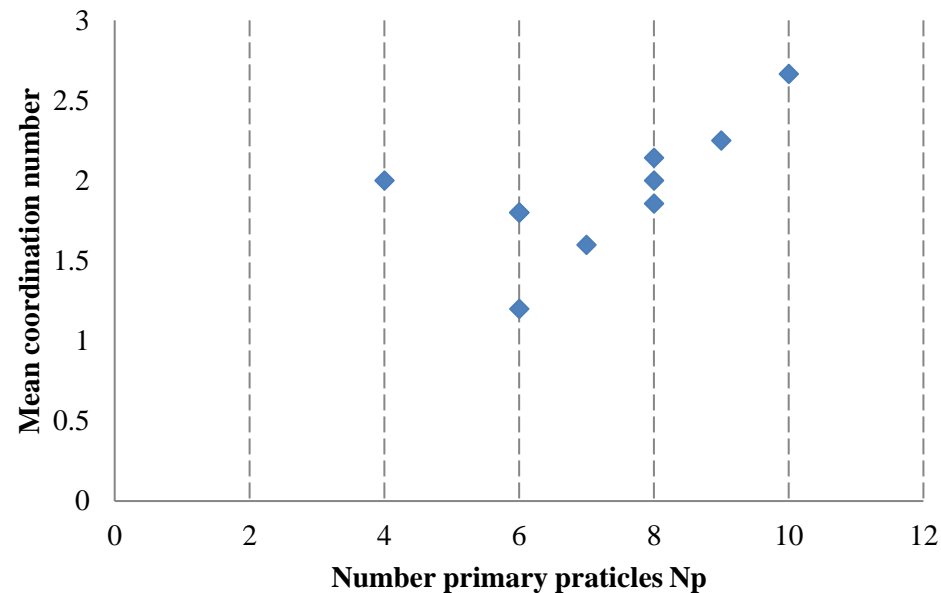
Figure C 6. Mean coordination number as a function of the primary particles number for alumina pellets produced at rotational velocity of 0.74 m/s, processing time of 15 min and binder content of 0.053 g/g
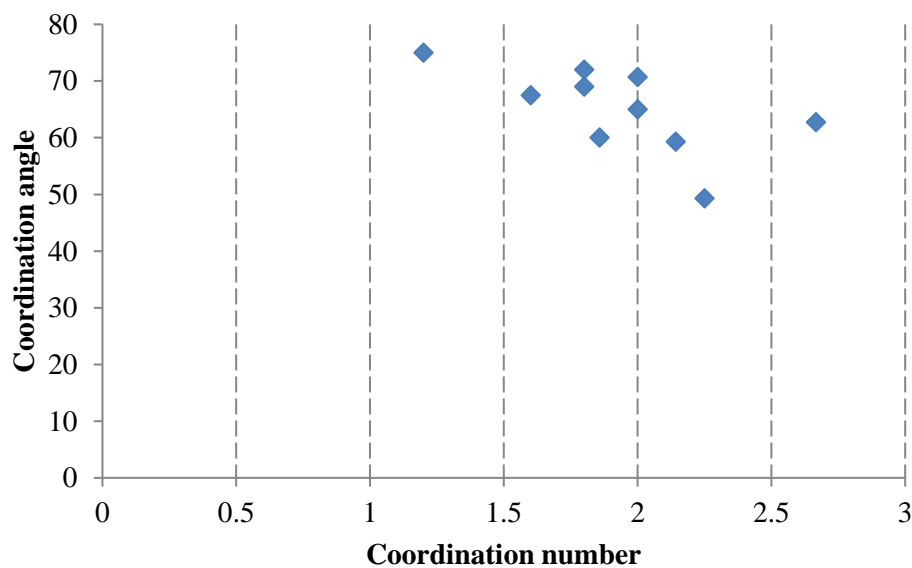
Figure C 7. Coordination angle as a function of the coordination number for zeolite pellets produced at rotational velocity of 0.74 m/s, processing time of 15 min and binder content of 0.053 g/g
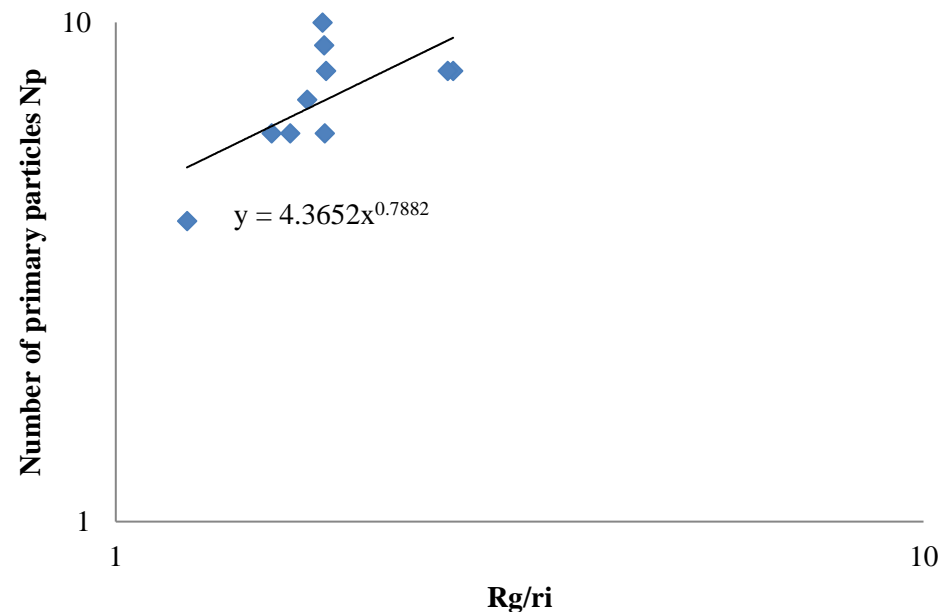
Figure C 8. Primary particle number as a function of normalized radius of gyration for zeolite pellets produced at rotational speed of 0.74 m/s, processing time of 15 min and with binder content of 0.053 g/g

Tabelle C 3: Results from μ-CT data evaluation received for zeolite pellets produced at rotational velocity 0.17 m/s, processing time of 15 minutes and with binder content of 0.109 g/g

N_p	r_i in mm	R_g in mm	$d_{c,max}$ in mm	$d_{c,max}/2R_g$	Porosity			Coordination number	Coordination angle in °
					From R_g	From CH	From dilation		
8	0.825	1.42	4.35	1.54	0.26	0.42	0.34	1.86	60.00
11	0.825	1.67	5.22	1.59	0.36	0.37	0.49	2.33	68.70
6	0.825	1.35	3.84	1.42	0.36	0.42	0.33	1.80	79.20
6	0.825	1.26	3.58	1.42	0.22	0.42	0.54	2.20	55.50
15	0.825	1.77	5.39	1.52	0.30	0.39	0.45	3.75	63.74
11	0.825	1.63	5.01	1.54	0.33	0.35	0.37	2.11	65.67
12	0.825	1.71	5.42	1.58	0.38	0.40	0.28	2.88	65.25
10	0.825	1.62	4.88	1.51	0.38	0.38	0.34	1.00	126.00
9	0.825	1.51	4.18	1.39	0.31	0.36	0.48	2.43	50.00
9	0.825	1.56	4.28	1.37	0.39	0.40	0.50	1.63	55.20
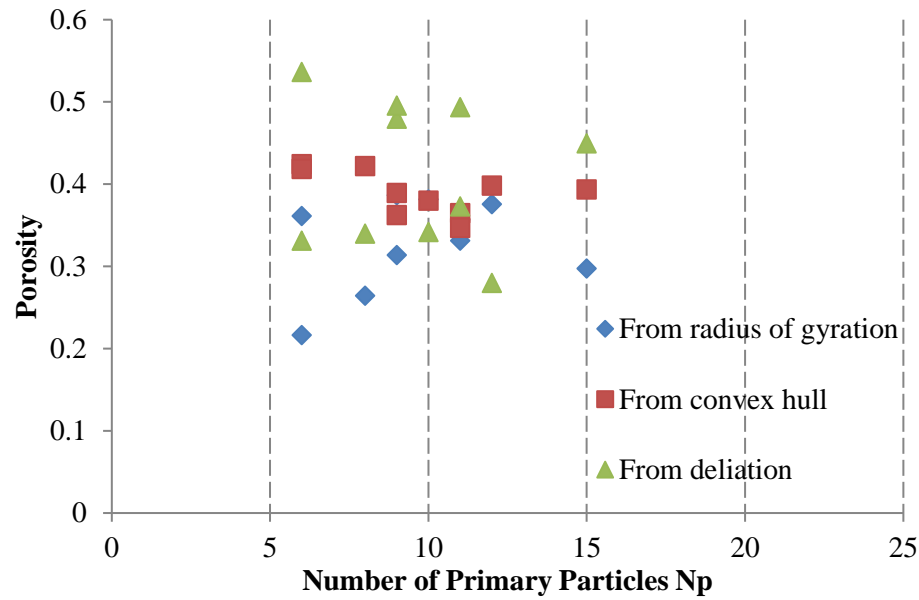
Figure C 9. Comparison between porosities calculated by three different methods for zeolite pellets produced at rotational speed of 0.74 m/s, processing time of 15 min and with binder content of 0.053 g/g
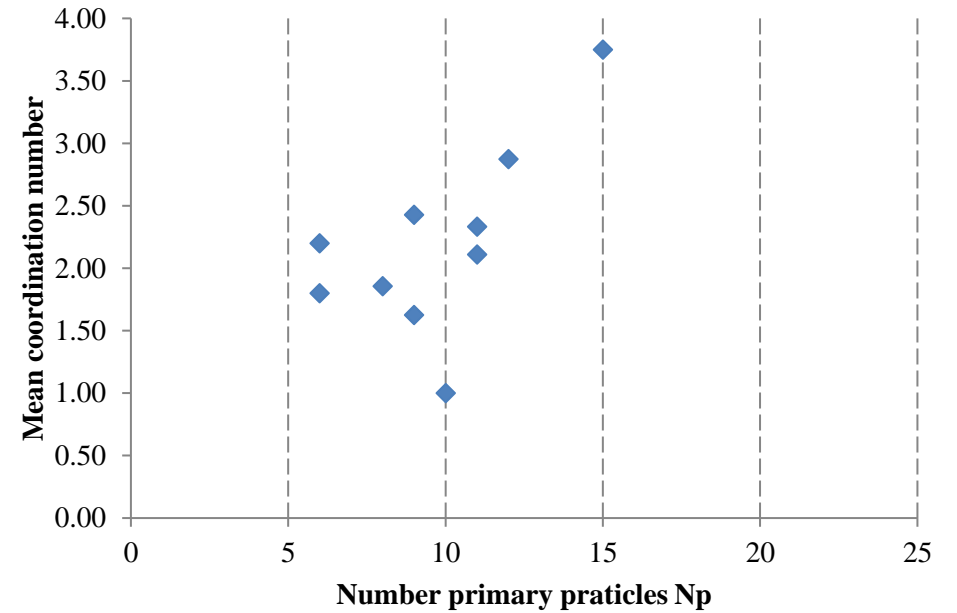
Figure C 10. Mean coordination number as a function of the primary particles number for zeolite pellets produced at rotational velocity of 0.74 m/s, processing time of 15 min and binder content of 0.053 g/g
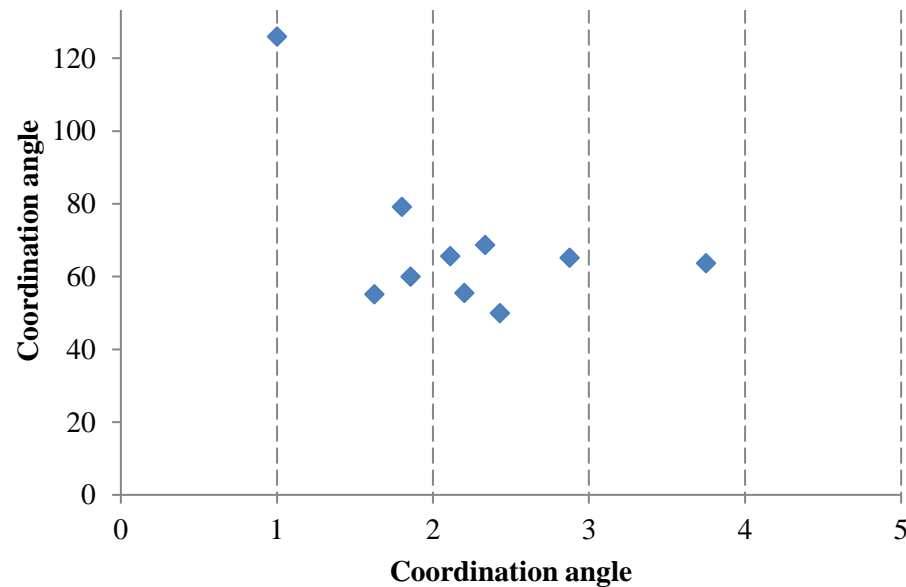
Figure C 11. Coordination angle as a function of the coordination number for zeolite pellets produced at rotational velocity of 0.74 m/s, processing time of 15 min and binder content of 0.053 g/g

$$y = 1.8455x^{2.6029}$$
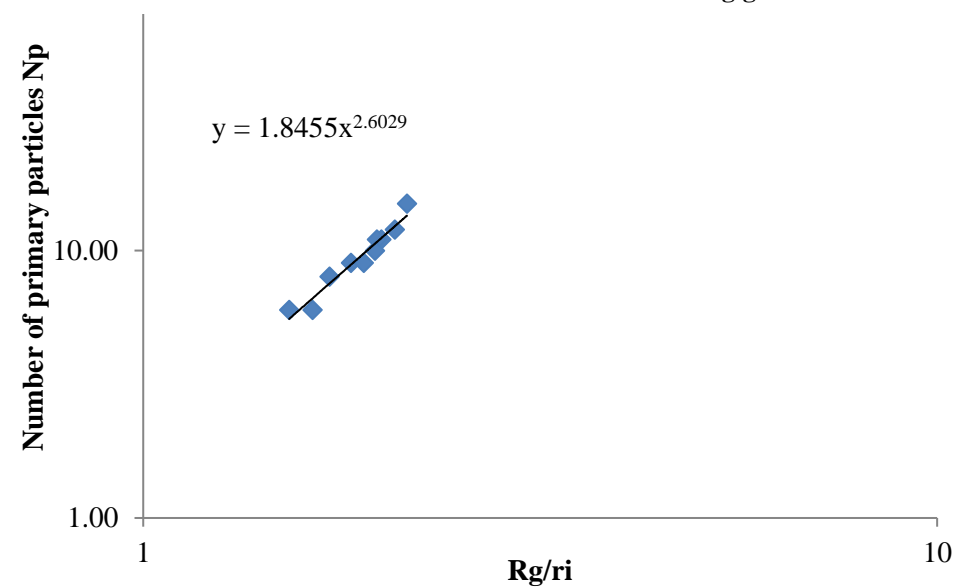
Figure C 12. Primary particle number as a function of normalized radius of gyration for zeolite pellets produced at rotational speed of 0.74 m/s, processing time of 15 min and with binder content of 0.053 g/g

Tabelle C 4: Results from μ-CT data evaluation received for zeolite pellets produced at rotational velocity 0.74 m/s, processing time of 15 minutes and with binder content of 0.109 g/g

N_p	r_i in mm	R_g in mm	$d_{c,max}$ in mm	$d_{c,max}/2R_g$	Porosity			Coordination number	Coordination angle in °
					From R_g	From CH	From dilation		
7	0.825	1.52	4.58	1.51	0.38	0.39	0.51	1.29	66.00
7	0.825	1.49	4.30	1.44	0.41	0.43	0.39	1.50	86.25
7	0.825	1.48	3.85	1.31	0.43	0.41	0.44	2.17	57.75
7	0.825	1.50	4.39	1.46	0.46	0.43	0.48	1.50	67.50
7	0.825	1.29	3.65	1.41	0.27	0.36	0.37	1.50	71.25
5	0.825	0.99	5.22	2.61	0.24	0.31	0.47	2.00	65.00
5	0.825	1.15	5.34	2.32	0.14	0.32	0.50	2.00	55.00
11	0.825	1.74	5.60	1.61	0.45	0.31	0.43	1.70	66.67
7	0.825	1.61	4.95	1.54	0.56	0.28	0.50	1.00	82.50
8	0.825	2.66	5.38	1.01	0.61	0.30	0.52	1.29	90.00
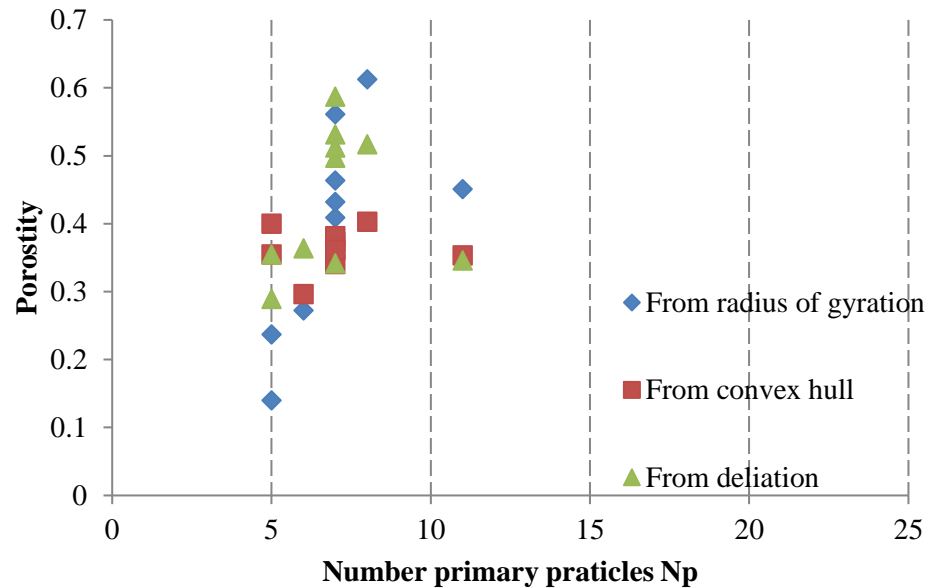
Figure C 13. Comparison between porosities calculated by three different methods for zeolite pellets produced at rotational speed of 0.74 m/s, processing time of 15 min and with binder content of 0.109 g/g
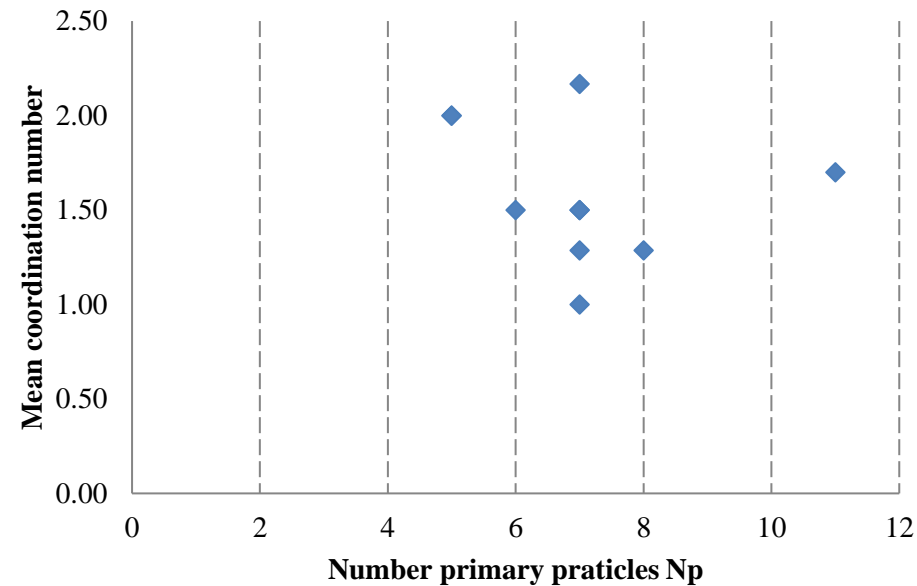
Figure C 14. Mean coordination number as a function of the primary particles number for zeolite pellets produced at rotational velocity of 0.74 m/s, processing time of 15 min and binder content of 0.109 g/g
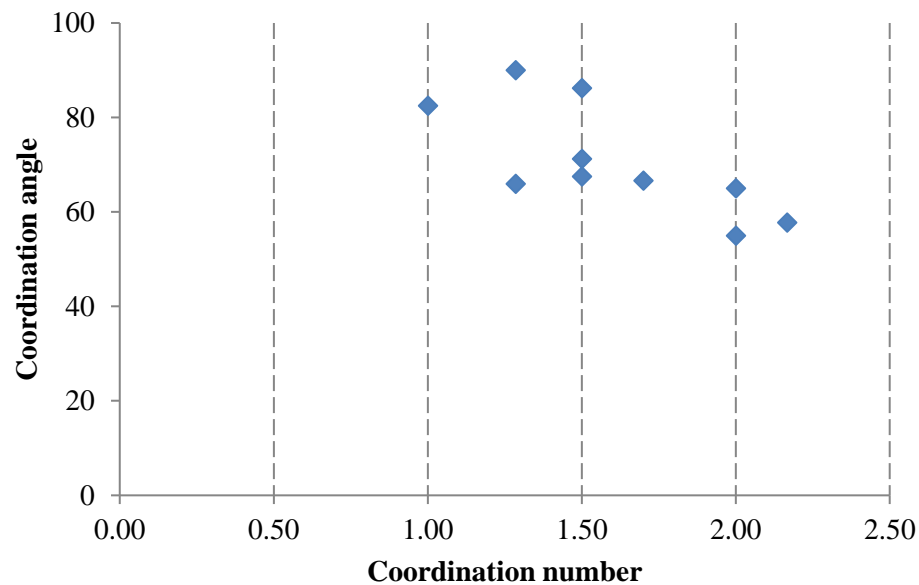
Figure C 15. Coordination angle as a function of the coordination number for zeolite pellets produced at rotational velocity of 0.74 m/s, processing time of 15 min and binder content of 0.109 g/g
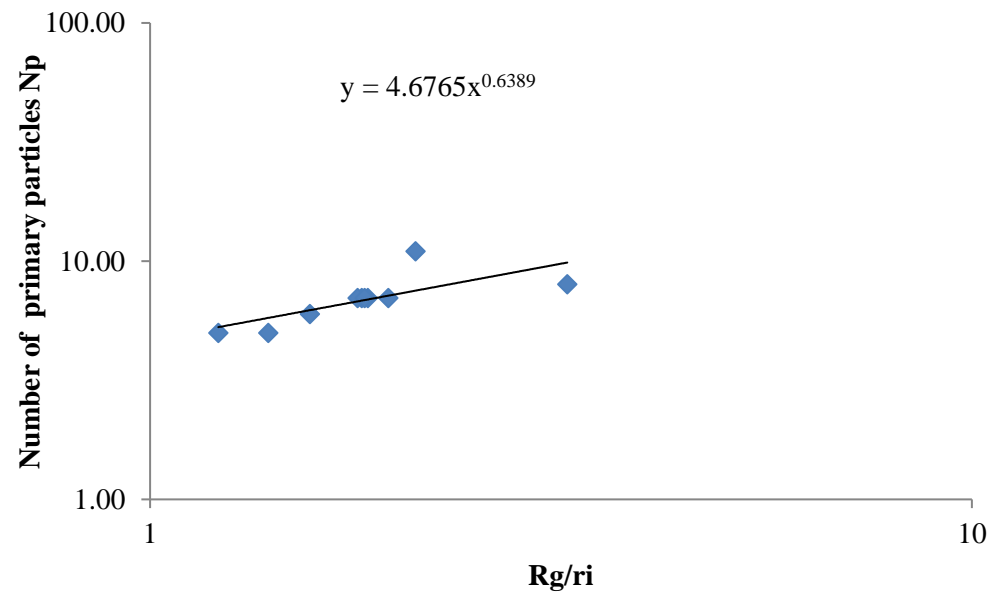
Figure C 16. Primary particle number as a function of normalized radius of gyration for zeolite pellets produced at rotational speed of 0.74 m/s, processing time of 15 min and with binder content of 0.109 g/g

Tabelle C 5: Results from μ-CT data evaluation received for zeolite pellets produced at rotational velocity 0.17 m/s, processing time of 30 minutes and with binder content of 0.109 g/g

N_p	r_i in mm	R_g in mm	$d_{c,max}$ in mm	$d_{c,max}/2R_g$	Porosity From R_g	Porosity From CH	Porosity From dilation	Coordination number	Coordination angle in °
14	0.825	1.64	5.77	1.76	0.29	0.35	0.34	2.93	58.78
15	0.825	1.32	6.11	2.32	0.34	0.40	0.55	2.71	77.13
11	0.825	1.35	5.46	2.02	0.41	0.42	0.37	2.00	56.70
12	0.825	1.25	0.55	0.22	0.35	0.37	0.34	5.36	44.78
7	0.825	1.42	4.66	1.64	0.66	0.38	0.44	2.29	58.50
11	0.825	1.12	5.25	2.36	0.36	0.35	0.41	1.89	61.50
8	0.825	1.36	0.43	0.16	0.40	0.33	0.44	3.86	36.54
8	0.825	1.43	4.78	1.68	0.39	0.23	0.37	2.00	88.20
14	0.825	1.57	5.80	1.85	0.38	0.31	0.31	2.64	71.21
8	0.825	1.54	5.64	1.83	0.69	0.42	0.51	2.73	76.38
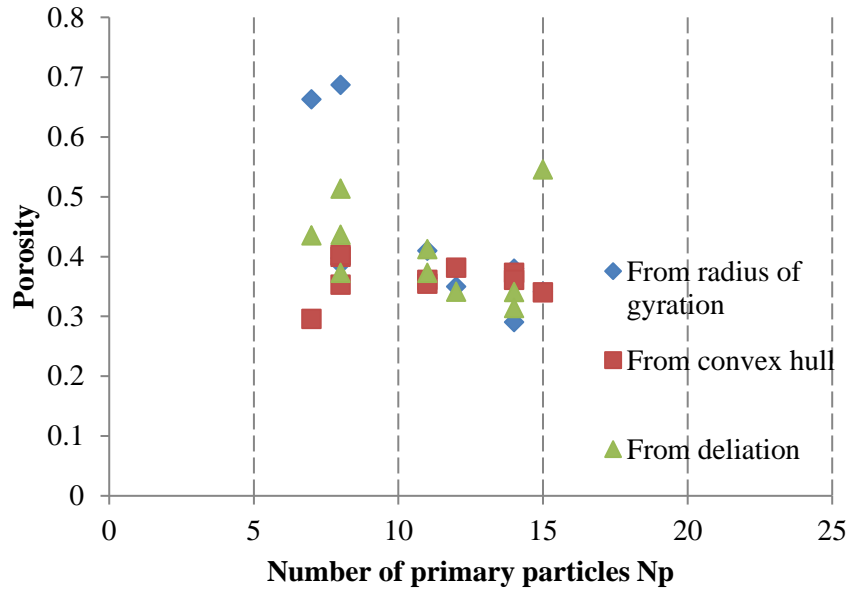
Figure C 17. Comparison between porosities calculated by three different methods for zeolite pellets produced at rotational speed of 0.74 m/s, processing time of 30 min and with binder content of 0.109 g/g
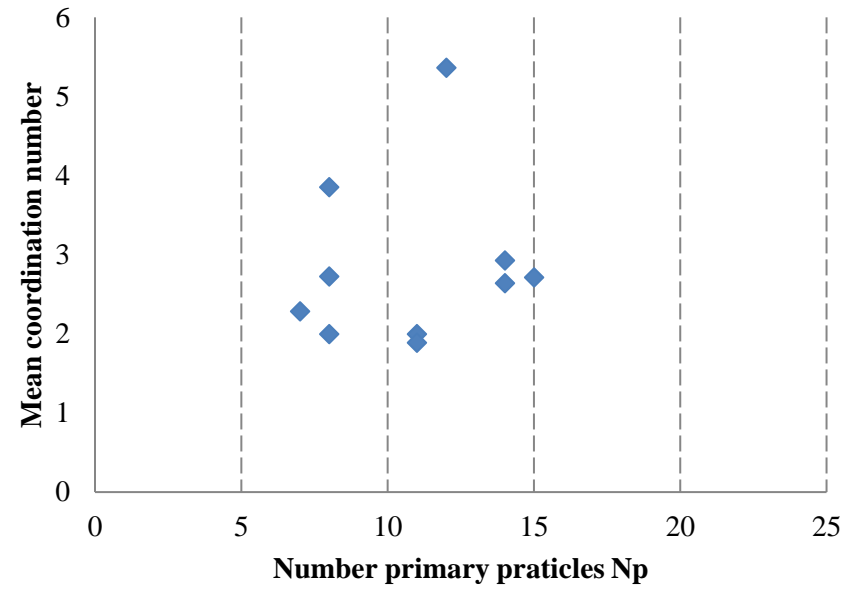
Figure C 18. Mean coordination number as a function of the primary particles number for zeolite pellets produced at rotational velocity of 0.74 m/s, processing time of 30 min and binder content of 0.109 g/g
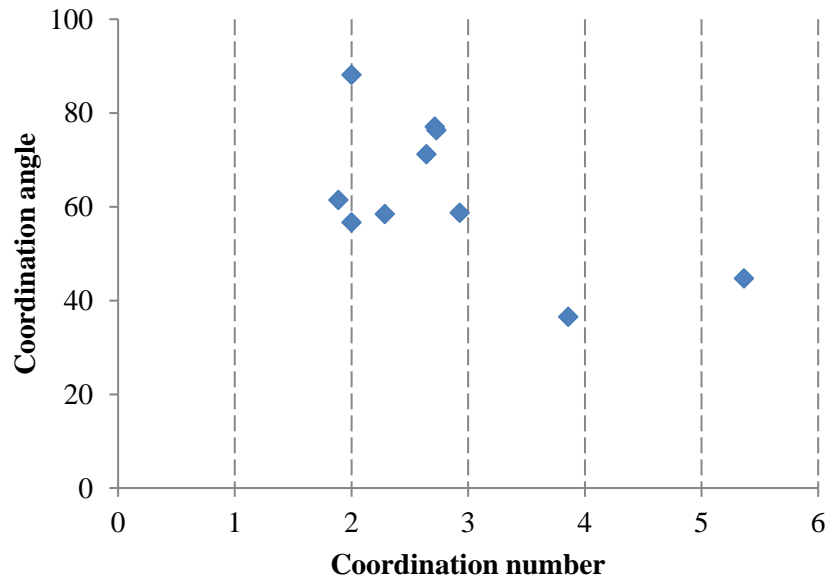
Figure C 19. Coordination angle as a function of mean coordination number for zeolite pellets produced at rotational velocity of 0.74 m/s, processing time of 30 min and binder content of 0.109 g/g

$y = 9.5209x^{0.1235}$
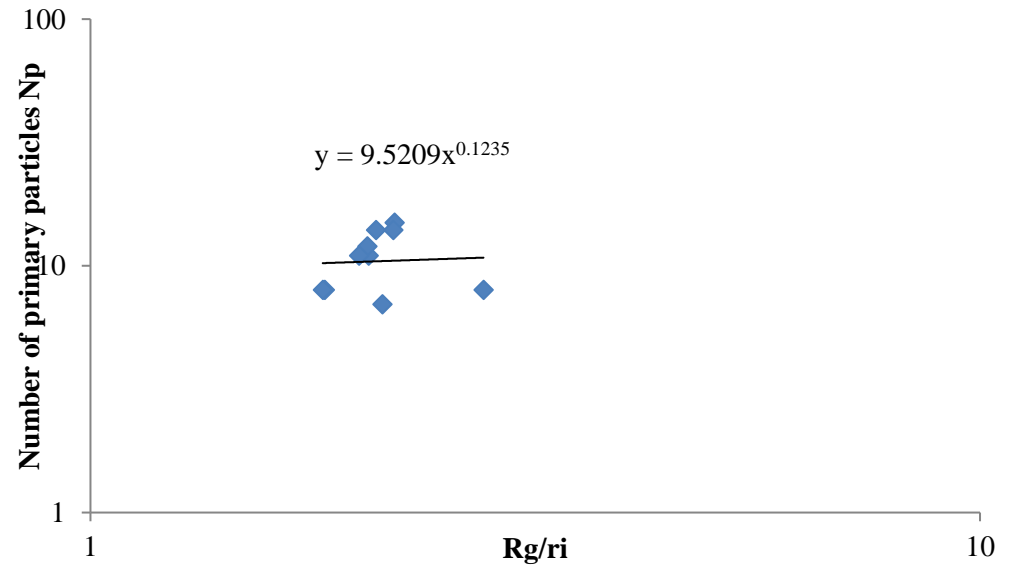
Figure C 20. Primary particle number as a function of normalized radius of gyration for zeolite pellets produced at rotational speed of 0.74 m/s, processing time of 30 min and with binder content of 0.109 g/g

Tabelle C 6: Results from μ-CT data evaluation received for zeolite pellets produced at rotational velocity 0.74 m/s, processing time of 30 minutes and with binder content of 0.109 g/g

N_p	r_i in mm	R_g in mm	$d_{c,max}$ in mm	$d_{c,max}/2R_g$	Porosity			Coordination number	Coordination angle in °
					From R_g	From CH	From dilation		
11	0.825	1.74	5.23	1.50	0.46	0.46	0.37	1.60	71.67
7	0.825	1.47	4.33	1.47	0.43	0.39	0.55	1.50	52.86
12	0.825	1.34	4.26	1.59	0.23	0.19	0.36	2.73	61.23
8	0.825	1.41	4.46	1.58	0.25	0.37	0.48	2.14	86.00
6	0.825	1.45	3.68	1.27	0.49	0.35	0.46	1.31	63.00
7	0.825	1.34	3.94	1.47	0.25	0.33	0.34	2.14	56.00
5	0.825	1.17	3.07	1.32	0.18	0.33	0.42	2.00	65.00
5	0.825	0.97	3.41	1.76	0.30	40.99	0.43	1.75	71.25
4	0.825	1.01	2.59	1.28	0.38	0.28	0.34	2.00	65.00
17	0.825	2.27	8.08	1.78	0.62	0.51	0.46	2.62	72.77
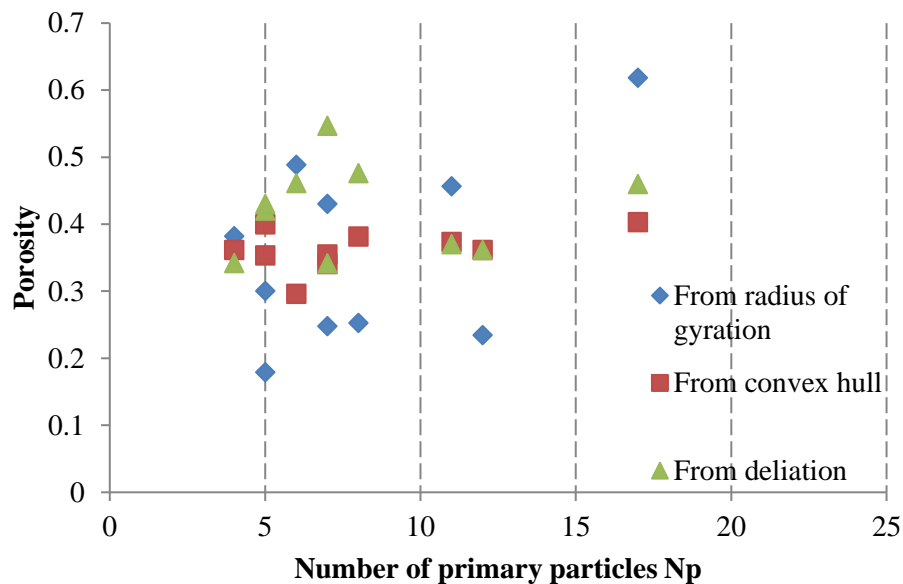
Figure C 21. Comparison between porosities calculated by three different methods for zeolite pellets produced at rotational speed of 0.74 m/s, processing time of 30 min and with binder content of 0.109 g/g
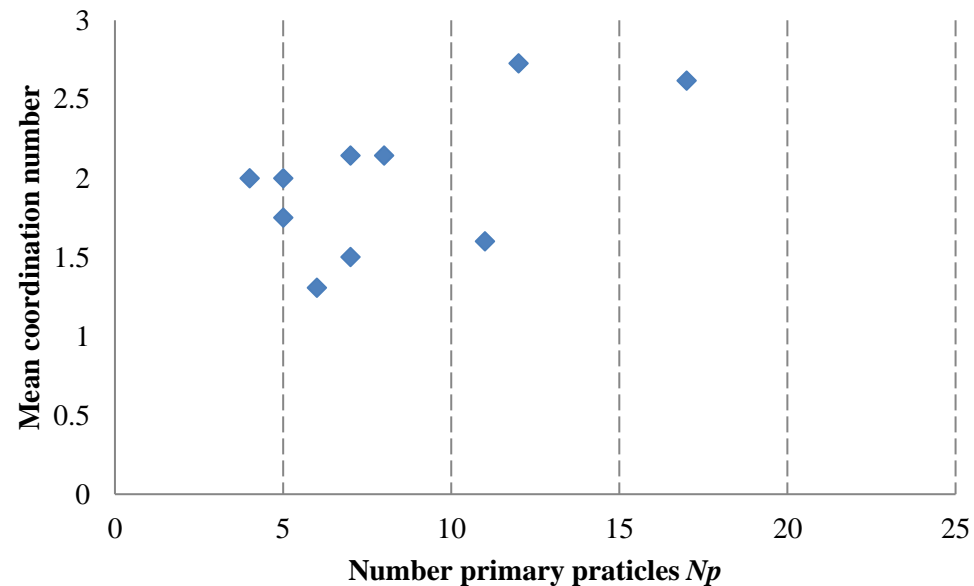
Figure C 22. Mean coordination number as a function of the primary particles number for zeolite pellets produced at rotational velocity of 0.74 m/s, processing time of 30 min and binder content of 0.109 g/g
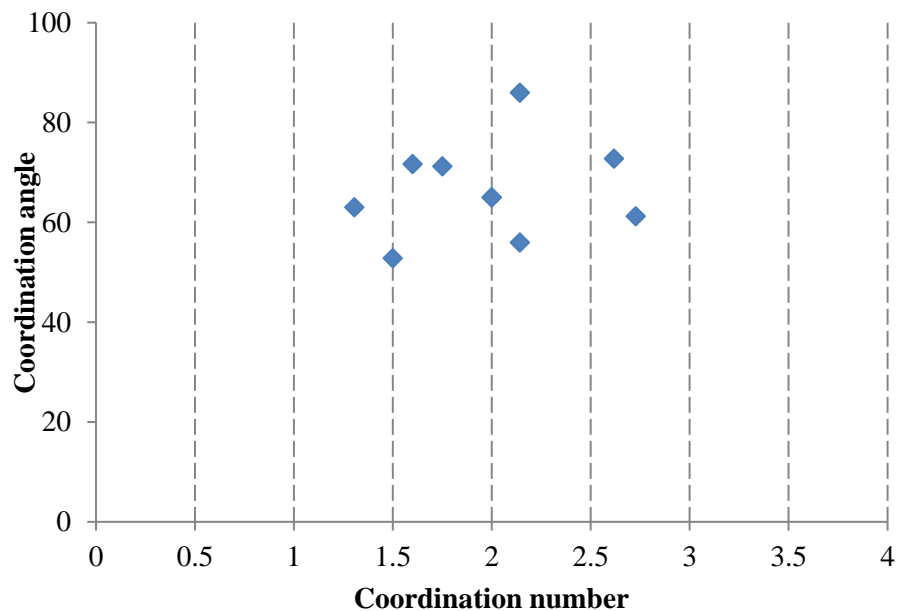
Figure C 23. Coordination angle as a function of the coordination number for zeolite pellets produced at rotational velocity of 0.74 m/s, processing time of 30 min and binder content of 0.109 g/g
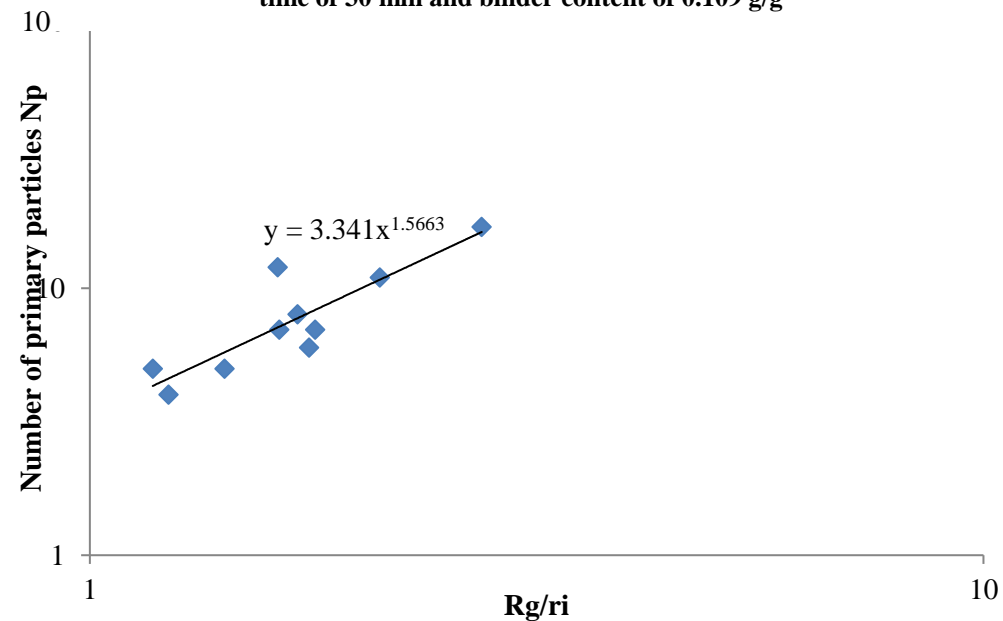
Figure C 24. Normalized radius of gyration as a function of the primary particle number for zeolite pellets produced at rotational speed of 0.74 m/s, processing time of 30 min and with binder content of 0.109 g/g

Tabelle C 7: Results from µ-CT data evaluation received for zeolite pellets produced at rotational velocity 0.17 m/s, processing time of 30 minutes and with binder content of 0.053 g/g

N_p	r_i in mm	R_g in mm	$d_{c,max}$ in mm	$d_{c,max}/2R_g$	Porosity			Coordination number	Coordination angle in °
					From R_g	From CH	From dilation		
10	0.825	1.64	5.14	1.57	0.47	0.43	0.51	2.11	69.00
8	0.825	1.32	4.83	1.84	0.31	0.41	0.49	1.71	65.00
10	0.825	1.35	4.99	1.85	0.36	0.39	0.33	2.00	56.14
8	0.825	1.25	3.78	1.52	0.33	0.36	0.33	2.00	57.00
7	0.825	1.42	5.26	1.85	0.37	0.37	0.42	2.50	55.96
10	0.825	1.12	4.42	1.98	0.25	0.37	0.47	2.56	50.14
9	0.825	1.36	4.58	1.68	0.38	0.40	0.50	2.50	55.96
9	0.825	1.43	4.97	1.75	0.28	0.44	0.38	2.13	59.57
11	0.825	1.57	5.12	1.63	0.33	0.39	0.43	2.20	66.60
8	0.825	1.54	4.67	1.52	0.43	0.43	0.40	1.56	68.25
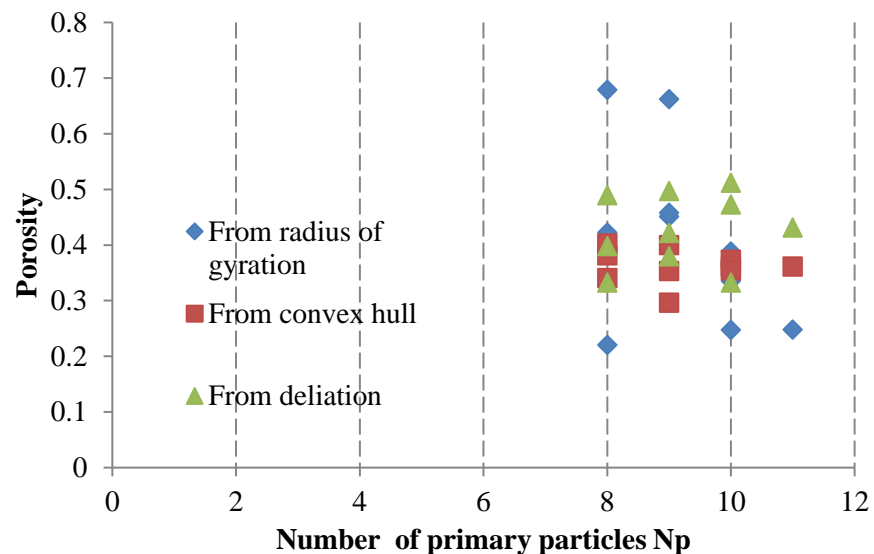
Figure C 26. Comparison between porosities calculated by three different methods for zeolite pellets produced at rotational speed of 0.17 m/s, processing time of 30 min and with binder content of 0.053 g/g
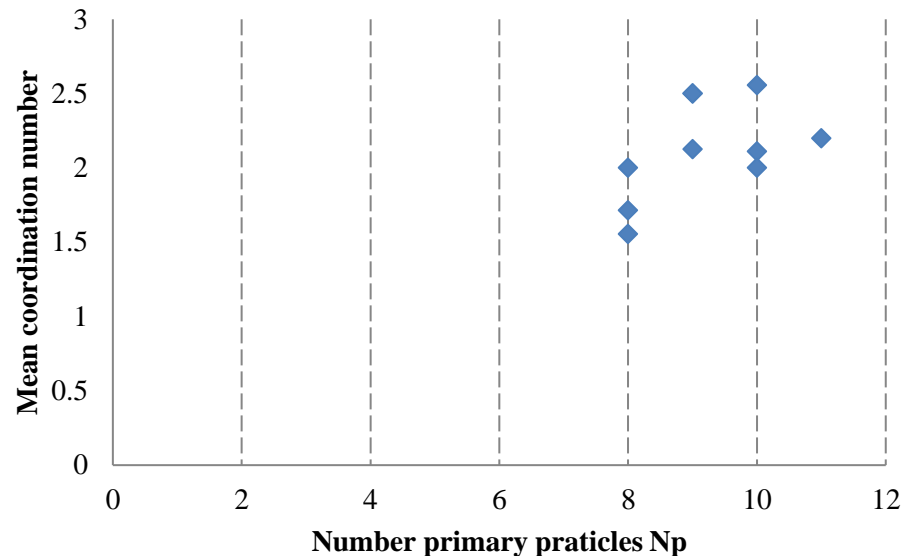
Figure C 27. Mean coordination number as a function of the primary particles number for zeolite pellets produced at rotational velocity of 0.17 m/s, processing time of 30 min and binder content of 0.053 g/g
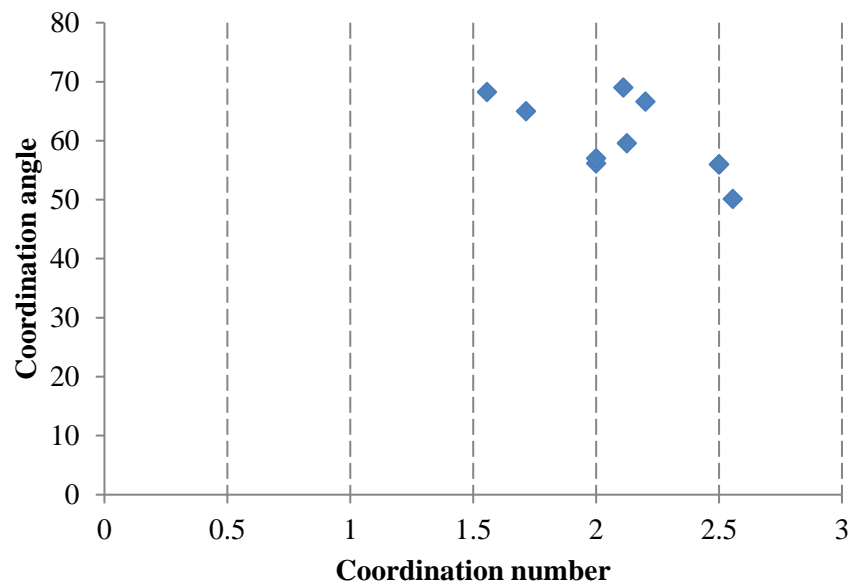
Figure C 28. Coordination angle as a function of the coordination number for zeolite pellets produced at rotational velocity of 0.17 m/s, processing time of 30 min and binder content of 0.053 g/g

$$y = 7.9894x^{0.1527}$$
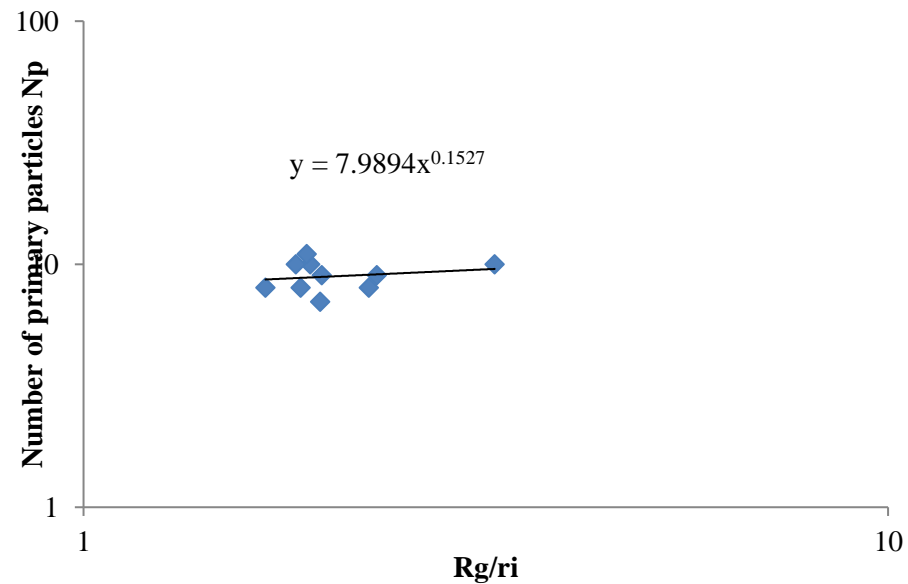
Figure C 29. Normalized radius of gyration as a function of the primary particle number for alumina pellets produced at rotational speed of 0.17 m/s, processing time of 30 min and with binder content of 0.053 g/g

Tabelle C 8: Results from μ-CT data evaluation received for zeolite pellets produced at rotational velocity 0.74 m/s, processing time of 30 minutes and with binder content of 0.053 g/g

N_p	r_i in mm	R_g in mm	$d_{c,max}$ in mm	$d_{c,max}/2R_g$	Porosity			Coordination number	Coordination angle in °
					From R_g	From CH*	From dilation		
12	0.825	1.64	5.80	1.77	0.46	0.35	0.49	2.09	50.25
9	0.825	1.32	5.15	1.96	0.48	0.36	0.45	2.00	55.00
10	0.825	1.35	4.92	1.82	0.28	0.37	0.49	2.67	55.74
9	0.825	1.25	4.90	1.96	0.46	0.39	0.48	1.88	65.14
7	0.825	1.42	4.44	1.56	0.24	0.44	0.49	2.43	52.00
9	0.825	1.12	4.81	2.16	0.31	0.31	0.34	2.50	50.29
10	0.825	1.36	4.66	1.71	0.41	0.32	0.53	1.78	66.38
7	0.825	1.43	4.21	1.48	0.33	0.31	0.39	2.00	66.43
12	0.825	1.57	5.46	1.74	0.34	0.38	0.37	2.91	50.39
8	0.825	1.54	4.85	1.57	0.92	0.41	0.51	2.38	46.79
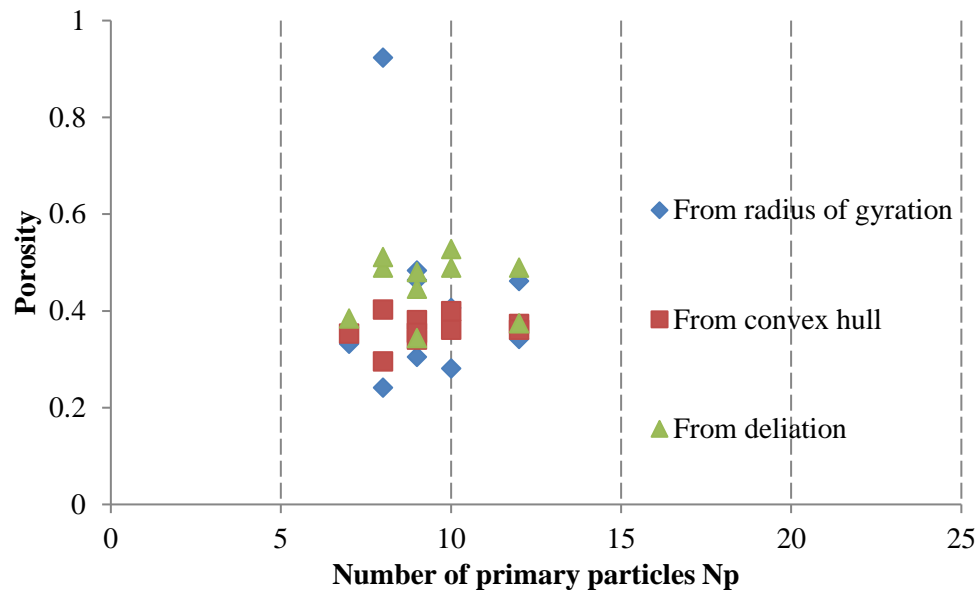
Figure C 30. Comparison between porosities calculated by three different methods for zeolite pellets produced at rotational speed of 0.74 m/s, processing time of 15 min and with binder content of 0.053 g/g
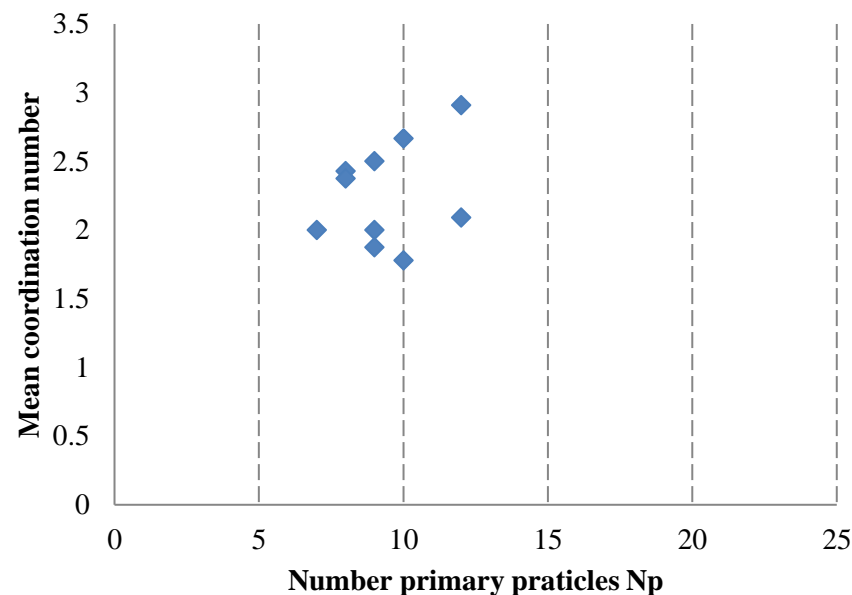
Figure C 31. Mean coordination number as a function of the primary particles number for zeolite pellets produced at rotational velocity of 0.74 m/s, processing time of 15 min and binder content of 0.053 g/g
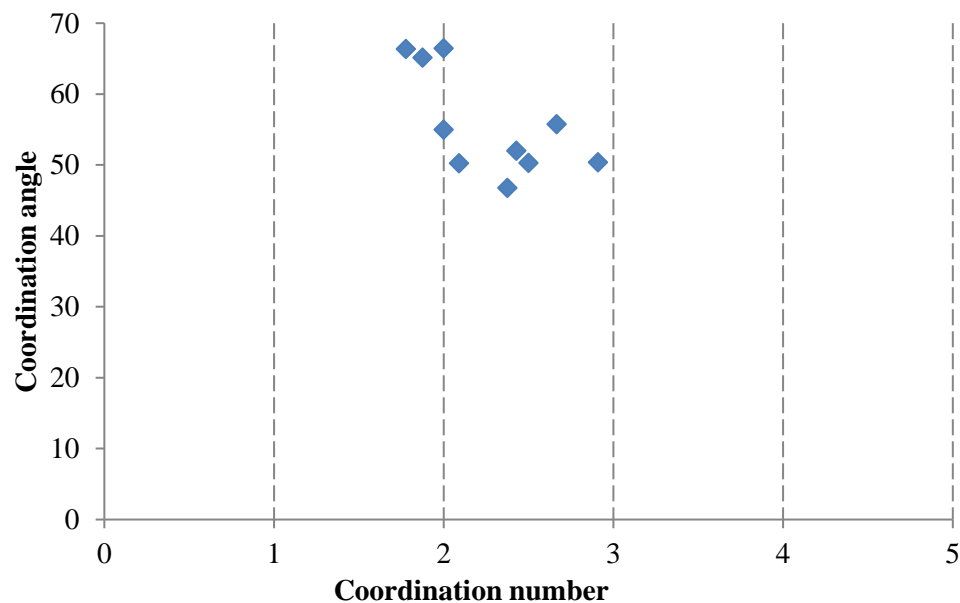
Figure C 32. Coordination angle as a function of the coordination number for zeolite pellets produced at rotational velocity of 0.74 m/s, processing time of 15 min and binder content of 0.053 g/g

$y = 8.6996x^{0.0708}$
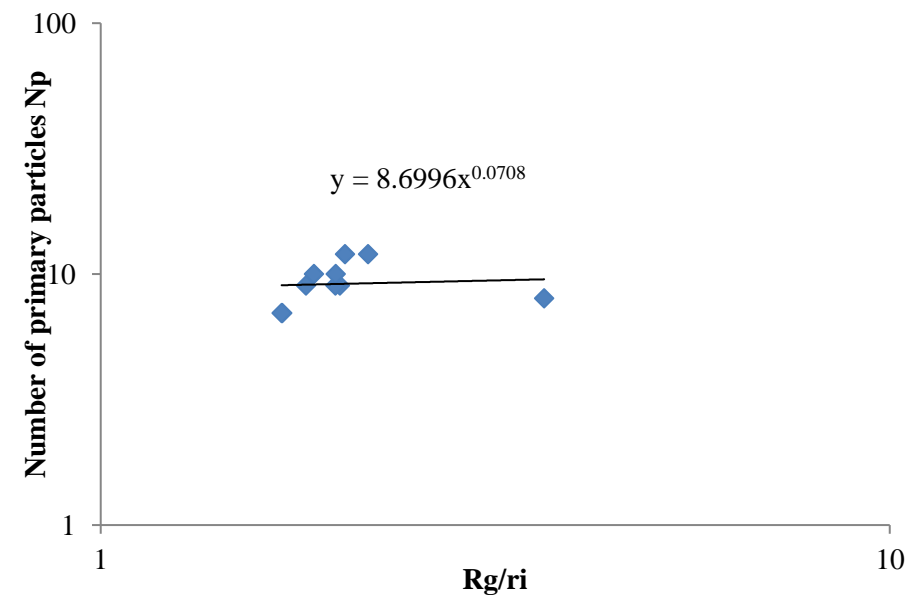
Figure C 33. Normalized radius of gyration as a function of the primary particle number for zeolite pellets produced at rotational speed of 0.74 m/s, processing time of 15 min and with binder content of 0.053 g/g
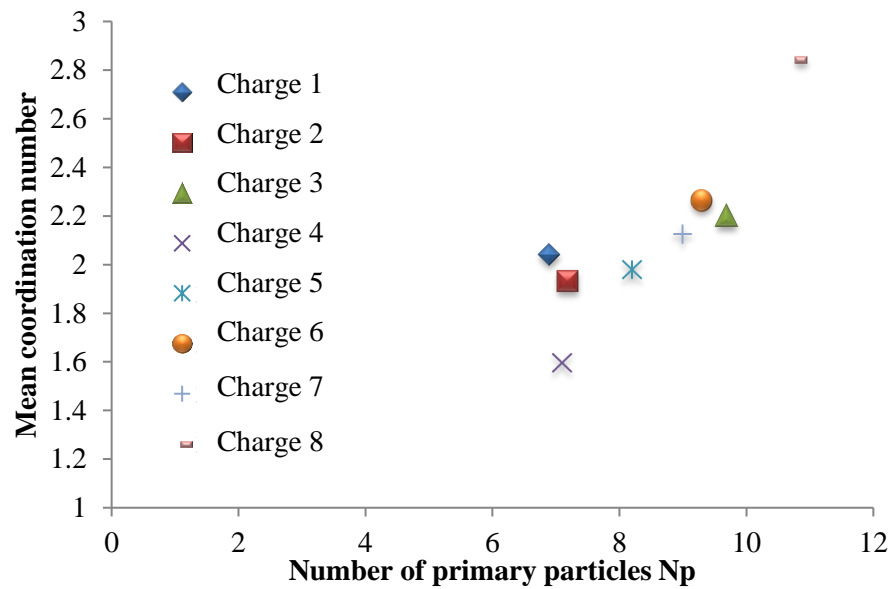
Figure C 34. Mean coordination number as a function of the primary particle number for zeolite charges
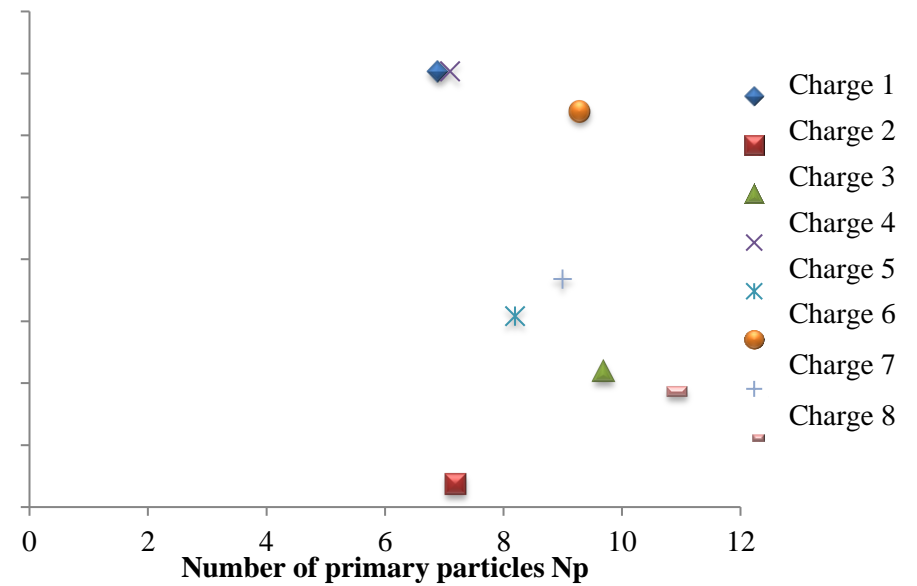
Figure C 35. Comparison of porosity of different zeolite charges, calculated from radius of gyration
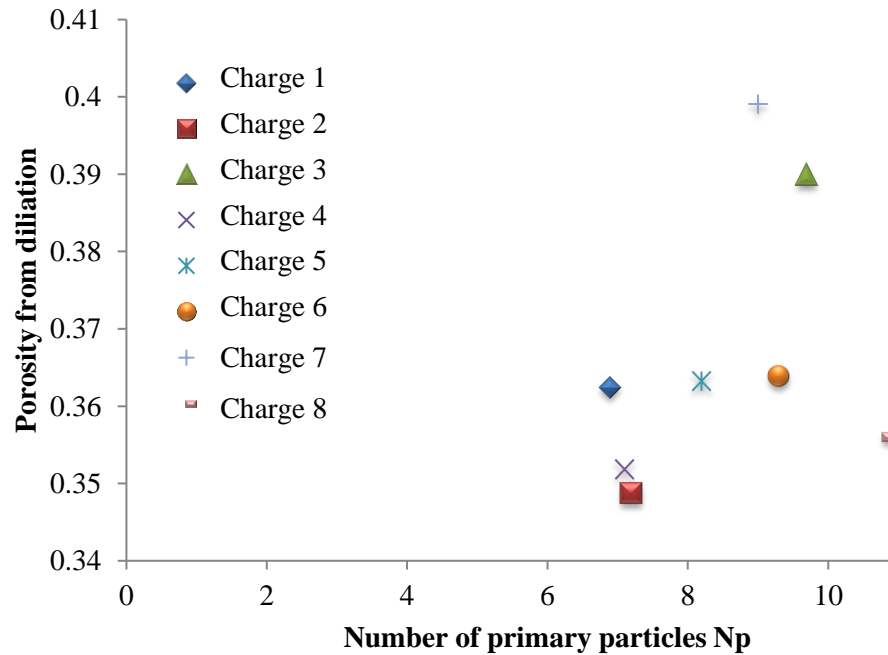
Figure C 36. Comparison of porosity of different zeolite charges, calculated by dilation
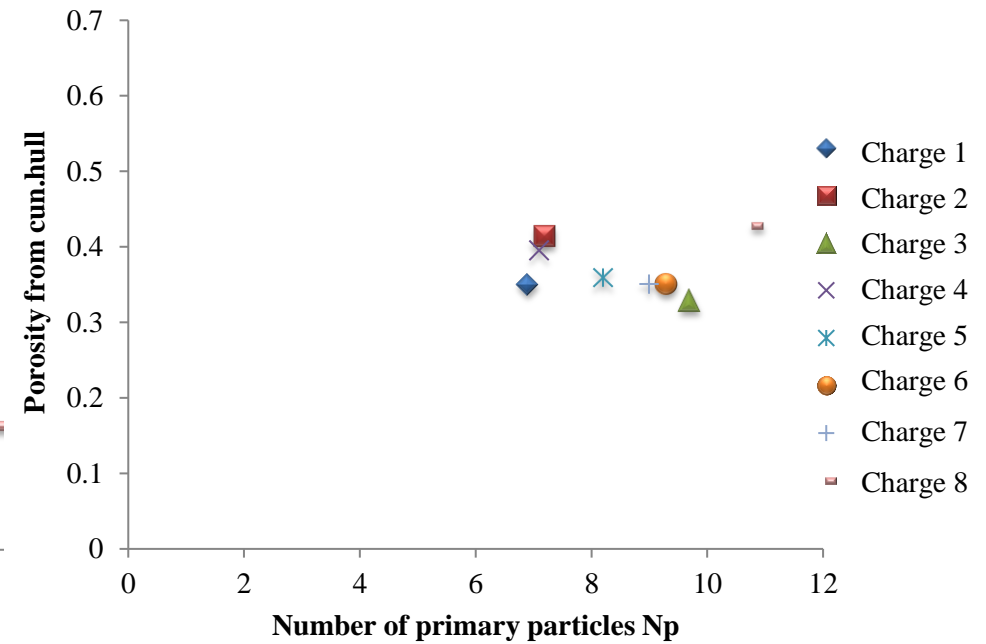
Figure C 37. Comparison of porosity of different zeolite charges, calculated from convex hull

Attachment D: List of bachelor and master thesises complited in the phrames of the thesis

1. L. Schneider, Agglomeration und Charakterisierung tetraederförmiger Agglomerate, supervisors: P. Müller, Z.R. Radeva, J. Tomas, Bachelor thesis, 2013
2. A. Hameed, Agglomeration of elastic-plastic agglomerates, supervisors: P. Müller, Z.R. Radeva, J. Tomas, Master thesis, 2012/13
3. F. Butt, Comparison between the agglomeration behaviour of γ-$A_{l2}O_3$ and Zeolite 4A granules. Influence of the process duration on the received agglomerate's properties, supervisors: P. Müller, Z.R. Radeva, J. Tomas, Master thesis, 2013/14
4. S. Xue, DEM simulations of the breakage of irregular model-pellets due to compression, supervisors: Z. Radeva, P. Müller, Master thesis, 2016/17

Attachment E: Licence agreements

LICENCE AGREEMENT

between

FEECO International Inc.

3913 Algoma Road, Green Bay, WI 54311-9707 USA

and

M.Sc. Zheni Radeva

Chair for Mechanical Process Engineering, University of Magdeburg, Germany

With this Licence Agreement the copyrights holder (FEECO International Inc.) allows the user (M.Sc Zheni Radeva) to use image of FEECO Disc Pelletizer from FEECO AGGLOMERATION HANDBOOK as an example of inclined disc pelletizer in her doctoral dissertation with title "Analysis and Simulation of the Deformation Behaviour at Quasi-Static Compressive Stressing of Bonded Model Pellets", accomplished at the Chair of Mechanical Process Engineering, Otto von Guericke University, Magdeburg, Germany.

Distribution or any other uses, not mentioned in this agreement are not permitted.

M.Sc. Zheni Radeva, Otto von Guericke
University of Magdeburg
Chair of Mechanical Process Engineering
Universitätsplatz 2
39106 Magdeburg Germany

Signature _____

Date __10.12.2018__

FEECO International Inc.
3913 Algoma Road, Green Bay, WI
54311-9707 USA

Signature _____

Date ___12 - 06 - 2018___